NUREG/CR-0868
LA-7867-PR
Progress Report

Nuclear Reactor Safety

Quarterly Progress Report

January 1—March 31, 1979

University of California

7908140104

634 049

LOS ALAMOS SCIENTIFIC LABORATORY
Post Office Box 1663 Los Alamos, New Mexico 87545

The four most recent reports in this series, unclassified, are NUREG/CR-0062 LA-7278-PR, NUREG/CR-0385 LA-7481-PR, NUREG/CR-0522 LA-7567-PR, and NUREG/CR-0762 LA-7769-PR.

This report was not edited by the Technical Information staff.

Work supported by the US Department of Energy, Division of Reactor Development and Demonstration.

NUREG/CR-0868
LA-7867-PR
Progress Report

R4, R7, and R8

Nuclear Reactor Safety

Quarterly Progress Report

January 1—March 31, 1979

Compiled by

James F. Jackson
Michael G. Stevenson

Manuscript submitted: May 1979
Date published: June 1979

Prepared for
Office of Nuclear Regulatory Research
Division of Reactor Safety Research
Office of Nuclear Reactor Regulation
Division of Systems Safety
US Nuclear Regulatory Commission
Washington, DC 20555

UNITED STATES
DEPARTMENT OF ENERGY
CONTRACT W-7405-ENG. 36

634 051

CONTENTS

CONTENTS (cont)

CONTENTS (cont)

CONTENTS (cont)

634 055

CONTENTS (cont)

CONTENTS (cont)

TABLES

634 057

TABLES (cont)

TABLES (cont)

FIGURES

FIGURES (cont)

FIGURES (cont)

FIGURES (cont)

FIGURES (cont)

FIGURES (cont)

634 065

ABSTRACT

An important milestone was reached this quarter with the release of the TRAC-P1A LWR safety analysis code to the National Energy Software Center. Prior to this release, a rather extensive set of assessment problems was successfully completed and will be documented in the near future. A posttest parametric study of the LOFT L2-2 test was completed using TRAC. This study showed that TRAC's ability to predict the early rewet behavior exhibited in the test is very sensitive to the minimum film boiling temperature correlation. It was found that TRAC predicts the initial rewet and dryout if the high-pressure correlation of Iloeje is used. An initial TRAC calculation of a complete LOCA sequence in a typical German PWR was completed in support of the multinational 2D/3D program. Combined injection studies of the Japanese Slab Core Test Facility were also performed to help determine the steam supply requirements for cold- and hot-leg injection tests. A new critical flow vapor production model was developed and successfully tested against Semiscale and Marviken data. The discrete-droplet model code, SPRAY, was improved by including the effect of splashing when droplets impinge on structural components. The initial stereo lens probe for use in the PKL test facility was completed, tested, and shipped to West Germany.

The SIMMER LMFBR disrupted core analysis code was used for the first time to examine the postdisassembly ejection of primary system materials into the reactor containment building. Other LMFBR safety research work involved using a statistical sensitivity study to determine an optimal set of numerical solution control parameters for SIMMER. The first Upper Structure Dynamics experiment to provide data for SIMMER postdisassembly expansion testing was performed successfully. SIMMER calculations of the two-phase blowdown mixture velocities are in qualitative agreement with the experiment.

In HTGR safety work, seismic tests on a two-dimensional plastic core block model were performed. Also, an evaluation was completed for the Fort St. Vrain reactor of the effect of region constraint devices on the seismic behavior of the core. In another area, checkout and documentation of the final version of the DASH fission product diffusion code were completed.

Preparation continued for a second 37-rod full-length subgroup (FLS) experiment simulating loss-of-cooling in a GCFR subassembly. A new wave-spring rod spacer-grid was fabricated and tested and is expected to lead to longer heater (simulated fuel) rod life.

In the area of reactor containment evaluation, the COMPARE code was further evaluated by comparing calculated results with Battelle-Frankfurt standard problem data.

634 066

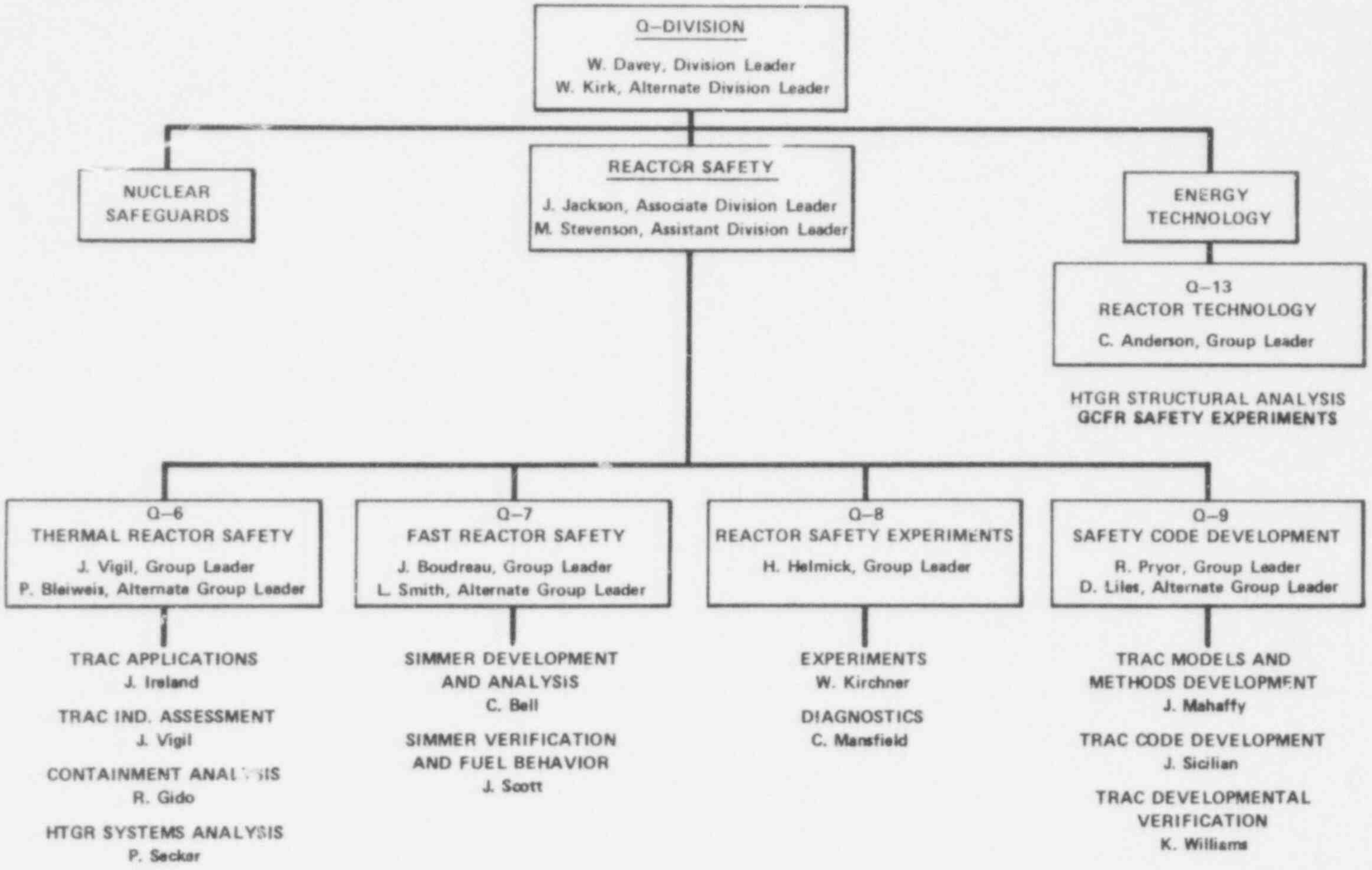
Q–DIVISION
W. Davey, Division Leader
W. Kirk, Alternate Division Leader
NUCLEAR SAFEGUARDS
REACTOR SAFETY
J. Jackson, Associate Division Leader
M. Stevenson, Assistant Division Leader
ENERGY TECHNOLOGY
Q–13
REACTOR TECHNOLOGY
C. Anderson, Group Leader
HTGR STRUCTURAL ANALYSIS
GCFR SAFETY EXPERIMENTS
Q–6
THERMAL REACTOR SAFETY
J. Vigil, Group Leader
P. Bleiweis, Alternate Group Leader
Q–7
FAST REACTOR SAFETY
J. Boudreau, Group Leader
L. Smith, Alternate Group Leader
Q–8
REACTOR SAFETY EXPERIMENTS
H. Helmick, Group Leader
Q–9
SAFETY CODE DEVELOPMENT
R. Pryor, Group Leader
D. Liles, Alternate Group Leader
TRAC APPLICATIONS
J. Ireland
TRAC IND. ASSESSMENT
J. Vigil
CONTAINMENT ANALYSIS
R. Gido
HTGR SYSTEMS ANALYSIS
P. Secker
SIMMER DEVELOPMENT AND ANALYSIS
C. Bell
SIMMER VERIFICATION AND FUEL BEHAVIOR
J. Scott
EXPERIMENTS
W. Kirchner
DIAGNOSTICS
C. Mansfield
TRAC MODELS AND METHODS DEVELOPMENT
J. Mahaffy
TRAC CODE DEVELOPMENT
J. Sicilian
TRAC DEVELOPMENTAL VERIFICATION
K. Williams

634 067

NUCLEAR REACTOR SAFETY

Compiled by
James F. Jackson
and
Michael G. Stevenson

I. INTRODUCTION

(J. F. Jackson and M. G. Stevenson, Q-DO)

This quarterly report summarizes technical progress from a continuing nuclear reactor safety research program conducted at the Los Alamos Scientific Laboratory (LASL). The reporting period is from January 1 to March 31, 1979. This research effort concentrates on providing an accurate and detailed understanding of the response of nuclear reactor systems to a broad range of postulated accident conditions. The bulk of the funding is provided by the U.S. Nuclear Regulatory Commission (NRC), with part of the advanced reactor work funded by the U.S. Department of Energy (DOE).

The report is mainly organized according to reactor type. Major sections deal with Light-Water Reactors (LWRs), Liquid Metal Fast Breeder Reactors (LMFBRs), High-Temperature Gas-Cooled Reactors (HTGRs), and Gas-Cooled Fast Reactors (GCFRs).

The research discussed was performed by several technical divisions and groups within LASL. The names and group affiliations of the individual staff members responsible for the work are given at the beginning of each section. Most of the work was performed in the reactor safety portion of the Energy (Q) Division. An organization chart showing the Q-Division groups with major reactor safety activities is presented on the facing page. Other divisions contributing to the program were the Theoretical (T) Division, Computer Science and Services (C) Division, the Systems, Analysis, and Assessment (S) Division, and the Dynamic Testing (M) Division.

II. LWR SAFETY RESEARCH

(J. F. Jackson, Q-DO)

Five major projects in LASL's light-water reactor safety research program are reported in this section. The first is the development and testing against experimental data of the Transient Reactor Analysis Code (TRAC). The second concentrates on the application of TRAC to the multinational 2D/3D LWR safety research program. The third area focuses on the independent assessment of the TRAC code by performing blind predictions of pertinent experiments. The fourth project involves component code development and thermal-hydraulic research in key LWR safety problem areas. The fifth, and final effort, is an experimental program that supports model development activities and provides advanced instrumentation for reactor safety experiments.

A. TRAC Code Development and Assessment

(R. J. Pryor, Q-9)

TRAC is an advanced, best estimate computer program for the analysis of postulated accidents in LWRs. It features a nonhomogeneous, nonequilibrium multidimensional fluid dynamics treatment; detailed heat transfer and reflood models; and a flow-regime-dependent constitutive equation package to describe the basic physical phenomena that occur under accident conditions. It calculates initial steady-state conditions and complete accident sequences in a continuous and consistent manner.

The first version of TRAC, called TRAC-P1, is primarily directed towards loss-of-coolant accidents (LOCAs) in pressurized water reactors (PWRs). A refinement of this version, called TRAC-P1A, was sent to the National Energy Software Center (NESC) in March for release. Later versions of the code will treat boiling water reactors (BWRs) and provide capabilities for Anticipated Transients Without Scram (ATWS), Reactivity Insertion Accidents (RIAs), and operational transient analyses.

634 069

As part of a closely coupled code assessment effort, TRAC is being applied to a broad range of water-reactor safety experiments. These experiments are designed to study separate and integral effects that occur during all phases of a LOCA. TRAC posttest calculations are compared with experimental results to evaluate the thermal-hydraulic models in the code. Pretest calculations are made to test the predictive capability of TRAC. Both types of analyses are in progress and will continue to receive increased emphasis.

During the past quarter, the most significant milestone reached was the release of TRAC-P1A to the NESC for distribution. Included with the code was Volume I of the users manual which describes models, methods, and problem input. Progress continued to be made on the development of a droplet field for inclusion in the vessel calculation and a six-equation, two-fluid model which will replace the five-equation, drift-flux model used in one-dimensional components. A study to investigate the sensitivity of the LOFT L2-2 test prediction to the minimum film boiling temperature correlation was initiated. Assessment calculations for the release of TRAC-P1A were completed and are being documented in Volume II of the TRAC users manual to be released shortly.

1. Fluid Dynamics and Heat Transfer Methods

(D. R. Liles, Q-9)

Work continued on a two-fluid, one-dimensional module for TRAC. The droplet field in the three-dimensional vessel module has been simplified and is now undergoing testing. A two-step, second-order time differencing has been implemented for testing in a separate code. An interface sharpener similar to that currently used in the three-dimensional vessel has been implemented in the one-dimensional hydrodynamics. Several correlations for the minimum film boiling temperature have been examined. A fuel rod radiation package suitable for BWRs has been tested. The thermodynamic properties for liquid water have been improved and this new package incorporated into TRAC.

a. Improved Stability for the TRAC One-Dimensional Semi-Implicit Numerical Method

(J. H. Mahaffy, Q-9)

A new technique has been developed to eliminate the Courant-type stability limit which occurs for the semi-implicit method^1 used for one-dimensional components in TRAC. The approach minimizes coding changes by adding only a stabilizing step to the basic semi-implicit procedure already in the code. A significant reduction in problem running times has been observed. Details will be made available in a future report.

b. Second-Order Time Differencing

(S. B. Woodruff, Q-9)

A replacement for the present backward Euler time integrator in TRAC by a second-order Gear^3 integrator is being considered. The Gear method was placed in a special version of TRAC for testing. A calculation of the Edwards' pipe blowdown problem shows that the first- and second-order methods give virtually identical results for small time steps. Testing of the second-order method for large time steps, comparison of the method with the Mahaffy two-step method, and development of a second-order, two-step method are under way.

c. Interface Sharpener for One-Dimensional Components

(J. H. Mahaffy, Q-9)

An interface sharpener analogous to the one currently used in the core and lower plenum regions of the vessel has been developed for the one-dimensional fluid dynamics routine DF1DS. This feature, although primarily designed for modeling accumulators and pressurizers, also allows users to sharpen the interface between liquid and vapor in pipe and tee components.

d. Radiative Heat Transfer Modeling

(D. A. Mandell, Q-9)

The radiative heat transfer model for the BWR version of TRAC has been completed and coded as a stand-alone program for checkout. In addition, sensitivity runs have been made in order to determine the influence of the variables. A report on this work has been written and is currently being reviewed.

The results obtained by using the stand-alone program, RADHT, indicate that five rod groups (including the channel wall) are sufficient for an accurate calculation of the radiative heat transfer within a BWR bundle. The input variables used in the base case of the sensitivity study are given in Table I and the heat transfer results are given in Table II.

In order to see the effect of neglecting radiative heat transfer to the fluid, results were obtained for surface-to-surface radiative heat transfer only and these results are shown in Table III.

The results indicate that the effect of the fluid should be included.

TABLE I

BASE CASE RADHT INPUT

Liquid Temperature	525 K
Vapor Temperature	525 K
Rod Pitch	0.016 256 m
Rod Diameter	0.012 522 m
Wall Emissivity	0.67
Pressure	4.14×10^6 N/m^2
Droplet Diameter	10^{-4} m
Void Fraction	0.9
Bundle Width	0.134 1 m

TABLE II

RADHT HEAT TRANSFER RESULTS

	Radiation Heat Transfer, W		
Number of Rod Groups	Channel Wall	Vapor	Liquid
2	0.253×10^4	0.135×10^5	0.258×10^5
5	0.253×10^4	0.133×10^5	0.272×10^5
11	0.253×10^4	0.131×10^5	0.275×10^5

TABLE III

RADHT SURFACE-TO-SURFACE HEAT TRANSFER RESULTS

Number of Rod Groups	Heat Transfer to the Channel Wall, W
2	0.165×10^5
5	0.130×10^5
11	0.127×10^5

e. Gap Conductance Modeling

(D. A. Mandell, Q-9)

The evaluation of various gap conductance models, described in the previous quarterly report, continued during this period. As indicated, FRAP-T4 cannot be run at LASL due to system errors in the segmented loader. The Computer Science and Services (C) Division will not support this loader; and, therefore, it will not be possible to run segmented codes in the future. Because of this problem, other methods of incorporating a gap conductance model in TRAC are being explored in cooperation with the Idaho Nuclear Engineering Laboratory (INEL).

f. Minimum Film Boiling Temperature

(D. A. Mandell, Q-9 and W. L. Kirchner, Q-8)

TRAC calculations of the LOFT Nuclear Test, L2-2, indicate that the present minimum stable film boiling temperature (T_{min}) correlation is predicting too low a temperature. Increasing this temperature significantly (T_{sat} + 550 K) results in the calculation predicting the first rewet of the hot rod, but subsequent dryouts and rewets are not obtained.

An examination of various correlations for T_{min} is being made in order to determine if a more suitable correlation is available. The present equation for T_{min} in TRAC is[4]

$$T_{min} = T_c + (T_c - T_\ell)\ \mathrm{RATIO}^{0.5} , \qquad (1)$$

where

$$\text{RATIO} = \frac{(k\ \rho\ c)_\ell}{(k\ \rho\ c)_w} . \tag{2}$$

Some competing correlations for T_{min} are:

Breneson's:

$$(\Delta T)_{Ber} = 0.127\ \frac{\rho_f}{k_f}\ h_{fg}\ \left(\frac{g\Delta\rho}{\rho_\ell + \rho_v}\right)^{2/3} \left(\frac{g_c\sigma}{g\Delta\rho}\right)^{1/2} \left(\frac{\mu_f}{g\Delta\rho}\right)^{1/3} ; \tag{3}$$

Iloeje's:[5]

$$T_{min} - T_{sat} = 0.29\ (\Delta T)_{Ber}\ (1 - 0.295\ x_e^{2.45})(1 + [G\cdot 10^{-4}]^{0.49}) ; \tag{4}$$

Henry's:[6]

$$T_{min} = 0.42 \left[(T_{min})_{Ber} - T_\ell) \left(\frac{\text{RATIO}^{0.5}\ h_{fg}}{(\Delta T)_{Ber}\ c_w}\right)^{0.6} \right] + (T_{min})_{Ber} \tag{5}$$

where $(T_{min})_{Ber} = (\Delta T)_{Ber} + T_{sat}$. Figure 1 shows these correlations as a function of pressure for a single mass flux [$G = 67.8\ kg/m^2\ s$ (50 000 $lbm/h\ ft^2$)] and an equilibrium quality of 0.95. Table IV defines the nomenclature for these equations. In addition to the above expressions, the saturation temperature and Kalinin's equation[5]

$$\frac{T_{cr2} - T_{sat}}{T_c - T_\ell} = 1.65\ (0.16 + 2.4\ \text{RATIO}^{0.25}) \tag{6}$$

is shown in Fig. 1.

It should be noted that the TRAC, Henry, and Kalinin correlations are affected by the surface conditions -- Zr or ZrO_2 -- but the other correlations showed no significant differences.

g. Improvement of Thermodynamic and Transport Properties for Steam and Water

(W. H. Lee and J. K. Meier, Q-9)

During this quarter, modifications to the thermodynamic and transport properties calculated in subroutine THERMO and FPROP were made. The purpose of this task was to obtain improved simple

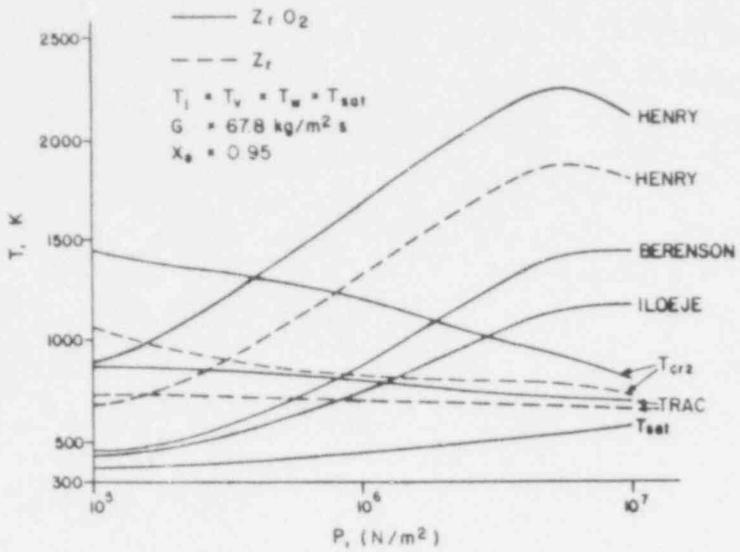

Fig. 1. Comparison of T_{min} correlations.

TABLE IV

NOMENCLATURE

Parameters	
c	specific heat
k	thermal conductivity
T_{min}	minimum film boiling temperature
T_c	critical temperature
T_ℓ	liquid temperature
G	mass flux
x_e	equilibrium quality
ρ	density
σ	surface tension
g	acceleration of gravity
g_c	constant of proportionality
μ	viscosity
h_{fg}	heat of vaporization
$\Delta\rho$	$\rho_\ell - \rho_v$

Subscripts	
Ber	Berenson value
ℓ	liquid
v	vapor
w	wall
f	a vapor property evaluated at the average of wall and saturation temperatures
sat	saturation conditions

polynomial fits to the properties as a function of pressure and temperature. These fits must represent the nonequilibrium effects while at the same time minimizing computer central processor unit (CPU) time and retaining accuracy. The new properties installed in subroutine THERMO are liquid density, ρ_ℓ, derivative of liquid density with respect to pressure, $\partial\rho_\ell/\partial P$, and to temperature, $\partial\rho_\ell/\partial T$, liquid internal energy, E_ℓ, derivative of liquid internal energy with respect to pressure, $\partial E_\ell/\partial P$, and to temperature, $\partial E_\ell/\partial T$. All of the new liquid properties are suitable for subcooled, saturated, and superheated regions in a nonequilibrium state. The range of pressure and temperature is $1 \le P \le 190$ and $1 < T \le 380$. The function for C_v (the vapor specific heat) has also been changed in subroutine FPROP.

The following functions describe the new fit to the properties with the input data P in N/M^2 and T in °C.

$$\frac{1}{\rho_\ell} = a_1 + b_1 P + c_1 P^2 + (d_1 + e_1 P + f_1 P^2)T + (g_1 + h_1 P + k_1 P^2)T^2 , \tag{7}$$

$$\left.\frac{\partial\rho_\ell}{\partial P}\right)_T = -\rho_\ell^2[b_1 + 2c_1 P + (e_1 + 2f_1 P)T + (h_1 + 2k_1 P)T^2] , \tag{8}$$

$$\left.\frac{\partial\rho_\ell}{\partial T}\right)_P = -\rho_\ell^2[d_1 + e_1 P + f_1 P^2 + 2(g_1 + h_1 P + k_1 P^2)T] \quad \text{for } 0 < T < 250 , \tag{9}$$

and

$$\frac{1}{\rho_\ell} = a_2 + b_2 P + c_2 P^2 + (d_2 + e_2 P + f_2 P^2)T + (g_2 + h_2 P + k_2 P^2)T^2 , \tag{10}$$

$$\left.\frac{\partial \rho_\ell}{\partial P}\right)_T = - \rho_\ell^2 [b_2 + 2\, c_2\, P + (e_2 + 2\, f_1\, P)T + (h_2 + 2\, k_2\, P)T^2] \ , \qquad (11)$$

$$\left.\frac{\partial \rho_\ell}{\partial T}\right)_P = - \rho_\ell^2 [d_2 + e_2\, P + f_2\, P^2 + 2(g_2 + h_2\, P + k_2\, P^2)T]$$

$$\text{for } 250 \le T \le 380 \ . \qquad (12)$$

The units of the left-hand terms in above functions are:

ρ_ℓ in kg/m^3,

$\left.\frac{\partial \rho_\ell}{\partial T}\right)_P$ in kg/m^3/K, and

$\left.\frac{\partial \rho_\ell}{\partial P}\right)_T$ in kg/m/N.

The liquid internal energy is:

$$E_\ell(P,T) = E_{\ell sat}(T) + [P - P_{sat}(T)]\ [a_3 + b_3\, P_{sat}(T)^2] \ , \qquad (13)$$

where

$$P_{sat}(T) = c_3(d_3\, T + e_3) f_3 \qquad \text{for } 0 \le T \le 380 \qquad (14)$$

and

$$E_{\ell sat}(T) = a_4 + b_4\, T + c_4\, T^2 + d_4\, T^3 + e_4\, T^4$$

$$\text{for } 0 < T < 275 \qquad (15)$$

$$E_{\ell sat}(T) = a_5 + b_5\, T + c_5\, T^2 + d_5\, T^3 + e_5\, T^4$$

$$\text{for } 275 \le T \le 338 \qquad (16)$$

$$E_{\ell sat}(T) = a_6 + b_6\ T + c_6\ T^2 + d_6\ T^3 + e_6\ T^4$$

$$\text{for } 338 < T \le 380\ . \qquad (17)$$

The derivatives of liquid interval energy with respect to pressure and temperature are:

$$\left.\frac{\partial E_{\ell sat}}{\partial P}\right)_T = a_3 + b_3\ P_{sat}^2 \qquad (18)$$

and

$$\left.\frac{\partial E_{\ell}}{\partial T}\right)_P = \frac{\partial E_{sat}}{\partial T} + (-a_3 + 2\ b_3\ P\ P_{sat} - 3\ b_3\ P_{sat}^2)(\frac{\partial P_{sat}}{\partial T})\ , \qquad (19)$$

where

$$\frac{\partial P_{sat}}{\partial T} = c_3\ d_3\ f_3(d_3\ T + e_3)^{f_3 - 1}\ , \qquad (20)$$

$$\frac{\partial E_{\ell sat}}{\partial T} = b_4 + 2\ c_4\ T + 3\ d_4\ T^2 + 4\ e_4\ T^3$$

$$\text{for } 0 < T < 275\ , \qquad (21)$$

$$\frac{\partial E_{\ell sat}}{\partial T} = b_5 + 2\ c_5\ T + 3\ d_5\ T^2 + 4\ e_5\ T^3$$

$$\text{for } 275 \le T \le 338\ , \qquad (22)$$

and

$$\frac{\partial E_{\ell sat}}{\partial T} = b_6 + 2\ c_6\ T + 3\ d_6\ T^2 + 4\ e_6\ T^3$$

$$\text{for } 338 < T \le 380\ . \qquad (23)$$

where the subscript "sat" means saturation state. The specific heat of vapor at constant pressure C_v (J/kg/K) is:

$$C_v(P,T) = a_7 + b_7\ T - c_7\ P(T - d_7)^{e_7} + f_7\ P^3\ (T - d_7)^{g_7}\ . \qquad (24)$$

The coefficients in Eqs. (7-24) are given in Table V.

TABLE V

COEFFICIENTS IN EQS. (7-24)

	a	b	c
1	$1.002\ 136\ 23 \times 10^{-3}$	$-5.632\ 785\ 5 \times 10^{-8}$	$-8.971\ 304\ 77 \times 10^{-12}$
2	$2.252\ 62 \times 10^{-3}$	$1.485\ 94 \times 10^{-5}$	$-7.154\ 88 \times 10^{-8}$
3	$-8.335\ 44 \times 10^{-4}$	$-2.247\ 45 \times 10^{-17}$	1.0×10^{5}
4	$1.749\ 71 \times 10^{4}$	$3.740\ 2 \times 10^{3}$	4.024 35
5	$6.185\ 27 \times 10^{6}$	$-8.145\ 47 \times 10^{4}$	$4.465\ 98 \times 10^{2}$
6	$2.283\ 788\ 5 \times 10^{9}$	$-2.622\ 156\ 77 \times 10^{7}$	$1.129\ 486\ 67 \times 10^{5}$
7	1 852.274 75	0.602 985 6	117.620 029

	d	e	f
1	$-2.282\ 874\ 59 \times 10^{-8}$	$4.765\ 967\ 87 \times 10^{-10}$	$5.021\ 318 \times 10^{-13}$
2	$-1.045\ 88 \times 10^{-5}$	$-1.029\ 62 \times 10^{-7}$	$5.091\ 35 \times 10^{-10}$
3	$8.488\ 96 \times 10^{-3}$	-2.166 383 7	4.484 304 95
4	-0.015 729 4	$3.130\ 1 \times 10^{-5}$	
5	-1.041 16	$9.260\ 22 \times 10^{-4}$	
6	$-2.162\ 339\ 85 \times 10^{2}$	0.155 283 438	
7	-17.444 4	-2.4	$1.488\ 803 \times 10^{5}$

	g	h	k
1	$4.101\ 156\ 58 \times 10^{-9}$	$-3.803\ 989\ 08 \times 10^{-12}$	$-1.421\ 997\ 52 \times 10^{-15}$
2	$2.592\ 66 \times 10^{-8}$	$1.724\ 1 \times 10^{-10}$	$-8.984\ 19 \times 10^{-13}$
3			
4			
5			
6			
7	9.0		

2. TRAC Code Development

(J. M. Sicilian, Q-9)

TRAC-P1A was released to users outside LASL together with a draft copy of Volume 1 of the TRAC-P1A users manual. Support of this new release version is being supplied as needed.

Programming improvements for TRAC-P2 have been initiated. These improvements include: implementation of the new graphics postprocessing system, a redesigned COMMON area structure, and simplified programming of one-dimensional components.

The new version of the file maintenance program, HORSE, is now in use. This version will allow simultaneous development of multiple versions of TRAC. The library files containing the current TRAC program have been reorganized into the format required by the new HORSE. In addition, a utility program, CMPR, has been developed to analyze update libraries in HORSE format.

a. Release of TRAC-P1A

(J. M. Sicilian, Q-9)

Completion of the TRAC-P1A assessment problems has permitted release of TRAC-P1A to users outside LASL. Because of numerous requests, we have distributed the version directly to those interested, in addition to supplying TRAC-P1A to the NESC. The package released to those requesting TRAC-P1A consisted of:

1. A magnetic tape containing: the FORTRAN source for TRAC-P1A, the sources for three utility programs associated with TRAC (TRCUPD, GRED, and GRIT), a COMPASS-assembler-language matrix-inversion package for CDC installations, and input decks for nine test problems,
2. A description of the format and contents of the tape,
3. A draft copy of Volume I of the TRAC-P1A users manual,
4. A description of the TRAC-P1A input file,
5. A "REQUEST FOR MODIFICATION OF TRAC-P1A" form,
6. "Comments on Release Versions of the TRAC Computer Program," and
7. Microfiche containing a listing of the TRAC-P1A source file and output from the test problems.

b. COMMON Block Reorganization

(J. R. Netuschil, Q-9)

The use of COMMON areas in TRAC-P1A is less than satisfactory. These areas are being reorganized to group variables which are used in the same locations into independent COMMON blocks. At the same time, integer and real variables are being separated into separate COMMON areas to simplify conversion of TRAC to IBM and similar computers. Passing of COMMON variables through argument lists is being eliminated wherever possible.

c. Simplification of Programming for One-Dimensional Components

(M. R. Turner, Q-9)

The reorganization of pointer tables for one-dimensional components[7] permits considerable simplification of the programming required for one-dimensional components through the use of low-level subprograms common to all such components. Extension of this simplification to the INPUT, EDIT, INIT, and STEADY overlays has begun this quarter; the other overlays have already been modified.

d. Improved Graphics Implementation

(J. C. Ferguson, Q-9)

The improved graphics postprocessing system has been included in the working version of TRAC-P2. This system consists of a format conversion program, EXCON (formerly CONVERT), and an interactive plotting program, TRAP (formerly TRCPLOT). The previous graphics programs GRED and GRIT have been modified to accept the new TRCGRF file format produced by TRAC.

TRAP has been improved in several areas this quarter in response to requests from users. These improvements include:

1. simplification of the command language syntax, particularly in defining default values for parameters,
2. separate treatment of the two sides of TEE and STGEN components,
3. inclusion of experimental data through auxilliary files, and

4. addition of fuel-rod-dependent variables to the graphics capabilities.

e. Provision of Comparison Utility

(M. R. Turner, Q-9)

A utility program named CMPR to pinpoint the changes made by a HORSE format update library has been provided for the use of TRAC developers. CMPR uses specified updates and source libraries to produce a listing of modified subprograms with line-by-line demarcation of modifications.

f. New HORSE Implementation

(R. P. Harper, Q-9)

With the completion of TRAC-P1A it has become possible to begin using the new version of HORSE which has been under development for six months. This version is designed to assist parallel development of multiple versions of TRAC and associated programs. Implementation of this version has been accompanied by reorganization of the TRAC source and binary libraries.

3. TRAC Code Assessment

(K. A. Williams, Q-9)

The final calculation of the assessment problems that will be included in Volume II of the TRAC-P1A documentation was completed this quarter. The final draft of this volume should be available shortly. The cladding temperature results for Standard Problem 5 are considerably improved over those reported last quarter due to the discovery of an error in the TRAC boron-nitride properties. This error is corrected in TRAC-P1A.

A posttest parametric study of LOFT Test L2-2 is presently under way as part of the near-term development of TRAC-P2. We hope to be able to make a minimal change from the models in P1A that will allow for calculation of the experimentally measured rewets/dryouts in the high-power region of the core. The present code does, however, predict these rewets/dryouts at the low-power rods and at the upper core elevations of the hot rod.

a. L2-2 Parametric Study

(D. A. Mandell and K. A. Williams, Q-9)

A recalculation of LOFT Test L2-2 with the released version of TRAC-P1A using the actual initial conditions was made. These conditions were quite different than those estimated before the test. The differences are summarized in Table VI. Although they effected the overall dynamics of the transient they had relatively little effect on the peak clad temperature (PCT) because the core high-power region still did not rewet. This recalculation served as a base case for this parametric study.

TABLE VI

COMPARISON BETWEEN L2-2 INITIAL CONDITIONS AND TRAC-P1A CALCULATIONS

L2-2 Steady State

Parameter	L2-2	TRAC (posttest)	TRAC (pretest)
Intact hot-leg temperature (K)	580.6	580.8	593.0
Intact cold-leg temperature (K)	558.8	559.0	566.0
Core ΔT (K)	21.8	21.8	26.6
Intact loop mass flow (kg/s)	197.5	207.1	186.6
Pump ΔP (Pa)	9.1×10^4	9.2×10^4	7.8×10^4
Pressurizer pressure (Pa)	155×10^5	155×10^5	155×10^5
Steam generator secondary pressure (Pa)	63×10^5	62×10^5	63×10^5
Maximum linear heat generation rate (kW/m)	26.38	26.38	28.87

Figure 2 shows the results of the base case calculation of the hot rod peak cladding temperature. This P1A calculation predicts that the core flow rate returns to positive at 4 s with a peak value of over 50 kg/s (Fig. 3). This is consistent with an experimentally measured rewet progressing upward from the bottom of the core at this time. This positive flow rate produces a significant increase in the core liquid mass, as shown in Fig. 4. When the liquid surges through the core, the low power rods are rewet (Fig. 5) as are the upper core locations of the high-power rods (Fig. 6). Other system parameters such as upper plenum pressure, ECC injection time and flow rates, and broken loop flow rates and densities are in very good agreement with the data.

At present, two separate parametric studies have been completed; both of which use the base case input deck and the same initial conditions. In case A, the fuel rod gap conductance (h_{gap}) was specified as a function of time as supplied by a FRAP calculation from INEL. Although the value of h_{gap} increased by roughly a factor of two, no significant change in the results was observed. The input value for the dimensionless radial gap is shown in Fig. 7.

In case B, the TRAC-P1A correlation for the minimum film boiling temperature (T_{min}) was replaced by the Iloeje[5] correlation, as suggested by Peter Griffith of MIT. This correlation is based on rod rewet data taken at high pressure and should be more applicable to the conditions in L2-2 than is the correlation in TRAC-P1A. With this single change, the calculated hot rod cladding did rewet at 6 s and also dryed out at 14 s, as shown in Fig. 8. However, the top-down quench at 19 s when the accumulator comes on is not predicted. This is due to the fact that there is no liquid calculated to remain in the upper plenum at this time. It is felt that this may be a result of the TRAC heat slabs in the upper plenum; a calculation is in progress to assess this hypothesis.

b. Standard Problem 5

(J. K. Meier, Q-9)

Standard Problem 5 (SP5) was analyzed using the release version of TRAC-P1A. Marked improvements were noted in predictions of

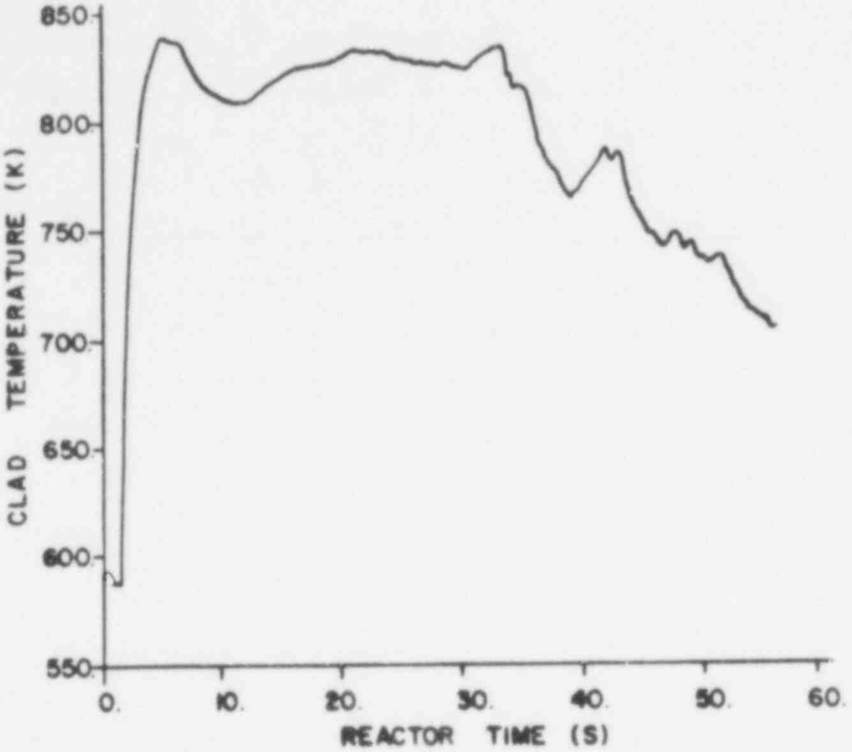

Fig. 2. TRAC-P1A calculation of L2-2 peak clad temperature.

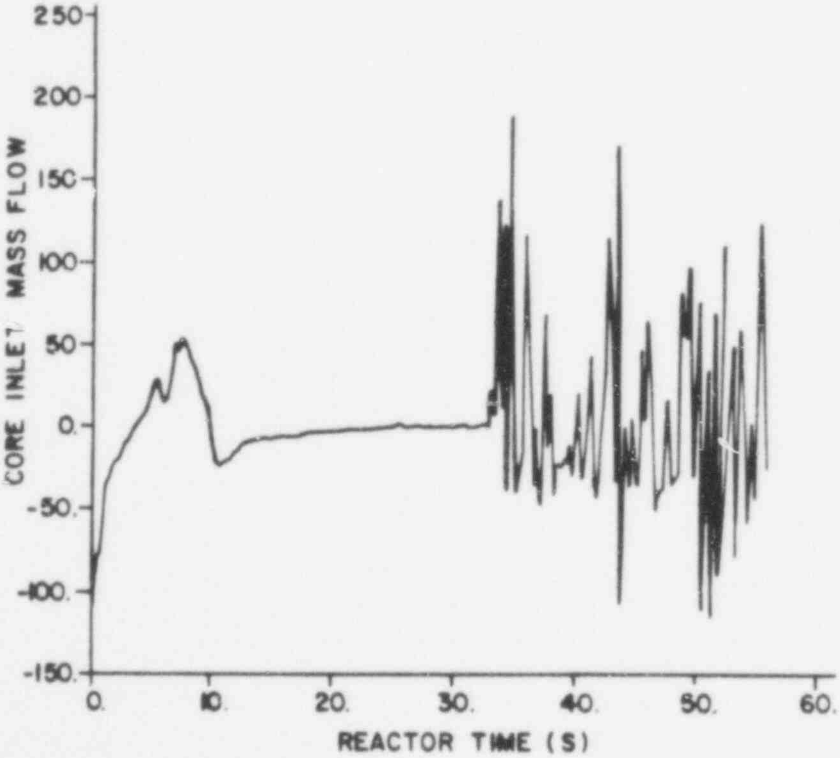

Fig. 3. TRAC-P1A calculation of L2-2 core inlet mass flow rate.

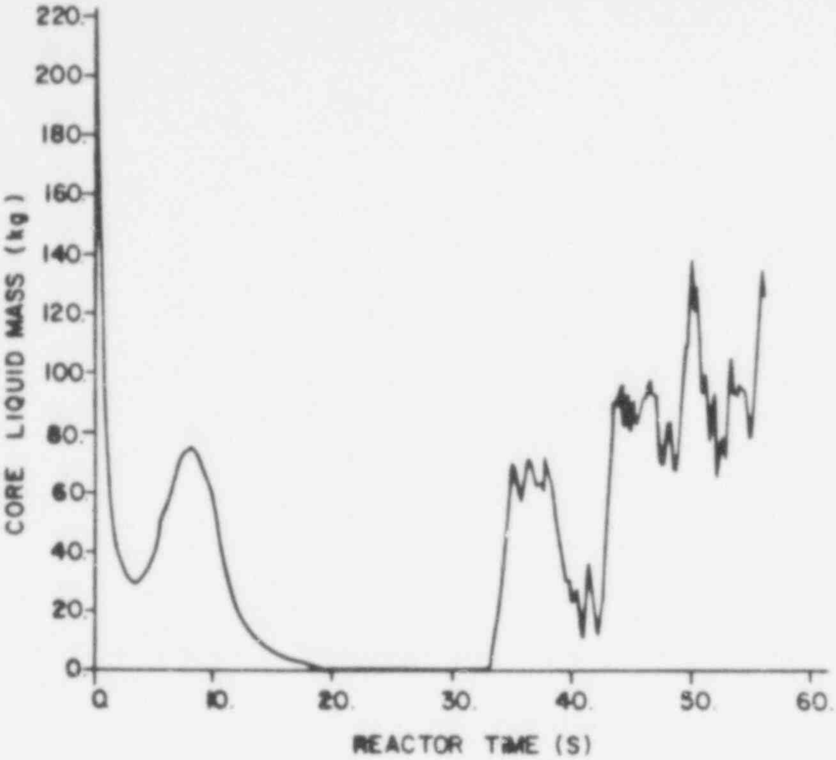

Fig. 4. TRAC-P1A calculation of L2-2 core liquid mass.

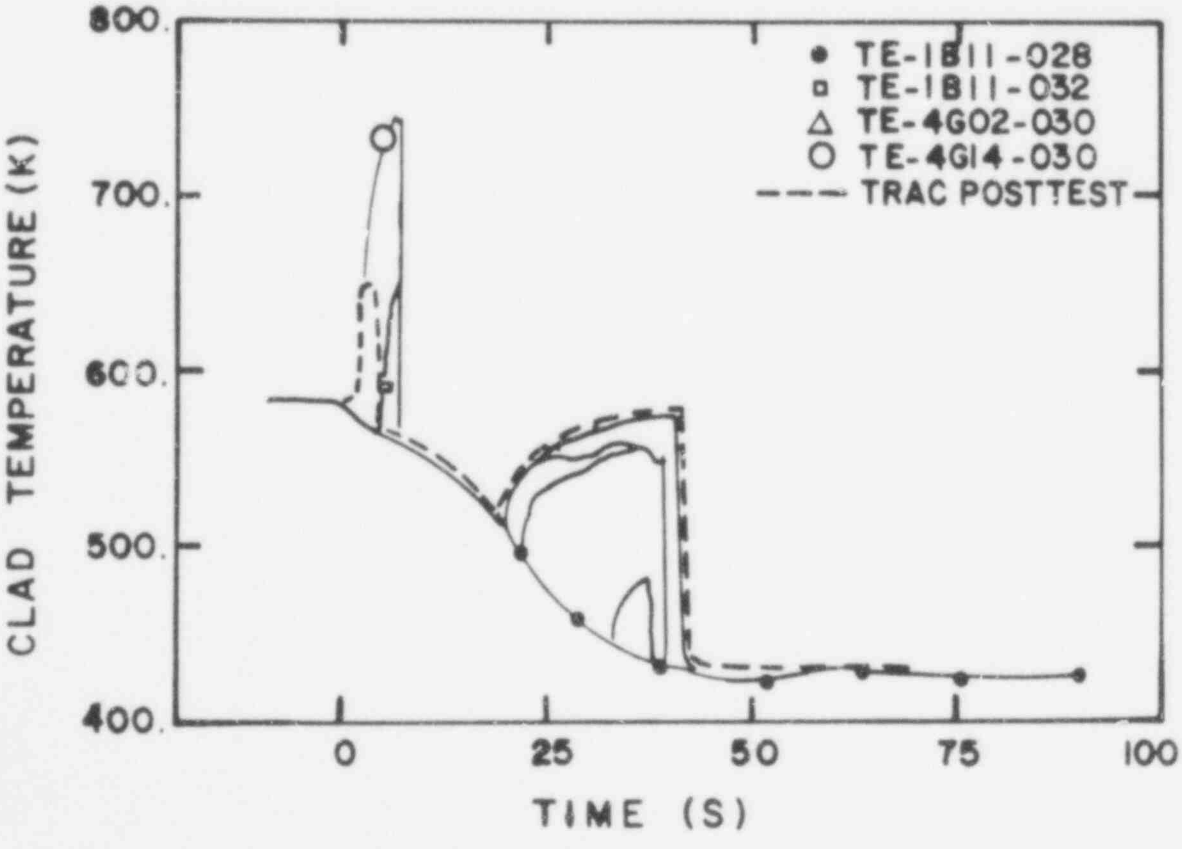

Fig. 5. LOFT Test L2-2: Temperature of cladding of fuel assembly 1, rod B11, and fuel assembly 4, rods G2 and G14.

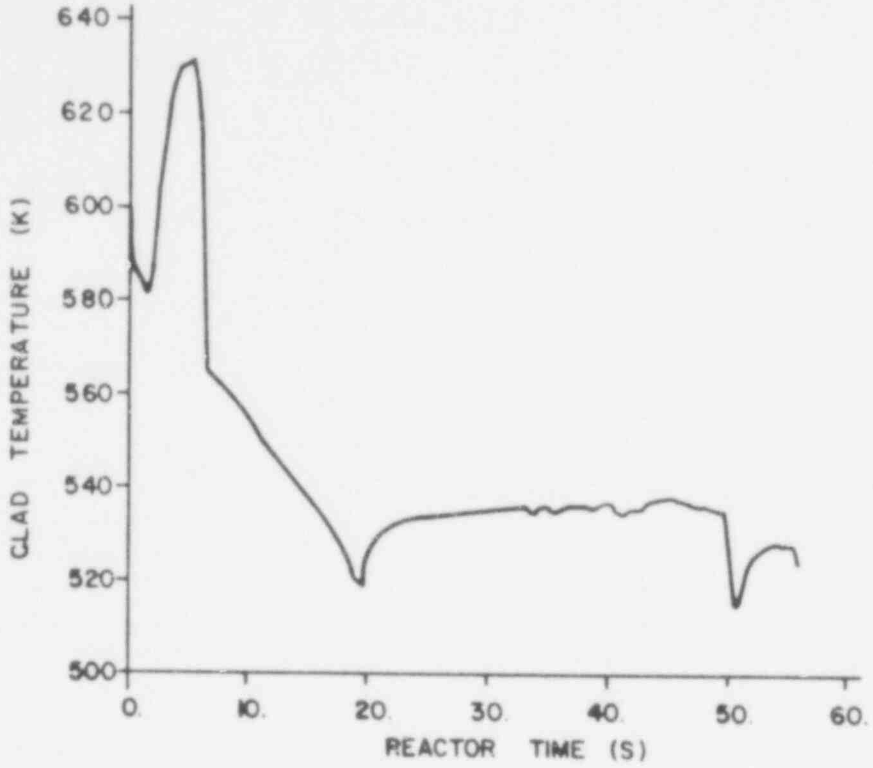

Fig. 6. TRAC-P1A calculation of L2-2 hot rod clad temperature at upper core region.

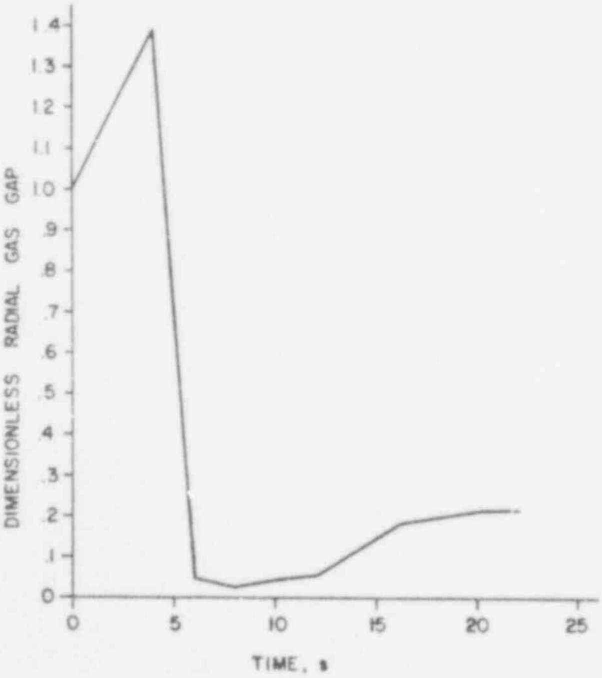

Fig. 7. FRAP-T4 LOFT L2-2 dimensionless radial gas gap.

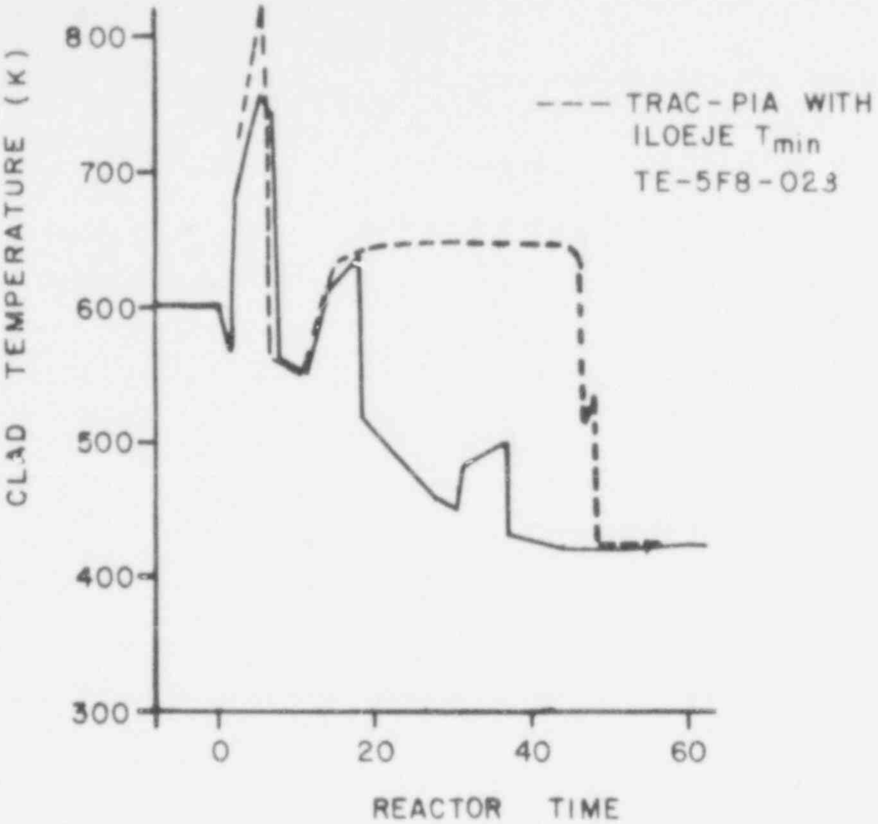

Fig. 8. L2-2 hot rod temperature using Iloeje T_{min} correlation.

cladding temperatures and system pressure as opposed to those reported previously.[7] The majority of these improvements are believed to be due to the correction of an error in the curve fit used in TRAC for the heat capacity of boron-nitride, although a number of changes in system noding probably improved the results also. Figure 9 shows that the TRAC calculation of the SP5 core midpoint cladding temperature falls within the band of experimental results. Figure 10 demonstrates that the TRAC calculation of the system pressure is in very good agreement with the test data. The divergence beginning at 10 s is thought to be due to a slightly higher degree of superheat at the upper core region in the test than in the calculation. Figure 11 shows that the broken hot-leg mass flow rate was noticeably improved in the new calculation. Other system parameters compared at least as well as in the previously reported calculation.

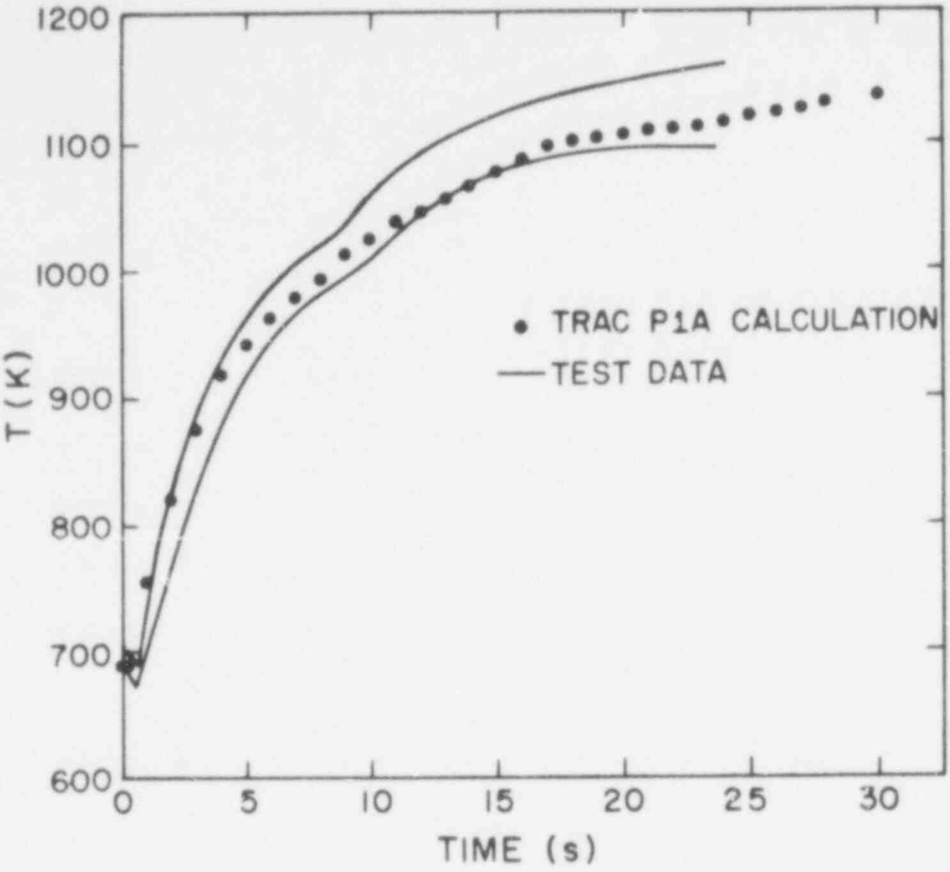

Fig. 9. Standard Problem 5: A comparison of TRAC-P1A results with the band of experimental cladding temperatures at 22-26 in. elevations in the core.

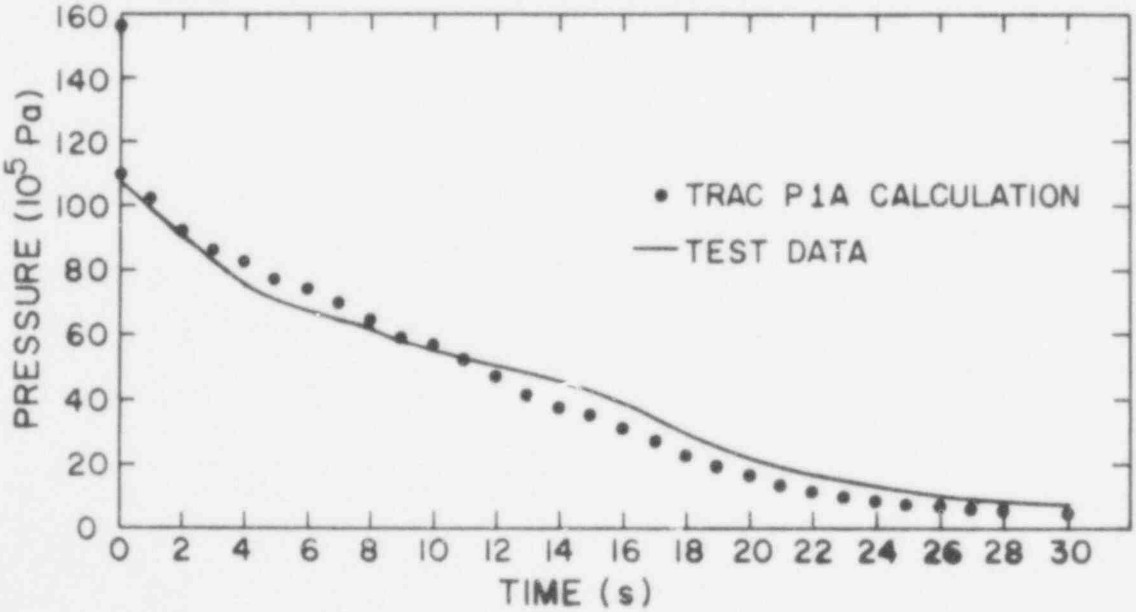

Fig. 10. Standard Problem 5: A comparison of TRAC-P1A results with the experimental lower plenum pressure.

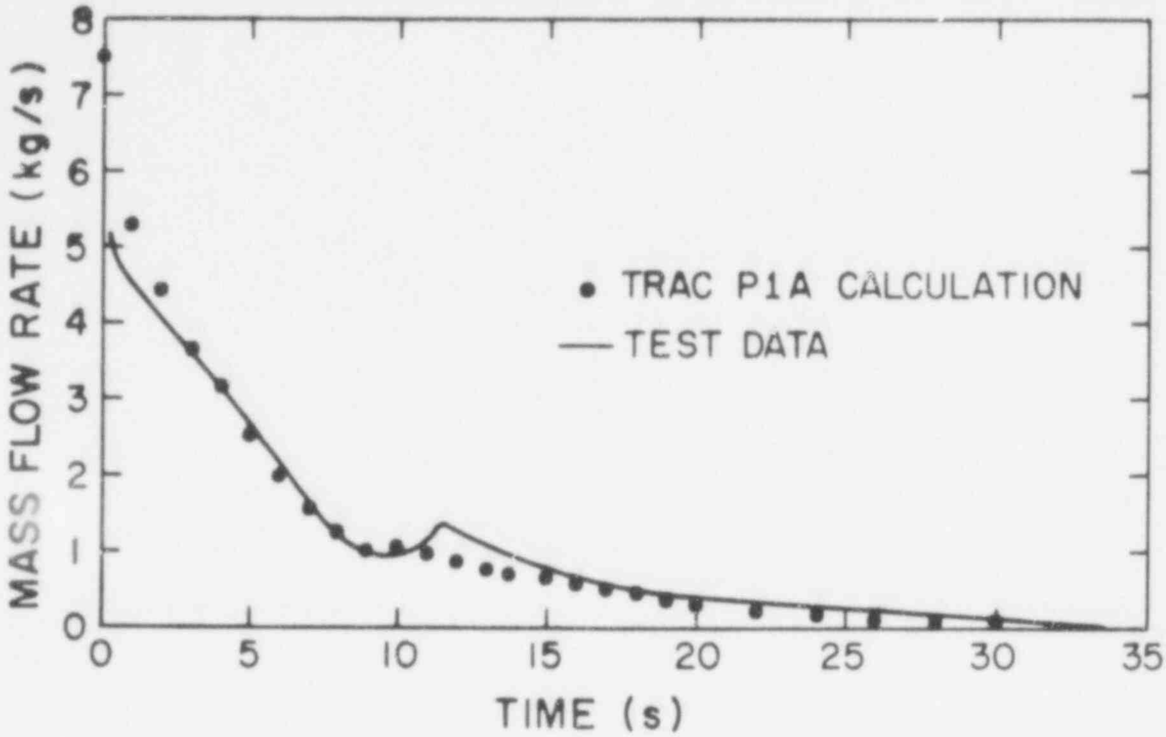

Fig. 11. Standard Problem 5: A comparison of TRAC-P1A results with the experimental broken hot-leg mass flow rate based on (FDB-42, GB-42).

c. TRAC-P1A Analysis of the CISE Blowdown Experiments

(J. S. Gilbert, Q-6)

The CISE vertical pipe blowdown experiment studied depressurization and heat transfer phenomena of initially flowing subcooled water.[8-10] This problem has been recently recalculated in preparation for the code assessment volume to be included with the TRAC-P1A release documentation. The CISE blowdown loop consisted of a vertical heated section and feeder and riser tubes which were helically coiled with a radius of approximately 1 m resulting in elevation changes of 3.6 m and 1.5 m, respectively. (See Fig. 12). The internal diameters of the loop tubing ranged from 0.169 4 m for the feeder to 0.026 18 m for the riser. The total length of the blowdown portion of the loop was 24.06 m. For comparison, some tests were conducted without heat addition to the test section. All tubing was AISI 304 SS with only the feeder and riser tubes insulated to reduce heat loss.

634 090

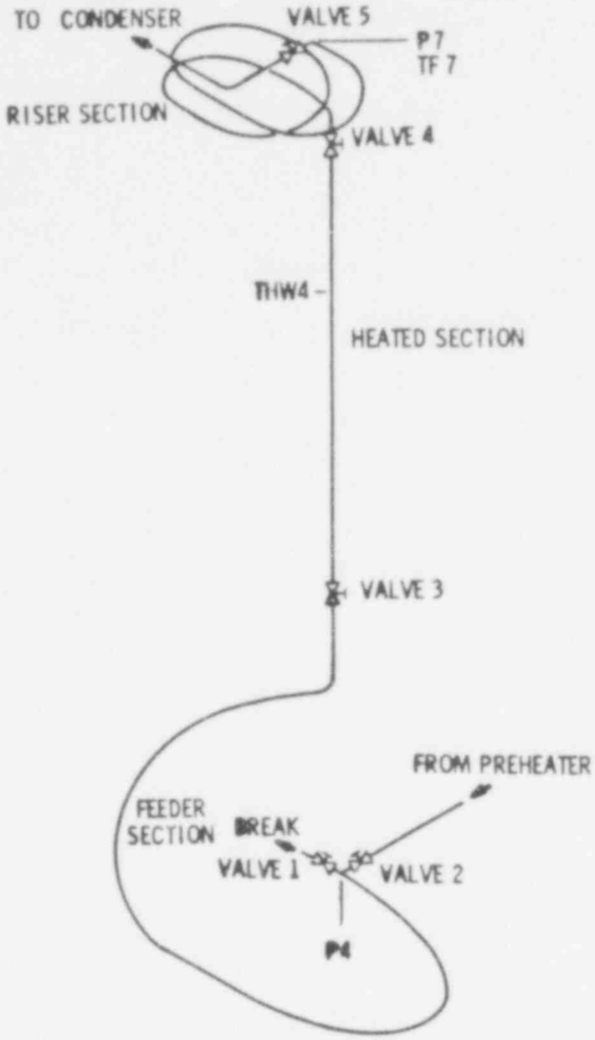

Fig. 12. CISE test section schematic adapted from Ref. 9. The external loop is not shown.

Four quick-closing valves (valves 2-5) and one quick-closing or quick-opening valve (valve 1) are used to isolate the test section from the external loop during blowdown and to isolate the contents of the feeder, heated section, and riser, respectively. All valves are gas actuated and close or open within 0.01 s. These valves offer no additional resistance to flow while in the fully open position. A dc electrical current (300 kW controllable power supply) passing through the heated section tube wall provided uniform axial heat generation.

Pressure and temperature transducers were located along the test section as indicated in Fig. 12. All transducers were connected to a digital data acquisition system while only selected transducers were connected to the analog strip chart recorders.

The operating procedure required that the experiment begin with subcooled water flowing under steady-state conditions through the test loop. At time zero the depressurization was initiated by closing valves 2 and 5 while simultaneously opening valve 1, the discharge valve. Thus, the test section was isolated from the remainder of the loop in less than 0.02 s. Next, the test section discharged to the atmosphere while energy input to the heater section was maintained at the initial rate. Pressure, fluid temperature, and heater wall temperatures were continuously recorded. The mass inventory was determined at selected stages of the blowdown by simultaneous closing of valves 1, 3, and 4. This procedure isolated the contents of the feeder, heated section, and riser, thus allowing the contents to be drained through a condenser and weighed. An experiment was terminated when the heated section wall temperature exceeded approximately 873 K.

The CISE experiment was modeled with three different types of TRAC-P1A one-dimensional components (one FILL, four PIPES, and one BREAK) coupled in series. The system is composed of three tubes of different sizes connected by gradual area transitions. The four pipe components are subdivided into 38 fluid cells. The noding given in Fig. 13 was determined by performing a noding sensitivity study. Based on a parametric study, the annular flow friction factor correlation option (NFF = 4) was used. Gravitational effects (GRAV) and flow area changes (FA) are included in the modeling. In the heated test section case the critical heat flux option (ICHF = 1) and the wall outer heat transfer coefficient (HOUTV = 50) were used.

Initial velocities, pressures, coolant temperatures, and wall temperatures were used to approximate the steady-state experimental conditions for both the heated and the unheated cases. In both the heated and the unheated test section case, five pipe wall nodes were used with a linear temperature drop of 20 K across the pipe

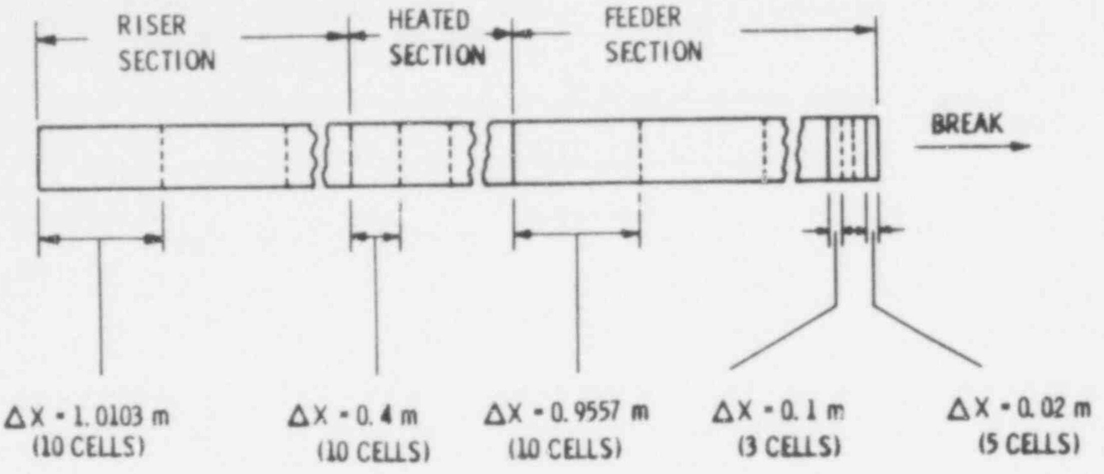

Fig. 13. Typical noding of CISE vertical pipe blowdown experiment.

for the heated case and a flat initial temperature distribution across the pipe wall for the unheated case.

Calculated results for the CISE heated case are compared with the appropriate experimental results in Figs. 14-18. The measurements selected are the following (see Fig. 12 for measurement locations):

P7:	fluid pressure near the closed end of test section,
TF7:	fluid temperature near the closed end of test section,
P4:	fluid pressure near the open end of test section,
THW4:	pipe wall temperature in heater test section, and
MT:	total test section water mass.

In Fig. 14, the fluid pressure comparison at P7 for the heated case is excellent until at about 2 s when the calculated pressure exceeds the measured results. When the blowdown is complete at about 6 s, the calculated pressure has dropped below the measured value. The calculated and measured fluid temperatures at TF7 are shown in Fig. 15. Agreement is good for the first 1.5 s of transient. At about 2 s the experimental values dip sharply then recover at 2.5 s; however, the calculated values continue to exceed the experimental until about 6 s when the calculation drops

634 093

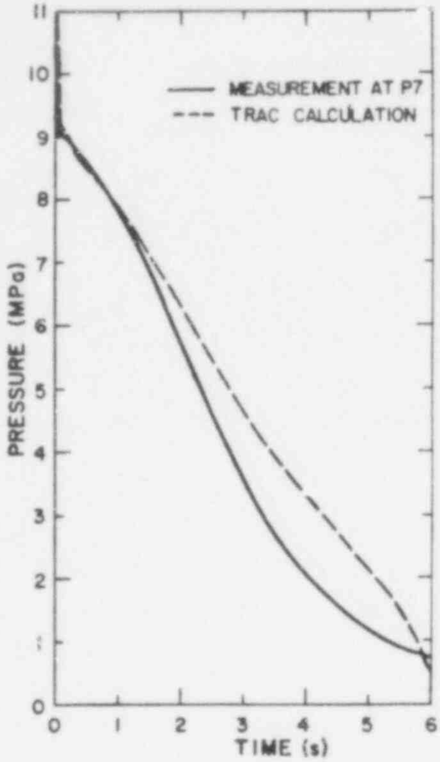

Fig. 14. TRAC-P1A calculation of CISE pressure at gage station 7.

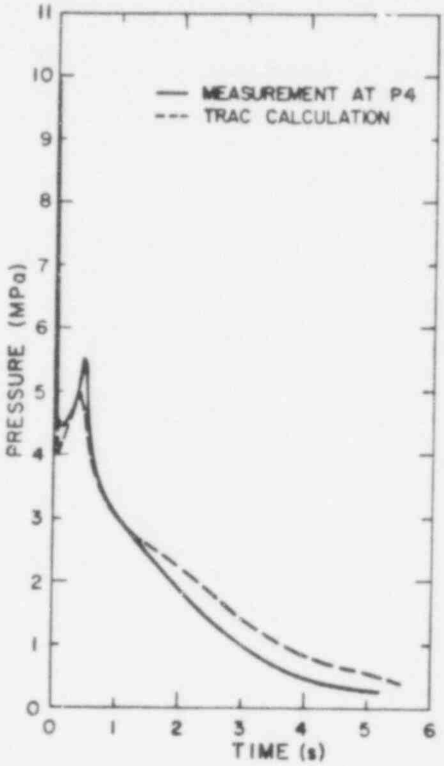

Fig. 16. TRAC-P1A calculation of CISE pressure at gage station 4.

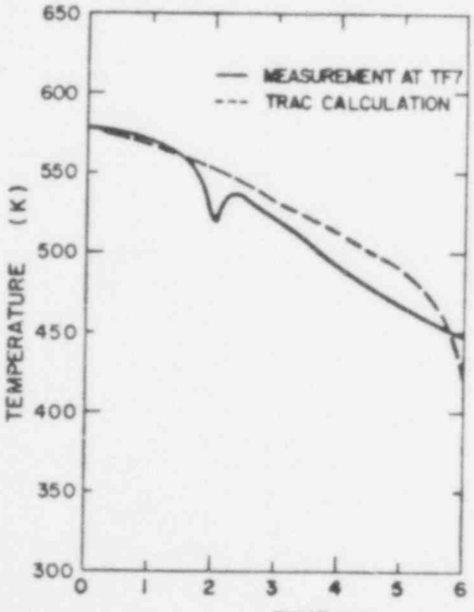

Fig. 15. TRAC-P1A calculation of CISE fluid temperature at gage station 7.

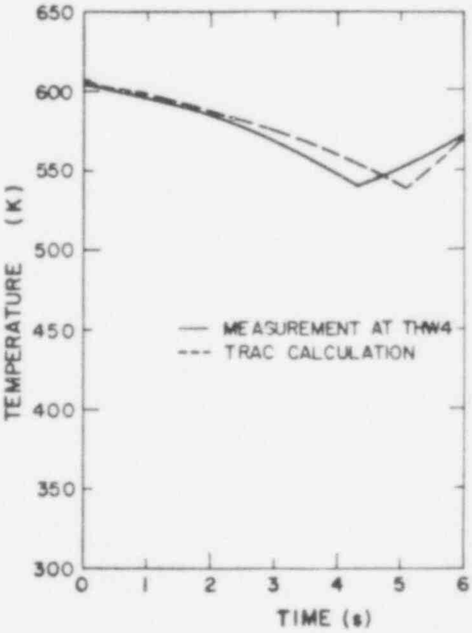

Fig. 17. TRAC-P1A calculation of CISE wall temperature at location THW4.

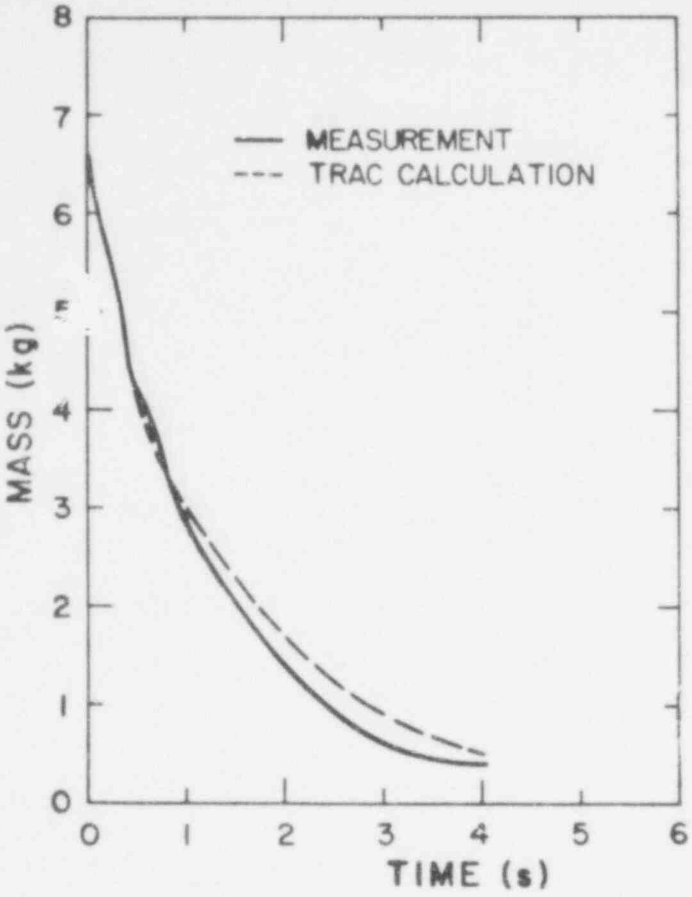

Fig. 18. TRAC-P1A calculation of CISE test section mass inventory.

off sharply. The reason for the dip in the experimental values is not known as there is no dip in the P7 pressure curve. The comparison curves for both pressure and temperature at P7 are very similar.

In Fig. 16 the calculated fluid pressure at P4 is in good agreement with the experimental results at early times in the transient, i.e., less than 2 s. The differences in the single oscillation magnitude may be due to the assumption in the calculation of instantaneous opening of the blowdown valve. This valve requires about 0.01 s to open completely.

The calculated and measured pipe wall temperature near the top of the heater section and at the radial midpoint of the wall, THW4, is plotted in Fig. 17. Agreement is good for the first 2 s of the transient. From 2-4.5 s when the critical heat flux (CHF) is reached, the wall temperature is overpredicted. This overprediction is consistent with the fluid temperature and pressure calculations at TF7 and P7. The CHF time is delayed about 1 s beyond the experimental time. Also, the calculated minimum heater wall temperature is slightly below the experimental value.

The calculated total test section mass is in good agreement with the experimental values for the first 1 s of the transient (see Fig. 18). After 1 s the calculated values are greater. This larger calculated mass in the test section may result in the excessive pressure and temperatures at P7 and TF7, respectively.

In summary, the CISE experiment provided assessment of the TRAC-P1A analytical models for a simple blowdown experiment with heat transfer. In general, agreement was good between calculated results and experimental data.

d. TRAC FLECHT-SEASET Model

(R. K. Fujita, Q-9)

A TRAC model of the FLECHT-SEASET test facility was prepared to analyze the unblocked, forced reflood tests currently being run by Westinghouse. The TRAC vessel module was used to simulate the heated rod bundle, test section housing, and the upper and lower plenums. Pipe components were used in conjunction with FILL and BREAK components to specify the necessary boundary conditions. The inlet flooding rate and fluid energy were established by the FILL component while the BREAK component sets the exit pressure in the upper plenum.

The FLECHT-SEASET model will be used to evaluate the reflood heat transfer model in the TRAC code. Also, predictions will be made for NRC Standard Problem Nine with the FLECHT model.

B. TRAC Applications

(J. C. Vigil and P. B. Bleiweis, Q-6)

The work described in this section includes the application of TRAC to full-scale LWR transients and to the large-scale German and Japanese 2D/3D experiments. TRAC applications to the 2D/3D experiments are used to help with the planning, coordination, and analyses of these experiments by providing design assistance, pretest predictions, and posttest analyses. These applications also help validate the code for use on full-scale LWR systems. Applications of TRAC to full-scale LWR systems provide best estimate predictions of the consequences of postulated transients. In addition to the above activities, TRAC is being used to analyze a variety of other tests and problems for NRC and outside users.

A TRAC calculation of a 200%, double-ended, cold-leg break LOCA in a typical German PWR was completed from blowdown through a complete reflood. Analyses of International Standard Problem Six, a level swell problem, were performed with TRAC to determine the capability of the code to analyze some of the phenomena

634 096

expected during the 2D/3D experiments. Combined injection studies of the Slab Core Test Facility (SCTF) were performed to determine the steam supply requirements for SCTF during cold- and hot-leg injection.

1. TRAC Calculation of a Typical German PWR LOCA

(J. R. Ireland, Q-6)

A 200%, double-ended, cold-leg break LOCA calculation of a typical German four-loop PWR with combined emergency core cooling (ECC) injection was completed during the quarter. This calculation used the steady-state results and noding described in the last quarterly report[7] as initial conditions. A schematic of the German PWR system illustrating the TRAC components and junctions is shown in Fig. 19. Table VII describes each TRAC component shown in Fig. 19. The broken cold leg is indicated by component 22. The break was initiated by combining components 22 and 18 into two fully implicit components connected to two breaks. The break was located 6.0 m from the vessel and it was assumed that there were no ECC systems operating on the broken cold leg. However, hot-leg injection was used on all loops. It should be noted that no high-pressure injection ECC was modeled for this calculation. The pressurizer is located on an intact loop.

The three-dimensional (r,θ,z) vessel noding is shown in Fig. 20. Since there are 3 radial rings with 8 cells per ring in the core, a total of 24 average rods are used for coupling the fuel rod heat transfer to the fluid dynamics. In addition, 12 hot rods were modeled at selected locations in the core, with a local peaking factor of 1.35. Table VIII shows some of the important input parameters for the calculation and Table IX summarizes the TRAC calculated initial conditions at steady state.

Table X gives a summary of most of the important events that occur during the transient calculation. At time 0.0 s the transient was initiated using the restart feature of TRAC. Table XI lists some of the transient input parameters used in the restart. The pump speed curves as well as the containment back pressure curve used during the transient are shown in Figs. 21 and 22,

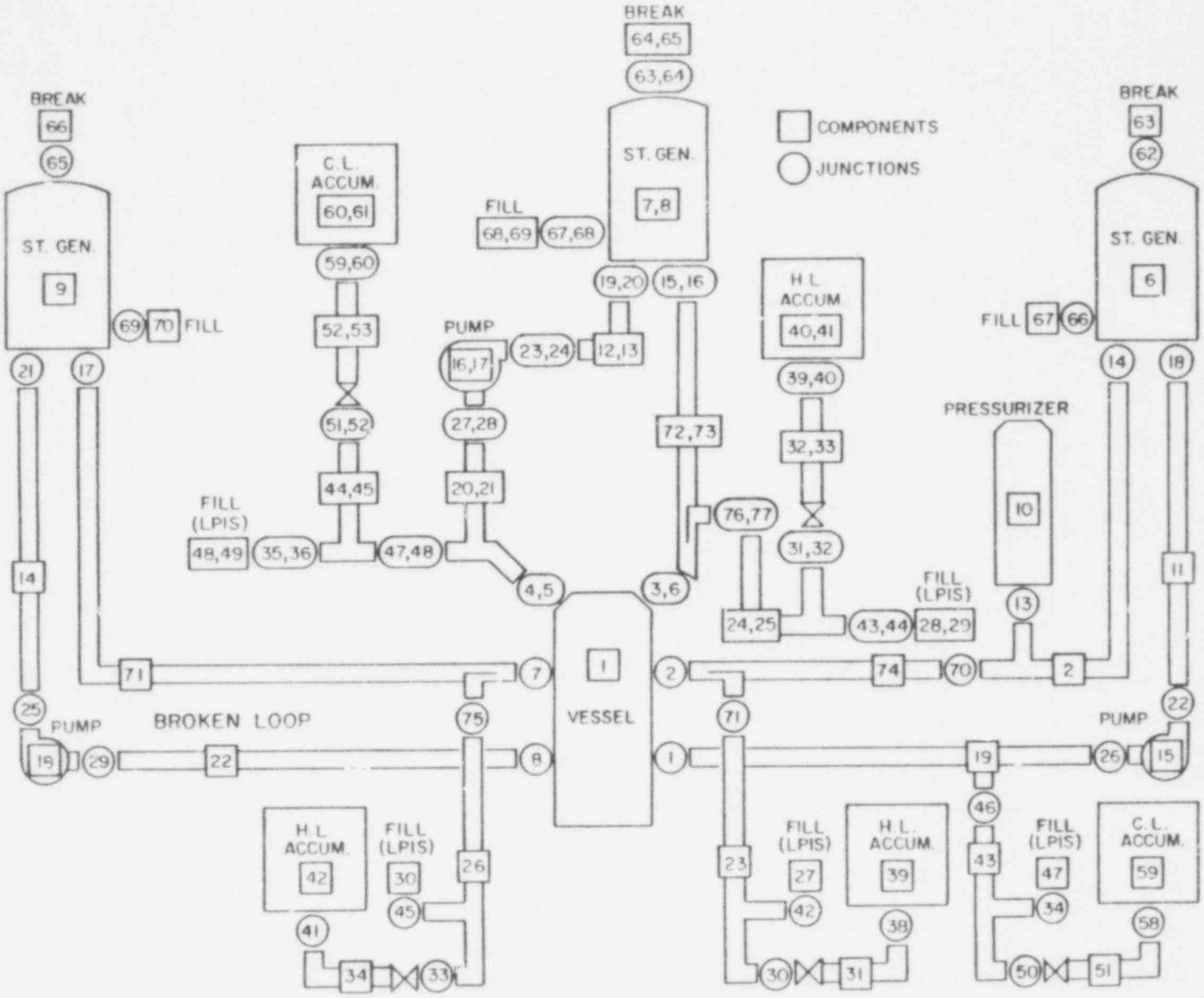

Fig. 19. TRAC model schematic for German PWR.

634 098

TABLE VII

COMPONENTS FOR GERMAN PWR

Component No.	Description	TRAC Component Type
1	Vessel with internals	VESSEL
2	Hot leg with pressurizer	TEE
71,72,73,74	Hot-leg injection tees	TEE
6,7,8,9	Steam generators	STGEN
10	Pressurizer	PRIZER
11,12,13,14	Cold legs from steam generators to pumps	PIPE
15,16,17,18	Cold-leg pumps	PUMP
19,20,21	Intact cold legs from pumps to vessel with injection systems	TEE
22	Broken cold leg	PIPE
23,24,25,26	Hot-leg injection piping for LPIS* and accumulators	TEE
27,28,29,30	LPIS fill systems -- hot legs	FILL
31,32,33,34	Valves between accumulators and hot-leg piping	VALVE
39,40,41,42	Hot-leg accumulators	ACCUM
43,44,45	Cold-leg injection piping for LPIS and accumulators	TEE
47,48,49	LPIS fill systems -- cold legs	FILL
51,52,53	Valves between accumulators and cold-leg piping	VALVE
59,60,61	Cold-leg accumulators	ACCUM
63,64,65,66	Secondary side of steam generators -- outlet	BREAK
67,68,69,70	Secondary side of steam generators -- inlet	FILL

Total number of Components = 59

Total number of Junctions = 62

---

*low-pressure injection system.

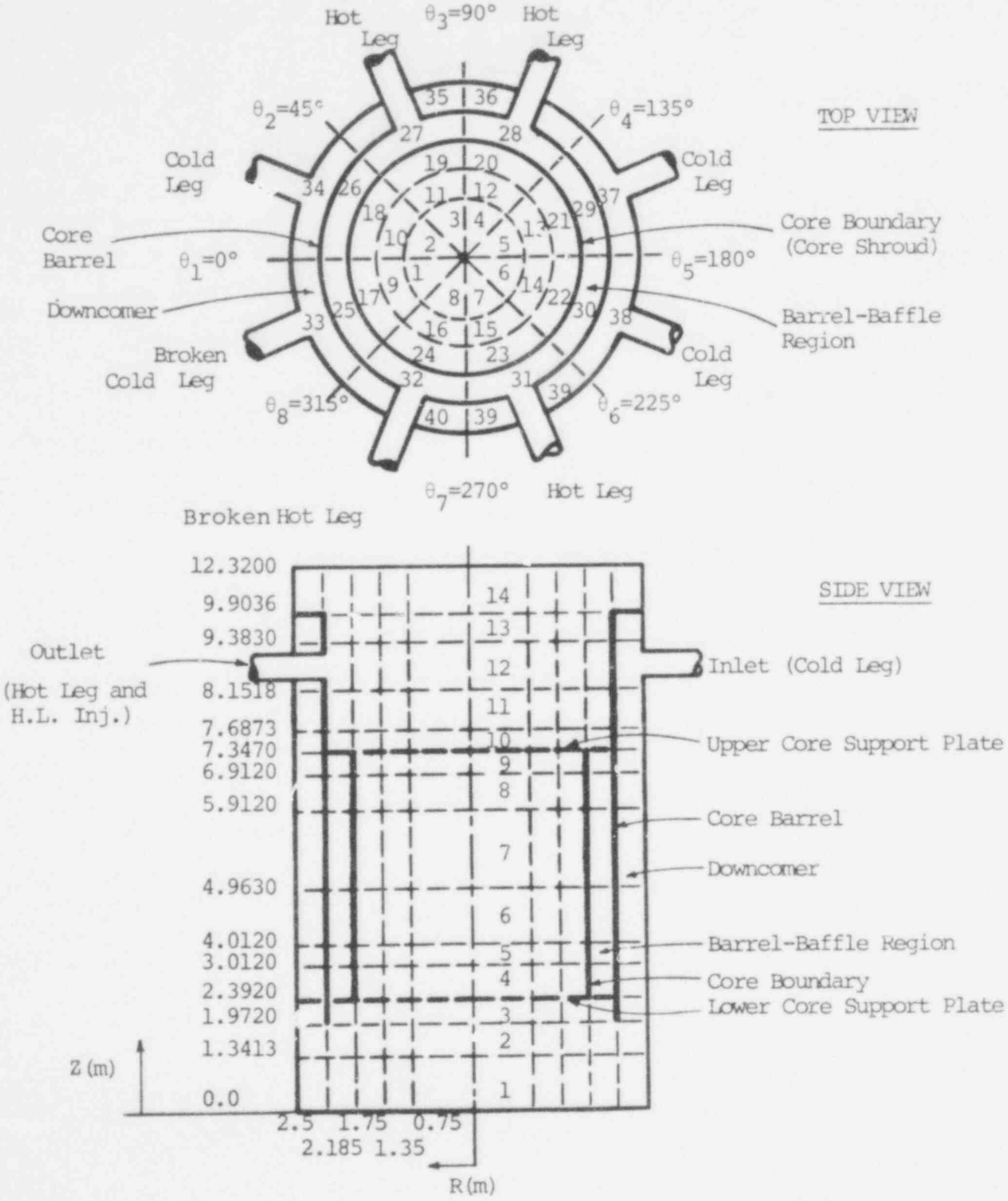

Fig. 20. TRAC noding for German PWR vessel.

TABLE VIII

GERMAN PWR INPUT PARAMETERS

	Parameter	Value
1.	Initial power	3.765×10^9 W
2.	Relative axial power shape (4 levels -- bottom to top)	0.532 5, 1.121 4, 1.121 4, 0.532 5
3.	Relative radial power shape (center to core shroud)	1.137 2, 1.108 0, 0.861 6
4.	Core average linear power	2.12×10^4 W/m
5.	Peak rod linear power	3.30×10^4 W/m
6.	Hot rod linear power	4.45×10^4 W/m
7.	Pump speed	135 rad/s
8.	Accumulator setpoint	26.0×10^5 Pa
9.	LPIS setpoint	10.0×10^5 Pa +34.0 s delay
10.	ECC water temperature	308.0 K
11.	Cold-leg break location (component 22 -- distance from vessel)	6.0 m

TABLE IX

GERMAN PWR CALCULATED INITIAL CONDITIONS AT STEADY STATE

	Parameter	Value
1.	Pump suction side pressure (average)	$1.540\ 2 \times 10^7$ Pa
2.	Pump discharge side pressure (average)	$1.582\ 8 \times 10^7$ Pa
3.	Cold-leg temperature at vessel inlet (average)	564.6 K
4.	Hot-leg temperature at vessel outlet (average)	601.3 K
5.	Cold-leg pressure at vessel inlet (average)	$1.582\ 3 \times 10^7$ Pa
6.	Hot-leg pressure at vessel outlet (average)	$1.561\ 1 \times 10^7$ Pa
7.	Total primary system flow rate (4 loops)	$1.931\ 3 \times 10^4$ kg/s
8.	Steam generator secondary side average pressure	6.9×10^6 Pa

634 101

TABLE IX (cont)

	Parameter	Value
9.	Steam generator secondary side total flow rate (4 loops)	$1.068\ 08 \times 10^4$ kg/s
10.	Cladding surface temperatures at core level 3 (average rod for each of 3 radial rings)	626.7, 626.7, 612.7 K
11.	Total system water mass	7.03×10^5 kg

TABLE X

GERMAN PWR CALCULATED TABLE OF EVENTS

	Event	Time (s)
1.	200%, double-ended cold-leg break (close off secondary side of steam generator; trip reactor power and pumps)	0.0
2.	Hot rod peak clad temperature of 118 2 K reached in rod 4, core level 3	6.7
3.	Accumulator flows begin in all loops	15.0
4.	Average rod peak clad temperature of 104 6 K reached in rod 12, core level 3	20.8
5.	Pressurizer empties (level below 0.1 m)	25.7
6.	LPIS flows initiated in cold legs (all loops)	58.0
7.	Lower plenum refilled	60.0
8.	LPIS flows initiated in hot legs (all loops)	68.0
9.	Quench fronts move through core midplane:	
	A. Central rods	90.0
	B. Peripheral rods	55.0
10.	Entire core quenches	100.0

634 102

TABLE XI

GERMAN PWR TRANSIENT INPUT PARAMETERS

1. Power decay -- ANS standard
2. LPIS -- 1. Cold legs - 170 kg/s
   2. Hot legs - 160 kg/s
3. Pump coastdown (see curve)
4. Containment back pressure (see curve)
5. Isolate secondary side of steam generators.

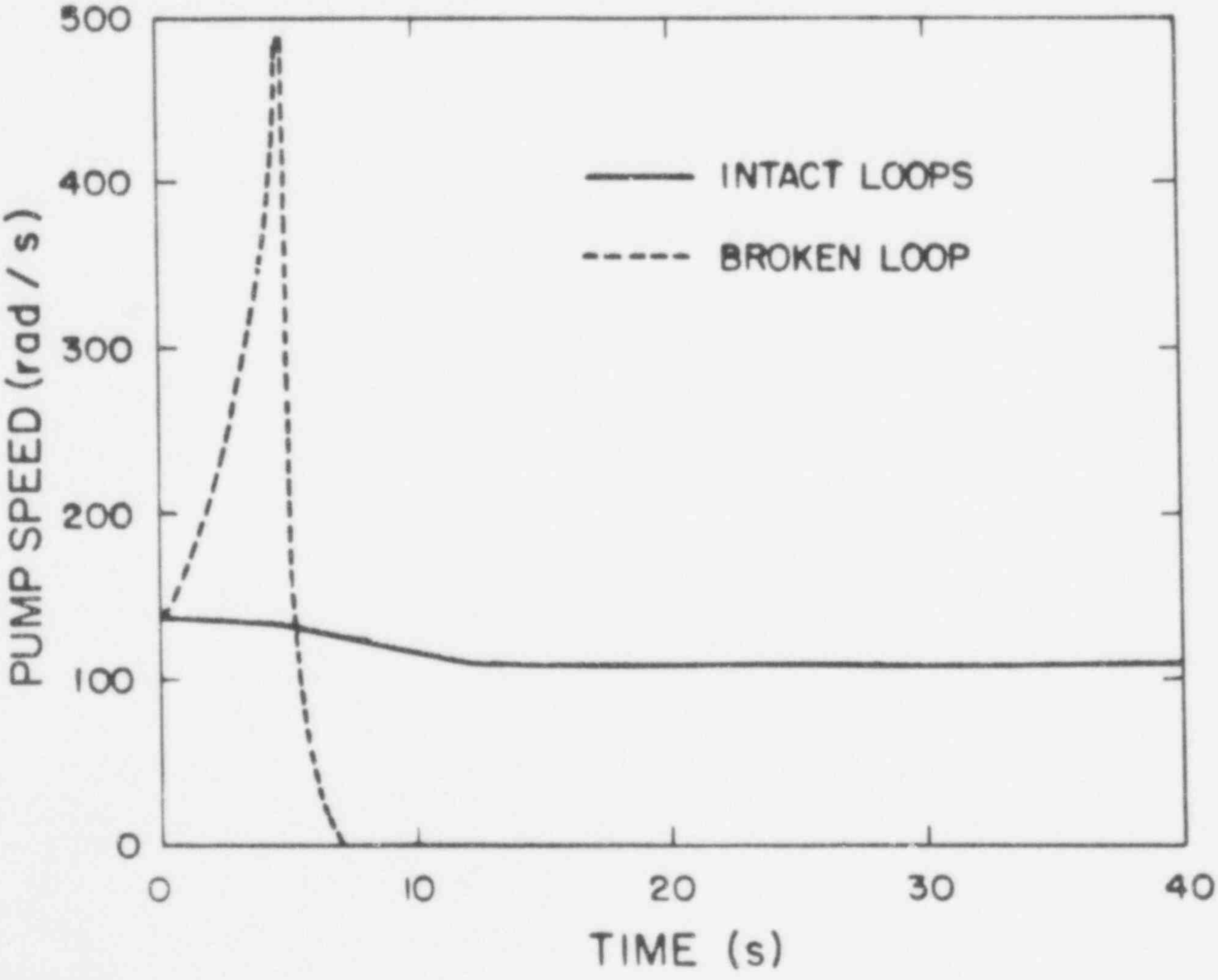

Fig. 21. German PWR pump speed in intact and broken loops.

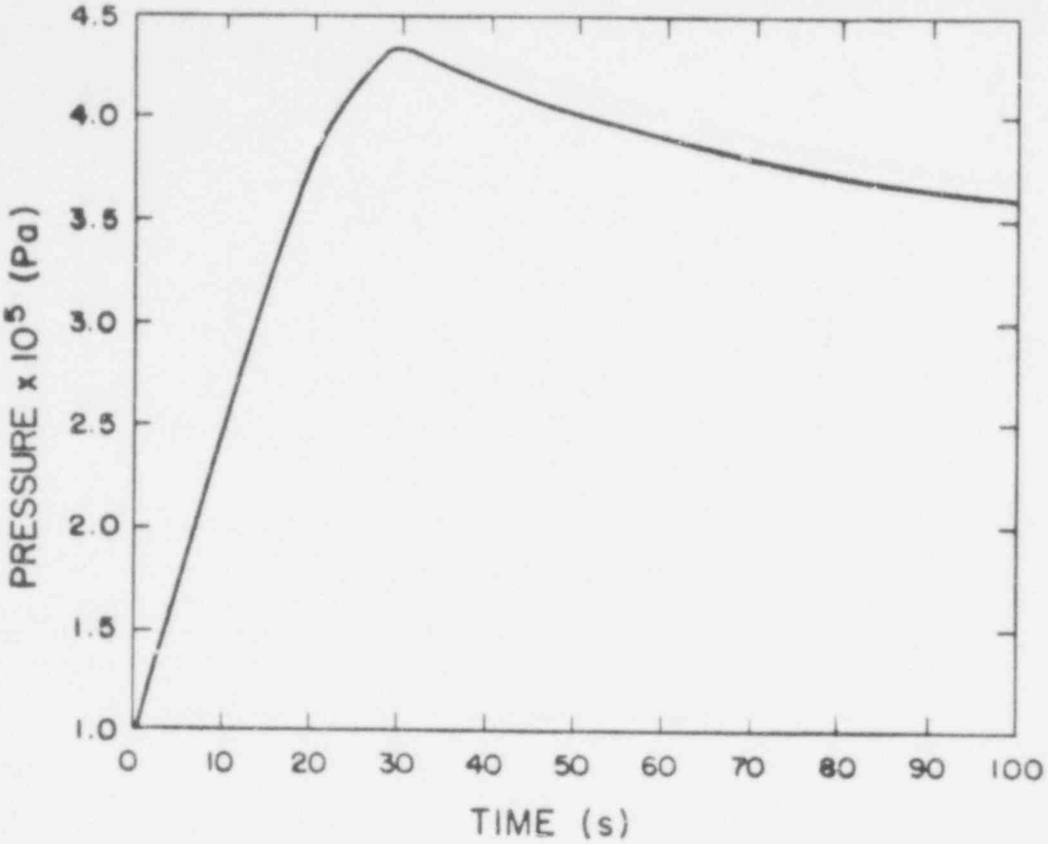

Fig. 22. German PWR containment back-pressure.

respectively. These curves were obtained from the Germans and were supplied as boundary conditions for TRAC.

From Table X it is seen that the peak clad temperatures for both the average and hot rods occur during blowdown. The peak clad temperature for the 24 average rods modeled occurred in the central region of the core, where the axial power distribution peak is located. Rod 12 (located in Cell 12 of Fig. 20) showed the highest peak clad temperature (1 046 K at 20.8 s) of all the average rods modeled. Note that rod 12 is located in a region of the core that is directly opposite the broken loop (see Fig. 20). The hot rod peak clad temperature of 1 182 K occurred in the inner radial core ring at 6.7 s in Rod 4. Note that Rod 4 is located adjacent to Rod 12 in Fig. 20.

Accumulator flows begin in both the cold and hot legs at 15.0 s after break initiation and the pressurizer empties at about 26.0 s. Due to a time delay caused by the startup of the

LPIS diesel motors, the LPIS is not actuated in the calculation until 58.0 s for the cold legs and 68.0 for the hot legs (this time delay was supplied by the Germans). The lower plenum fills at 60.0 s and it is at this time that ECC bypass ends.

As can be seen from Table X, the first rods to quench through the core midplane (axial level 6 of Fig. 20) were the peripheral, low power rods next to the core shroud. The rods in the central region of the core finally quench through the core midplane at 90.0 s. Due to both falling films from the hot-leg injection and bottom quench front motion from the lower plenum, the entire core quenches by 100 s.

The clad temperature time histories at the core midplane of three adjacent average rods and peak hot rod are shown in Fig. 23. As mentioned previously, the peak clad temperature for the average rods occurs in Rod 12 at 20.8 s and at 6.7 s for the hot rods. The clad temperatures remain essentially flat during blowdown and then begin to decrease during refill. The main reason for the constant cladding temperatures during blowdown is the constant pressure established in the vessel due to combined ECC injection. For cold-leg injection only, a significant pressure gradient is established across the core which produces large, negative vapor velocities that cool the rods and a sharp decrease in cladding temperatures is observed.[11]

From Fig. 23 it is seen that Rod 20, which is representative of the peripheral rods, quenches considerably earlier than the center rods. This is mainly due to the falling film quench front motion that occurs early in the transient and the relatively low power production in the peripheral region. The other rods in the central core region quench through the core midplane at about 100 s as shown in Fig. 23. These rods are quenched mainly by bottom quench fronts. Note that due to both bottom and top quench front motion, the entire core quenches by 100 s.

Plots of the lower plenum average pressure and lower plenum average fluid temperature are shown in Figs. 24 and 25, respectively. From Fig. 24 it is seen that blowdown is essentially complete after 30 s. During this time the lower plenum fluid

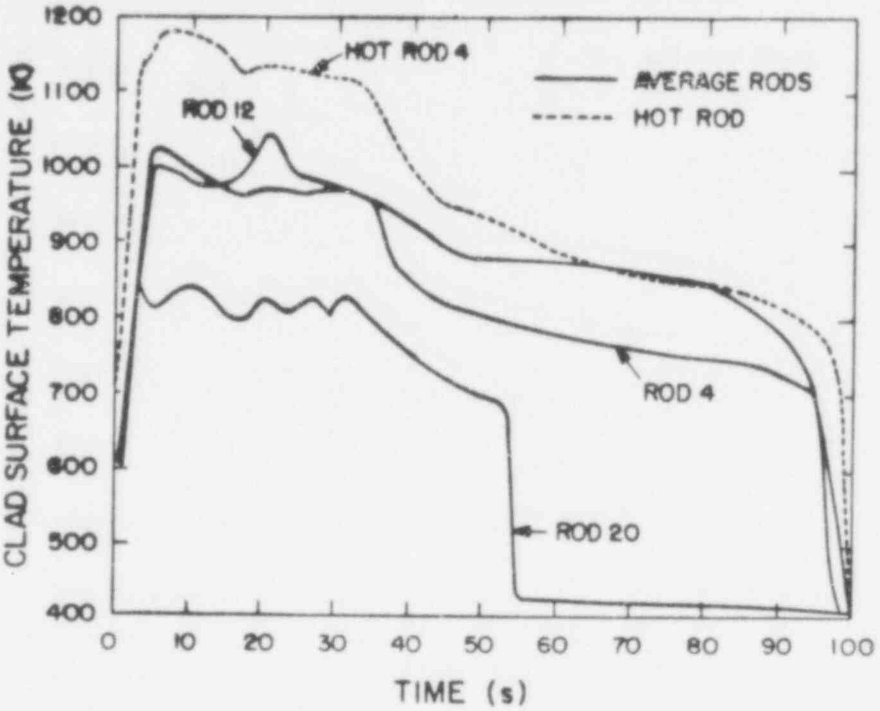

Fig. 23. German PWR cladding temperatures -- core level 3.

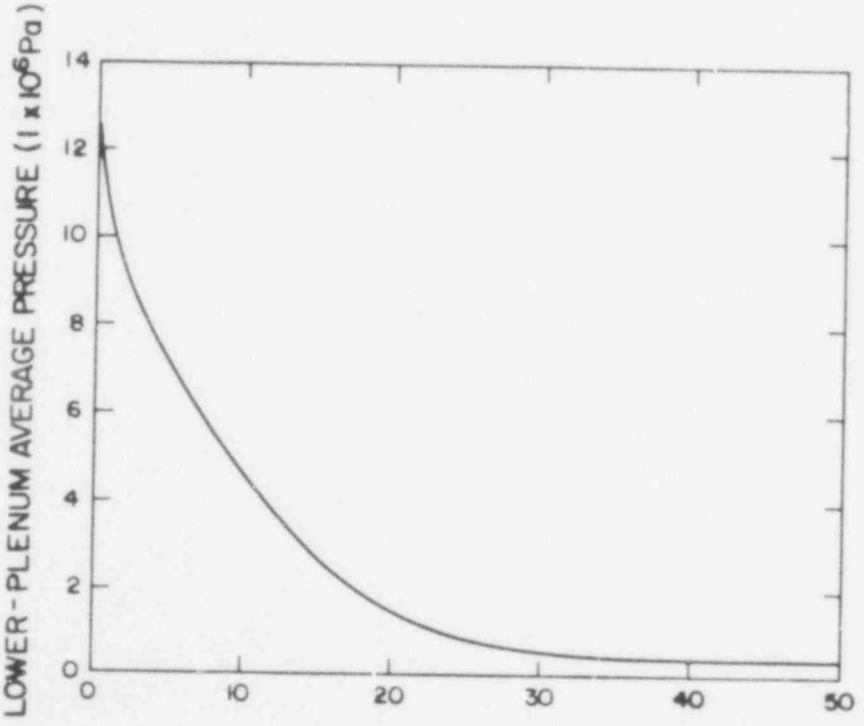

Fig. 24. German PWR lower plenum average pressure.

634 106

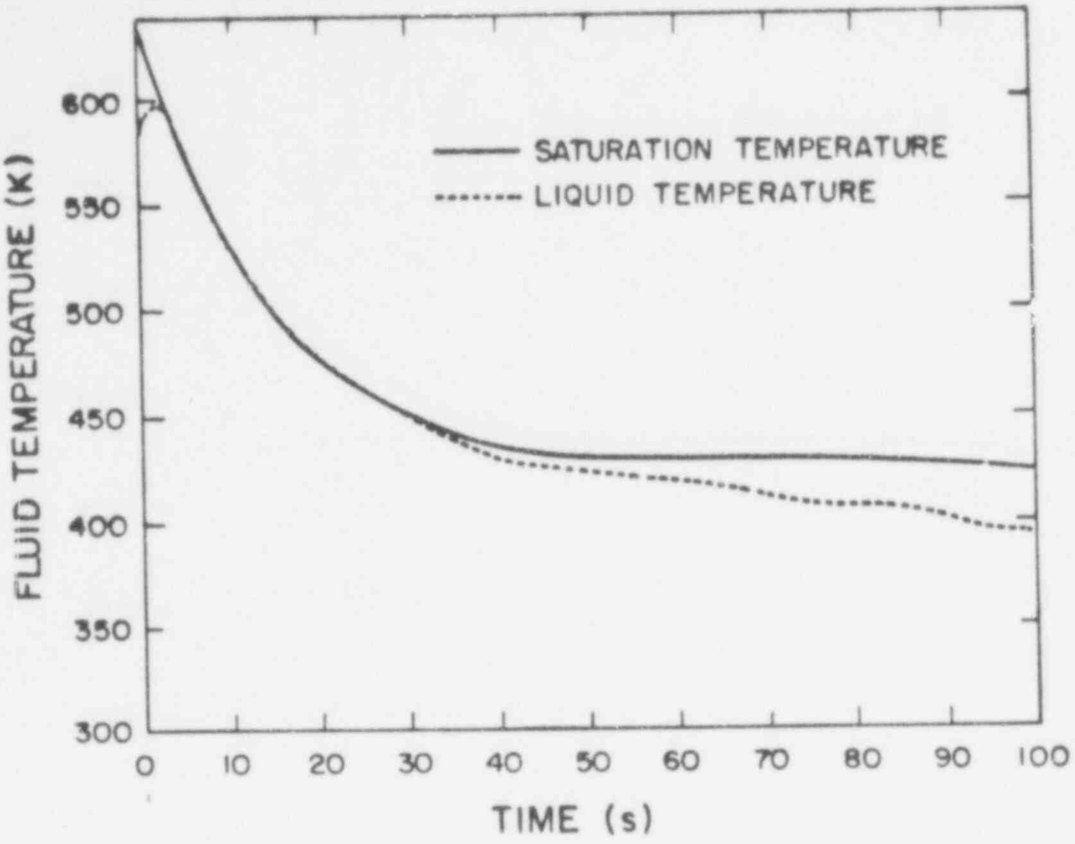

Fig. 25. German PWR lower plenum fluid temperature.

temperature is saturated. After 30 s, the subcooling in the lower plenum continues to increase due to cold-leg ECC injection.

A plot of the average void fraction above the upper core support plate is shown in Fig. 26. This plot shows that there is essentially no stable pool predicted to form during reflood and only a small pool during blowdown. It appears that most of the ECC entering the upper plenum from hot-leg injection reaches saturation by the time the liquid falls to the upper core support plate. This conclusion is highly dependent on the condensation modeling in TRAC, which has not been well assessed for hot-leg injection conditions. Any liquid that does reach the support plate drains mainly down the peripheral assemblies next to the core shroud. This is what causes the peripheral rods to quench early. Due to higher power production in the central region of the core, higher vapor velocities occur at the upper core support plate and more of a countercurrent flow limiting (CCFL) process occurs which prevents falling quench front motion in this region.

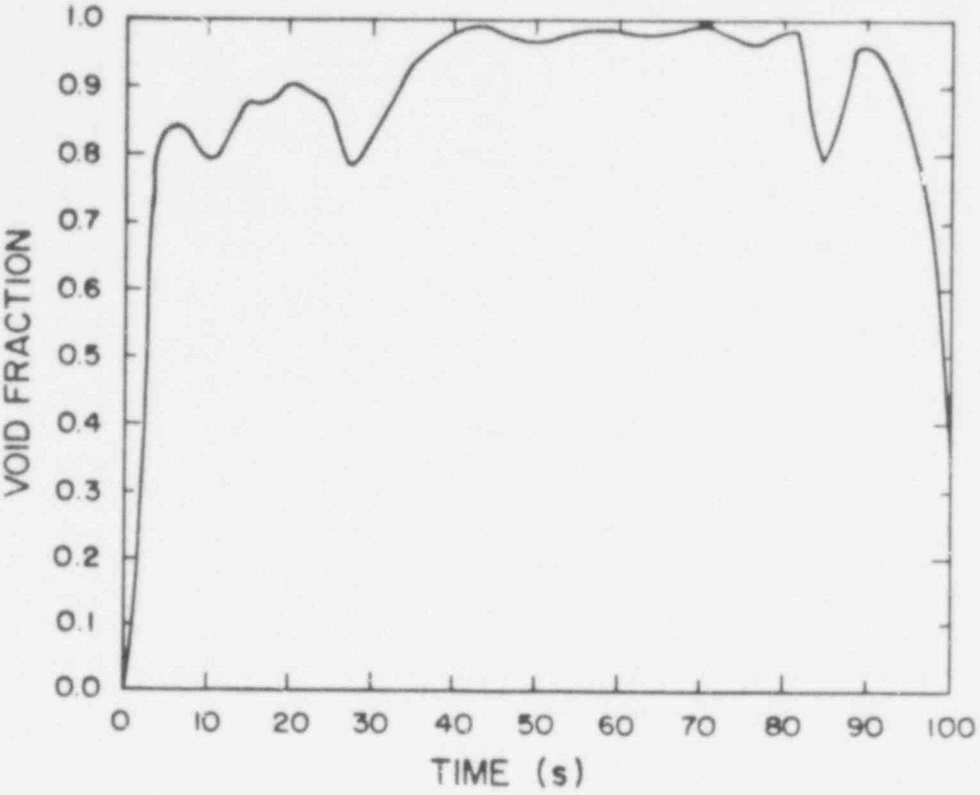

Fig. 26. German PWR average void fraction in first two levels above upper core support plate.

As mentioned previously, TRAC-P1A predicts that the hot-leg ECC water will essentially be at saturation at the upper core support plate. However, before reaching saturation the subcooled water causes the upper plenum pressure to decrease significantly below the core pressure. Figure 27 illustrates this phenomenon by showing a graph of the average core and upper plenum pressures. During reflood, about a 1.7×10^5 Pa pressure drop exists between the core and upper plenum. This pressure drop enhances the bottom quench front velocity and helps to speed up the quenching process. This appears to be the main advantage of hot-leg injection in this calculation. It should be noted again, however, that this conclusion results in part from the high degree of condensation predicted by the modeling in TRAC-P1A.

To further illustrate the refill, reflood, and bypass phases of the transient, the downcomer, core, and lower plenum liquid masses and liquid volume fractions are plotted in Figs. 28-31. From Fig. 28 it is seen that the lower plenum fills at about 60 s (right after

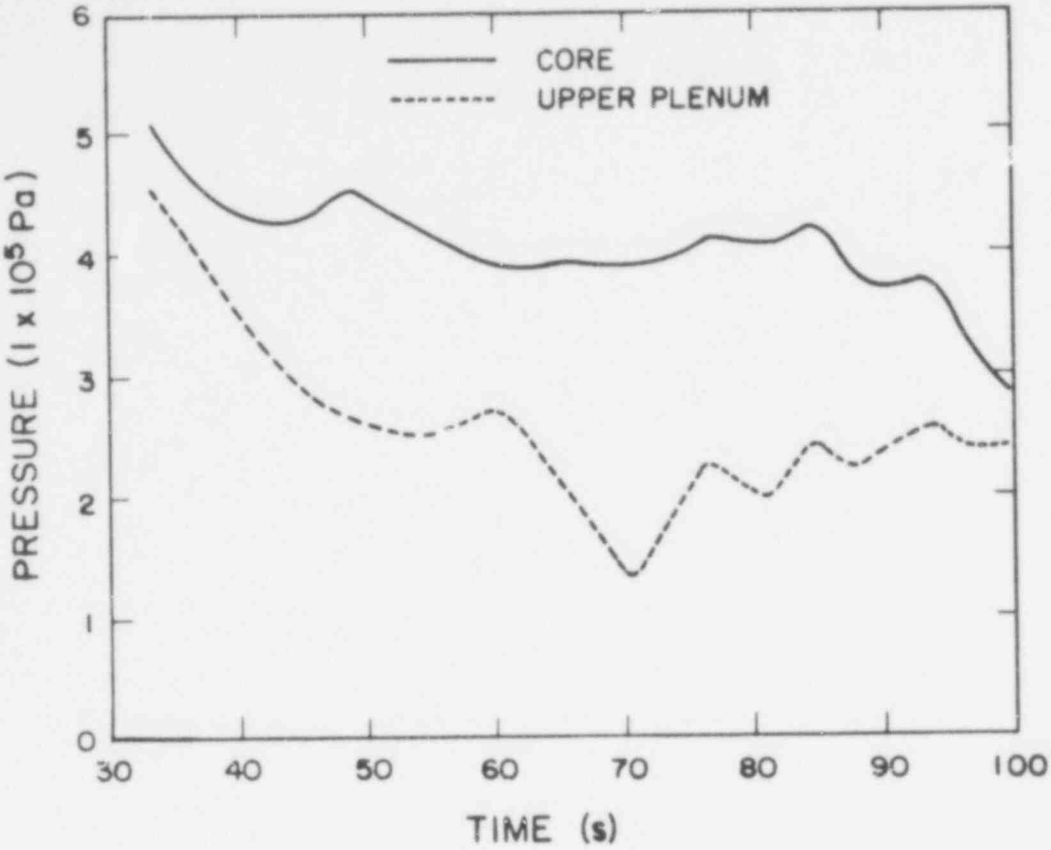

Fig. 27. German PWR core and upper plenum average pressures.

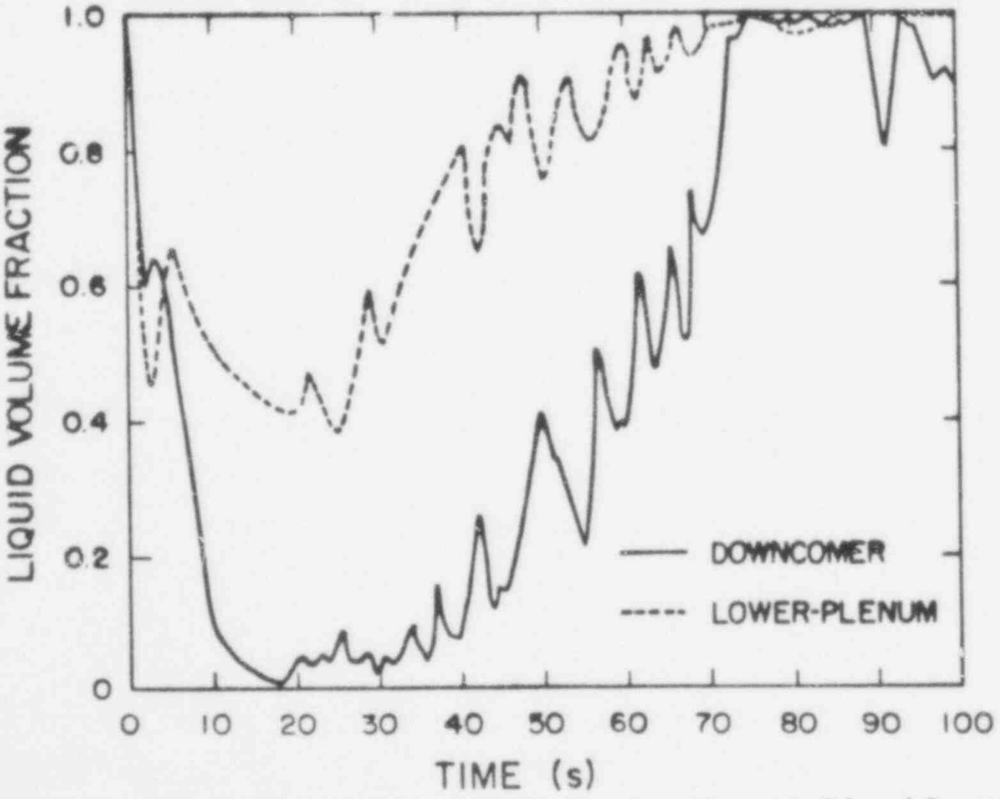

Fig. 28. German PWR downcomer and lower plenum liquid volume fractions.

634 109

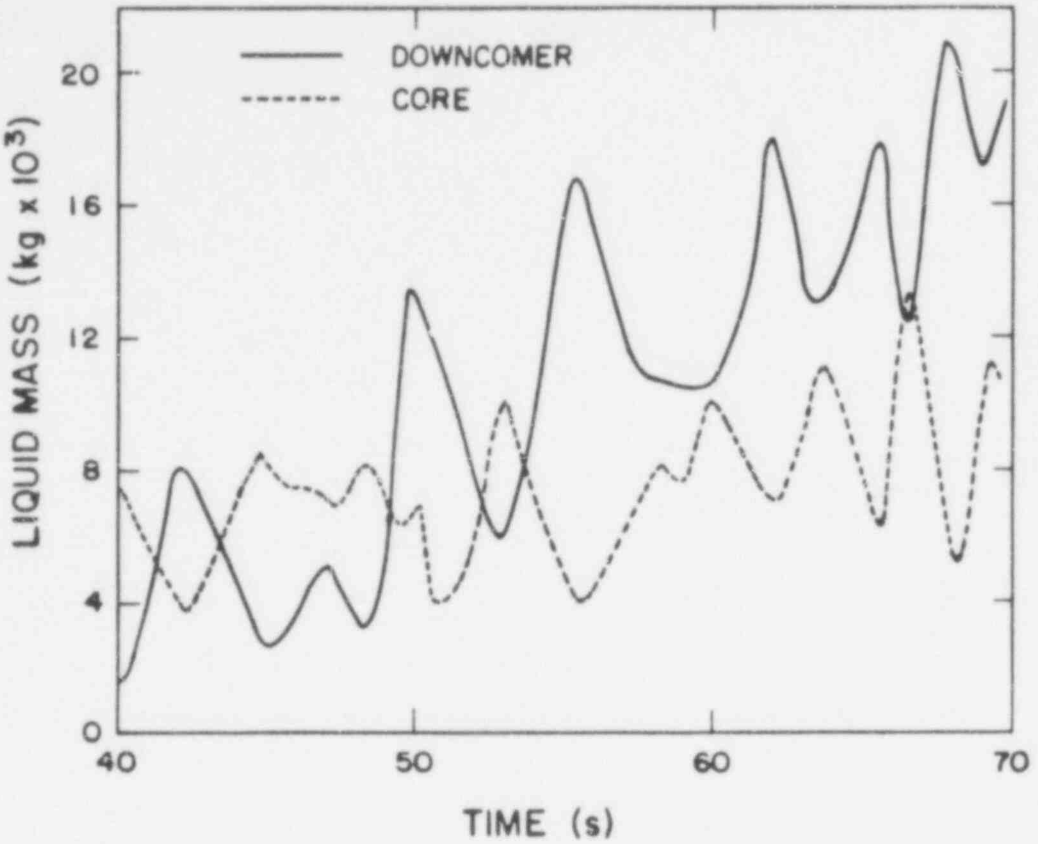

Fig. 29. German PWR downcomer and core liquid mass.

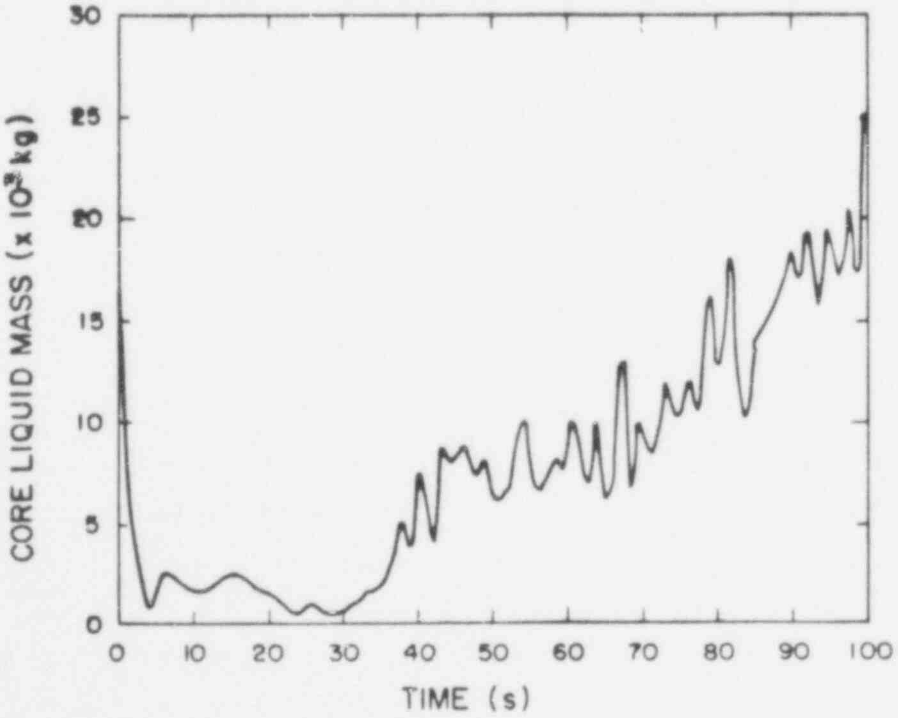

Fig. 30. German PWR core liquid mass.

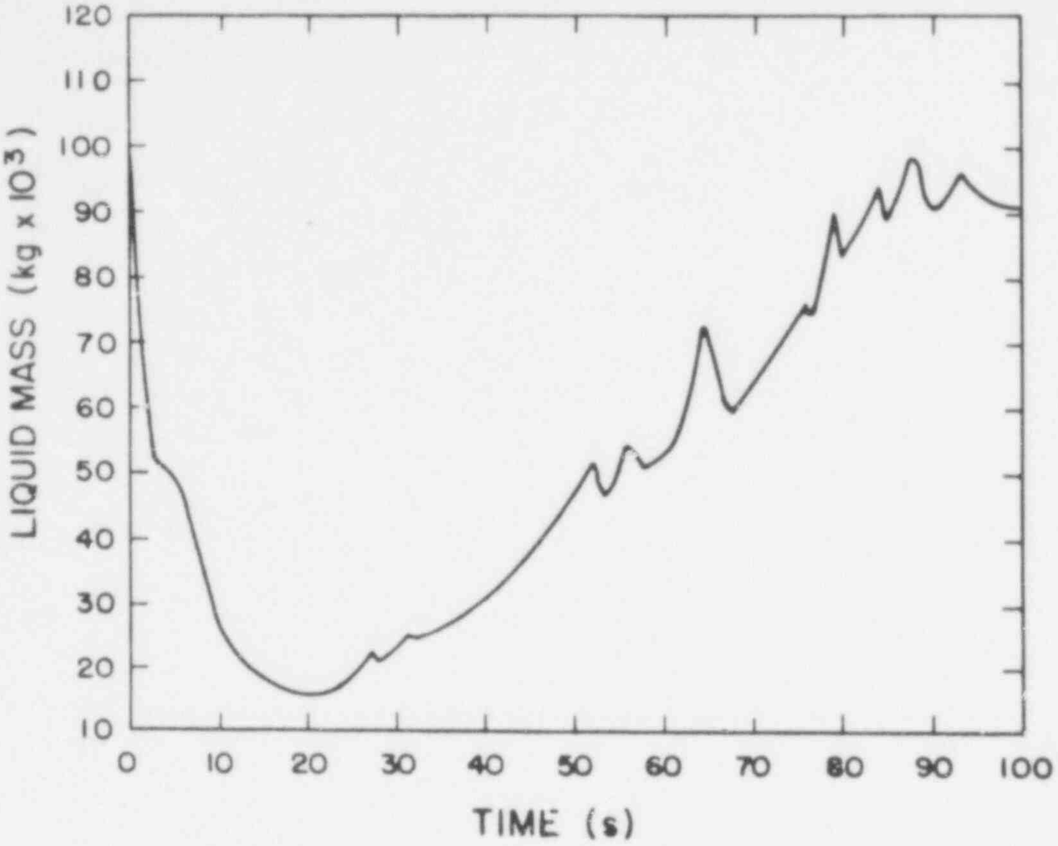

Fig. 31. German PWR vessel liquid mass.

the cold-leg LPIS is initiated) and the downcomer fills at about 70 s. Oscillations in the liquid fractions and liquid masses during refill are calculated between the downcomer, lower plenum, and core. Figure 29 clearly shows these oscillations which appear to be manometer-type oscillations that are out of phase with a period of 4-7 s. Referring back to the lower plenum liquid volume fraction plot in Fig. 28, it is seen that ECC bypass occurs from the time that accumulator flows are initiated (15 s) until the lower plenum refills (60 s). Note that is is only a partial bypass of the cold-leg ECC liquid, as most of the ECC penetrates the downcomer and refills the lower plenum. The core and vessel liquid masses are plotted in Figs. 30 and 31. The core is essentially full of liquid at 100 s, and the vessel is about 85% full.

Figures 32-34 show velocity vectors for both vapor and liquid in the downcomer (which has been graphically unwrapped) for different times in the transient. Both the vapor and liquid vectors shown are normalized to maximum values occurring at each specific time.

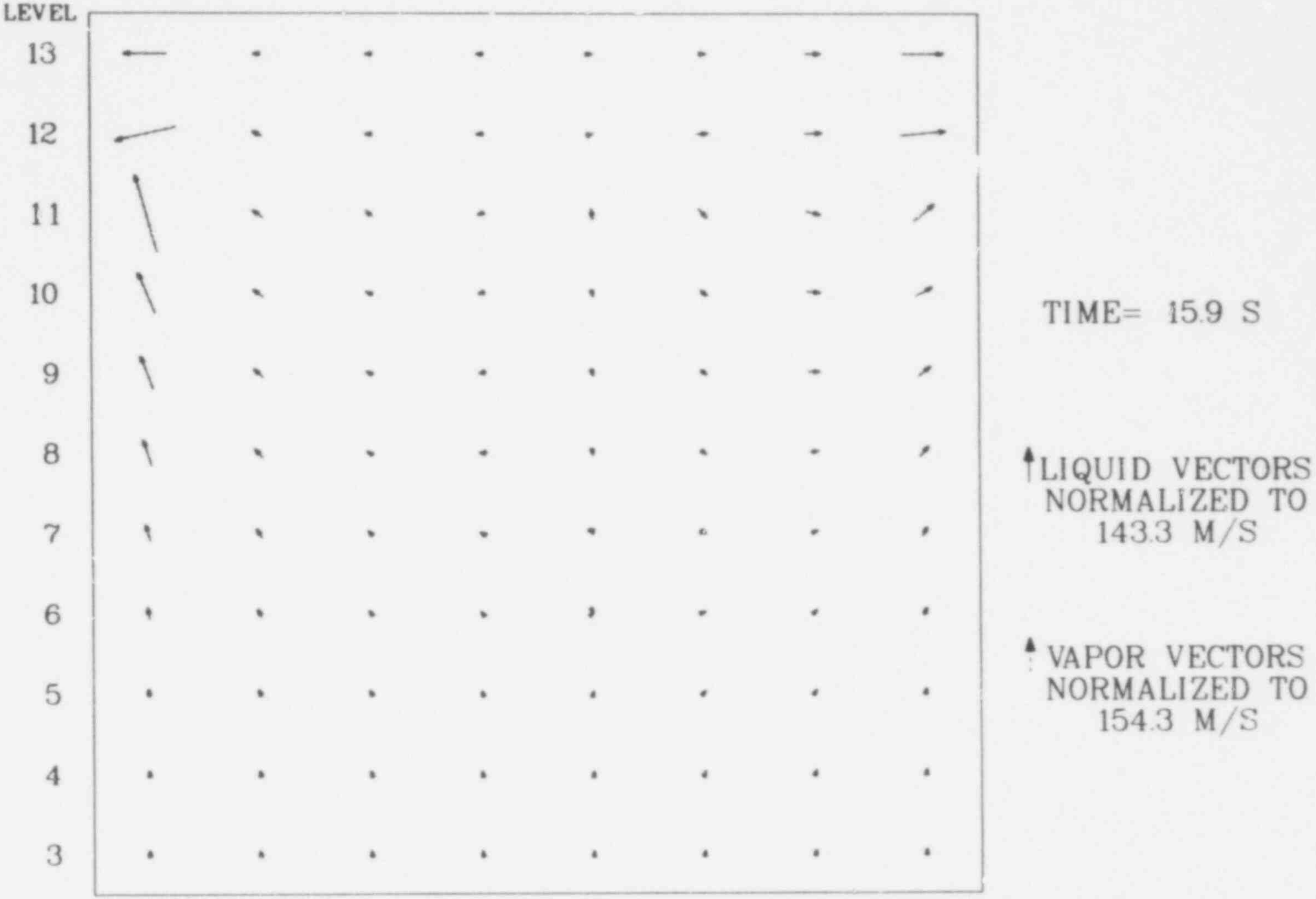

Fig. 32. German PWR downcomer velocities at 15.9 s.

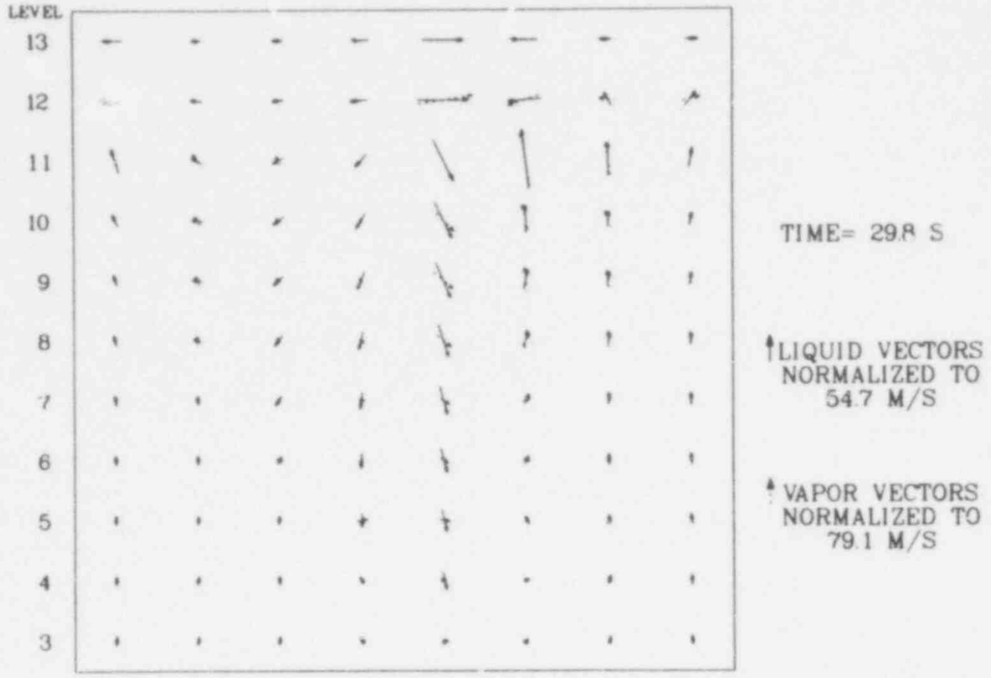

Fig. 33. German PWR downcomer velocities at 29.8 s.

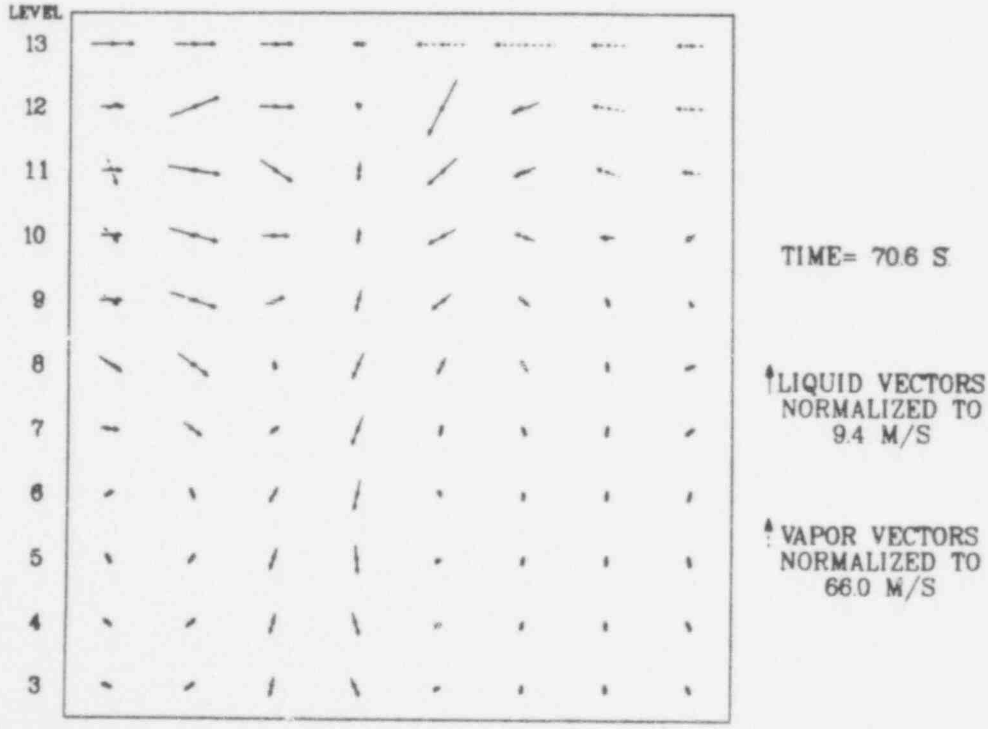

Fig. 34. Germ R downcomer velocities at 70.6 s.

At 15.9 s into blowdown, the downcomer velocities reach their maximum values (see Fig. 32). Note that in the unwrapped downcomer plots the broken cold leg is located in axial level 12, first column. The intact cold legs are located in columns 2, 5, and 6 in level 12. At 15.9 s, it is seen that all of the liquid and vapor velocities are directed toward the broken cold leg with the highest velocities being near the break. There is some evidence of cold-leg ECC penetration in the downcomer from the intact cold legs farthest away from the break, as accumulator flows are initiated at 15 s.

At the end of blowdown, which is about 30 s into the transient, substantial ECC penetration in the downcomer occurs which is shown in Fig. 33. There is still a significant amount of liquid and vapor directed toward the broken cold leg. At this time, however, these velocities are much lower than those occurring at 15.9 s (see Fig. 32). As mentioned previously, the downcomer fills up at about 70 s. Figure 34 shows that the flows in the downcomer at this time are mainly liquid flows and a swirling, or circulation, pattern is present. Note that at this time the flow is into the vessel from the break.

Some of the important parameters calculated in the components of the intact loops are plotted in Figs. 35-39. The pressurizer water level and discharge flow rate are shown in Fig. 35. The pressurizer is essentially empty by about 26 s. The hot-leg mixture velocities at the exit of the vessel are plotted for two representative hot legs in Fig. 36. Tee 71 is the broken hot leg that is connected to cell 32 of the vessel in Fig. 20. Tee 74 is an intact hot leg (with pressurizer) that is connected to cell 27 of the vessel in Fig. 20. Note that these hot legs are opposite each other. From Fig. 36 it is seen that these velocities oscillate and are out of phase with each other. Positive velocity implies flow is out of the vessel. Due to pressure gradients established in the upper plenum, these flows oscillate after hot-leg ECC is initiated until the later stages of reflood, at which time (70 s) the flows stabilize. The other two hot legs show similar behavior, and it appears that when the flows of two hot legs on one side of the vessel are into the vessel, the flows of

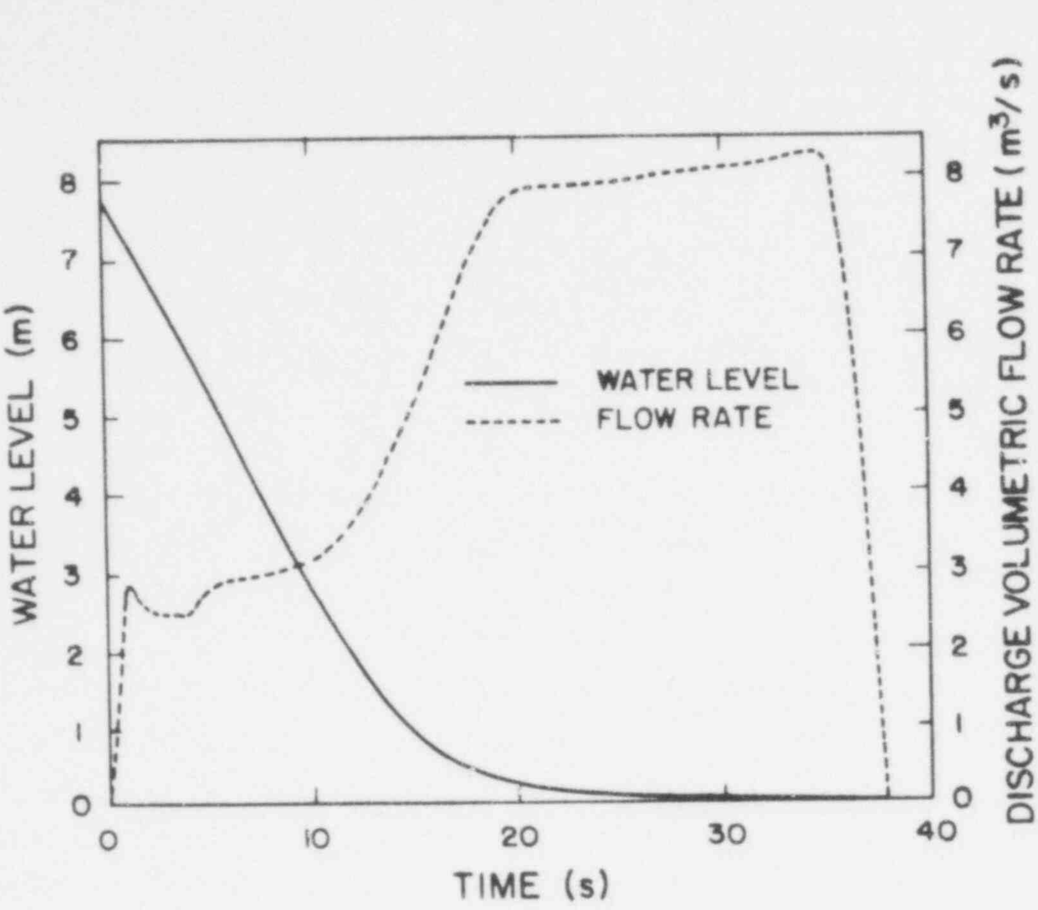

Fig. 35. German PWR pressurizer water level and discharge flow rate.

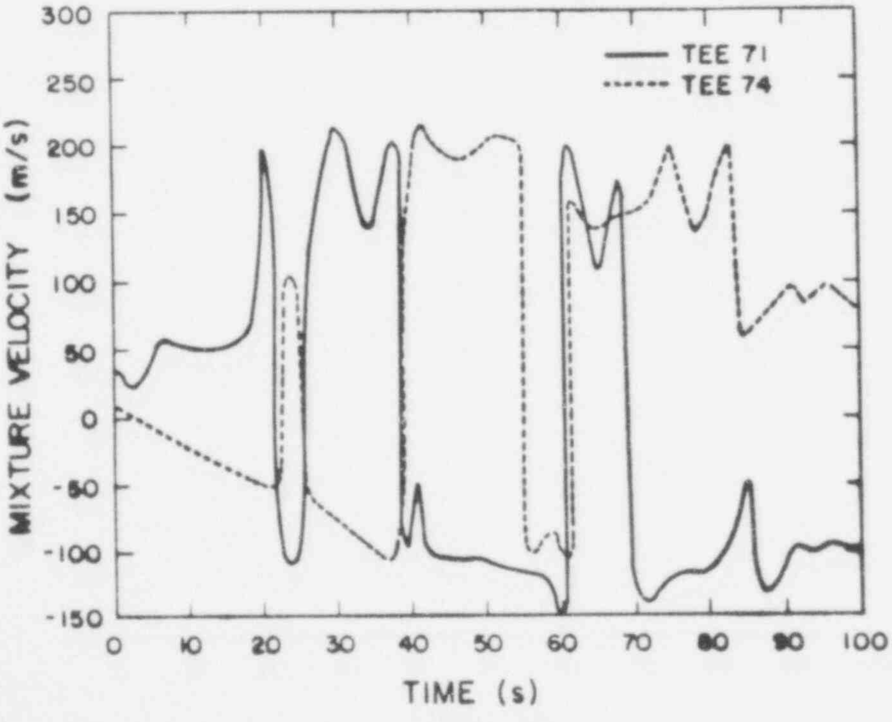

Fig. 36. German PWR hot-leg mixture velocities.

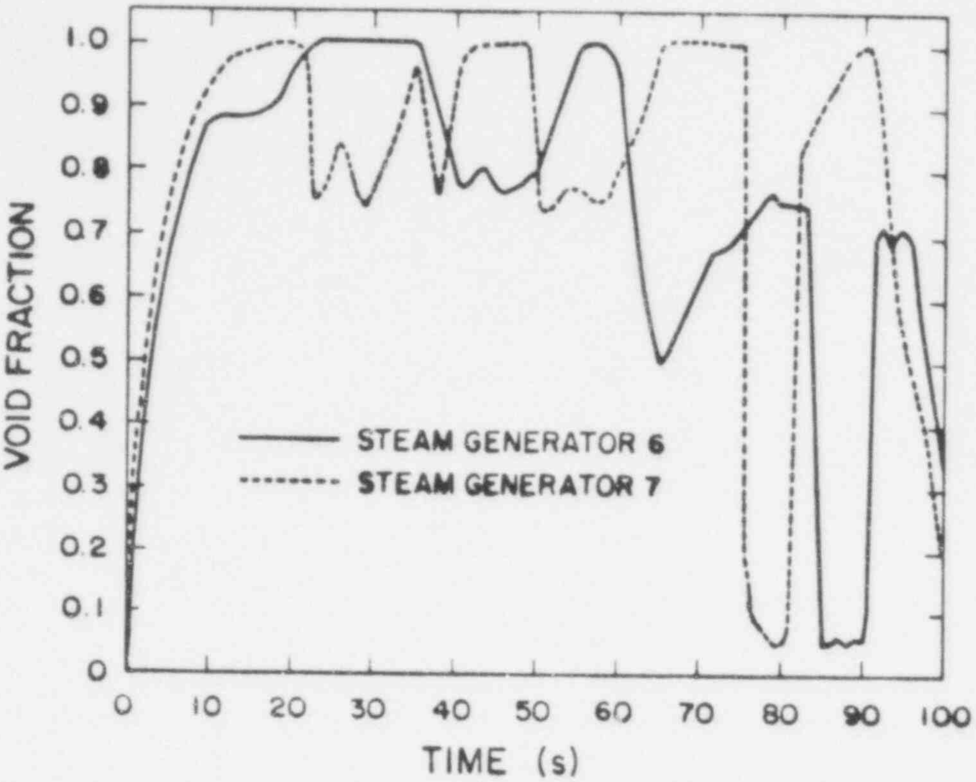

Fig. 37. German PWR steam generator primary side void fraction.

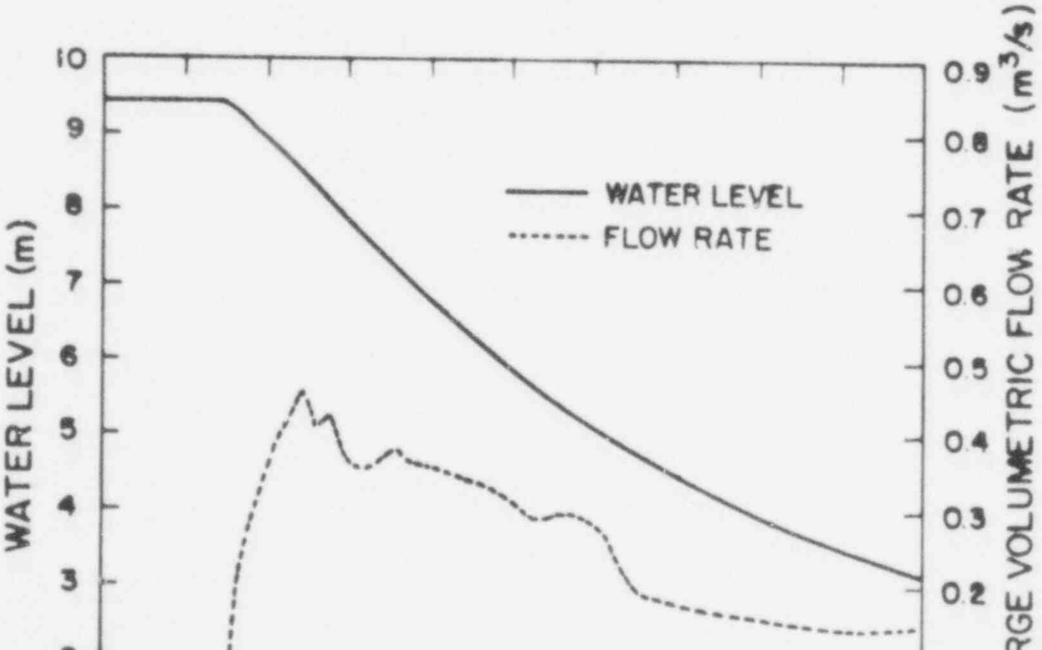

Fig. 38. German PWR hot-leg accumulator water level and discharge volumetric flow rate.

634 116

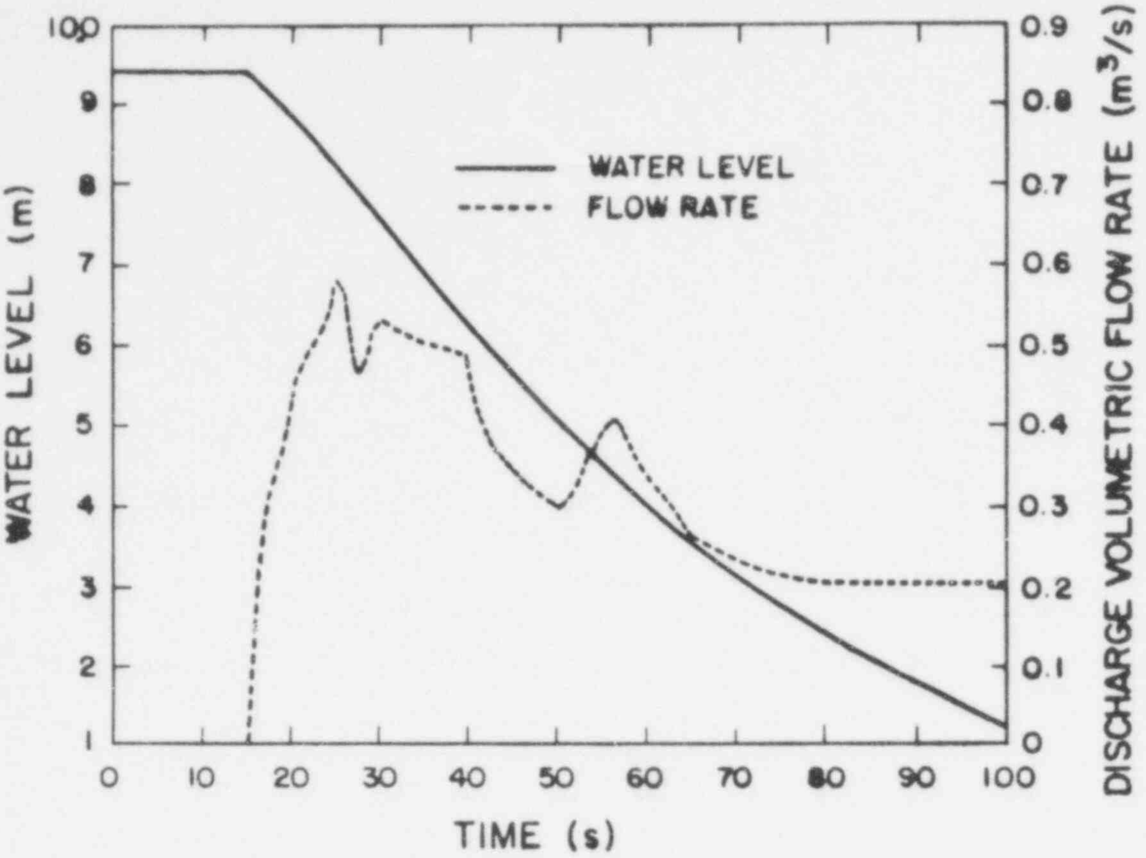

Fig. 39. German PWR cold-leg accumulator water level and discharge volumetric flow rate.

the opposite two hot legs are out of the vessel. These oscillations are believed to result from the predicted violent condensation in the upper plenum causing localized depressurization in regions adjacent to the hot-leg penetrations.

When the hot-leg flows are positive (i.e., flows out of the vessel), the ECC water is carried back through the steam generators. A plot of the primary side void fraction is shown in Fig. 37 for two steam generators. Again, the hot-leg mixture velocity oscillations cause the void fractions to also oscillate. From the calculation it was observed that any ECC liquid reaching the steam generator was vaporized upon exiting, and the vapor appears to be condensing in the closed loop seals next to the pumps. The hot- and cold-leg accumulator water levels and discharge volumetric flow rates are shown in Figs. 38 and 39, respectively. Note that the accumulators do not empty during the calculation.

Some of the broken cold-leg details are shown in Figs. 40-42. The break mass flow rates are plotted in Fig. 40. The spikes in the flow rate between 20 and 60 s are due to ECC bypass. The bypass period is also evident in the mixture density plot in Fig. 41. The void fraction and mixture velocity for the broken cold leg next to the vessel are shown in Fig. 42. ECC bypass is clearly shown in the void fraction plot between 20 and 60 s. Note that at about 58 s the flow reverses into the broken cold leg and vapor is pulled in from the break. The flow reversal is due to initiation of the cold-leg LPIS at 58 s which provides an additional source of subcooled water to the downcomer and lowers the downcomer pressure below the break pressure, causing flow reversal in the broken cold leg. The void fraction drop at 78 s occurs when the downcomer fills and ECC water is expelled out the broken cold leg.

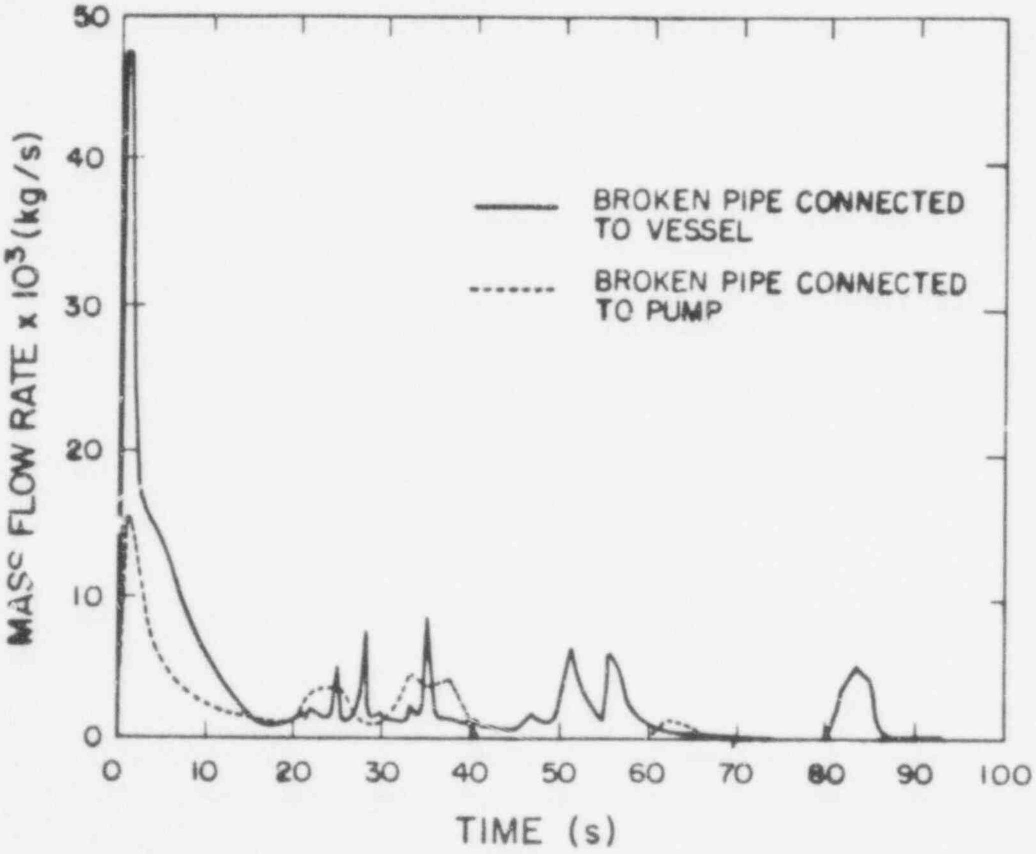

Fig. 40. German PWR break mass flow rates.

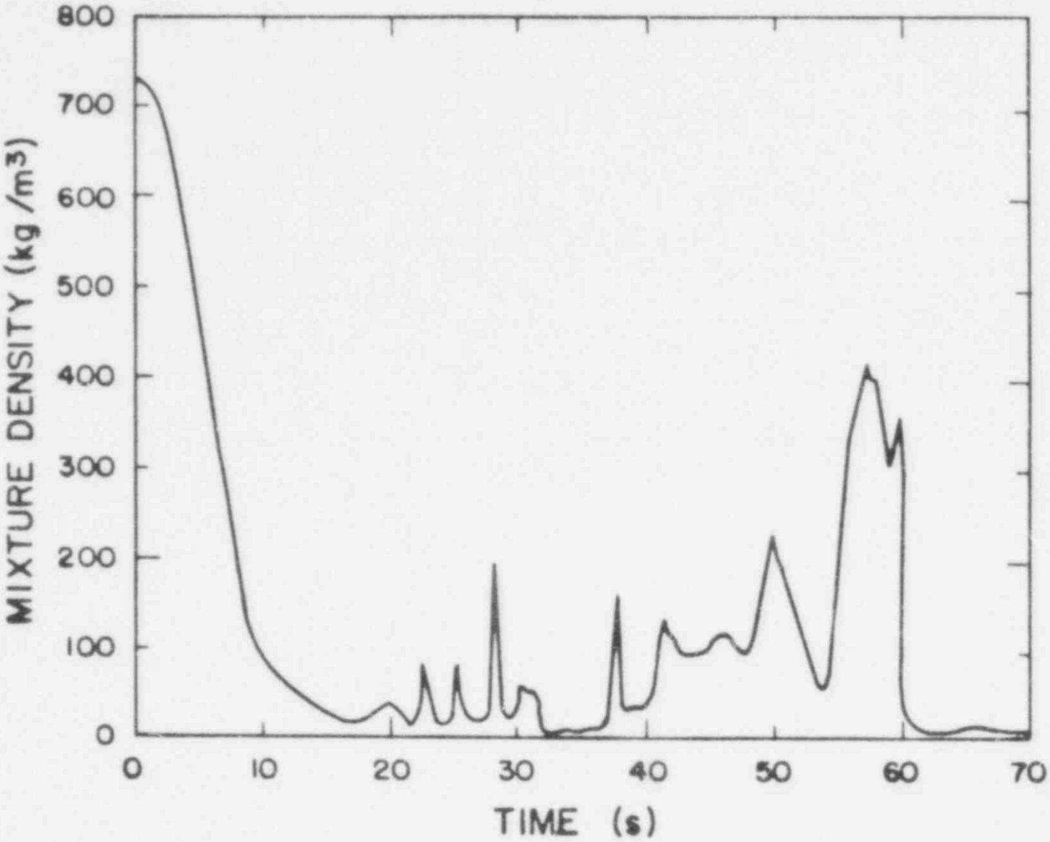

Fig. 41. German PWR mixture density in broken cold-leg pipe next to vessel.

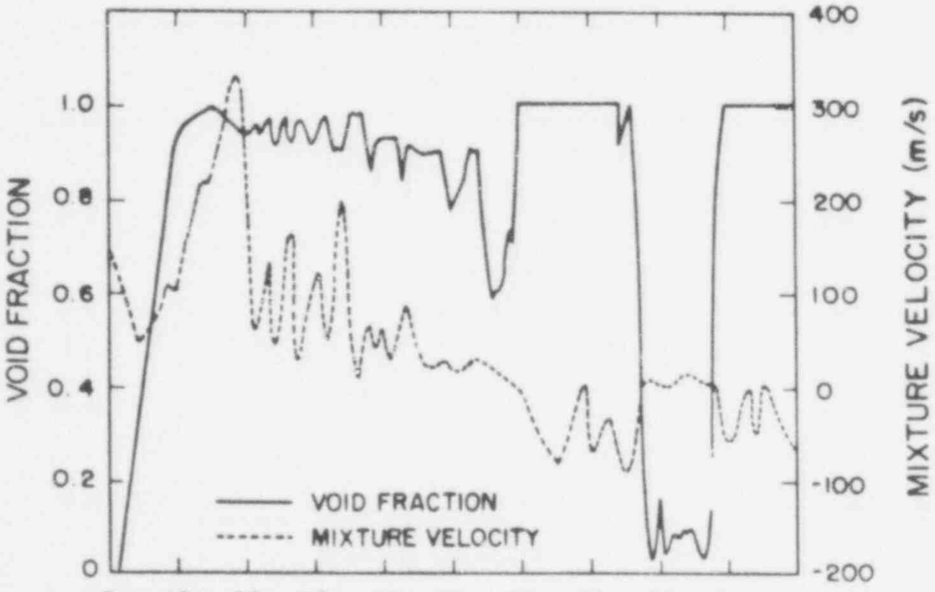

Fig. 42. German PWR void fraction and mixture velocity in broken cold leg.

In conclusion, the combined ECC injection calculation described above exhibited some of the following characteristics:

1. early quenching of peripheral fuel rods results from falling films,
2. a significant pressure gradient is established between the core and upper plenum during reflood which enhances bottom quench front motion, and
3. the entire core is quenched by 100 s by combined falling films and bottom quench fronts.

2. TRAC Calculation of International Standard Problem 6

(S. T. Smith, Q-6)

International Standard Problem 6 is based on one of the series of vessel blowdown experiments performed at the Battelle Institute, Frankfurt.[12] The purpose of these experiments is twofold: to study the physical phenomena occurring after a pipe rupture in a water-cooled reactor and to check the adequacy of computer codes used for licensing such reactors.

The particular experiment modeled is Test SWR-2R which simulates a steam-line break accident. The basic computational problem is to calculate, for the first 3 s of the blowdown, the time histories of pressure and temperature at several specified levels of the main vessel and in the discharge nozzles (break), the mass flow rate in the break, and the water level in the vessel.

The physical system consists of a pressure vessel having a height of 11.9 m, an inner diameter of 0.77 m, a volume of 5.2 m^3, and an initial water depth of 7.07 m. The vessel has no internal structure and was heated electrically between 2.69 m and 5.19 m to achieve the initial temperature distribution shown in Table XII.

At a height of 10.05 m the discharge pipe, attached at 90° like a sharp-edged orifice, has an inner diameter of 0.064 m; its length from the vessel to the break is 0.582 m. The initial vessel pressure was 71.1 x 10^5 Pa and initial mass flow rates in the vessel were zero.

TABLE XII

INITIAL TEMPERATURE DISTRIBUTION FOR INTERNATIONAL STANDARD PROBLEM 6

Height (m)	Temperature (K)
0.6	548.65
1.7	562.55
3.8	562.65
6.4	561.15
7.07	558.15

This system was modeled in two ways for TRAC calculations. One model was a vessel having 10 axial, 2 radial, and 4 azimuthal segments, with a pipe (0.582 m long) attached to the vessel at the ninth axial level at one end and having a break at the opposite end. The other model was a tee with a break at the end of the secondary pipe and two zero velocity fills capping the primary pipe. The axial noding for the primary pipe was identical to that of the vessel, and the noding for the secondary pipe was identical to that of the pipe component in the vessel model. Table XIII compares the calculational aspects of the two models.

Several cases have been run with both models in which the additive friction loss coefficient[13] at the junction of the pipe and the main vessel was varied to account both for the sudden flow contraction and the 90° change in flow direction. The results from both models agree reasonably well with the experimental data for temperatures and pressures; varying the additive friction loss coefficient does not have a large effect for either model on the

TABLE XIII

COMPARISON OF THE VESSEL AND TEE COMPUTATIONAL MODELS FOR STANDARD PROBLEM 6

	Vessel	Tee
CPU Time (s)	141	17.2
Number of time steps	657	302
Average time step size (s)	6.0E-3	1.5E-2

634 121

calculated temperatures and pressures. Figures 43 and 44 show this agreement at the junction level of the vessel and the tee. However, the tee model yields better results for break mass flow rate as shown in Fig. 45.

The main reason for this study was to determine how well TRAC calculates level swell in preparation for the 2D/3D experimental program. We conclude that level swell can be adequately treated using one-dimensional components but additional model development is needed for the vessel component.

3. SCTF Combined Injection Steam Supply Studies

(D. Dobranich, S. T. Smith, J. R. Ireland, and P. B. Bleiweis, Q-6)

Design-related TRAC calculations to simulate hot- and cold-leg ECC injection operation in the SCTF are described in this section. The purpose of these calculations was to determine if an additional steam supply system is necessary during combined ECC injection tests and if it is possible to arrange the vessel steam flows to make the SCTF behave in a manner similar to a PWR. After

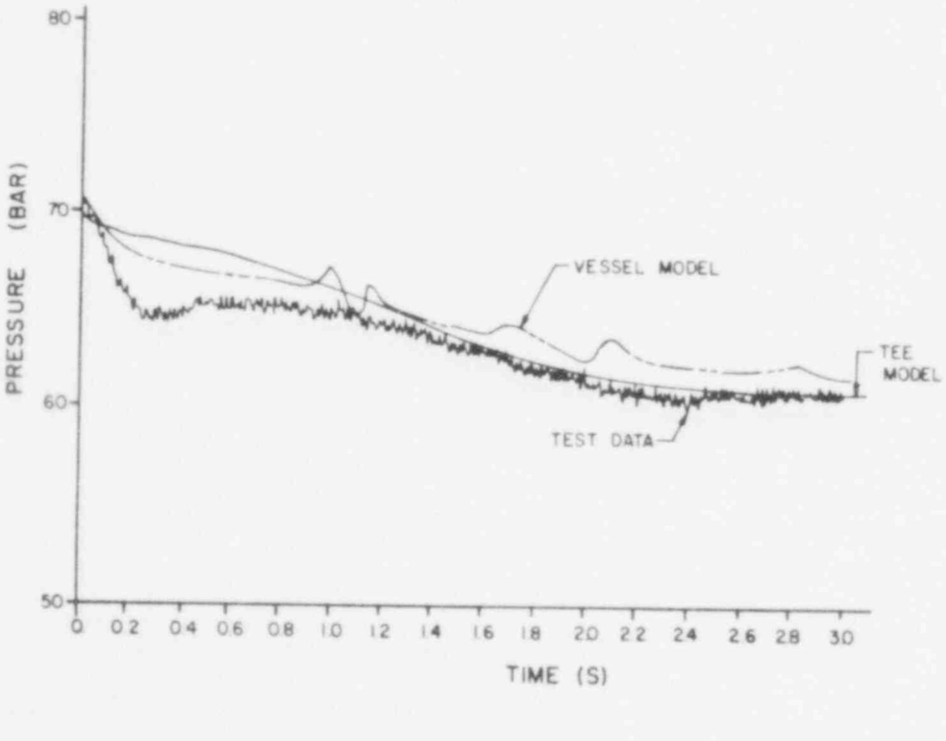

Fig. 43. International Standard Problem 6: pressure at junction level.

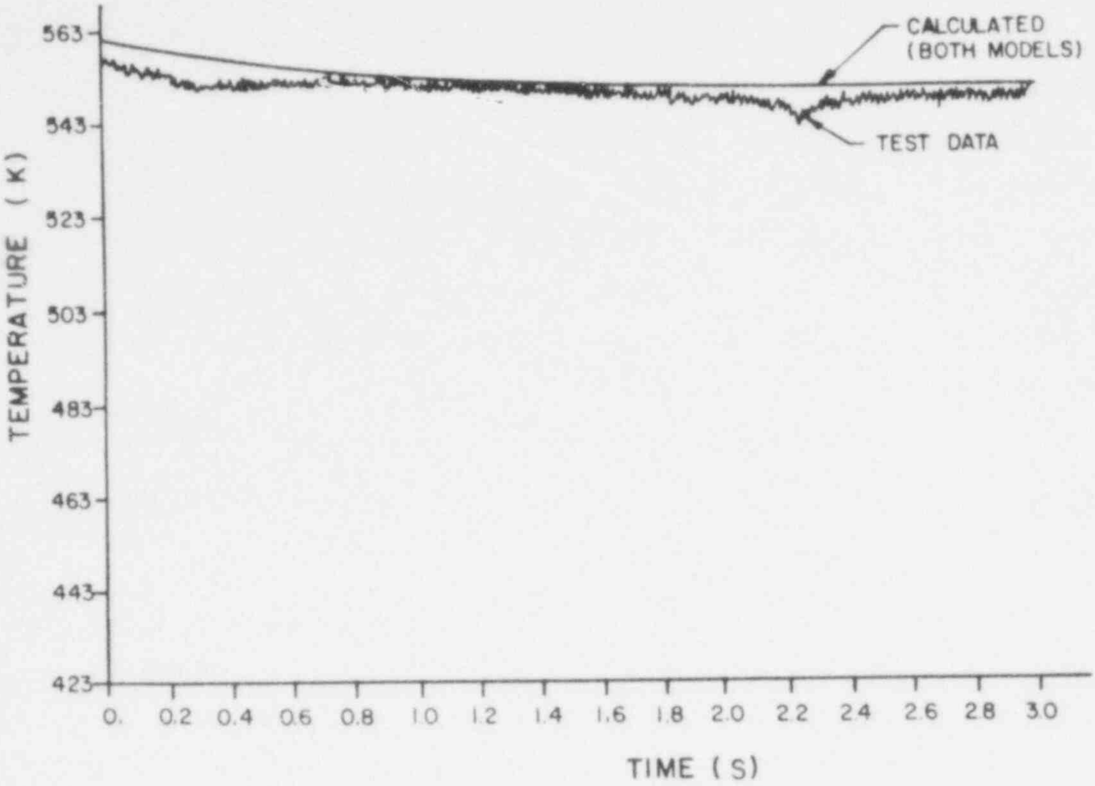

Fig. 44. International Standard Problem 6: liquid temperature at junction level.

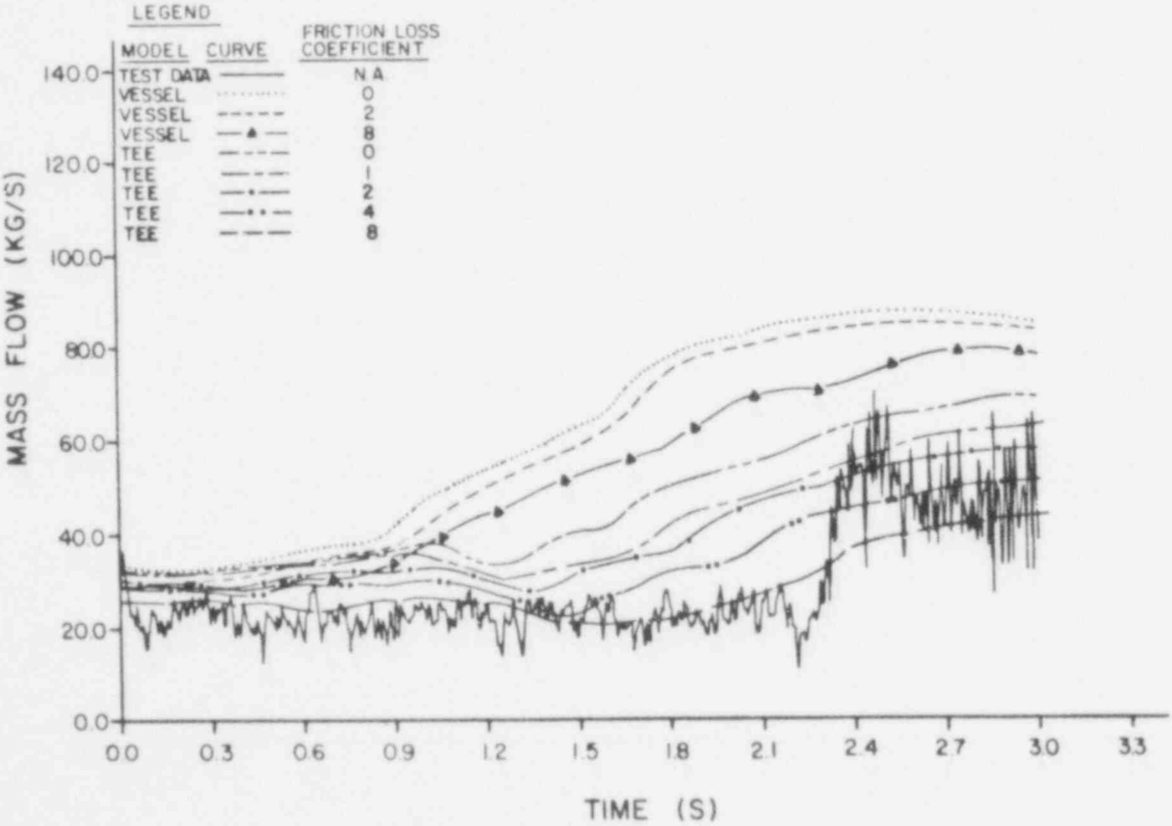

Fig. 45. International Standard Problem 6: break mass flow rate.

a number of preliminary TRAC calculations using vertical pipes to simulate the hot-leg ECC injection, it was recommended[14] that the ECC injection should be simulated with four horizontal pipes entering the vessel above the upper core support plate (UCSP).

The TRAC vessel noding for the combined injection studies is shown in Fig. 46. The TRAC system schematic remained basically the same as that used for the cold-leg injection studies described in a previous quarterly.[7]

A number of TRAC calculations were performed in an attempt to generate prototypical SCTF initial conditions soon after the test is initiated from stagnant conditions. It was found that variations in ECC subcooling and inlet flow rates alone were not sufficient to obtain prototypic end-of-blowdown conditions when compared to a full-scale PWR calculation. In all cases it was found that the blowdown from 6.0 x 10^5 Pa to 3.0 x 10^5 Pa produced core steam flows in a direction opposite to the PWR (flows were from top to bottom instead of bottom to top). This behavior under combined injection was similar to that observed with cold-leg injection only; the flow was dominated by the pressure drop toward the break.

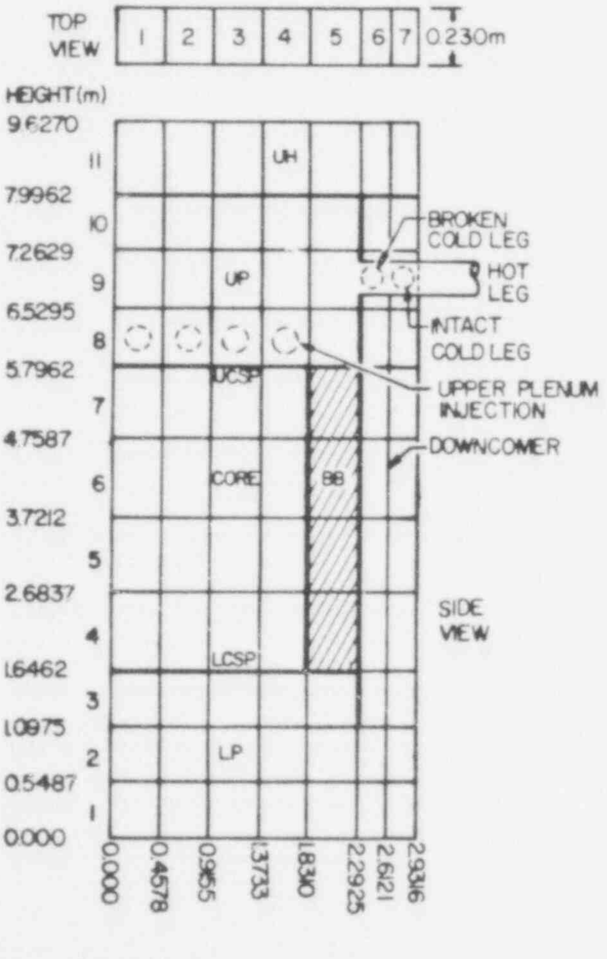

Fig. 46. Slab core two-dimensional vessel.

In an attempt to generate core steam mass flows in the same direction and about the same magnitude as that calculated in a German PWR, a few TRAC calculations were performed which modified the operation of the break valves and ECC initiation. It was found that by delaying the cold-leg ECC injection by 2 s (from t = 0 s), starting the hot-leg injection at t = 0 s, delaying the opening of the cold-leg break valve by 2 s (opening at a linear rate over the next 4 s), and opening the hot-leg break valve at t = 0 s (over a 2 s interval), a base case could be defined which generated steam flows which match the PWR calculation for the first few seconds of the transient.

Figure 47 is a graph of core steam mass flow rate (near the top of the core) for the base case in SCTF and the German PWR scaled down to match the SCTF at the end of the blowdown. Other cases shown in the figure are discussed later. The general trend of the mass flow behavior in the SCTF matches the PWR quite well but the magnitude of the SCTF mass flow rate is much lower than the PWR for the first 20 s of the transient. At about 25 s liquid is entering the core to produce enough steam to generate about the same mass flows as in the PWR. Figure 48 shows the average core pressure vs time for both the SCTF and German PWR. The SCTF blows down faster and to a lower pressure than the PWR and during the refill period the pressure stays lower than the PWR.

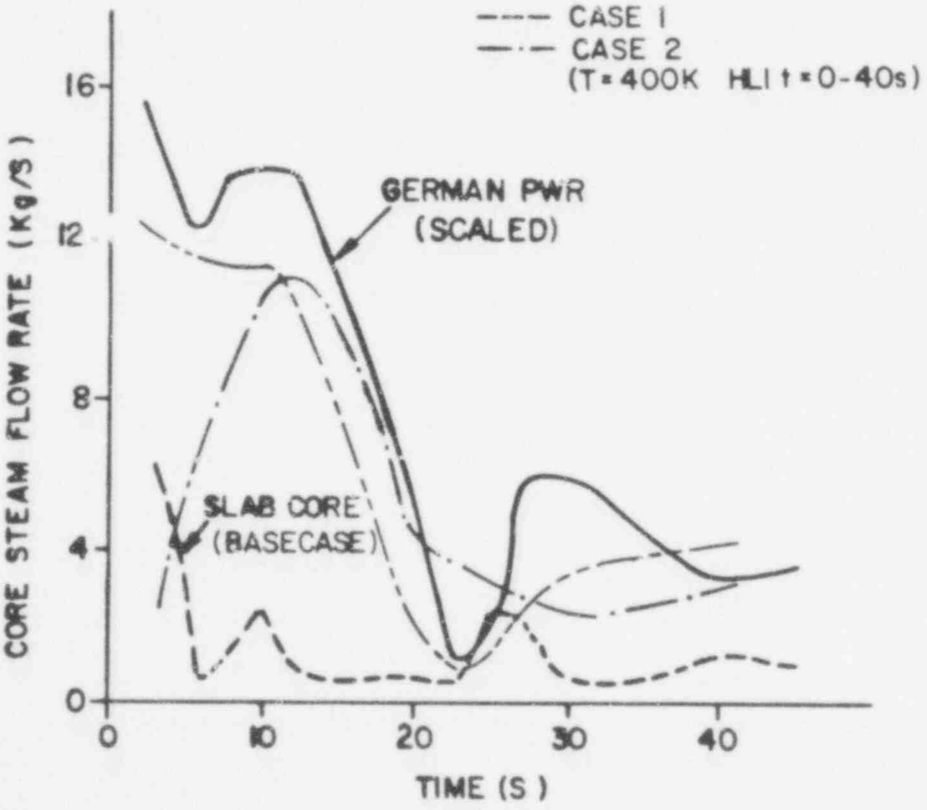

Fig. 47. Core steam flow rates during reflood.

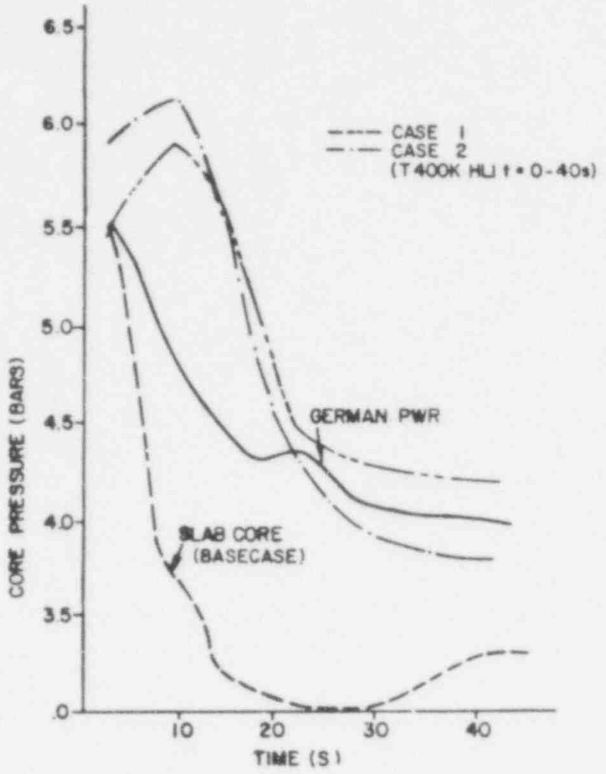

Fig. 48. Core pressure during reflood.

If it is desired that the SCTF behave in a manner similar to a PWR during combined injection, it is probably necessary to change the basic facility design and add an extra steam supply to the vessel. This steam supply would hold the pressure up and allow flexibility in the test so that parametric tests could be run to bound some of the PWR conditions. Table XIV shows the difference between the scaled PWR and base case SCTF maximum steam mass flow rates through the UCSP at various points in time for the first 40 s of the SCTF transient. As can be seen from this table the largest amount of steam is needed during the first 20 s of the transient. After this time enough steam is generated in the SCTF to match the PWR flow rates.

In an attempt to increase the magnitude of the SCTF steam flows shown in Fig. 47, a steam supply system was modeled consisting of two pipes (0.20 m diam) supplying slightly superheated steam at 4.6 bar through the lower core support plate in the

TABLE XIV
ADDITIONAL SCTF STEAM NEEDED

Time (s)	Mass Flow (kg/s)
3.0	10.0
5.6	10.0
7.2	13.0
12.3	14.0
22.8	0.0
27.3	3.0
39.4	2.0

vertical direction. A time-dependent velocity profile was used for each pipe as shown in Fig. 49. Two cases were run using the following steam supply system assumptions.

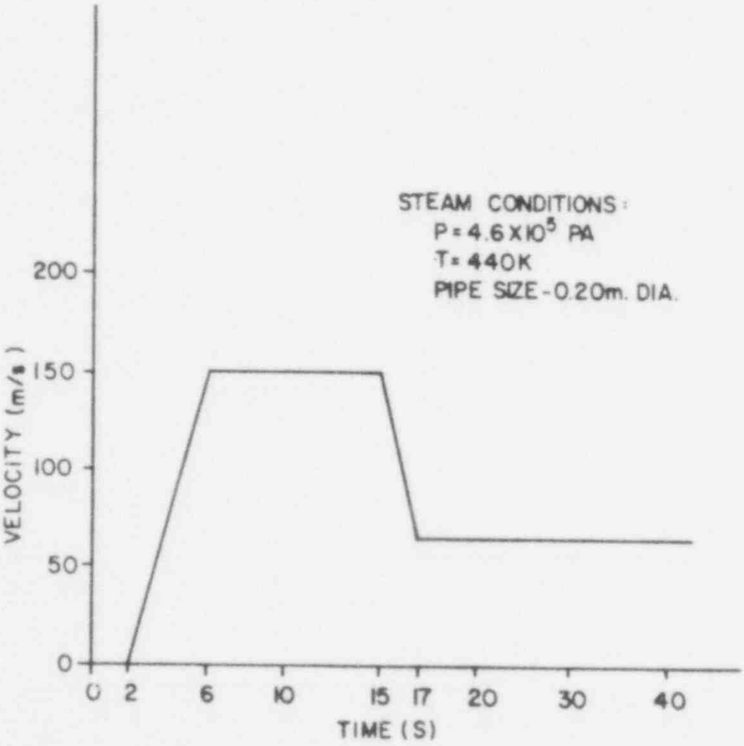

Fig. 49. Steam supply velocity requirements for SCTF (2 pipes required).

Case 1 - Highly subcooled (100 K) hot-leg ECC injection for the first 3 s, and 15 K subcooled for the remainder of the transient.

Case 2 - Slightly subcooled (15 K) hot-leg ECC injection used throughout transient.

The results of these calculations are also plotted in Figs. 47 and 48. To match the German PWR calculation during the initial part of the transient, it was determined that highly subcooled ECC injection into the upper plenum is needed for the first 3 s (Case 1). For Case 2 the initial steam flows and core pressure do not match the German PWR; however, the cladding temperature response is better during the later stages of the transient. Note that both cases compare well with each other and the PWR after about 15 s. With an additional steam supply in the core the pressure increases dramatically from the base case and is somewhat higher than the PWR for the first 20 s.

Figure 50 shows the lower plenum liquid volume fraction comparisons with the base case calculation. From this plot it is seen that the disadvantage of using the extra steam supply is the delay in lower plenum refill. This is caused by the high pressure in the core preventing cold-leg ECC from filling the lower plenum. If the steam supply is ended between 30 and 40 s then it is expected that the lower plenum will refill at about 60-70 s into the transient which is about a 30 s delay.

The upper plenum liquid volume fraction comparisons with the base case are shown in Fig. 51. More pool formation is seen to occur in Case 1 due to the initial high subcooling when compared to Case 2, but both cases in general show less pool formation than the base case due to the additional steam supply. However, toward the end of the transient the agreement is quite good.

In conclusion, it appears that an additional steam supply system is needed for the SCTF to provide prototypical flows, pressures, and clad temperatures in the core. However, in order for the lower plenum to refill and for bottom quench front motion to

634 128

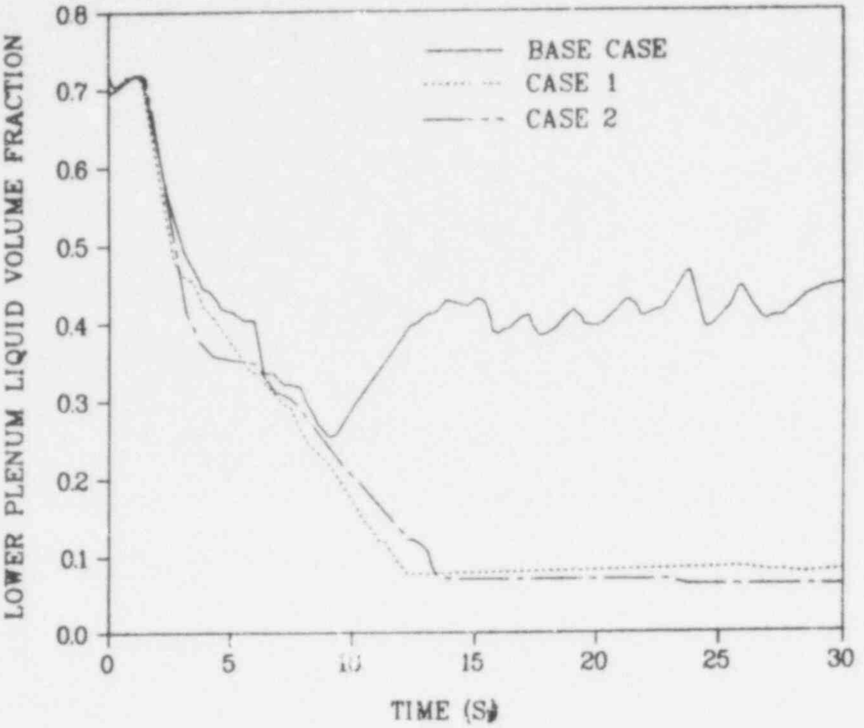

Fig. 50. SCTF lower plenum liquid volume fraction.

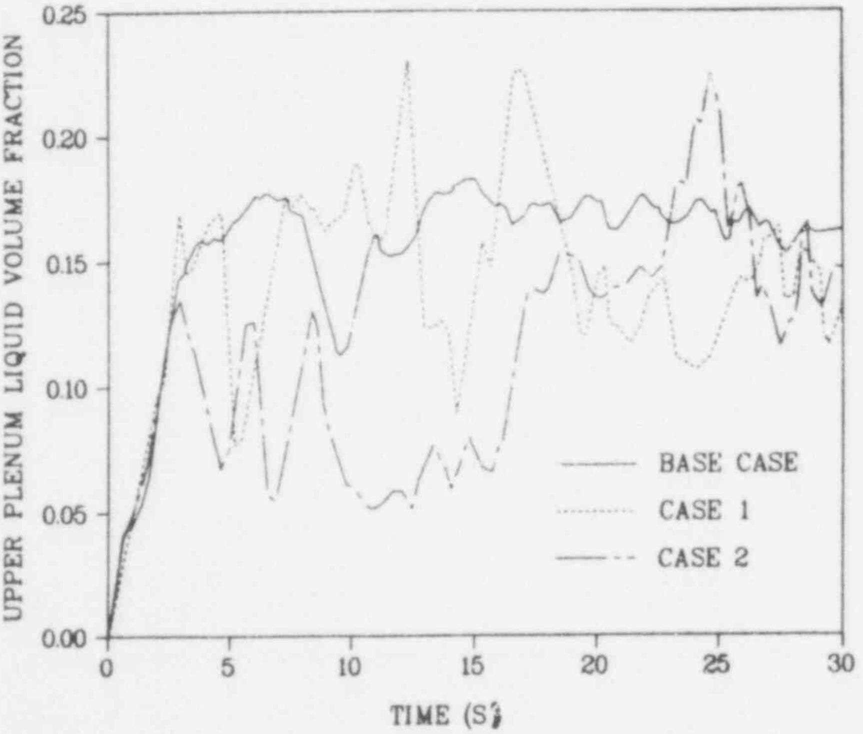

Fig. 51. SCTF upper plenum liquid volume fraction.

634 129

occur, the additional steam supply should be discontinued after about 30-40 s into the transient.

C. Independent TRAC Assessment

(J. C. Vigil, Q-6 and K. A. Williams, Q-9)

Independent assessment of TRAC mainly involves pretest and posttest predictions of tests in designated facilities using the publicly released and documented versions of TRAC. The primary objective of this activity is to determine the predictive capability of TRAC when applied to new tests involving different scales and experimental configurations. Facilities which are currently included are LOFT, Semiscale MOD 3, LOBI, FLECHT-SEASET, and Marviken III. The scope of the Independent Assessment Program (IAP) includes posttest analyses to resolve discrepancies between the code predictions and the test results. If needed to resolve discrepancies, these analyses will include tests in other facilities. Recommendations for future code development or experiments and participation in the NRC standard problem exercises are also included in the scope of this activity.

Posttest analyses of LOFT Test L2-2 were performed during the quarter. Results of these analyses are reported in Sec. II.A. The main conclusion from these analyses is that better agreement between calculated and measured clad temperature histories can be obtained by use of an improved rewetting correlation. The status of the L2-3, Semiscale MOD 3, and LOBI predictions is described below.

1. Status of TRAC Pretest Prediction for LOFT Test L2-3

(A. C. Peterson, Q-6 and K. A. Williams, Q-9)

The TRAC model for the pretest prediction for LOFT experiment L2-3 has been developed. This model has some differences from the model used for the pretest prediction of experiment L2-2. The upper plenum volume was increased to correspond with the revised value calculated by the INEL. The volume of the reflood assist lines was also added to the broken loop hot and cold legs to agree with the system configuration.

634 130

A steady-state calculation has been performed for experiment L2-3. Specified test conditions and the TRAC calculated initial conditions are given in Table XV.

2. TRAC Calculation of Semiscale MOD 3 Test S-07-6

(J. J. Pyun and J. C. Vigil, Q-6)

Test S-07-6 was the sixth test in the Semiscale MOD 3 baseline test series and was the first integral blowdown reflood test conducted in the MOD 3 system.[15] The purpose of Test S-07-6 is to provide reference data to evaluate the integral blowdown and reflood behavior during a 200%, cold-leg break with emergency core coolant injection into the intact and broken loop cold legs. In addition, test results were used to investigate the effects of the MOD 3 system changes (relative to the MOD 1 system) on the thermal-hydraulic behavior.

The TRAC model for Test S-07-6 is identical to that for Test S-07-1 reported in a previous quarterly report,[16] except that a TEE module is used to model the inlet annulus transition region and downcomer pipe. In addition, the TRAC code was modified to allow specification of the measured, time-dependent heat flux from the outer downcomer pipe to the downcomer fluid as a boundary condition.

The preliminary TRAC analysis of Test S-07-6 was completed and results were presented to NRC on February 7, 1979. The results of this preliminary analysis show good agreement between the TRAC calculations and test data during the blowdown period. However,

TABLE XV

INITIAL CONDITIONS FOR LOFT TEST L2-3

	Power MW(t)	T_{hot} (K)	Core ΔT (K)	Intact Loop Flow (kg/s)	Steam Pressure (Pa)
Test Specifications	37.2	591.5	35.8	187.7	1.495×10^7
TRAC	37.2	591.4	35.6	185.4	1.504×10^7

the TRAC calculations only qualitatively agree with test data during the reflood period, indicating multiple downcomer and core liquid mass depletions with a period of approximately the right magnitude. It was found that the one-dimensional, drift-flux model currently in TRAC does not treat countercurrent flow very well. Therefore, a VESSEL module is being used to model the downcomer pipe to better calculate the liquid penetration during the reflood period.

3. Semiscale MOD 3 Test S-07-10B -- Small Break Standard Problem

(T. D. Knight, Q-6)

The Semiscale MOD 3 system drawings are being reviewed in order to revise and update the TRAC input model prior to running the small break standard problem calculation. To date, small differences in piping volumes have been noted and are being resolved. Particular attention is directed toward component elevations and lengths.

All information (initial and boundary conditions) required for running the calculation has been assembled. Preliminary modeling techniques have been discussed in-house for the break configuration and for the blowdown of the secondary side of the broken loop steam generator. Representation of downcomer heat transfer remains a problem.

4. TRAC Posttest Prediction of the First LOBI Experiment

(A. B. Forge, CEA, France)

The LOBI test facility is an approximately 1/700-scale model of a 4-loop, 1 300 MWe PWR primary cooling system. It consists of a 5.3 MW electrically heated rod bundle within the reactor vessel and two primary loops: one simulating three loops of a PWR, the other simulating the broken loop in a hypothetical LOCA. Both loops are active loops. They are designed for a pressure of 160 x 10^5 Pa and a temperature of 600 K. Breaks of various sizes and locations will be simulated. At this time the only ECC water injected will come from one or two accumulators. The facility will be used to study the blowdown and refill phases of a LOCA. The

634 132

first experiment is scheduled for May 1979. It will be a 200%, cold-leg break.

The preparation of the input data for TRAC is almost complete. A steady-state calculation has been run to compare calculated pressure losses with measured losses furnished by the LOBI facility. We are waiting for some additional information before performing a transient calculation with nominal initial conditions.

D. Thermal-Hydraulic Research for Reactor Safety Analysis

(W. C. Rivard, T-3)

The research reported in this section focuses on the modeling of nonequlibrium vapor production for critical flow and the dynamics of droplet spray flow through an array of circular cylinders.

1. A paper has been written that describes a turbulence-centered nonequilibrium vapor production model for critical flow. The model is shown to provide an accurate description of flow rate and throat pressure data for the Semiscale and Marviken blowdown tests. A description of the model and the data comparisons are provided.
2. The dynamics of a spectrum of entrained droplets flowing past single and multiple circular cylinders is being calculated to investigate net capture efficiency. A model has been developed to describe the re-entrainment effects of splash, which have been observed in tests to produce a significant reduction in capture efficiency.

1. A Nonequilibrium Vapor Production Model for Critical Flow

(W. C. Rivard and J. R. Travis, T-3)

The purpose of this section is to describe a new nonequilibrium model for flashing and to demonstrate its capability by comparison of calculated results with flow rate and pressure data from small- and large-scale critical flow experiments. The model is based on the well known conduction controlled rate[17-19] but includes the effects of dynamics on the liquid thermal diffusivity and on the size scale of vapor bubbles. The initial vapor production that accompanies rapid depressurization of initially subcooled water is controlled by specification of the nucleation site density and the dissolved gas content. The model is suited for use in conjunction with homogeneous, drift-flux, or two-fluid descriptions of the two-phase flow. The calculated results are compared with data from two small-scale experiments[20,21] performed at INEL on the Semiscale MOD 1 apparatus and with the data from two large-scale experiments performed at the Marviken Power Station in Sweden.[22]

Nonequilibrium effects are significant only during the early portion of the blowdown when single-phase subcooled water enters the nozzle. Consequently, we focus our attention on a description of the onset of vapor production that occurs as initially subcooled water is rapidly depressurized. In a stationary environment, depressurization leads to vapor production and bubble growth that is well described by the classic conduction controlled rate in which the bubble radius r grows according to the relation

$$\frac{dr}{dt} = (6/\pi)(1/r)(\rho_\ell/\rho_g)^2 \; \alpha_\ell[C_\ell(T_\ell - T_s)/L]^2 \; , \tag{25}$$

where ρ_ℓ and ρ_g are liquid and gas microscopic densities, α_ℓ is the liquid thermal diffusivity, C_ℓ is the liquid specific heat, T_ℓ is the bulk liquid temperature, T_s is the saturation temperature determined by the pressure, and L is the heat of vaporization. The void fraction θ is related to r and the number of bubbles per unit of mixture volume N as

$$\theta = N \; 4\pi \; r^3/3 \; . \tag{26}$$

The rate of production of vapor mass per unit of mixture volume J_e is obtained from a combination of Eqs. (25) and (26) as

$$J_e = \rho_g \frac{d\theta}{dt} = \rho_\ell(18/\pi)(\theta/r^2)(\rho_\ell/\rho_g) \; \alpha_\ell[C_\ell(T_\ell - T_s)/L]^2 \; . \tag{27}$$

This rate expression has been used in the transient, two-dimensional, two-fluid code K-FIX[23] for calculation of the growth of an isolated bubble[24] (N = 1) in a stationary medium. The calculated radius history compared with the analytic solution of Eq. (25) shows excellent agreement to within the resolution of a computational cell. Because our primary interest is for applications involving water, which has a relatively low thermal conductivity, we neglect the very brief inertia dominated portion of the bubble growth.[25]

For application to the highly dynamic environment of a critical flow, we retain the form of Eq. (27) but use a thermal diffusivity and bubble radius that reflect the combined effects of relative motion and turbulence. This allows the model to approach the correct limit in a quiescent environment. Physically, we visualize bubbles, with an initial radius determined by specification of initial values of N and θ, that grow at a rate close to but somewhat larger than the conduction controlled rate because of the enhanced heat transfer from the bulk liquid to the bubble interface by relative motion and turbulent fluctuations in the liquid. The bubbles continue to grow until they reach a critical size, determined by a Weber number criterion, and then begin to break up. From this point on, the typical bubble size is taken as the critical size and the specified initial number of bubbles no longer plays a role. The critical radius for bubble breakup is given by Levich[26] as

$$r_{crit} = 2.3\sigma/[\bar{V}^2(\rho_\ell^2\ \rho_g)^{1/3}]\ , \tag{28}$$

where σ is the surface tension and $\bar{V}$ is the relative speed between the bubble and the surrounding fluid. The surface tension of water in contact with saturated steam is given quite accurately by the empirical relation

$$\sigma = 70.9[\rho_\ell - (\rho_g)_s]^4\ , \tag{29}$$

where $(\rho_g)_s$ is the saturated steam density. The relative speed $\bar{V}$ reflects the combination of the average relative speed and the contribution of local turbulent fluctuations in the liquid. To minimize the complexities of the model, in view of the limited departure of equilibrium calculations from the data, we propose to describe the combined effects of these contributing elements by writing $\bar{V}$ as

$$\bar{V} = \beta \, V_\ell \ , \tag{30}$$

where V_ℓ is the liquid speed and β is a parametric function of void fraction. Values of β vary from 0.01 at low void fractions to 0.05 at $\theta = 1/2$ according to the expression

$$\beta = 0.01[1 + 64\bar{\theta}^3 \ (2 - 3\bar{\theta})] \ , \tag{31}$$

where $\bar{\theta} = \theta$ for $\theta \leq 1/2$ and $\bar{\theta} = 1 - \theta$ for $\theta > 1/2$. In critical two-phase flow the mean relative velocity is known to be very low for bubbly flow,[27] which is our regime of interest. Consequently, the primary role of β is to model the effects of turbulent mixing. The magnitudes of β are consistent with observed turbulent velocity fluctuations that are generally less than 10% of the mean flow velocity. The increase in β toward the middle void range models the effects of increased mixing due to a postulated increase in turbulence intensity from higher shear flow associated with thinning liquid sheets as well as a possible increase in mean relative velocity. The extension of β to values of $\theta > 1/2$ is only done to provide a smooth continuation of the function. At these larger void fractions, the flow rates are essentially independent of the vapor production rate.

A typical value of r_{crit}, calculated from Eqs. (28-31), is 0.2 mm in the throat of the Semiscale nozzle shown in Fig. 52. The initial bubble radius is determined by specification of $N = 1\ 000\ cm^{-3}$ from the data of Friz, et al.,[28] and the specification of initial void fraction at 2×10^{-4} for subcooled liquid (see Ref. 25) or at its measured

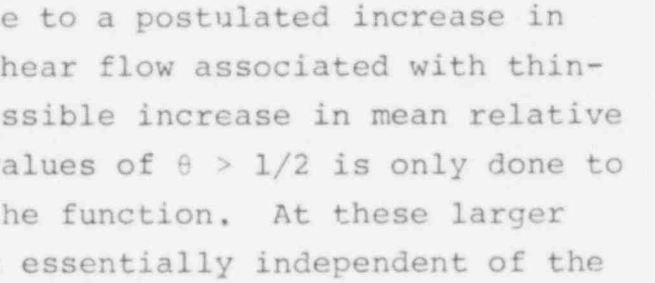

Fig. 52. Design of the Henry nozzle for Semiscale experiment S-02-4 (from Ref. 21). Flow is from left to right.

value for saturated two-phase flow. This initial void fraction value for subcooled liquid agrees very well with measured values of dissolved gas content in the water used for the large-scale blowdown tests at the Marviken Power Station in Sweden. The initial bubble radius calculated from Eq. (26) with the above values of N and θ is r = 0.036 mm. Although these initial values of N and θ may vary considerably with the dissolved gas content, impurities in the water, and the nozzle surface conditions, a sensitivity study has shown that the calculated results are relatively insensitive to order of magnitude variations. This relative insensitivity is not surprising because the bubbles grow very quickly to a size controlled by the Weber number criterion.

The enhanced liquid thermal diffusivity $\bar{\alpha}$ that replaces the molecular value to account for the effects of relative motion and liquid turbulence is

$$\bar{\alpha} = \alpha_\ell + A\, r\, \bar{V} ,$$

where A is an empirically determined, dimensionless constant. The value of A = 0.1 has been determined to match the flow rate data at 1 s for the Semiscale test S-02-4. This value is held fixed for all calculations reported below.

The calculations have been made with the transient, two-dimensional, two-fluid code K-FIX. For the calculational results presented, the value of the interfacial drag function is chosen sufficiently large that there is essentially no relative motion and the interfacial heat transfer term is chosen so that the steam is always saturated. Although the K-FIX code can treat interpenetrating flow and temperature nonequilibrium in the gas field, the above choices are simple and are shown to be adequate to describe a broad range of critical flow data. They are also compatible with commonly used homogeneous flow and drift-flux treatments. An alternate choice for the interfacial heat transfer term is to set R large, which results in the gas temperature being very nearly equal to the liquid temperature. This alternate choice has very little effect on the calculated mass flow rates and throat

634 137

pressures because the heat capacity of the liquid is so much larger than that of the gas. Furthermore, the liquid and saturation temperatures differ by only a few degrees when nonequilibrium flashing is occurring. The state equations for steam and water are obtained from analytic fits to steam table data and are accurate to within a few per cent for the pressure and temperature range of interest.

The calculations are made in one dimension using the variable area capability of the code. The axial spacing of the computational cells is uniform and equal to 0.5 cm for the Semiscale tests S-02-4 and S-06-5 and equal to 2.5 cm for the Marviken tests. The upstream boundary conditions are specified from measured data at about 1.5 entrance diameters upstream of the initial area change. The computing mesh extends well into the expansion region downstream of the nozzle throat for all cases. The flow rate and throat pressure calculated with K-FIX have been shown to be independent of the downstream pressure (Ref. 29) so long as it is below a critical value. No break-flow multiplier is used in any of the calculations, other than to correct the flow rates for multidimensional effects as described in Ref. 29. It is interesting to note that one- and two-dimensional calculations for the Marviken nozzles used in tests 1 and 4 indicated that the one-dimensional flow rates would be too high by the factor 1.06, which is in excellent agreement with Ref. 29 for nozzles with a throat length to throat diameter ratio of 3.

The calculated mass flow rates and throat pressures are compared with the data for Semiscale test S-02-4 (nozzle design shown in Fig. 52) in Figs. 53 and 54. The results for the nonequilibrium model described in the previous section are denoted with circles. The results for a very large vapor production rate that produces, very nearly, continuous equilibrium states in which the liquid, saturation, and gas temperatures are the same are denoted with triangles. Subcooled liquid enters the nozzle for t < 3 s and a two-phase mixture enters thereafter. By 20 s the void fraction entering the nozzle is 95%.

634 138

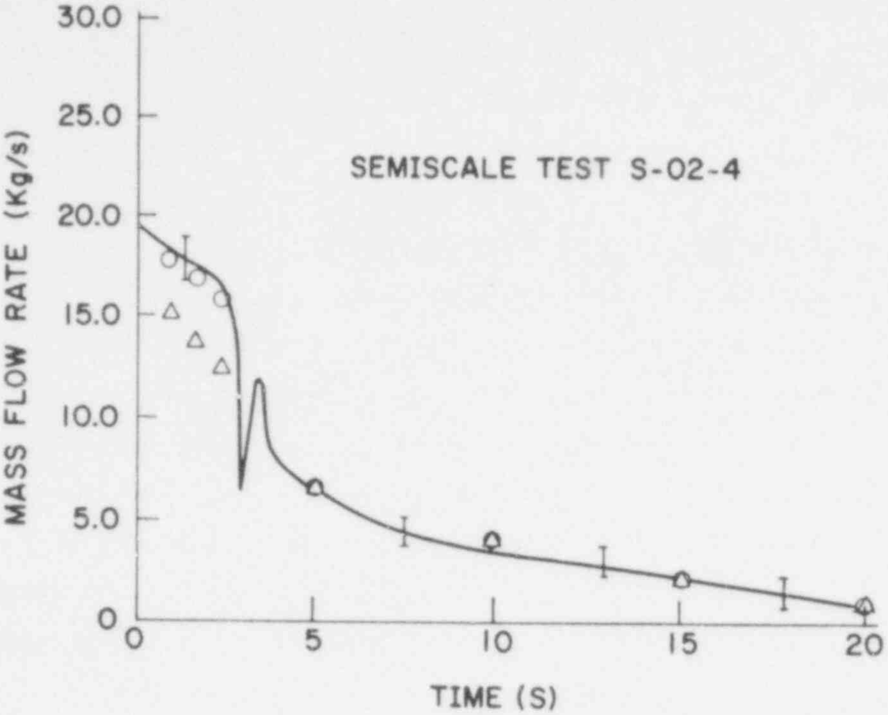

Fig. 53. Comparison of the measured mass flow rate (—) from Ref. 21, the computed mass flow rate with the nonequilibrium model (o), and the computed mass flow rate for equilibrium (Δ).

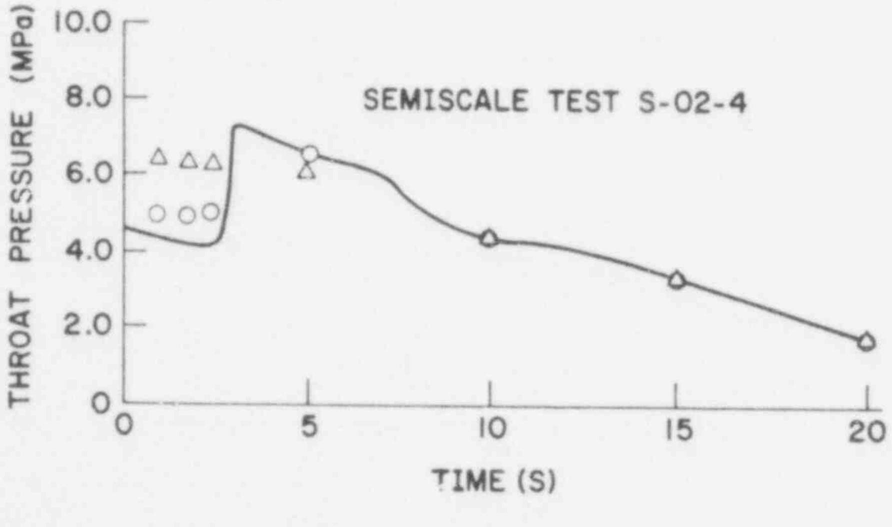

Fig. 54. Comparison of the measured wall pressure at the throat entrance (—) from Ref. 21, the computed pressure with the nonequilibrium model (o), and the computed pressure for equilibrium (Δ).

634 139

The nonequilibrium results agree very well with the measured mass flow rate during the entire period of blowdown. The elevation of the calculated throat pressures over the measured wall pressures at the throat entrance at early times is believed to result from the combination of nonequilibrium and two-dimensional flow in the proximity of the corner. When subcooled liquid enters the nozzle a nonequilibrium condition may result in the rarefaction region that allows the local pressure to drop slightly below the saturation pressure based on the liquid temperature. When two-phase flow enters the nozzle, however, the increased surface area of contact between the phases and increased mixing result in a much higher flashing rate and hence much less departure from equilibrium. It is important to recognize in comparing pressures that the one-dimensional calculated results yield an area-averaged pressure whereas the data reflect a local wall value close to a corner. Comparisons with mass flow rate, on the other hand, involve integral quantities that should be accurately calculated even in the limited resolution of one dimension.

Semiscale test S-06-5 used the nozzle design shown in Fig. 55, which has the same throat diameter but about three times the throat length of the nozzle in test S-02-4. Calculations of this test are of interest to investigate the significance of the increased fluid residence time in the throat on the degree of nonequilibrium. The effects of flow two-dimensionality were shown to be significantly reduced for this nozzle compared to what they were in test S-02-4 because of the longer throat length (Ref. 29). Figures 56 and 57 show the equilibrium and nonequilibrium calculated results compared with data from test S-06-5.

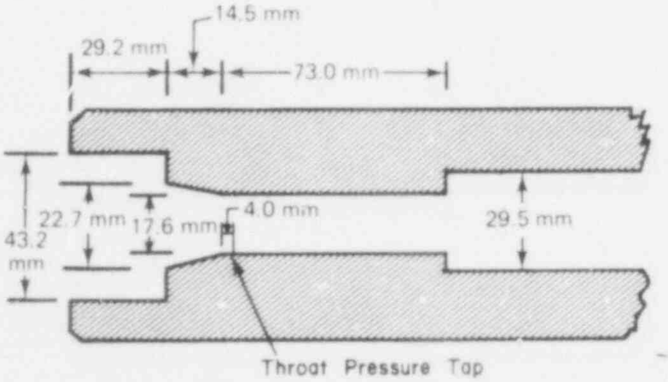

Fig. 55. Design of the LOFT nozzle for Semiscale experiment S-06-5 (from Ref. 20). Flow is from left to right.

As in the previous test, subcooled liquid enters the nozzle during about the first 3 s

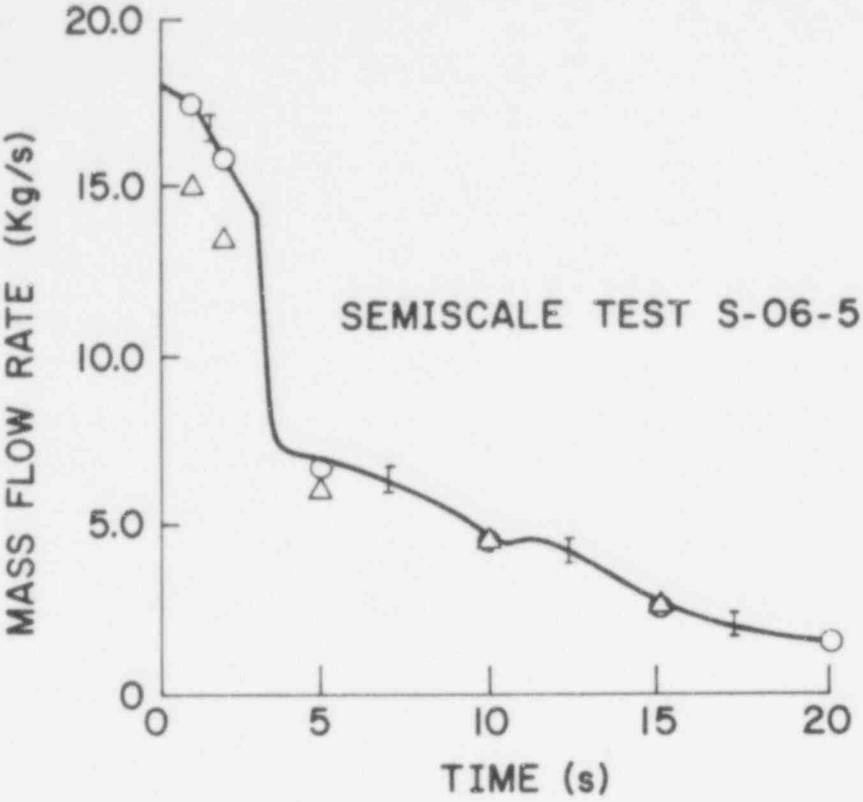

Fig. 56. Comparison of the measured mass flow rate (—) from Ref. 20, the computed mass flow rate with the nonequilibrium model (o), and the computed mass flow rate for equilibrium (Δ).

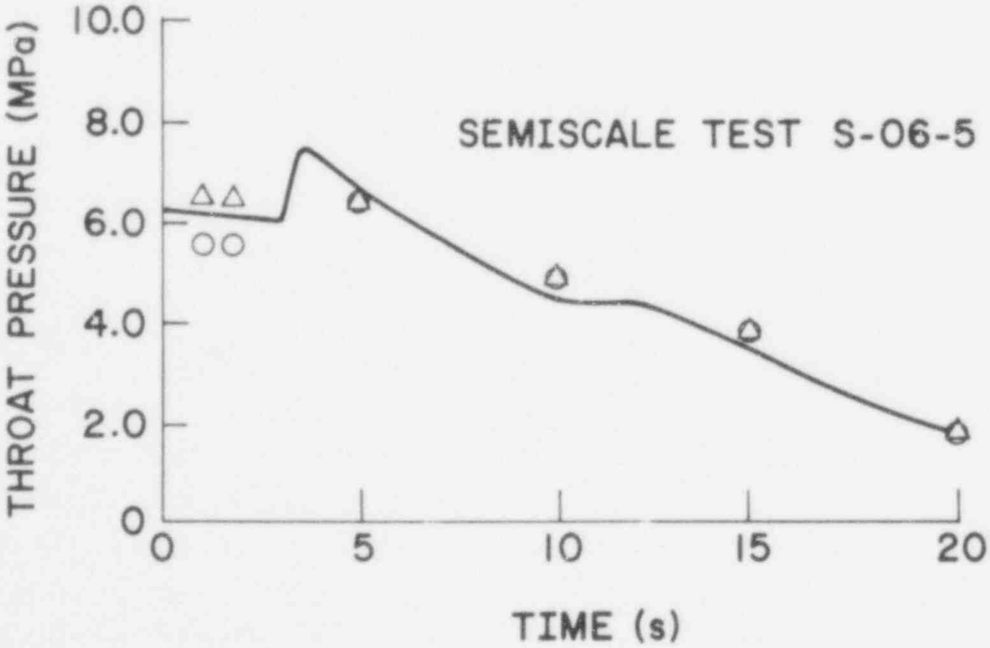

Fig. 57. Comparison of the measured wall pressure at the throat entrance (—) from Ref. 20, the computed pressure with the nonequilibrium model (o), and the computed pressure for equilibrium (Δ).

and two-phase flow enters thereafter. The void fraction entering the nozzle at 20 s is 98%. The agreement with mass flow rate is again very good for the nonequilibrium results, which are shown as circles. Substantial nonequilibrium exists at early time even with the longer throat length, since the data lie well above the equilibrium results. It is interesting to note that instead of slightly overpredicting the wall pressure in the throat at early time that we now slightly underpredict it and that the data are much closer to the equilibrium results. The fact that the observed wall pressure at the throat entrance is close to the calculated equilibrium value while the observed mass flow rate is considerably higher than the calculated value indicates the occurrence of significant local vapor production near the pressure tap. This detail may well be a consequence of the abrupt entrance combined with a considerably greater distance from the corner to the pressure tap for this nozzle than for the nozzle in test S-02-4.

To investigate the predictive capability of the model at large scale, calculations were performed for two blowdown tests of a series made at the Marviken Power Station. Test 1 used the nozzle design shown in Fig. 58. The throat diameter is 17 times larger than in the Semiscale tests. Subcooled water enters the nozzle for about 60 s. Six steady-state calculations are made during this period that use measured data for the boundary condition 1 m upstream of the initial area change. Changes in the upstream boundary conditions are negligible during the 100 ms required to achieve steady state locally through the nozzle. Calculated results are compared with the observed mass flow rate in Fig. 59 and with the differential pressure across the area change in Fig. 60. As in the Semiscale test comparisons, equilibrium results are shown as triangles and the nonequilibrium results as circles. Two curves are shown for the mass flow rates that were determined through different measurement techniques. The nonequilibrium results agree with the measured flow rate and differential pressure to within the measurement accuracy. The equilibrium results systematically underpredict both measured quantities. The differential pressure measurement essentially

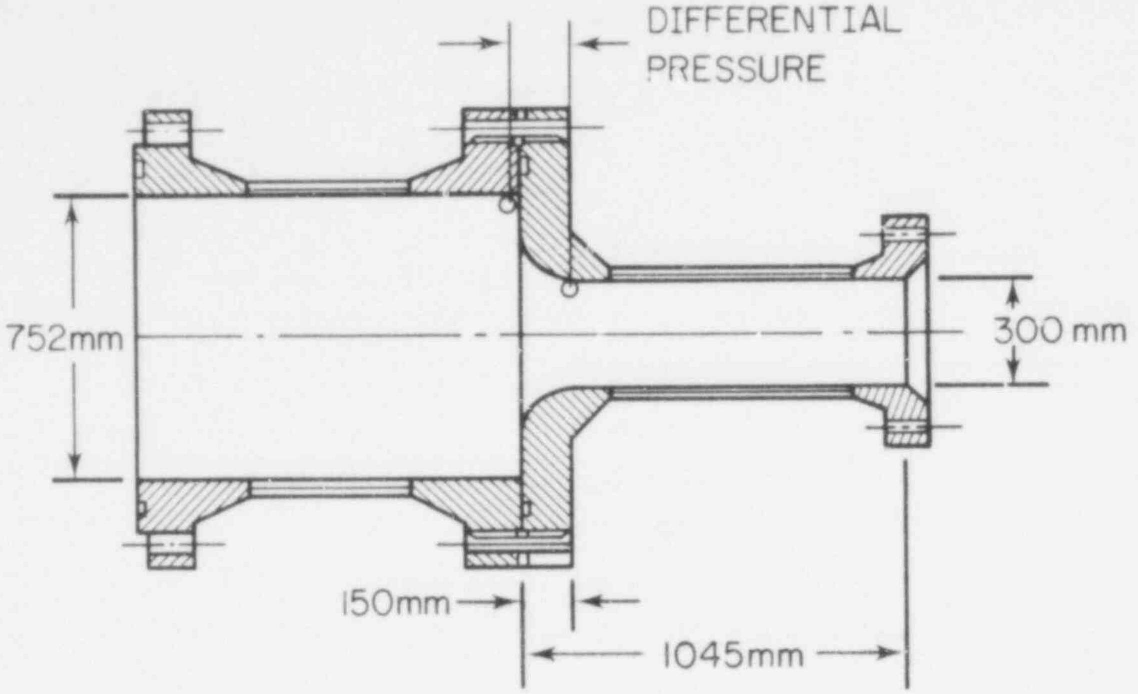

Fig. 58. Nozzle design for Marviken test 1. Flow is from left to right.

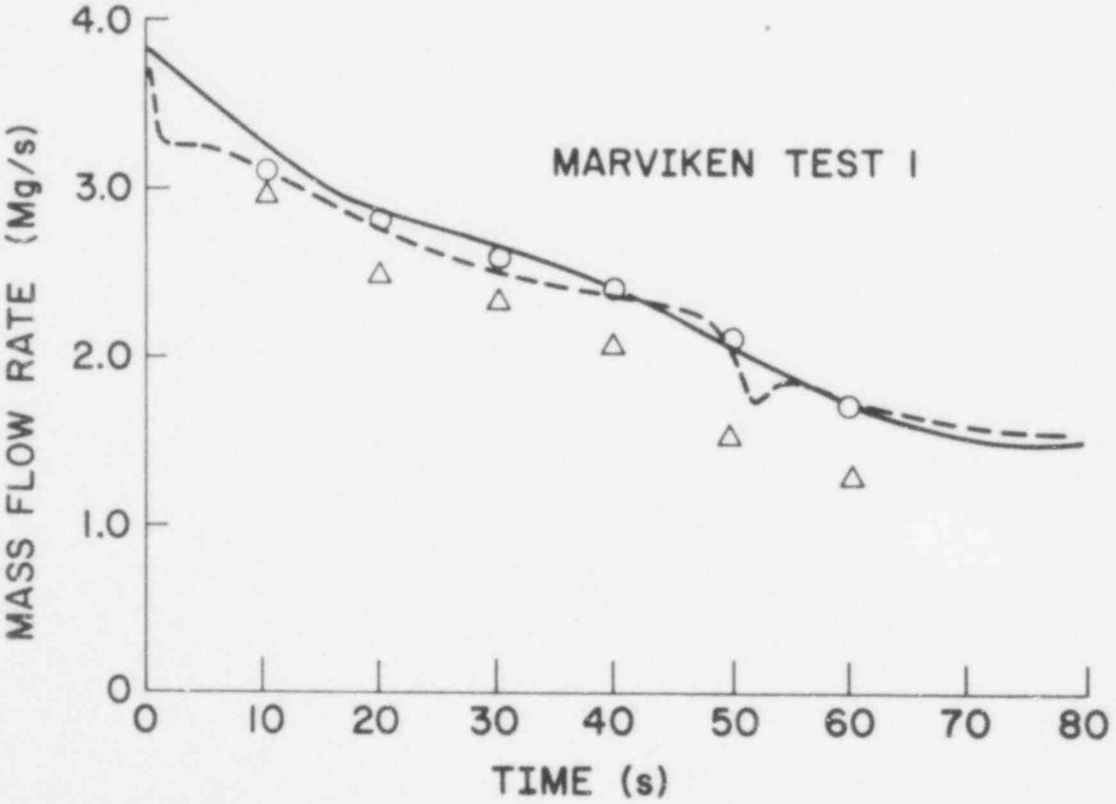

Fig. 59. Comparison of the measured mass flow rate determined by vessel mass change (—-) and pitot-static velocity profile (---), the computed mass flow rate with the nonequilibrium model (o), and the computed mass flow rate for equilibrium (Δ).

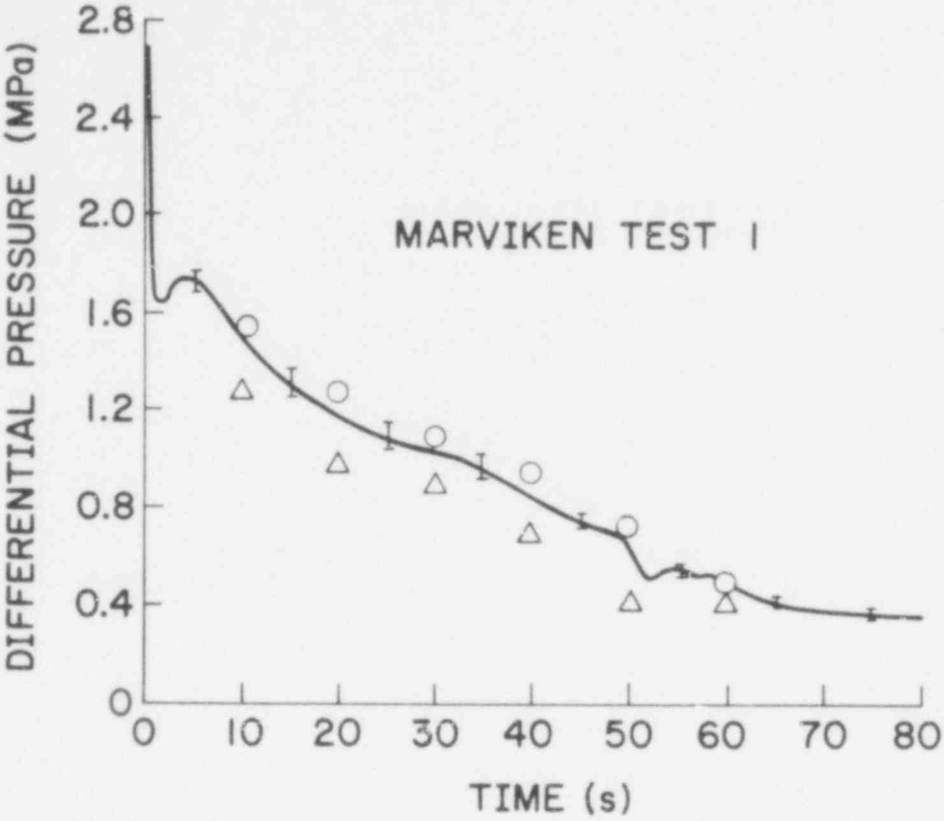

Fig. 60. Comparison of measured and calculated differential wall pressures across the nozzle area change. Measured values are shown as (—), calculated values with the nonequilibrium model are (o), and calculated values for equilibrium are (Δ).

provides a static pressure differential (even though one of the taps is located in a stagnation region) because the dynamic pressure is less than 1% of the total pressure upstream of the area change. Hence, calculated static pressures are used for comparison with the data.

The second large-scale calculation was for test 4, which had a nozzle throat diameter 29 times larger than in the Semiscale tests. This nozzle design is shown in Fig. 61. The blowdown occurs significantly faster with this larger nozzle. Subcooled liquid enters the nozzle for only about 20 s and the flow rate is about three times larger. The calculated mass flow rates are compared with data in Fig. 62 and the differential pressures are compared in Fig. 63. The nonequilibrium results, shown with circles, are again in good agreement with the data. The equilibrium results,

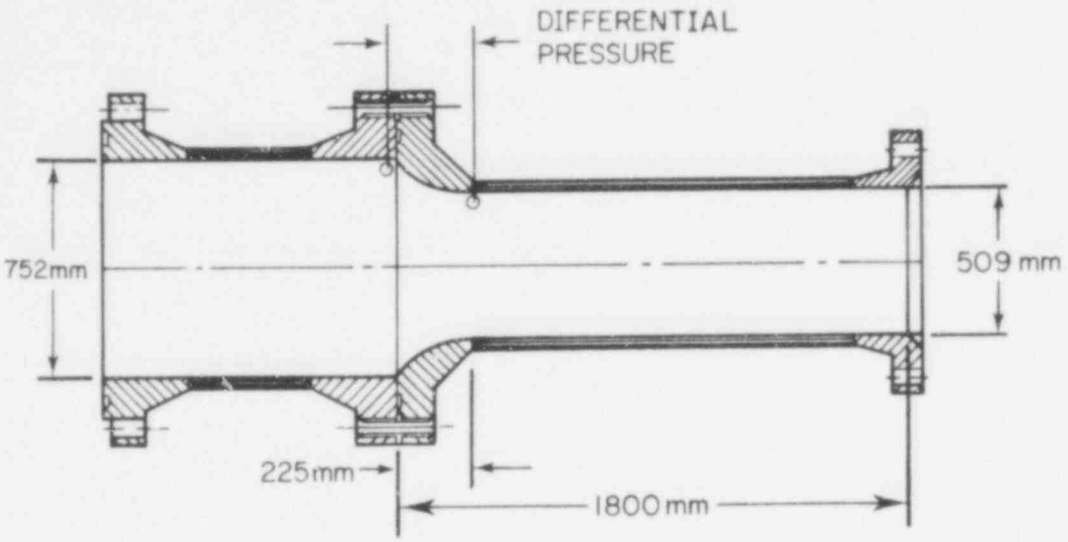

Fig. 61. Nozzle design for Marviken test 4. Flow is from left to right.

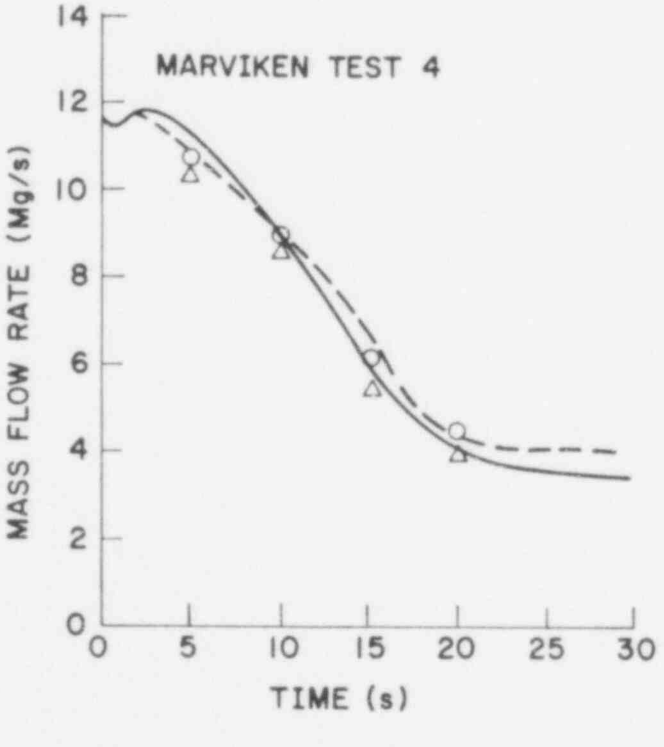

Fig. 62. Comparison of the measured mass flow rate determined by vessel mass change (—) and pitot-static velocity profile (---), the computed mass flow rate with the non-equilibrium model (o), and the computed mass flow rate for equilibrium (Δ).

634 145

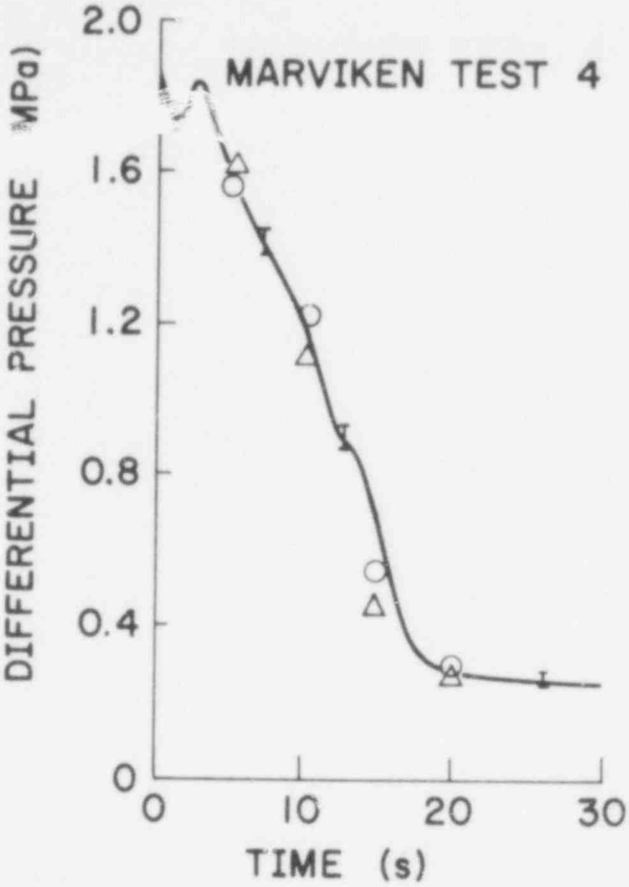

Fig. 63. Comparison of measured and calculated differential wall pressures across the nozzle area change. Measured values are shown as (—), calculated values with the nonequilibrium model are (o), and calculated values for equilibrium are (Δ).

shown with triangles, are also in quite good agreement. The tendency to depart from equilibrium is reduced for this nozzle because of the reduced rate of depressurization associated with the smaller area change and increased distance over which it occurs.

2. Droplet Spray Modeling

(H. M. Ruppel, A. A. Amsden, and F. H. Harlow, T-3)

The discrete-droplet model of Dukowicz and Butler[30] has been combined with the ALE[31] technique for flow analysis in an arbitrary configuration of curved walls to form the SPRAY code. The purpose is to furnish a theoretical complement to the upper plenum de-entrainment experiments in LASL Group Q-8 and at Harwell.

The discrete-droplet model permits the calculation of the dynamics of a spectrum of droplet sizes. In the SPRAY code, these

634 146

droplets can interact with one of several cylinders arranged with arbitrary offset and spacing.

Calculations have been performed to test the code for the case of droplets captured by one cylinder. Comparison with single-particle trajectory calculations shows excellent agreement for circumstances in which the interaction onto the flow field of gas is negligible. Even when the coupling to the flow field is appreciable, the stream lines in the gas in front of the cylinder are not strongly altered; the pressure gradients are not raised sufficiently to change noticeably the droplet trajectories. An example of uncoupled steady-state flow is shown in Fig. 64.

Calculations have been performed with two cylinders offset from each other, showing that the upstream cylinder appreciably alters the flow of droplets in the vicinity of the downstream cylinder.

Visual observations of the experimental apparatus in operation and discussion with the Group Q-8 staff convince us that inclusion in the analysis of splash effects from droplet collisions on the cylinder are of crucial importance to the assessment of net collection efficiency and re-entrainment. Also apparent was the fact that re-entrainment of water at the flow separation point does not contribute appreciably to loss of net collection efficiency. Accordingly, we have included in the code a splash model to describe the droplet flux out of each cylinder, locally proportional to the flux of droplets colliding with the film of water. Data from observations and calculations of individual splashes are supplemented by force-balance arguments to estimate the ratio of outgoing-to-incoming water flux and the mean size of the droplets produced by the collisions. Results obtained with this enhanced capability show that the net transport of water through the array of rods is appreciably greater. This is illustrated by the example calculation shown in Fig. 65.

Our current emphasis is on the coordination of splash-dominated air-water dynamics calculations with a series of experiments that are designed to test the numerical procedure in as broad a set of circumstances as possible.

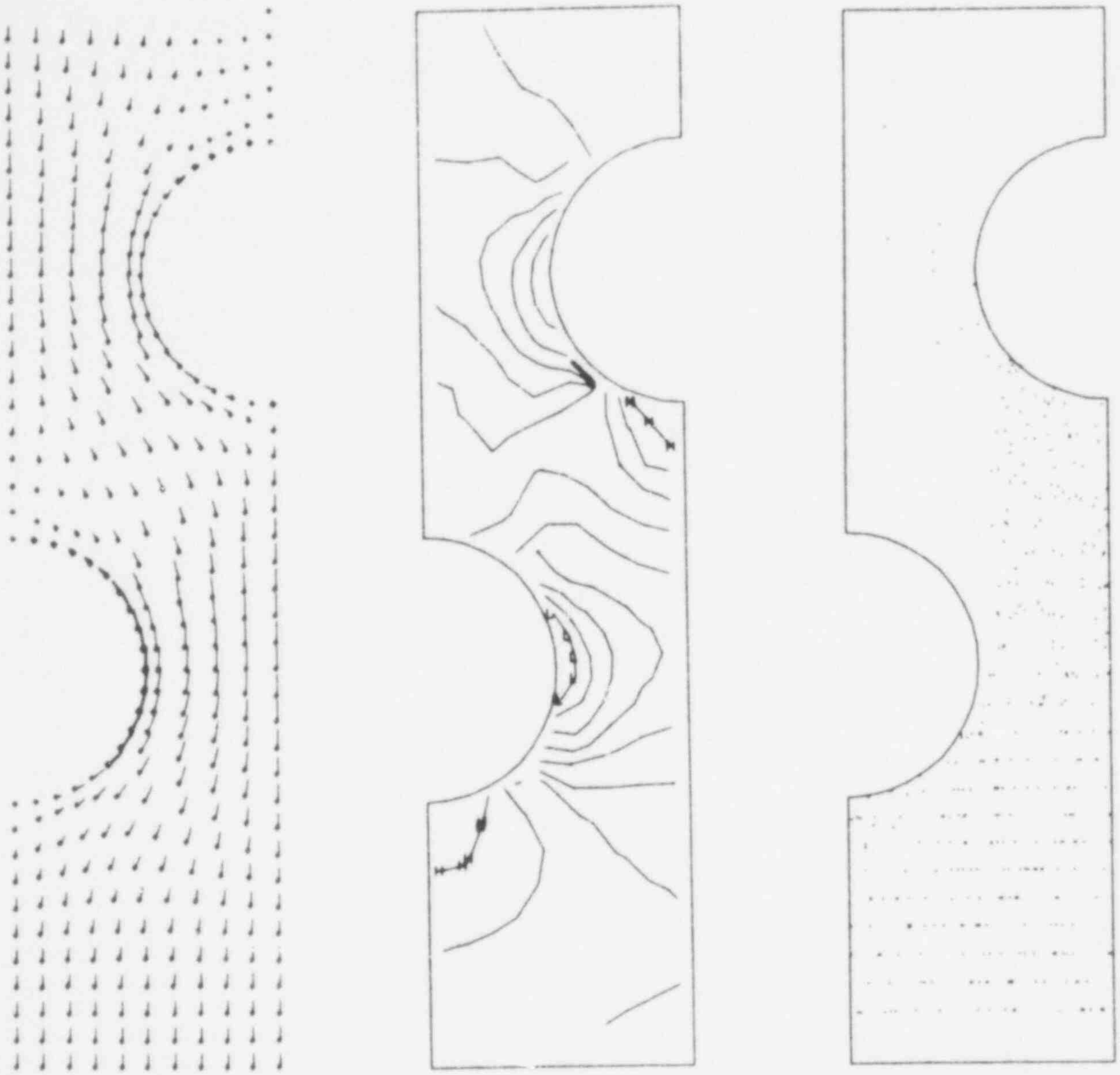

Fig. 64. The velocity vectors, pressure contours, and droplet positions at steady state in the flow past offset cylinders. Splash effects are included by introducing new, smaller droplets following collisions with the cylinders. These smaller droplets, which more easily accommodate to the air stream, have much less tendency toward de-entrainment.

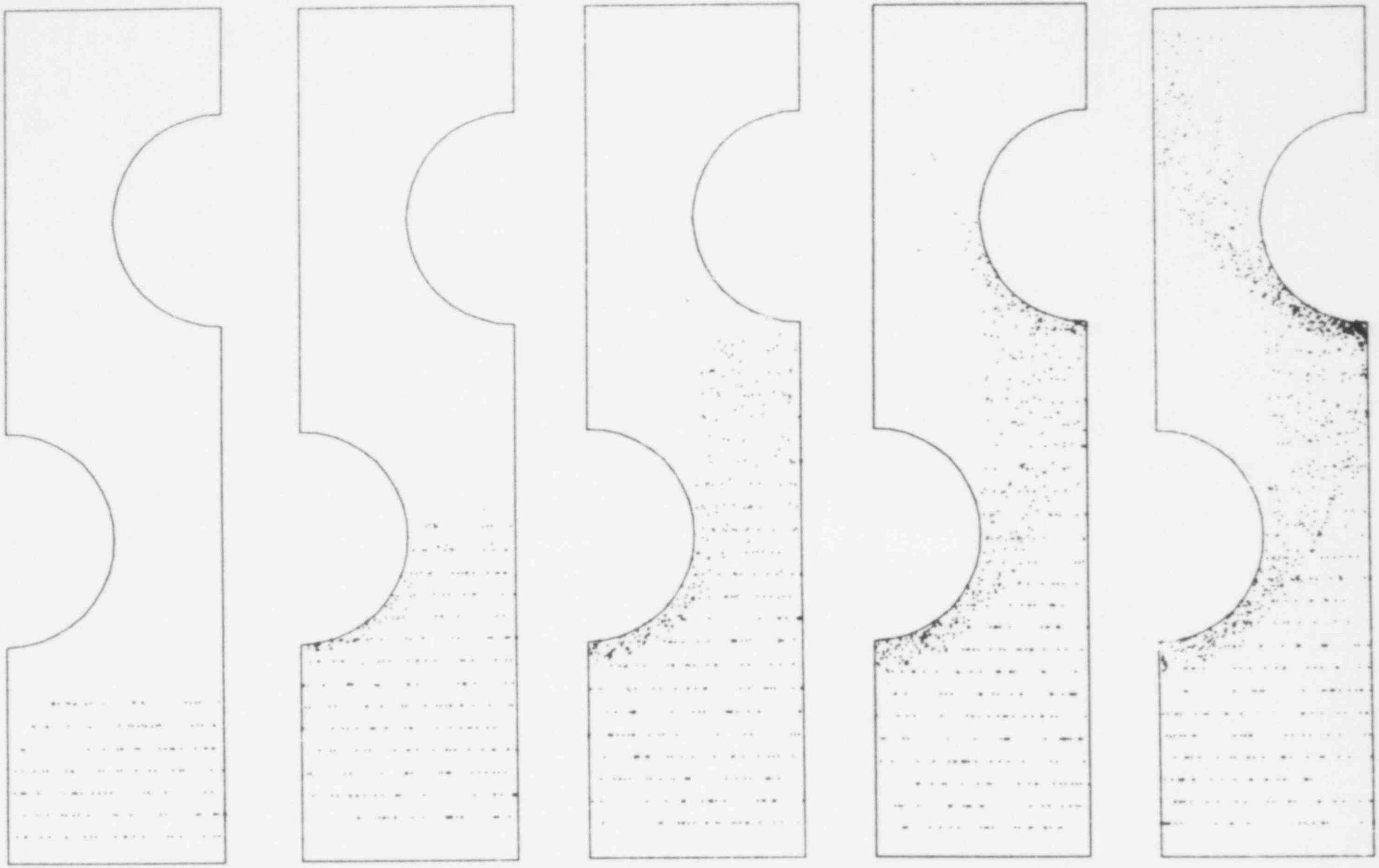

Fig. 65. Transport of water droplets past cylinders in the upper plenum. Splashing from the obstacles enhances the flux of water that passes through the array.

E. LWR Experiments

(H. H. Helmick and W. L. Kirchner, Q-8)

The objectives of LASL's LWR Safety Experimental Program remain to provide experimental support for model development activities and to develop advanced instrumentation techniques. The program is conducted in close cooperation with code and model development efforts at LASL and is coordinated with the multinational 2D/3D program for which rod lens systems are being provided.

Video data from the de-entrainment experiment has been recorded using the optical probe described in the last reporting period. The instrument has been shipped to Germany for testing in the PKL experiments and computer analysis of the de-entrainment data is in progress. Assembly of another optical probe for use in the JAERI experiments is nearing completion.

The Upper Plenum De-entrainment experiment is proceeding with improvements in droplet distribution uniformity and mass flux measurement techniques using a Pitot tube sampler. Water film thickness measurements are being implemented and preliminary results are being analyzed.

An apparatus is being constructed to produce water droplets of uniform size. This equipment is needed for studies of droplets impinging on surfaces over a range of attack angles.

1. Stereo Lens Development

(C. R. Mansfield, J. F. Spalding, P. F. Bird, and C. L. Renz, Q-8)

a. Rod Lens Probe for PKL

The stereo lens system which was built for the PKL-I experiments has been completed, tested, and shipped to West Germany. The probe and its associated instrument box are shown in Fig. 66. During this first field test, the probe is configured for continuous illumination only. Stereo views of the hot-leg region will be obtained.

During the final tests before shipment, multiple stroboscopic exposure data were obtained in the LASL de-entrainment facility. We have selected and digitized 30 frames of recorded video data

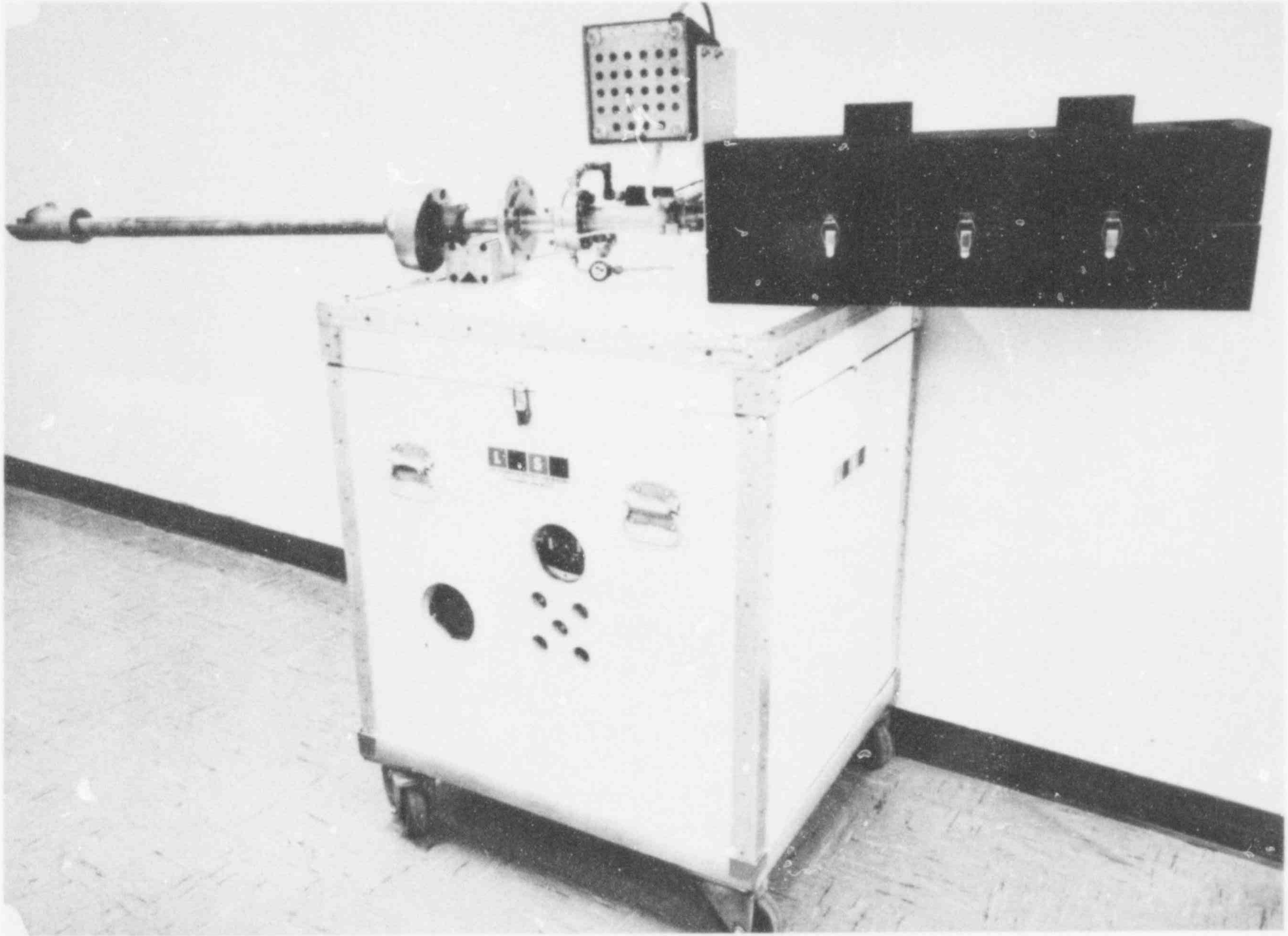

Fig. 66. Initial stereo lens probe for PKL.

representing 15 stereo pairs taken through the PKL probe system. The stroboscopic light source was double pulsed, with a time between pulses of 1.6 ms every fifth frame. In addition, we digitized four frames of a calibration target under steady illumination. These data are being analyzed in order to evaluate total system performance of the PKL stereo lens probe.

b. Rod Lens Probe for CCTF

The initial probe being built for the Cylindrical Core Test Facility (CCTF) at Tokai, Japan, is in the final stages of assembly. Hydrostatic pressure tests have been run at room temperature and a pressure of 1.4 MPa (200 psi). These tests were followed by dye penetrant examination to detect any flaws. No flaws were found. The optical views through both channels of the 3.5-m-long lenses appear nearly as good as were obtained with the PKL unit. This judgement was determined by viewing standard Air Force three-bar optical resolution charts.

c. Stroboscopic Flash Illuminator

We have redesigned the stroboscopic flash illuminator to provide greater light output and improved reliability. It was found by experiment that the desired minimum time between pulses was too short to permit recharge of the energy storage capacitors to the required voltage without self-firing of the flash lamp. The self-firing occurred even if the recharge did not commence until a time which was substantially greater than the nominal deionization time of the lamp. This implies a kinetic process, the characteristics of which were not obvious in the manufacturer's literature. The solution to the problem was to go to two slower reactive charging systems driving separate lamps which can be triggered to provide the desired minimum time between pulses. The redesigned system is being constructed and its adequacy will be evaluated on the CCTF probe system.

2. Data Acquisition System

(P. F. Bird and D. C. Berry, Q-8)

All hardware has been received to provide high quality, CAMAC-based, computerized data collection and experimental control at locations up to several hundred feet from our PDP-11/34 computer. The hardware is being checked out and brought operational, communication lines are being installed, and some software is either ready or being written. Additional software development work is necessary, however, before the entire system becomes operational.

3. Upper Plenum De-entrainment Experiment

(J. C. Dallman, Q-8)

During this quarter, single and multiple simulated reactor internal de-entrainment studies were expanded with the primary objectives being: a) improvements in the droplet mass distribution in the test area and b) improvement in the measurement accuracy. Major modifications in the technique for total droplet mass flux measurement have resulted in excellent agreement (differences less than 8%) between the integrated mass flux measurement and integrated Pitot tube sampling of the two-phase mixture. These measurements are continuing and have already resulted in greater confidence in the single structure measurements.

In collaboration with NRC-sponsored researchers from Lehigh University, a number of circumferential averaged film thickness measurements were obtained during droplet de-entrainment on a 101.6 mm cylindrical simulated internal. Analysis of these measurements and the resulting implications on droplet field de-entrainment are under way. In addition, construction of an instrumented 101.6 mm cylindrical pin has begun. This pin will have three circumferential rings of eight discrete film thickness probes (approximately 45° apart). These rings will be located 101.6 mm, 279.4, and 508.0 mm from the top of a 560-mm-long, 101.6 mm cylindrical stainless steel tube. This will allow not only further study of average film thickness, but also allow investigation of local differences around the tube circumference.

Installation plans for the new, larger wind tunnel facility are complete. Delays have been incurred initially due to weather and later in the quarter due to the unavailability of construction crews.

4. Drop Generator

(D. B. Jensen, Q-8)

A preliminary design for an apparatus to generate uniform sized droplets has been assembled and tested. The drops are formed by sending water under constant pressure through a hypodermic needle at a known flow rate. Future refinements include vibrating a long hypodermic needle so the emerging stream of water is broken into large (100-1 000μ in diam) droplets at a high flow rate. A schematic of the apparatus is shown in Fig. 67.

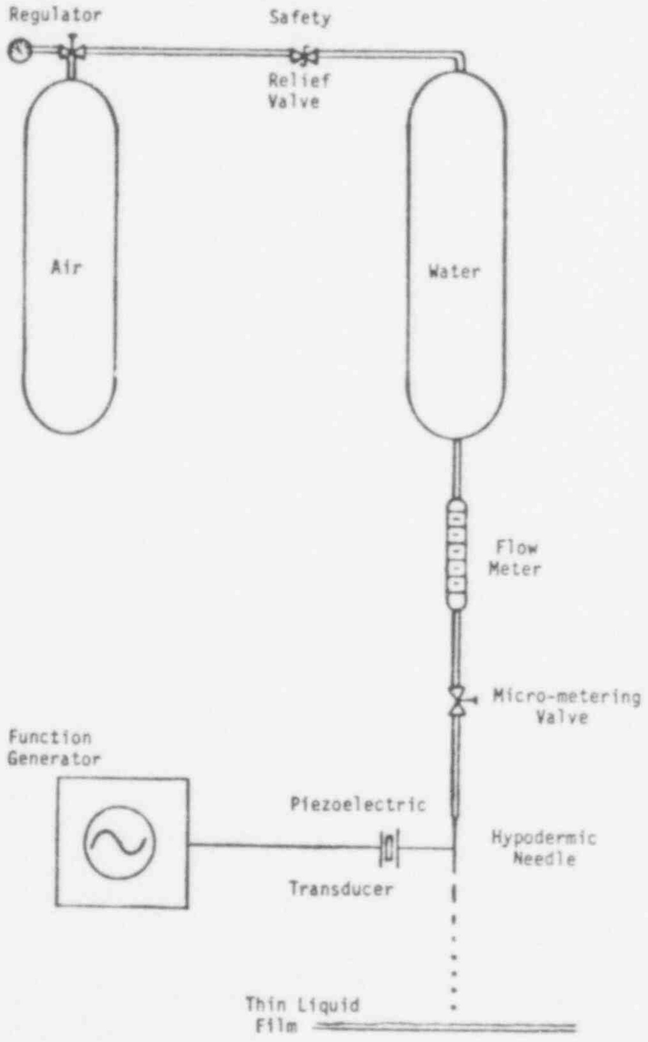

Fig. 67. Schematic of uniform drop generator.

III. LMFBR SAFETY RESEARCH

(M. G. Stevenson, Q-DO and J. E. Boudreau, Q-7)

The LMFBR safety research effort at LASL consists of several programs. In the first of these, the SIMMER code is being developed and applied to core disruptive accident (CDA) analysis with support from the Division of Reactor Safety Research (RSR) of NRC. SIMMER is a two-dimensional, coupled neutronics-fluid dynamics code intended for transition phase, core disassembly, and extended fuel-motion analysis. The second version of the code, SIMMER-II, has been completed and is now being used in the analysis of CDA problems.

In a separate, but closely related program funded by DOE, models are being developed for phenomena important to the progression and consequences of CDAs. Some of this work is basic research on phenomena, but in most cases the developed models will be included directly in accident analysis codes and, particularly, in SIMMER. Another part of this DOE program is focused on the application of the accident codes, particularly the SIMMER code, to the study of specific aspects of accident sequences. The work in the SIMMER code development and application area is reported in Sec. III.A.

Experimental investigation, including confirmation of reactor safety analysis methods, is an important part of safety research. Section III.B provides a summary of recent analytical and experimental work in a program funded by NRC/RSR to support SIMMER model development and testing.

A. SIMMER Code Development and Applications

(C. R. Bell and L. L. Smith, Q-7)

The major activities in the SIMMER code development and application areas during this reporting period have generally been continuations of work previously reported. Code modifications are being performed as needed to correct difficulties encountered in various code applications, to improve complete areas of the code such as the space-time neutronics and phase transition methods, and to extend the applicability of the code to new areas such as plug ejections from the reactor head and the blowdown of reactor materials into the containment building during postdisassembly expansion. Applications are continuing in the areas of neutronics testing, single subassembly transition phase analysis, and plug ejection and vessel blowdown analysis. Some of the specific code modifications and analysis results are presented below.

1. SIMMER Energy Equation Solution Modifications

(W. R. Bohl, Q-7)

The current approach to the solution of the material conservation equations in SIMMER-II[32] is: (a) to calculate explicitly internal energies, (b) to calculate implicitly cell pressures, field velocities, and cell densities, and (c) to calculate implicitly the liquid and vapor component densities. In some problems the final step can significantly change cell material compositions. This can lead to unusual and sometimes even unacceptable thermodynamic states because the vapor internal energy for a cell is not consistent with the new cell composition. To minimize these thermodynamic inconsistencies, the solution procedure for the vapor energy equation has been modified. The explicit energy calculation is now used only to estimate the end-of-cycle (EOC) pressures. The actual calculation of the vapor internal energies is a final implicit operation such that the treatment of convective terms in the vapor energy equation is consistent with the solution of the conservation equations for the component densities. Further, the pressure-volume work term is now averaged over the beginning-of-cycle (BOC) and EOC conditions. These changes are quite useful in improving EOC thermodynamic states in problems with small mesh cells and large pressure gradients.

2. Application of SIMMER-II to the Coupled Problems of Postdisassembly Expansion, Plug Dynamics, and Material Ejection

(C. R. Bell, Q-7)

The expansion characteristics of high-temperature core material following an energetic core disruptive accident in an LMFBR strongly influence the loads on the rotating plugs in the reactor head and the discharge of materials to the Reactor Containment Building (RCB) if a plug is ejected. SIMMER-II[32] is uniquely capable of addressing these coupled problems in that it has the multiphase, multicomponent, multifield treatment required to follow the individual reactor materials in an interactive environment over large distances. The only modifications to SIMMER-II required to treat this problem are the addition of plug mechanics and special editing.

The plug mechanics are modeled very simply by Newton's law. The acceleration is computed from the mass of the plug and the integrated forces acting on it. SIMMER-II computes the pressure at the lower surface of the plug whereas an opposing pressure of 0.1 MPa is assumed to act on the upper surface of the plug. Of course, gravity is included. A breakaway force, which represents the restraint from bolts or shear keys, is used as a threshold for initiation of plug motion. The velocity and displacement of the plug are obtained through successive time integrals of the acceleration and the velocity.

The plug mechanics are computed in an explicit manner within SIMMER-II. The coupling to the fluid dynamics is accomplished by a time-dependent structure volume fraction. Initially the nodes through which the plug lower interface travels are about 90% filled with "effective" structure or nonflow volume. As the plug mechanics model predicts motion of the lower plug interface, effective structure is removed to simulate the additional volume available to the impinging fluid. The SIMMER-II fluid dynamics then follows a natural course in which the fluid maintains contact with the moving plug to produce an accelerating force.
If the fluid cannot maintain contact, cavitation occurs and a downward force on the plug results.

Node boundaries of the plug and the breakaway force are input to SIMMER-II. This provides the flexibility to treat various plug sizes and restraining characteristics. The plug must be centrally located to be compatible with the r-z treatment.

The exploratory calculations have produced several interesting features. First, the scale of SIMMER-II calculations can be extended to include the RCB. Second, the plug velocity may be influenced by the impinging jet of discharging fluid long after the

634 157

plug leaves the reactor head. Also, a large portion of the plug acceleration may result from the postimpact pressures in the expansion zone in addition to the initial pool impact. Third, the character of the discharge jet into the RCB is greatly modified if flashing liquid is ejected from the vessel. The jet in this case disperses through flashing. Fourth, the expansion zone within the pressure vessel tends to expand preferentially toward the opening in the reactor head. This results in substantial release of molten fuel and fuel vapor to the RCB when fuel-quenching mechanisms such as heat transfer from liquid fuel to sodium and steel and fuel vapor condensation are neglected. Finally, the introduction of sodium into the RCB is highly nonuniform and somewhat localized. We expect that the efficiency of the sodium burning and subsequent RCB pressurization would be strongly affected.

The work completed at this time indicates that valuable, mechanistic source term information for sodium burning analysis and radiological source behavior can be generated with this approach. These source terms are both space and time dependent. Coupling these detailed source terms to techniques for sodium burning and radiological analyses appears to be a logical next step.

B. SIMMER Verification Experiment Planning, Analysis, and Performance

(J. H. Scott, Q-7 and H. H. Helmick, Q-8)

Work continues on the testing of the SIMMER-II computer code; during this reporting period, analyses of the previously reported Oak Ridge National Laboratory (ORNL) CRI/FAST experiments, the SRI International fluid dynamics experiments, and the Argonne National Laboratory (ANL) AX-1 experiment were extended.

In addition to previously reported work, efforts were begun in several new areas including development of advanced statistical techniques for experiment analysis and advanced momentum exchange models.

The work on the LASL Upper Structure Dynamics experiments continues; in particular, the Phase I hardware has been completed and an initial demonstration test and SIMMER analysis have been performed.

1. SIMMER Performance Analysis

(R. D. Burns, Q-7)

A sensitivity analysis was performed to determine the effect of varying the input parameters controlling convergence of numerical algorithms and time step selection on SIMMER-II SRI International experiment calculations.[33] The purpose was to minimize the running time of the code, while maintaining an acceptable level of accuracy in the computations. The analysis, which required 11 SIMMER runs, revealed an optimum input configuration, permitting a typical code running time reduction of 40% with an approximate 1% uncertainty in the calculations of system kinetic energy and vessel head impact time. The sensitivity procedure is based on a method devised for SIMMER sensitivity analysis.[16] We recommend that similar analyses be performed before future large-scale SIMMER studies.

The SIMMER-II calculations of the hypothetical core disruptive accident (HCDA) vessel fluid dynamics experiments at SRI International are in support of the SIMMER-II verification program. These experiments involve scaled geometry and simulant materials and study the characteristics of rapid bubble expansion into a liquid pool. The time scale of the experiment is a few milliseconds. No phase changes occur. The SIMMER input parameters that influence the calculation include[32] single- and two-phase convergence criteria, matrix inversion convergence criteria, critical cut-off values, and time step controls. The effect of varying 15 of these parameters was studied in the performance analysis.

Eight of the 15 input parameters (convergence criteria and minimum vapor density) were included because no single value is suggested for them in the SIMMER-II manual. Instead, ranges of values are recommended. These parameters were varied over the manual's suggested ranges in this analysis.

The remaining seven parameters have recommended values in the manual, but other values were used in SRI International calculations previous to this study. The ranges of variation for these parameters were chosen to be the same order of magnitude as the recommended and used values. Variations of the 15 parameters covered as much as 5 orders of magnitude.

All 15 parameters were varied simulatneously and independently in each of 11 separate calculations. Each calculation was permitted to run to completion or for a maximum of four minutes on the CRAY-1 computer. The time was projected for seven runs that did not complete. Running time ranged from 3-10 min. among all 11 runs. This correlated to variation in the time step control based on the Courant parameter, COURNT, as shown in Fig. 68. Note that while all parameters were varied in each SIMMER run, only COURNT affected running time. The results suggest that COURNT should be kept above about 0.12 to minimize running time and that all convergence criteria can be tightened without affecting running time.

As a further check of code performance, variations in calculated quantities were studied. These included system kinetic energy, vessel head impact time, and deviations from mass and energy conservation. Also, the number of nonconvergence messages appearing in the SIMMER output was studied. It was found that kinetic energy and impact time varied as much as ± 20% among the 11 SIMMER runs. This uncertainty in SIMMER calculated results was due solely to uncertainty in the selection of convergence and time step control parameters. This behavior was found to be most sensitive to variations in COURNT. Above a value of 0.16 for COURNT the deviations in mass and energy conservation at an early point in the calculation are typically 0.01 kg and 1 MJ, respectively. Below 0.16 they are approximately 0.003 kg and 1 kJ. In addition, particle radius nonconvergence messages began to appear in the output of runs with COURNT above 0.15, as illustrated in Fig. 69. These results suggest an upper limit for COURNT of about 0.14 for these SRI International calculations. Again, convergence criteria restrictions are not indicated.

The results of the performance analysis lead to an optimal configuration for SIMMER input in the SRI International calculations: COURNT equals 0.12-0.14 and all convergence criteria values at the low end of the manual's suggested ranges.

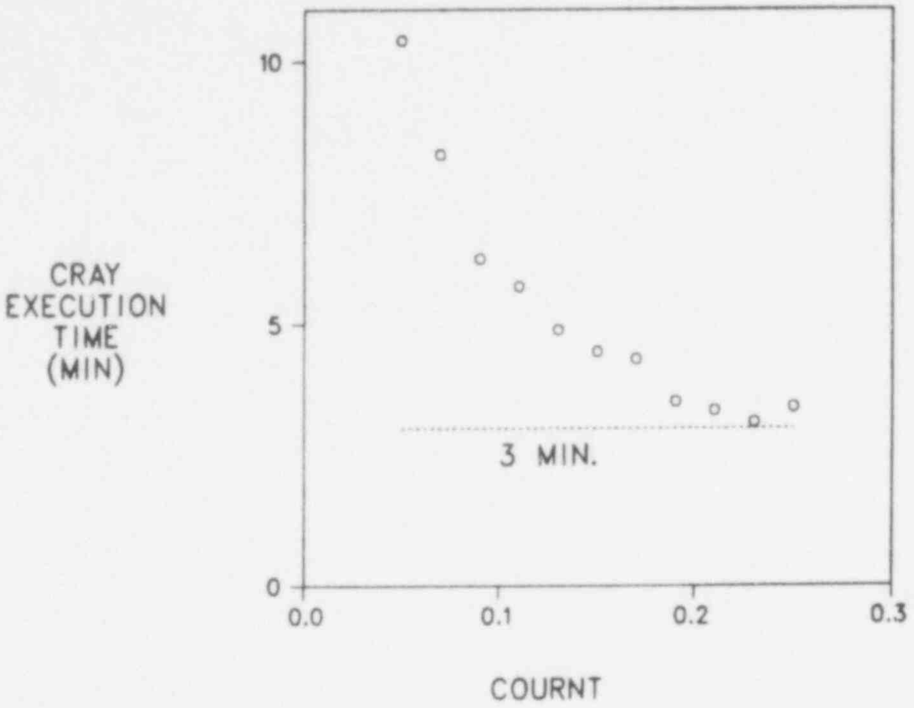

Fig. 68. Dependence of SIMMER running time on COURNT for SRI International calculations.

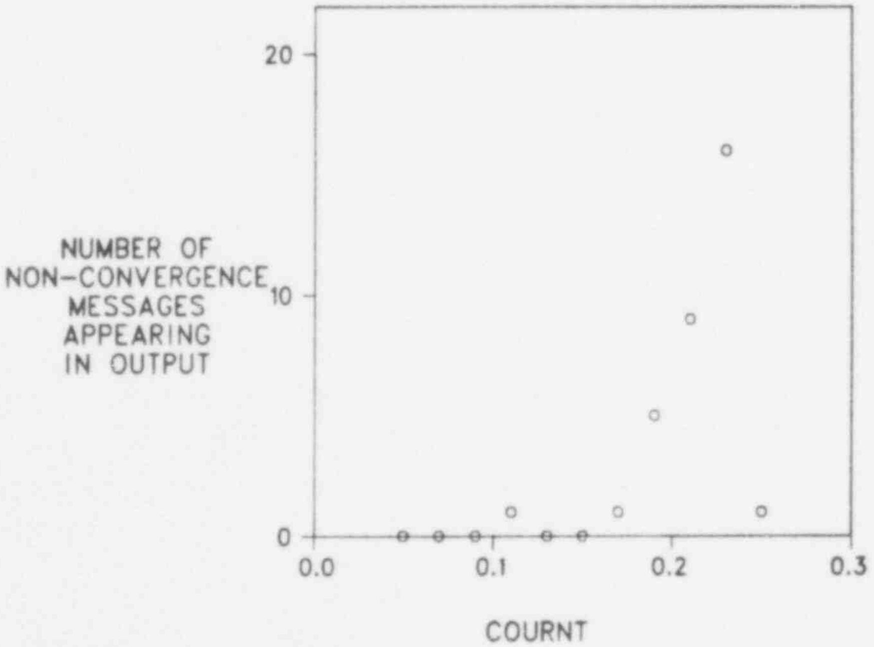

Fig. 69. Dependence of SIMMER convergence characteristics on COURNT for SRI International calculations.

634 161

The study was repeated using the above recommended range for COURNT and variations from 10-100% of the above recommended values for convergence criteria. The results for kinetic energy and head impact time varied less than 1% among 11 runs, and code running time varied from 4.5-5.0 min. Further, it was found that only eight runs were successful; three failed with the single-phase convergence criterion, EPIR, less than 4×10^{-5}. These runs were not included in the subsequent analysis because SIMMER could not converge in the first cycle of transient calculation.

2. SIMMER Sensitivity Analysis

(R. D. Burns, Q-7)

The methodology for SIMMER sensitivity analysis involves variation of all uncertain input parameter values in each separate computer run performed.[34] The objective of this procedure is to obtain the maximum amount of information from a minimum number of SIMMER runs. Previously, the only quantitative method of determining the minimum number of runs required was based on the desired probability that a given fraction of the range of all possible computed outcomes would be spanned in the runs to be performed.[16] Since then, experience with new sensitivity analyses of SIMMER results and of randomly generated uncorrelated data have indicated the need for a method to define better the required number of computer runs.

A procedure for preselecting the minimum number of separate computer runs required in sensitivity analyses is reported here. The purpose of this procedure is to assure high probabilities of finding correlations between input and output parameters when they exist and of not finding chance correlations when real correlations do not exist. This is necessary for the following reasons. First, if too few runs are performed in an analysis, there may not be sufficient statistical information generated to find weak correlations amid the scatter. Note that a correlation refers to the primary effect of an input value variation on an output value variation and scatter refers to the combined impact of all other lesser input variations. Second, it is possible to find apparent

634 162

good correlation among completely uncorrelated data, a situation which is more possible when fewer data points are available (i.e., which is more likely when fewer data points are available (i.e., fewer computer runs) or when more pairs of input and output param-

The probability of finding correlations of given strength when they exist is P_a, and of not finding chance correlations when real ones do not exist is P_b. The strength of a correlation is a measure of the extent to which the influence of one input value variation dominates all others in their effect on an output quantity. In the statistical analysis, this is measured in terms of a signal-to-noise ratio(S/N) where the signal is defined as the total range of variation in an output value due to variation in one input value, and the noise is the standard deviation of the scatter in a correlation due to the superposition of variations in all other input parameters. By choosing the number of computer runs (n) to be used in a sensitivity analysis, an acceptable combination of P_a and P_b can be found for a desired S/N ratio.

The probability P_b depends on the number of tests for correlation that are expected to be performed in the statistical analysis of computer run results. This number (m) can be as large as the product of the number of varied input values and the number of output quantities to be considered. However, m can be reduced by deciding not to check for correlation with some input variations (i.e., those thought to have no dominating impact on output values) and by reducing the number of output quantities to be tested for correlation. The latter can be done if a set of output quantities are all thought to be related. Then, most of the output variations need only be cross-correlated with some key output variations to verify that they are indeed related, rather than checking each individually for correlation with input variations.

Once P_b and m have been chosen, the correlation acceptance level C can be calculated. This is simply the probability of not finding correlation in a single pair of uncorrelated sequences of parameter variations. Correspondingly, P_b is the same probability, but among m pairs together. If all output variations are mutually independent as are all input variations, then $P_b = C^m$. Because all output variations are not always completely independent, this equation gives an upper limit for C. The parameters C, P_a, and S/N are needed to determine the minimum required number of computer runs n as shown in Table XVI. The asterisk indicates more than 40 runs.

In some cases, it may be advisable to accept a low P_b value such that one can expect to find chance correlation among uncorrelated data. It will then be necessary to verify any apparent correlations through additional calculations after the statistical analyses are complete.

The parameter C is directly translatable into critical values for correlation coefficients. It is simply the quantile (percentile) of the statistic used as the correlation coefficient, which can be found in an appropriate table for the type of correlation for which one is testing (e.g., monotonic, linear, exponential). The Kendall tau statistic is recommended for tests of monotonic relationships and a table of quantiles can be found in Ref. 35. Additionally, if one wishes to test for linear or exponential relationships, quantiles, or confidence levels of the correlation, statistics, can be found in tables in most statistics texts dealing with least-squares regression (e.g., see Ref. 36).

The parameter S/N needs some further discussion. The numbers in Table XVI were generated using a simplified linear model approximating the types of nonlinear input-output relationships that appear in SIMMER sensitivity analyses. It is assumed that variation in input parameter x over its range of uncertainty produces a linear response in output parameter y when all other input parameter values are fixed at some nominal values. This relationship is illustrated in Fig. 70 as a solid line. The vertical rise of the line Δy_s is the magnitude of the signal in the S/N ratio. Actual data points generated in a sensitivity analysis will usually deviate from the line because of the combined impact of variations in all other input parameters on the value of the output parameter. A data point from one of the n computer runs is shown as a circle in Fig. 70 and its deviation from the solid line is Δy_N. Each of the n data points will have different magnitudes of deviation, and the

TABLE XVI

MINIMUM NUMBER OF COMPUTER RUNS REQUIRED FOR SENSITIVITY ANALYSIS

	$P_a = 0.80$				$P_a = 0.85$				$P_a = 0.90$				$P_a = 0.95$				$P_a = 0.99$			
S/N =	10	5	3	2	10	5	3	2	10	5	3	2	10	5	3	2	10	5	3	2
C = 0.999	7	13	25	*	8	14	28	*	9	16	32	*	10	18	37	*	10	21	*	*
C = 0.995	6	8	19	38	6	9	21	*	6	10	23	*	7	12	28	*	7	16	38	*
C = 0.990	5	7	16	33	5	8	18	37	5	9	19	*	5	10	23	*	5	14	32	*
C = 0.950	4	4	8	18	4	4	10	22	4	5	12	27	4	6	15	37	4	8	23	*
C = 0.900	4	4	6	13	4	4	7	16	4	5	8	19	4	6	12	27	4	7	18	36

standard deviation of these Δy_N values is σ. Assuming that the values of Δy_N are normally distributed around the solid line with a mean value of zero and standard deviation of σ, the S/N ratio is defined as $\Delta y_S/\sigma$.

Examples of scatter for various S/N values are presented in Fig. 71. Note that 60% of the n data points are expected to lie between the ± 1σ lines, and 95% between the ± 2σ lines. Selection of an S/N ratio specifies the strength of correlation above which x and y are to be considered to be correlated. Lesser correlation strengths are ignored. Note that according to Table XVI, 30-80% fewer computer runs are needed to find correlations as strong as S/N = 10 as are needed for S/N = 3.

3. Upper Structure Dynamics (USD) Experiment

(E. J. Chapyak, Q-7
and V. S. Starkovich,
Q-8)

Assembly of the Phase I USD experimental hardware was completed on schedule and initial demonstration tests and SIMMER analyses have been performed. A summary of this work and a movie of a demonstration test using Freon-113 as the active

634 165

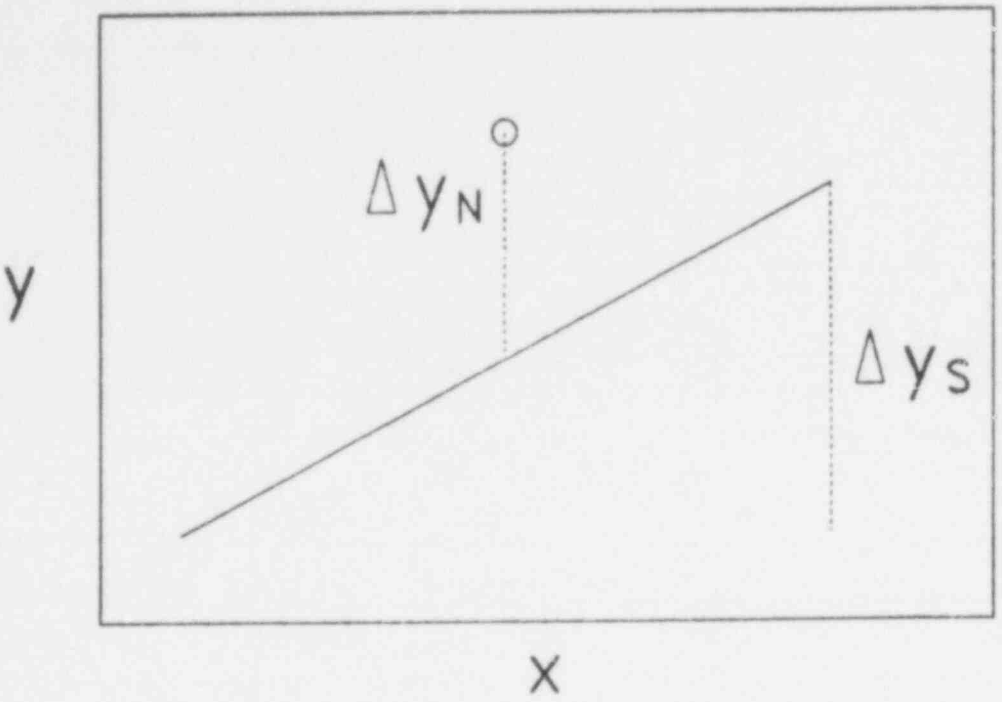

Fig. 70. Illustration of S/N ratio for sensitivity correlations.

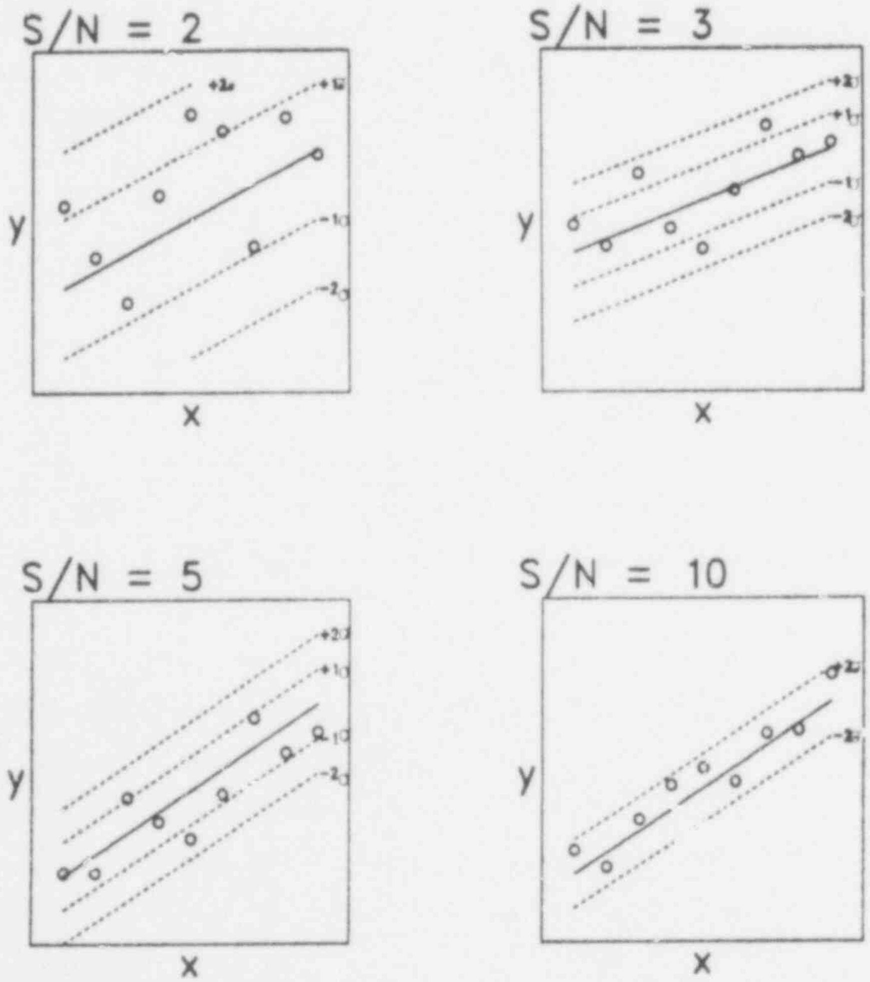

Fig. 71. Examples of strengths of correlations for various S/N ratios.

core simulant were presented to the Advanced Reactor Safety Research Division of NRC at the midyear review meeting in late February.

A picture of the experimental apparatus is shown in Fig. 72 along with supporting hardware. Initial Phase I experiments will continue to use rupture diaphragms to release the simulated active core materials through an experimental component which has the same flow area fraction as the upper core structure (UCS). Although the design of an explosively driven gate valve has been completed, it will not be fabricated unless the use of the rupture diaphragms results in unpredictable flow conditions. SIMMER calculations performed to date indicate that system response is relatively insensitive to the final rupture diaphragm aperture, provided that this aperture is large compared to the relatively small hydraulic diameter utilized in the scaled UCS component.

Two different UCS equivalent flow area components have been fabricated. One consists of a 19-hole array with hole diameters of 7.54 mm (19/64 in.) and the other is a 7-hole array composed of 12.7 mm (1/2-in.) diameter holes. In addition, a scaled-down (1/2.5), wire-wrapped, 217-pin array is in the fabrication stage.

All three UCS components, the core, and the viewing chamber will be instrumented with pressure transducers and thermocouples. Two different pressure transducers will be used; for dynamic pressure measurements above 398 K, a quartz-crystal based, water-cooled transducer will be employed. For applications at temperatures below 398 K, we intend to use pressure transducers with built-in four-arm Wheatstone bridges. The latter transducers are capable of measuring both static and dynamic pressures with high frequency response. The signal conditioning electronics necessary to ensure proper bridge excitation and balancing, along with a calibration of each channel, has been obtained, with work continuing on the fabrication of the cable assemblies. A 14-channel FM tape deck has been ordered for signal recording. In addition, an order has been placed for wide-band differential amplifiers for all temperature and pressure channels.

634 167

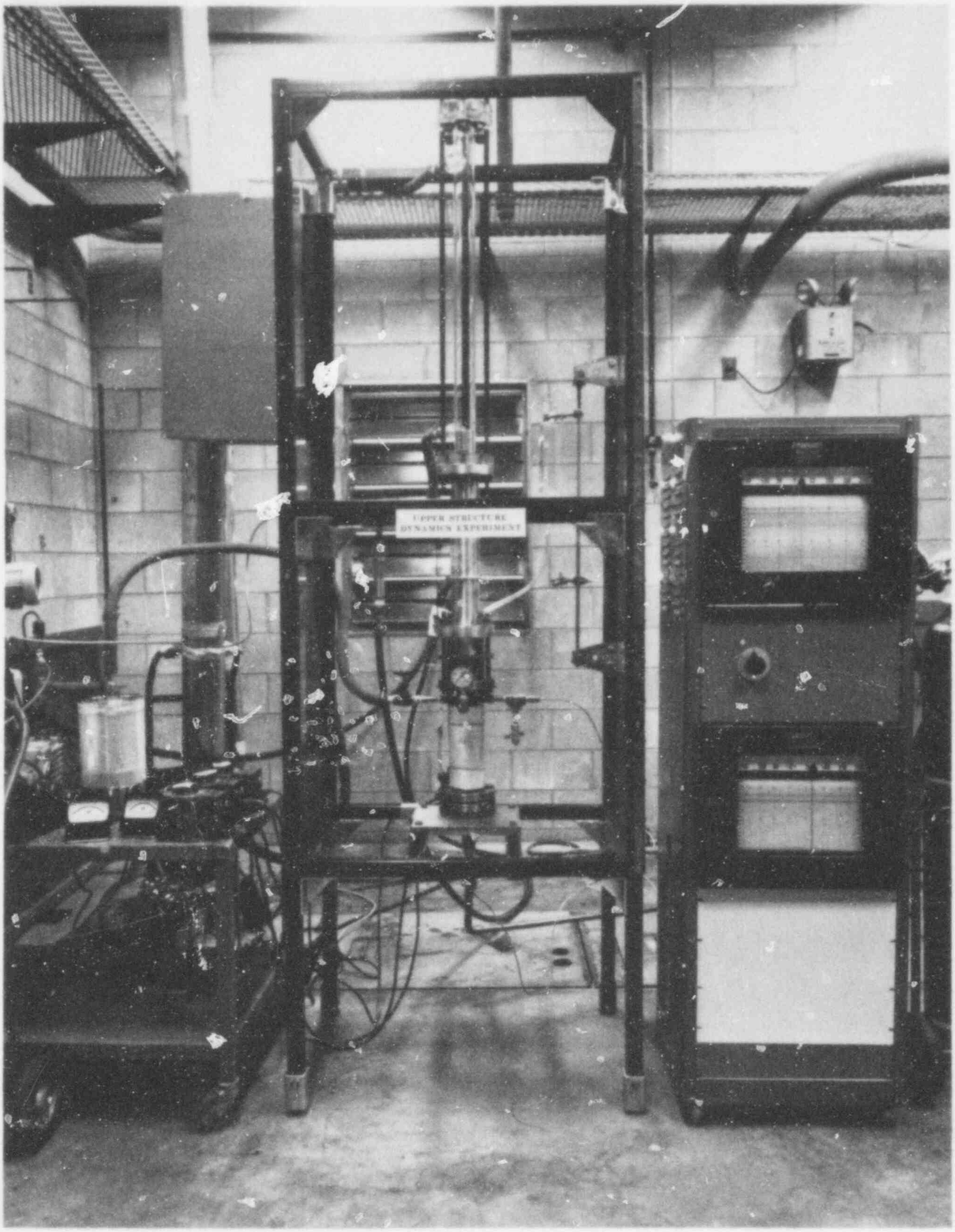

Fig. 72. Upper structure dynamics experiment.

The SIMMER analyses performed to date modeled the demonstration experiment described previously. Initial core conditions for the experiment were T = 443 K and P = 2 MPa (300 psi). Calculations for the velocity of the liquid and gas through the UCS for these initial conditions are in qualitative agreement with the experiment. In addition, excellent agreement was obtained between SIMMER prediction and measurement of the core "relaxation" temperature, i.e., the constant asymptotic temperature of the core after approximately 3 s into the test. No time-dependent pressure measurements were made for this initial run. For future experiments, a number of pressure and temperature measurements will be made which will greatly assist in analysis and code validation. A study is also being made to determine the feasibility of using Nuclear Magnetic Resonance (NMR) techniques to measure the time-dependent mass flux transported through the viewing chamber region above the UCS during a test.

In summary, the USD experiment has progressed into the initial testing phase on schedule, with emphasis still being placed on check out of the equipment and experimental techniques. A SIMMER analysis of some of the preliminary demonstration experiments indicates very good agreement with available measurements. Additional details of the scaling analysis will be presented at the International Meeting on Fast Reactor Safety to be held in Seattle, Washington on August 19-23, 1979.

4. Advanced Momentum Exchange Models

(E. J. Chapyak, Q-7)

A methodology for including advanced momentum exchange models into the SIMMER code was developed during the last quarter. The procedure is based on the single-particle momentum conservation equation and can be extended to include particle-particle or particle-boundary interactions. A generalized form of the single-particle equation is used in conjunction with the total momentum conservation equation (both of which are well-founded theoretically) to derive the SIMMER field equations. The generalization of the single-particle equation is accomplished by replacing

634 169

$$\frac{d\vec{u}}{dt} \text{ with } \frac{\partial\vec{u}}{\partial t} + (\vec{u} \cdot \vec{\nabla})\vec{u} \text{ and}$$

$$\frac{d\vec{v}}{dt} \text{ with } \frac{\partial\vec{v}}{\partial t} + (\vec{v} \cdot \vec{\nabla})\vec{v} \ ,$$

where $\vec{u}$ is the particle velocity and $\vec{v}$ is the fluid velocity. These substitutions ensure that first, a single particle is being followed and secondly, the coordinate frame in which the single-particle equation is written is always moving with the same fluid particle. They represent the only possible generalization of the single-particle equation that reproduces the standard SIMMER equations when the conventional drag formulation is used.

As an example, consider a spherical particle described by a single-particle equation that includes both Basset forces and virtual mass, but neglects particle-particle interactions (i.e., the low-particle density, dispersed flow limit). The SIMMER momentum-field equations that result from the procedure described above are

$$\bar{\rho}_p\left[1 + \left(1/2\right)\alpha_p(1 + \bar{\rho}/\bar{\rho}_p)\right]\left[\frac{\partial\vec{u}}{\partial t} + (\vec{u} \cdot \vec{\nabla})\vec{u}\right]$$
$$= -\frac{3}{2}\alpha_p\,\vec{\nabla}p - \bar{\rho}_p\vec{g}\left[1 + \left(1/2\right)\alpha_p(1 + \bar{\rho}/\bar{\rho}_p)\right] + \alpha\alpha_p(\text{Drag}) \qquad (32)$$

and

$$\bar{\rho}\left[1 + \left(1/2\right)\alpha_p(1 + \bar{\rho}/\bar{\rho}_p)\right]\left[\frac{\partial\vec{v}}{\partial t} + (\vec{v} \cdot \vec{\nabla})\vec{v}\right]$$
$$= -\alpha\vec{\nabla}_p\left[1 + \left(1/2\right)\frac{\rho}{\rho_p}\right] - \bar{\rho}\vec{g}\left[1 + \left(1/2\right)\alpha_p(1 + \bar{\rho}/\bar{\rho}_p)\right] - \alpha\alpha_p(\text{Drag}), \qquad (33)$$

where

$$\text{Drag} = -\frac{9}{2} - \rho\frac{\nu}{R^2}(\vec{u} - \vec{v}) - \frac{3}{8}C_d\,\frac{\rho(\vec{u} - \vec{v})\left|\vec{u} - \vec{v}\right|}{R}$$
$$- \frac{9}{2}\,\frac{\rho}{R}\sqrt{\frac{\nu}{\pi}}\int_{-\infty}^{t}\left(\left[\frac{\partial\vec{u}}{\partial\tau} + (\vec{u} \cdot \vec{\nabla})\vec{u}\right] - \left[\frac{\partial\vec{v}}{\partial\tau} + (\vec{v} \cdot \vec{\nabla})\vec{v}\right]\right)\frac{d\,\tau}{\sqrt{t - \tau}}, \qquad (34)$$

and bars over the densities indicate macroscopic variables. We emphasize that these equations are valid only in the low-particle density, dispersed flow limit, and that a nonrigorous (in the finite velocity limit) expression for the Basset drag component has been employed. Equations (32) and (33) can be compared to the SIMMER momentum field equations derived from the same procedure but with the neglect of virtual mass and Basset forces

$$\bar{\rho}_p\left[\frac{\partial\vec{u}}{\partial t} + (\vec{u}\cdot\vec{\nabla})\vec{u}\right] = -\alpha_p\vec{\nabla}p - \bar{\rho}_p\vec{g} + \alpha\alpha_p(\mathrm{Drag}) \tag{35}$$

and

$$\bar{\rho}\left[\frac{\partial\vec{v}}{\partial t} + (\vec{v}\cdot\vec{\nabla})\vec{v}\right] = -\alpha\vec{\nabla}p - \bar{\rho}\vec{g} - \alpha\alpha_p(\mathrm{Drag}) \ , \tag{36}$$

where in this case "Drag" has no component due to the Basset force. Equations (35) and (36) are the conventional SIMMER momentum conservation equations (without mass exchange).

In the near future, we plan to examine similar modifications to SIMMER's energy equations. Incorporation into SIMMER on an experimental basis will then be considered. One major problem with these modifications is that the coefficient of virtual mass [the factor 1/2 in Eqs. (32) and (33) in the low-particle density dispersed flow limit] is known to be a function of particle density, but with very little quantitative information available.

5. Evaluation of LMFBR Fuel-Motion Diagnostics

(A. E. Evans, M. B. Diaz, R. E. Malenfant, B. Pena. and E. A. Plassmann, Q-14)

We have previously measured, as discussed in the last progress report, the effect of a 22-mm-thick steel sleeve on the neutron and gamma-ray images of a 37-pin fast test reactor (FTR) test bundle in PARKA. This was done by withdrawing the central pin from the test bundle and determining the resulting loss in total count rate. During this reporting period, we repeated these measurements, except that pins were removed from the side rather than the center of the bundle.

The neutron and gamma-ray backgrounds, as measured by the scanning hodoscope when there is no fuel in the test region, are not uniform across the entire field of view. At the edges of the field of view, background levels are nearly equal to signal levels from the center of a 37-pin bundle. For this reason and because the major diameter of the 37-pin test bundle is greater than the field of view of the scanner, it was necessary to displace the test section 19 mm to one side of the axis of the through-slot in PARKA. This was easily accomplished by removing the test section and its liner from the reactor core, shifting seven of the PARKA fuel rods, and then replacing the test section in its new position into the core. The entire operation was completed in less than four hours.

The image of this off-center, 37-pin test assembly was then studied with the scanning hodoscope, using stilbene scintillation detectors with pulse-shape discrimination to simultaneously count gamma rays and neutrons. The results of scanning the hexagonal test array with an edge parallel to the line-of-sight are shown in Fig. 73 for neutrons and Fig. 74 for gamma rays. The effect of a 22-mm-thick steel casing on the image is also shown in these figures.

Neutron scans of the test region without fuel pins show that the presence of the steel casing does not appreciably affect the fast-neutron background in the center of the test region, although there is some flattening of the hodoscope background across the region when the steel is in place. The neutron signal from the test pins is, however, reduced about 40% by the steel, with resultant loss of S/N ratio and mass resolution. The effect is more pronounced for gamma rays. We find the net gamma counting rate from the fuel pins reduced by more than 50% while the background is undiminished. These effects, for both neutron and gamma-ray imaging, are not appreciably different from those previously reported for hodoscope scans of the center of the fuel bundle.[7]

Figure 73 also shows a 10-15% increase in the hodoscope neutron background from the test region caused by the presence of the test fuel. This is attributed to a power distribution shift with

634 172

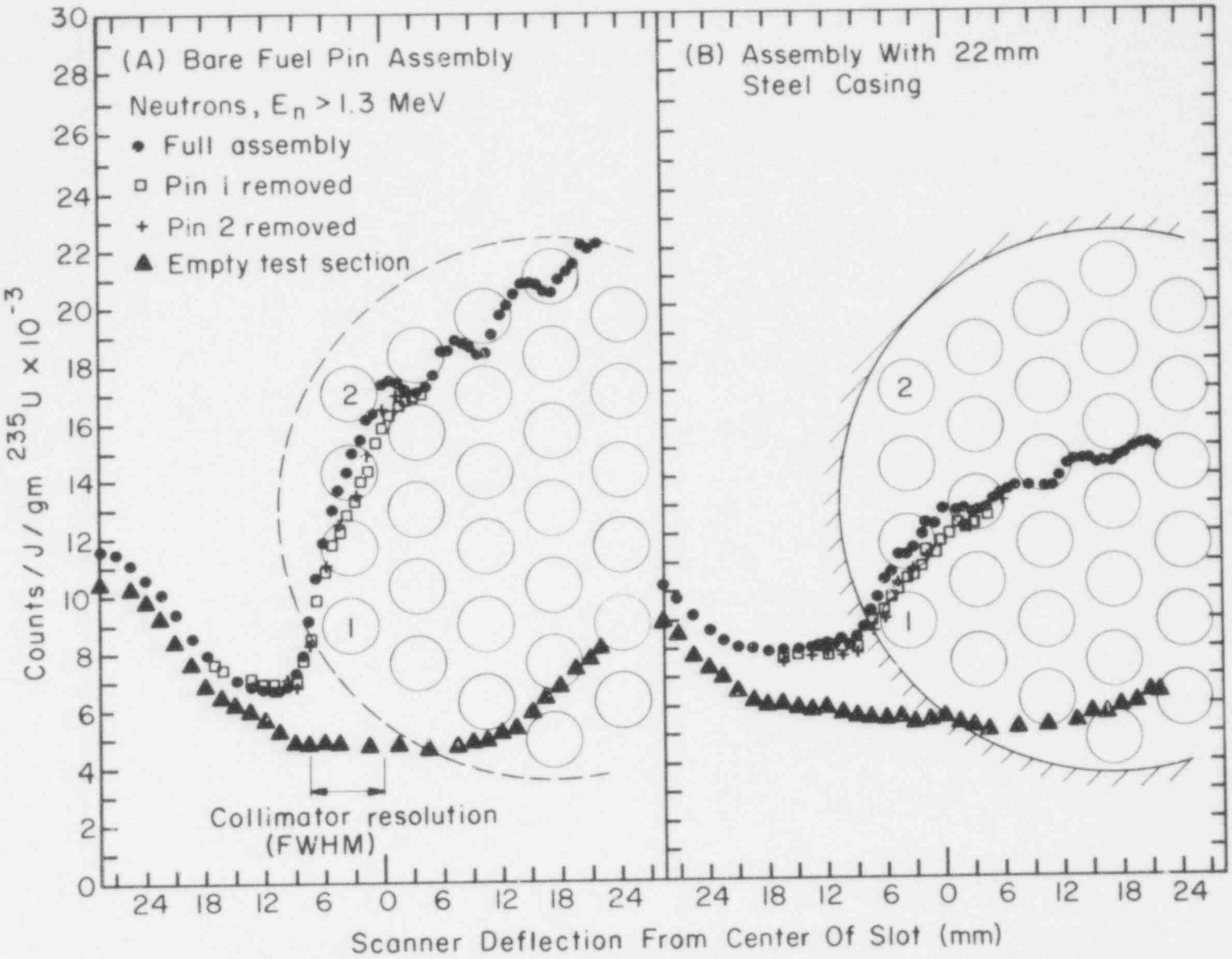

Fig. 73. Results of hodoscope neutron scans of a 37-pin fuel bundle mounted 19 mm off axis of the PARKA viewing slot, with and without the removable 22-mm-thick steel casing.

634 173

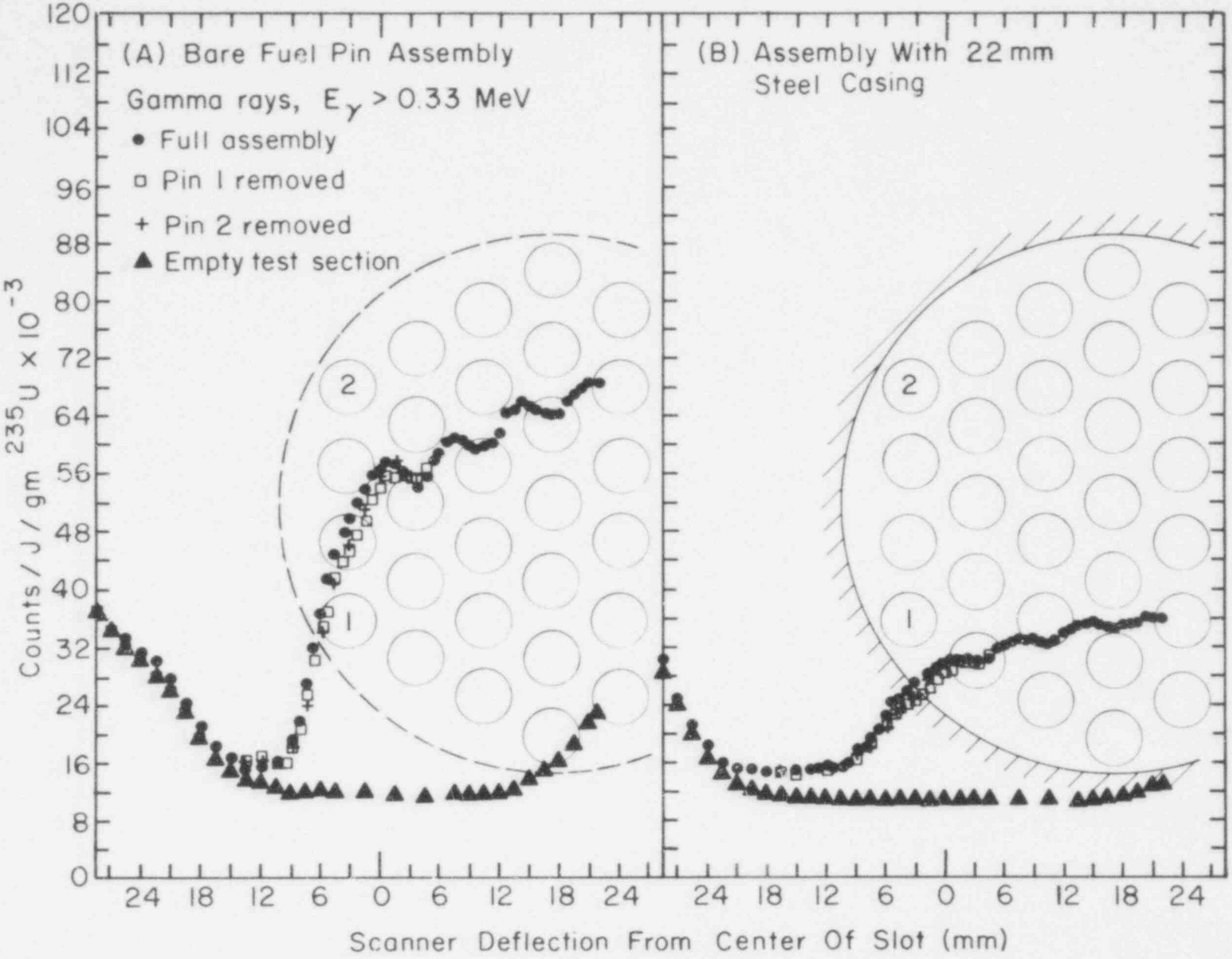

Fig. 74. Results of hodoscope gamma scans of the 37-pin fuel bundle.

respect to the flux at the ion chamber being used as a power monitor and controller. The monitoring chamber is external to the reactor core.

Preparations are under way to use the PARKA facility to test coded aperture imaging techniques being developed by the Sandia Laboratories in Albuquerque (SLA). We exposed x-ray films at the hodoscope collimator slots to demonstrate that there is sufficient intensity of radiation from the test area to form an image of a test assembly with an exposure of 2-4 h at a power level of 5 mW/g ^{235}U. Apertures and shielding components, being fabricated by SLA, will be installed in the wall of the shielded instrumentation room in place of the present collimator. A two to three month experimental program is anticipated.

Not all proposed techniques for STF fuel-motion monitoring have involved fast-neutron imaging. Many of the coded aperture techniques use gamma radiation as their image-forming medium. Furthermore, it has been proposed that clad motion be monitored by imaging high-energy capture-gamma radiation from iron.[37] The use of the hodoscope for gamma-ray imaging, particularly for imaging capture-gammas from iron in the face of an intense but lower-average-energy fission-gamma spectrum, requires optimization of the gamma detector. Ideally, one would like a detector which is small (to minimize sensitivity to ambient backgrounds and to make arrays of large numbers of detectors practical), has a high overall detection efficiency for high-energy radiation, and has a response peaked at full-energy absorption to assure good energy discrimination.

We have used thallium-activated sodium iodide detectors, 12.7-mm-diam x 12.7-mm-long, with the PARKA hodoscope for some gamma-ray measurements.[38] However, these NaI(Tl) detectors have a rather low peak-to-Compton ratio for gamma rays at energies greater than 1 MeV. Moreover, activation of iodine with resultant buildup and decay of the 25-min. ^{128}I activity has been a deterrent to their use. Plastic and stilbene detectors have even less desirable pulse-height responses for the range of gamma-ray energies involved.

Newly introduced scintillation-grade bismuth germanate ($Bi_4Ge_3O_{12}$) crystals have the desired detector characteristics.[39] This material, twice as dense as NaI, has an efficiency for gamma absorption such that pulse-height distributions from a bismuth germanate (BGO) crystal are equivalent to those from a NaI(Tl) crystal with linear dimensions three times its size. Thus, a $600, 38 mm x 38 mm (1-1/2 in. x 1-1/2 in.) BGO detector is nearly equivalent to a 125 mm x 125 mm (5 in. x 5 in.) NaI(Tl) detector worth $2000.

Three BGO crystals, the above-mentioned 38 mm x 38 mm cylinder, a 12.5 mm x 12.5 mm cylinder, and a rectangular piece 12.5 mm square by 6.2 mm thick, have been purchased from the Harshaw Chemical Company for evaluation. The latter two pieces are intended for use with the PARKA hodoscope. Since the light output of BGO is only 8% of that of NaI(Tl) for incident photons of a given energy, a low-noise photomultiplier is needed to obtain optimum pulse-height resolution. We found that an Amperex-type XP-2000 2-in. tube gave satisfactory results. Amperex-type XP-1110 19-mm-diam photomultipliers, which have been used for the Hornyak buttons and stilbene scintillators in the hodoscope measurements, were found to be quite satisfactory for use with the smaller BGO detectors. The BGO crystals were coated on the cylindrical surface and one end with titanium dioxide reflector paint. Electronic equipment used for testing included an ORTEC model 266 photomultiplier base an ORTEC model 113 preamplifier, and an ORTEC model 472 spectroscopy amplifier. The amplifier shaping time constant was 3 μs. The photomultiplier was operated at 1 300 V.

In Fig. 75, the pulse-height response of the 38 mm BGO crystal for ^{137}Cs gamma rays is compared to that of a 38 mm NaI(Tl) detector. The full-width at half-maximum from the full-energy peak of the BGO response is nearly twice that of the NaI(Tl) distribution. However, the peak-to-Compton ratio is considerably better for the BGO detector and its backscatter peak is somewhat smaller. The latter characteristics should simplify the unfolding of continuous spectra. The full-energy peak efficiency of the BGO is 3.3 times that of the NaI(Tl) crystal.

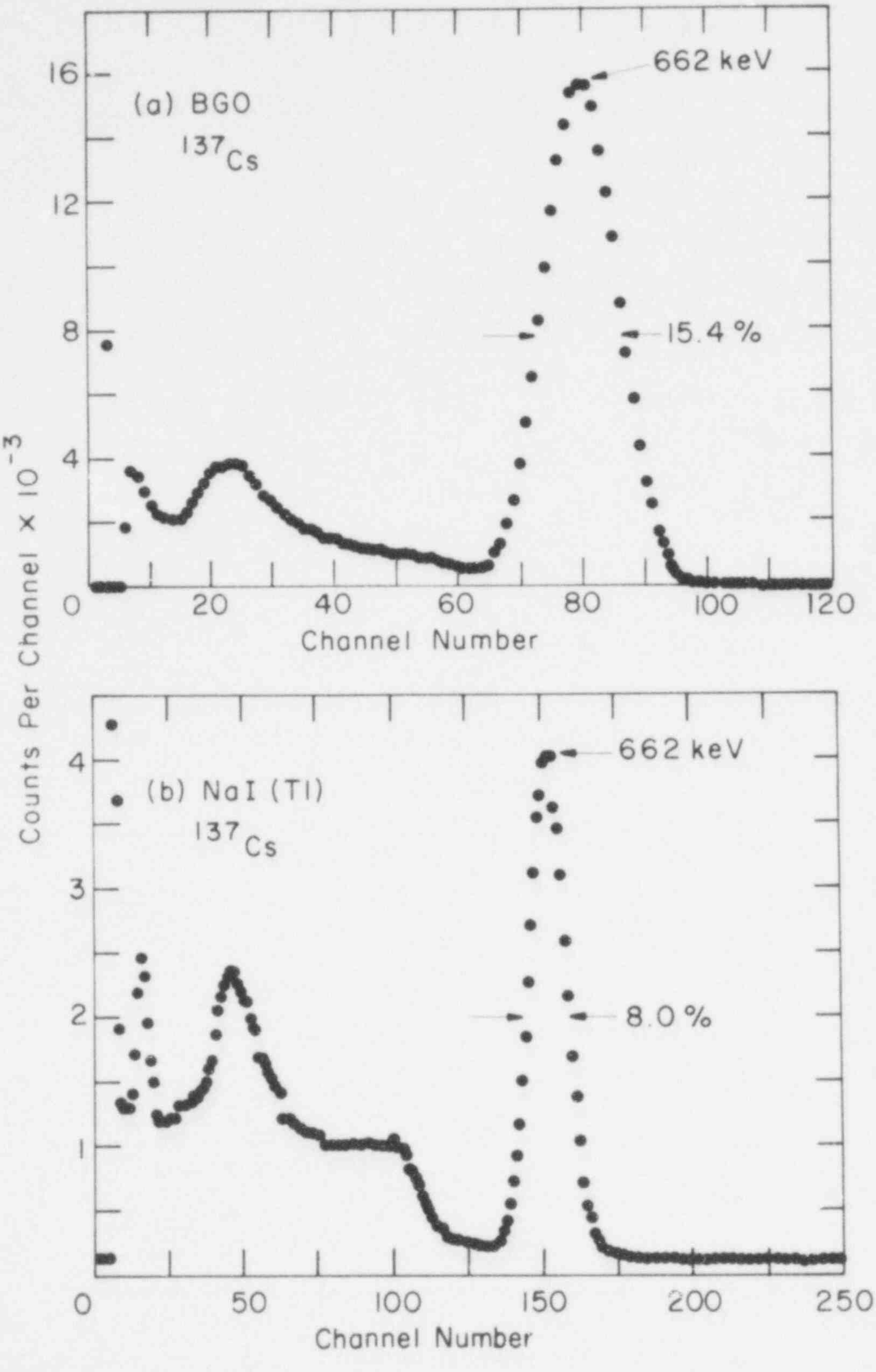

Fig. 75. Pulse-height response functions of 38 mm x 38 mm bismuth germanate (a) and thallium-activated sodium-iodide (b) scintillators to ^{137}Cs gamma radiation. A 1 μC source was counted for 200 s on contact with the face of each detector.

The comparison for ^{60}Co gamma rays is shown in Fig. 76. The resolution of the BGO detector is not quite good enough to resolve the 1.17 and 1.33 MeV photopeaks. However, the Compton peak in the NaI(Tl) detector is now prominent enough to interfere with the detection of small amounts of lower-energy gamma rays and makes spectrum unfolding difficult. At 1.33 MeV, the full-energy peak efficiency of the BGO is 4.5 times that of the NaI(Tl) detector.

As photon energy increases, BGO becomes the clear choice with respect to NaI(Tl). We illustrate this in Fig. 77, which is a comparison of the responses of the two detectors to 1.37 and 2.75 MeV gamma rays from the decay of ^{24}Na. Here, the BGO detector at 2.75 MeV shows a predominance of the full-energy peak over the annihilation-escape peaks and the Compton shoulders. For the NaI(Tl) detector, the full-energy and escape peaks of the 2.75 MeV line are approximately equal and the Compton peak is quite evident. The strong Compton peak is also seen for the 1.37 MeV line. The efficiency of the BGO crystal for the 2.75 MeV full-energy peak is 5.6 times that of the NaI(Tl).

Figure 78 shows the response of the 12.5 mm BGO cylinder to ^{24}Na radiation. In terms of peak-to-total ratio and total counts per photon incident upon the crystal, this detector is roughly equivalent to the 38 mm NaI(Tl) detector.

The response of the large BGO detector to 4.43 MeV radiation is plotted in Fig. 79. This radiation, from the decay of the first excited state of ^{12}C, was derived from the ^{9}Be(α,n)^{12}C* reaction in a ^{238}Pu-Be(α,n) neutron source.

The responses of the detector for higher energies was measured by observing gamma rays from the decay of the 8.28 MeV excited level of ^{15}O. To produce this radiation, a thin film of tantalum nitride on a platinum backing was bombarded by 1.06 MeV protons at the Group Q-1 Van de Graaf accelerator. The observed gamma rays result from a 5-keV-wide resonance in the ^{14}N(p,γ)^{15}O reaction. With the detector 2 cm in front of the target, we obtained the pulse-height distribution shown in Fig. 80 in 84 min. with a 2 μA proton beam. The 8.28, 5.24, and 3.04 MeV lines are from the decay of the 8.28 MeV level of ^{15}O to the ground state.

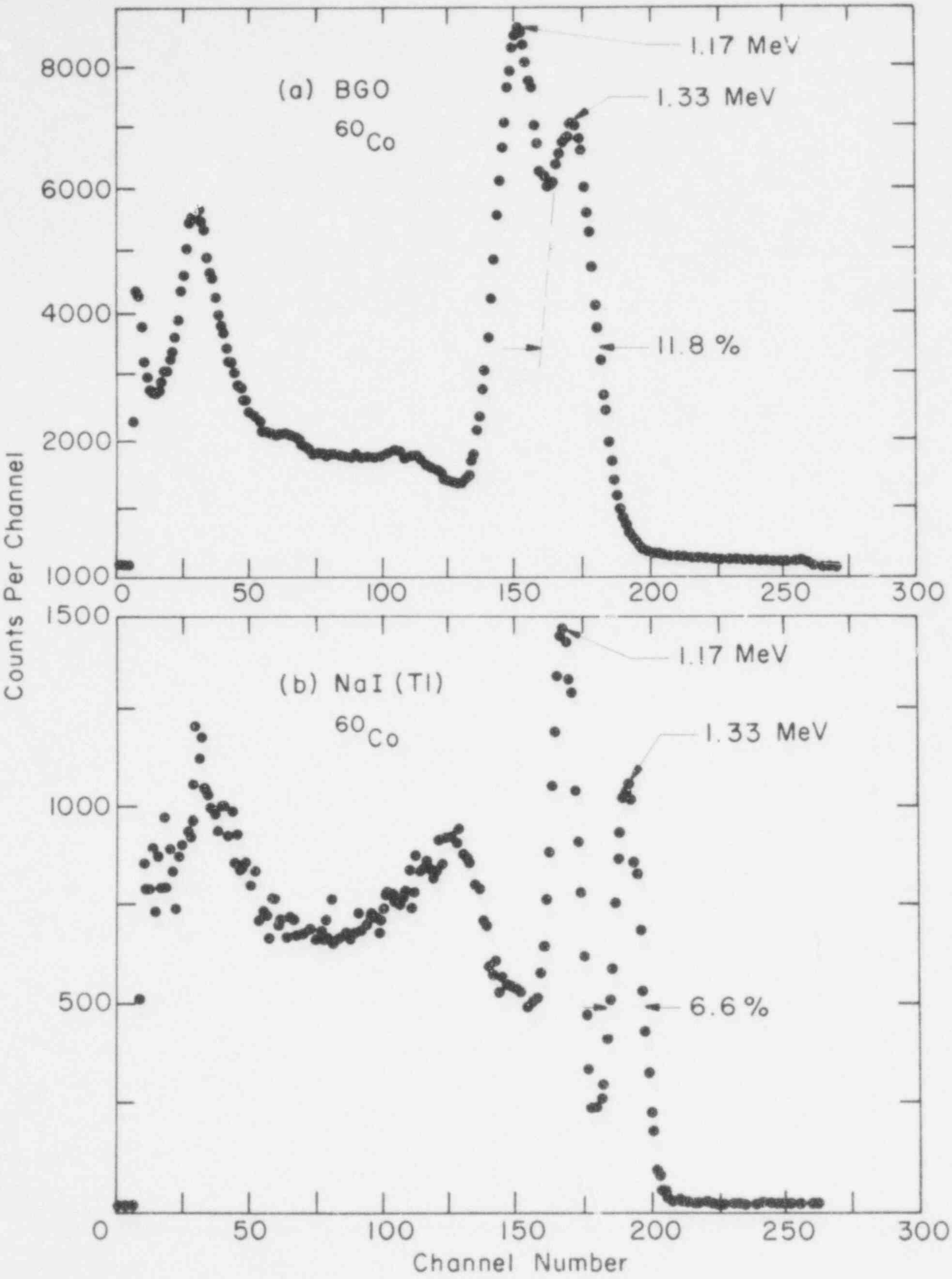

Fig. 76. Comparison of pulse-height response functions of 1-1/2 in. x 1-1/2 in. BGO (a) and NaI(Tl) (b) scintillators to ^{60}Co gamma radiation.

654 179

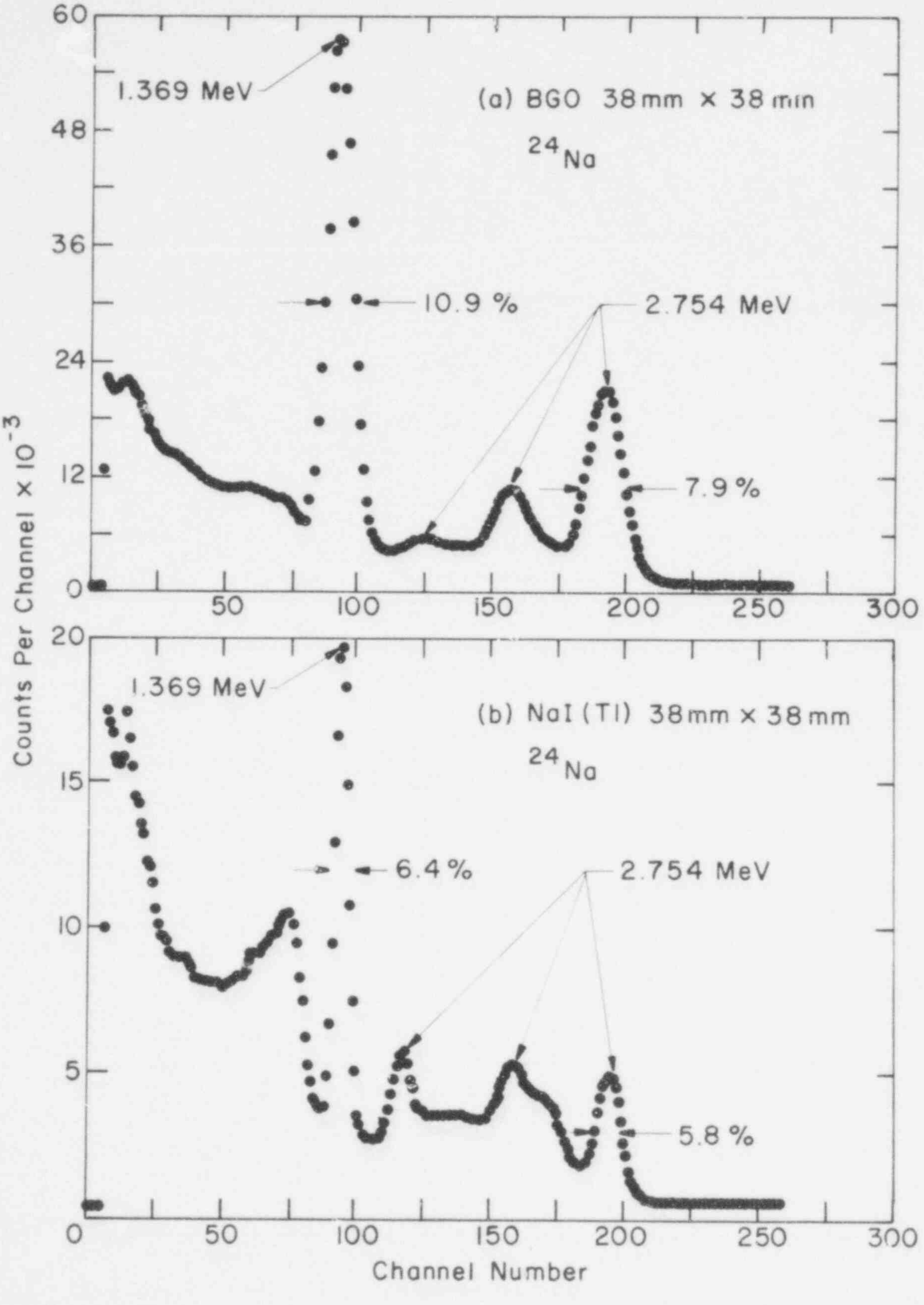

Fig. 77. Pulse-height distributions from 38 mm x 38 mm BGO and NaI(Tl) scintillators for gamma radiation from ^{24}Na.

634 180

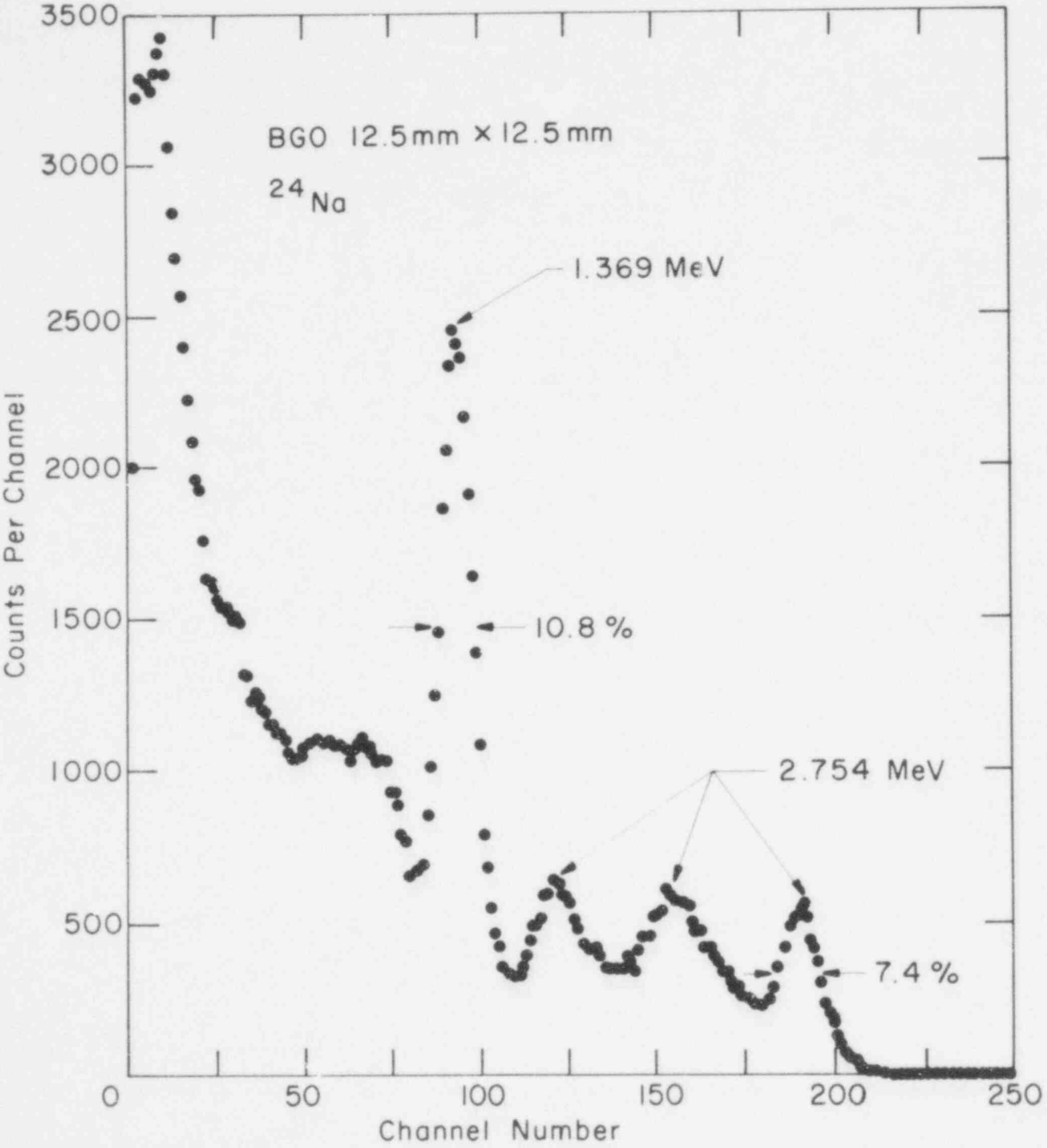

Fig. 78. Response of a 12.5 mm diam x 12.5 mm long BGO scintillator to ^{24}Na gamma rays.

634 181

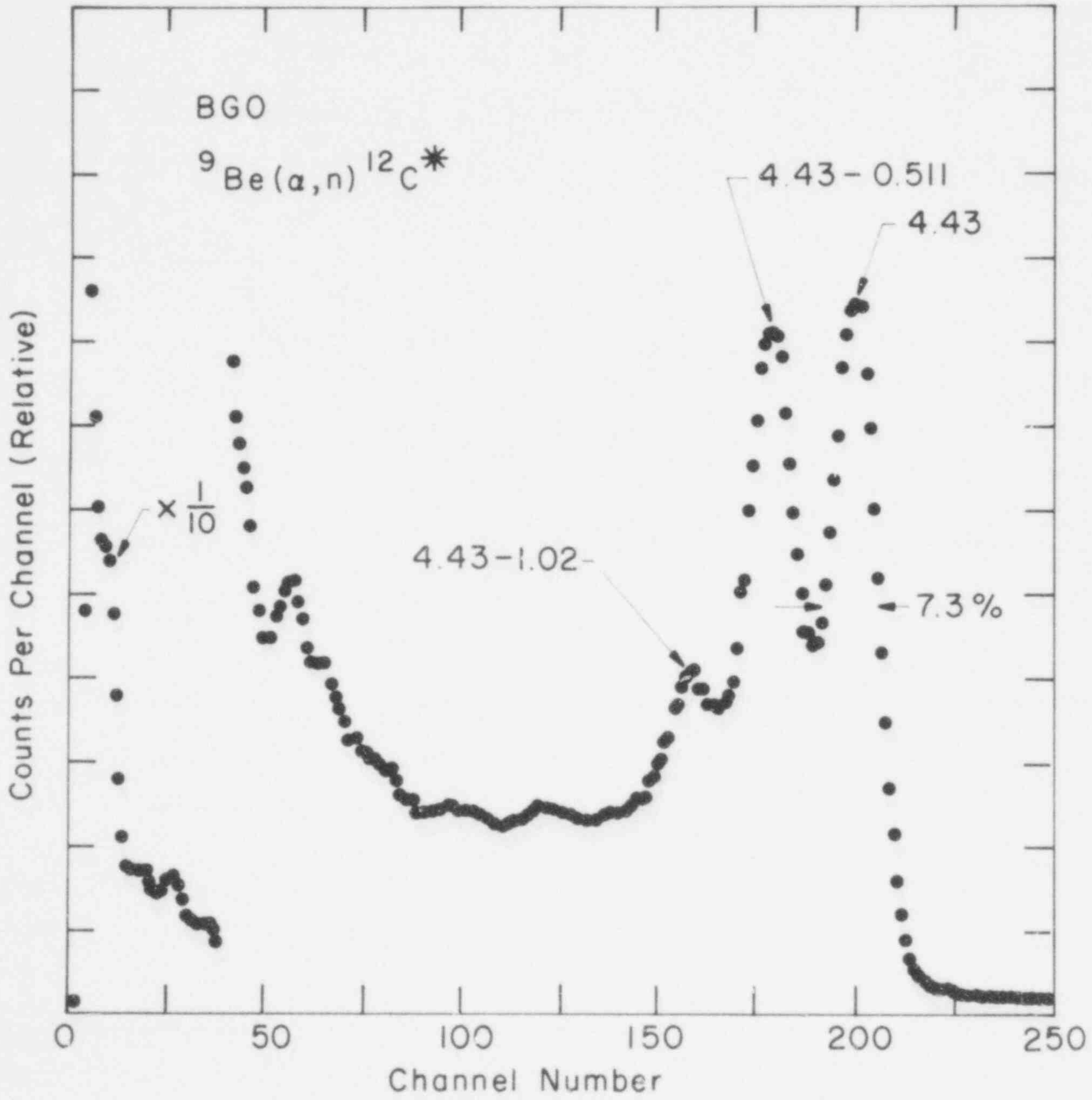

Fig. 79. Response of a 38 mm x 38 mm BGO scintillator to 4.43 MeV gamma rays.

634 182

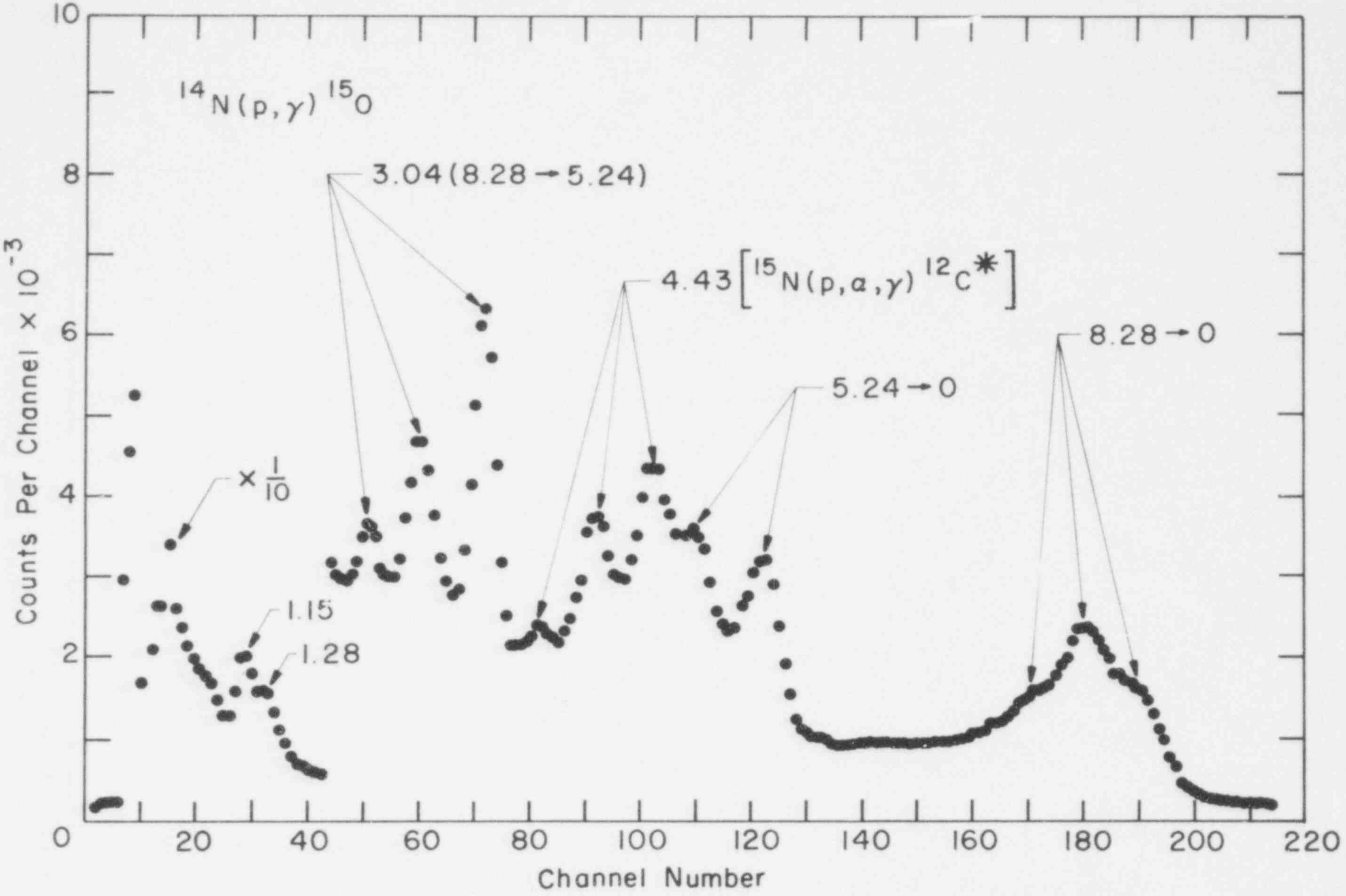

Fig. 80. Response of the large BGO scintillator to gamma rays from the 1.058 MeV resonance of the $^{14}N(p,\gamma)^{15}O$ reaction.

The 4.43 MeV radiation is from the $^{15}N(p,\alpha\gamma)C^{12}$ reaction, which is always evident when nitrogen of normal isotopic content is used as a target for this reaction.[40]

In Fig. 81, the full-energy peak efficiency of the BGO crystal for 0.1-8.28 MeV gamma rays is compared with that of a NaI(Tl) crystal of the same size. For energies less than 2.6 MeV, absolute efficiencies were obtained by placing calibrated radioisotope sources 10 cm from the front face of the detector. Relative efficiencies from 3.04-8.28 MeV were obtained from the known branching ratios of the decay of the 8.28 MeV level of ^{15}O (Ref. 40) and normalized to the radioisotope data by matching the slopes of the two parts of the curve.

Finally, the resolution performance of the large BGO detector is shown in Fig. 82. Although this resolution is only about half as good as can be obtained with equivalent NaI(Tl) crystals, the higher efficiency of the BGO and the near absence of Compton continuum make this detector the choice for high-energy measurements when a high-resolution detector is not needed. Its ruggedness, comparable to Pyrex, and its nonhygroscopicity, make it an ideal candidate for field applications such as environmental and health monitoring, assay for nuclear safeguards, and uranium exploration. It would be an ideal detector for down-hole assay by capture-gamma-ray measurements. Immediate applications for our activities include gamma-ray spectral distribution measurements of LMFBR fuel-pin assemblies in the PARKA critical assembly machine.

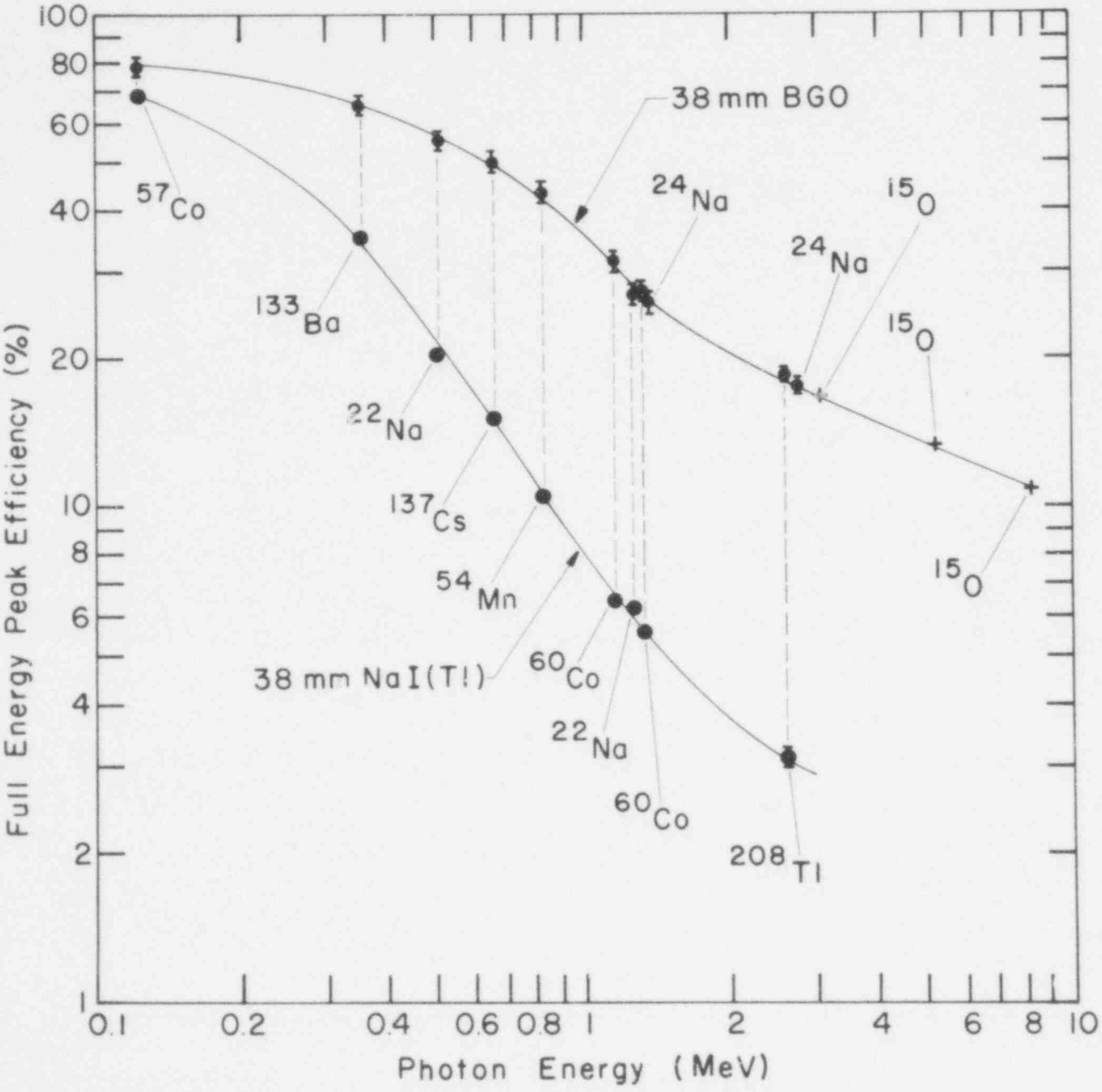

Fig. 81. Full-energy peak efficiencies of 38 mm BGO and NaI(Tl) scintillators as a function of gamma-ray energy.

634 185

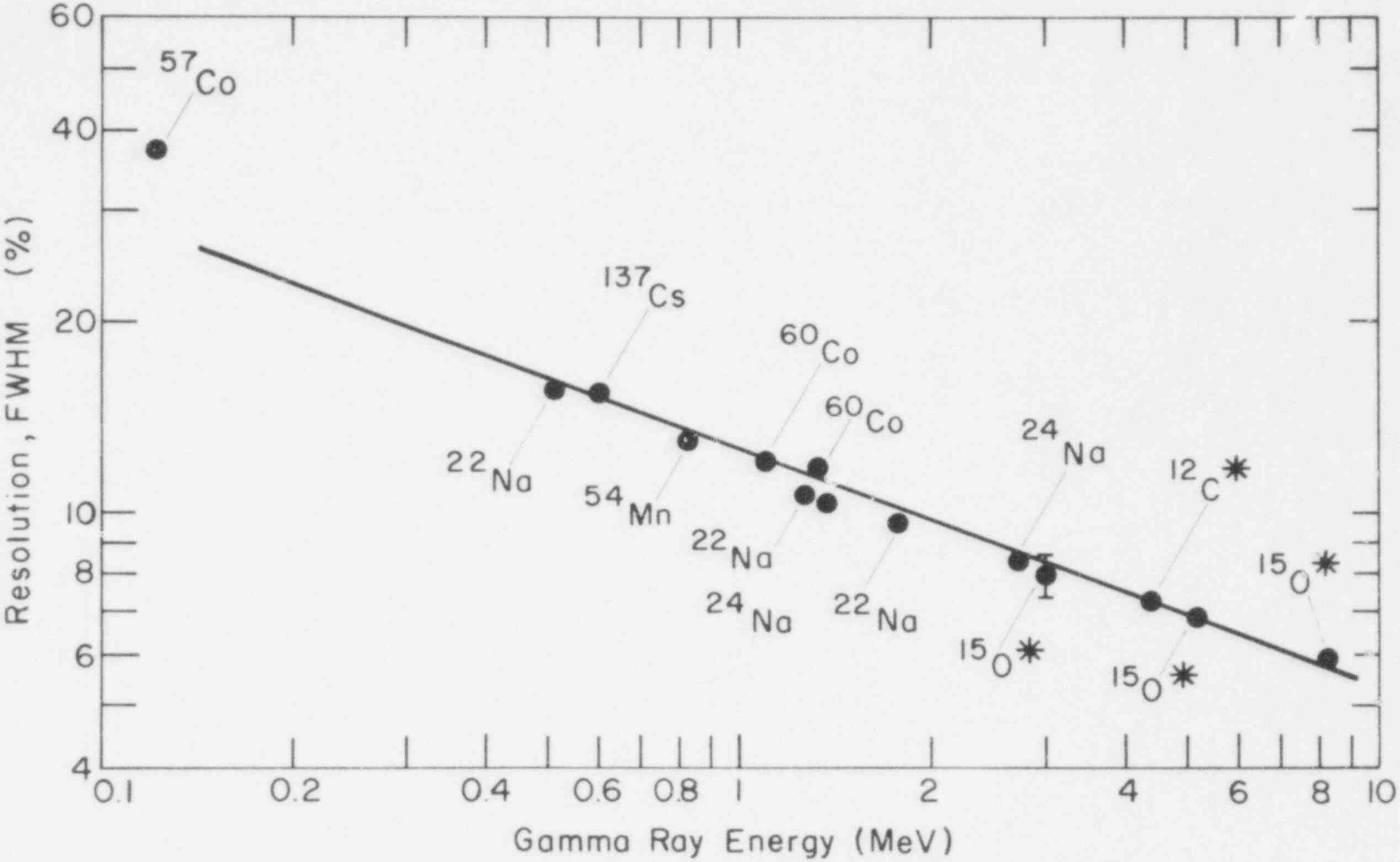

Fig. 82 Resolution of the 38 mm $Bi_4Ge_3O_{12}$ scintillator as a function of gamma-ray energy.

IV. HTGR SAFETY RESEARCH PROGRAM

(M. G. Stevenson, Q-DO)

Under the sponsorship of the NRC/RSR, LASL is conducting a program of research in High-Temperature Gas-Cooled Reactor (HTGR) safety technology in the following task areas:

- Structure Evaluation

- Phenomena Modeling, Systems Analysis, and Accident Delineation

Progress for this quarter in these two areas is reported below.

A. Structural Investigation

(C. A. Anderson, Q-13)

Activities in the HTGR Structural Investigation task during the last quarter consisted of work in the experimental seismic program and structural work related to Fort St. Vrain temperature fluctuation problems. In the former activity, preliminary tests on the two-dimensional plastic model have been carried out at the White Sands Missile Range (WSMR) and results are reported on dowel pin shear forces and block impact forces. In the Fort St. Vrain activity, we completed an evaluation of the effect of the region constraint devices on the seismic behavior of the core.

1. Experimental Seismic Program

(R. C. Dove and W. E. Dunwoody, Q-13)

As previously reported, three series of core blocks have been constructed and instrumented to measure side wall contact and pin forces. Static and dynamic calibration of the force transducers incorporated into these blocks was conducted during this quarter. The static calibration of the transducers designed to measure side-wall contact forces gave the data shown in Fig. 83. Notice that the HLM graphite blocks show some nonlinearity. The same transducers were also calibrated dynamically by impacting a moving

634 187

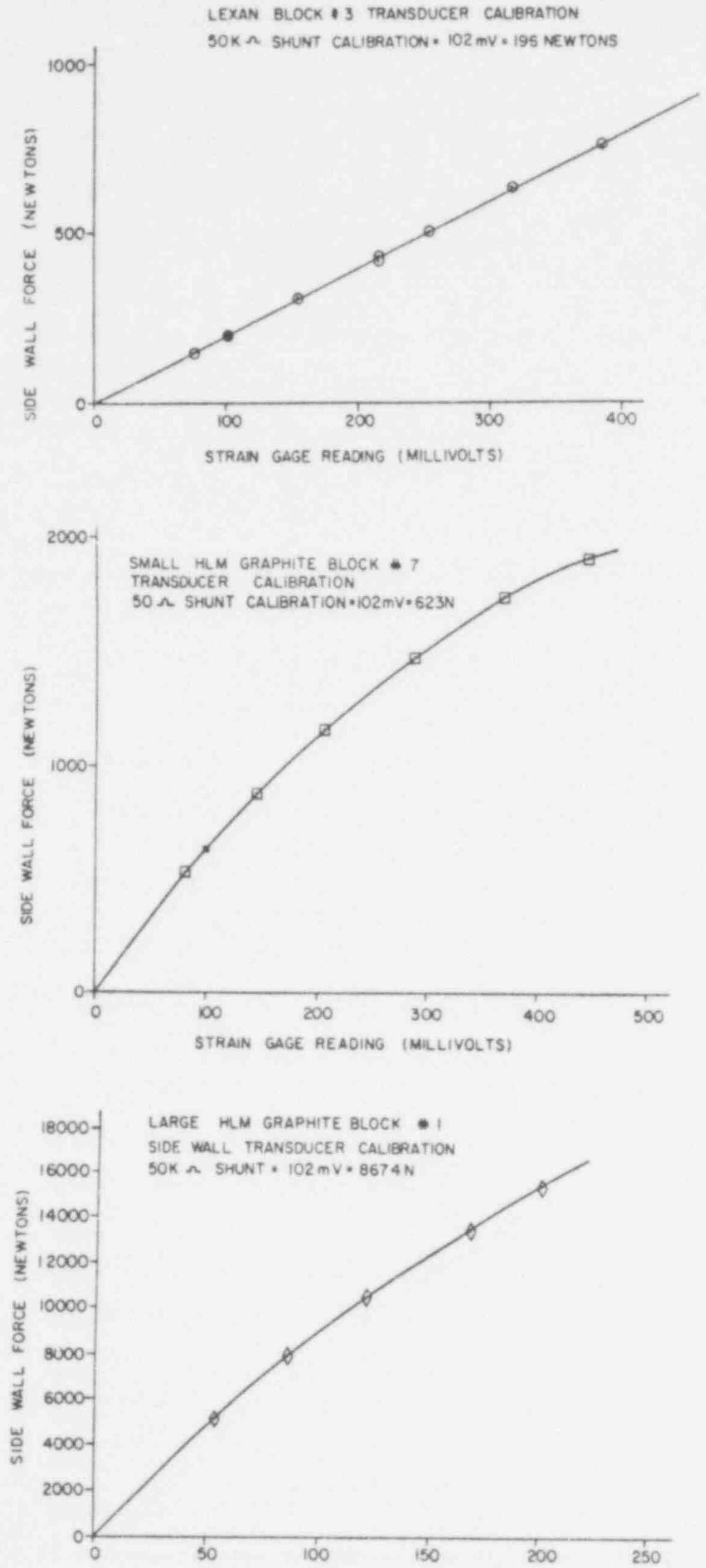

Fig. 83. Static calibration curves for side-wall contact forces on graphite and Lexan blocks.

mass, which carried a precision load cell, onto the block to be calibrated.

The shear force transducers on the Lexan model blocks were also calibrated both statically and dynamically. The dynamic calibration was not judged to be useful because there is no unique relationship between the measured force applied and the signal developed by the bending of the gaged pins. The reason for this is that the impacted block is accelerated by the pin socket; the block is then decelerated by pin resistance and as a result, considerable out-of-phase vibration of the two signals (force link and strain gages) results. Under static loading, these shear force transducers show good linearity up to 89 Newtons (20 lbs.).

Following these calibration tests, single impact tests were conducted on a pair of each of the three blocks (Lexan, small HLM, and large HLM). The purpose of these tests was as a final check on our ability to model the large HLM blocks using either HLM or Lexan. Table XVII summarizes the test conditions and results. Table XVIII compares the results as obtained from prototype (large HLM) tests to the predictions made from each of the two model (small HLM and Lexan) tests.

This was considered to be good agreement and as a result the Lexan model system was prepared for testing in a two-dimensional array.

The two-dimensional Lexan model was tested at the WSMR during the period February 12-14. Tests were conducted using both sinusoidal motion and simulated earthquake excitation. Figure 84 shows the forces which were measured during these tests. The shear forces (S_n) and the side-wall contact forces (F_n) were reduced from the measured strain gage signals using calibration curves developed as previously explained.

In these tests, the shear pin and the side-wall gap clearances were set as shown in Fig. 85. Blocks 1-4 and 21-24 are clamped to the holding fixture to simulate side reflector blocks which move with the prestressed concrete reactor vessel (PCRV). The pin clearance (C') is fixed by the relative size of the pin in the block above and its receiving hole in the block (or base plate)

TABLE XVII

SINGLE IMPACT MODEL TESTS

System	Impact Velocity	Measured Time Duration (μs)	Maximum Force (N)
Large HLM Graphite	v_i	1 000	9 985
Small HLM Graphite	1 x v_i[a]	295	1 796
Lexan	1.85 x v_i[b]	515	187

---

[a] When the small HLM is used as a model for the large HLM, the velocity scale (N_x) is unity; hence, $V_{i_m} = V_{i_p}$.

[b] When the Lexan is used as a model for the large HLM, the velocity scale (N_x) is equal to the square root of the length of length scale (N_x); hence, $V_{i_m} = \sqrt{3.45}\ V_{i_p}$.

TABLE XVIII

COMPARISON OF MEASURED AND PREDICTED RESULTS

	Measured Prototype Test	Predicted by HLM Model	Predicted by Lexan Model
Pulse Duration (μs)	1 000	1 018[a]	958[b]
Peak Force (N)	9 985	10 835[c]	10 800[d]

---

[a] For the HLM model, the time scale (N_t) is equal to the length scale (N_x); hence, $T_p = 3.45\ T_m$.

[b] For the Lexan model, the time scale (N_t) is equal to the square root of the length scale (N_x); hence, $T_p = \sqrt{3.45} \times T_m$.

[c] For the HLM model, the force scale (N_f) is equal to the length scale (N_x) squared; hence, $F_p = 3.45^2 \times F_m$.

[d] For the Lexan model, the force scale (N_f) is equal to the modulus scale (N_e) times the length scale (N_x) squared; hence, $F_p = 4.87 \times (3.45)^2\ F_m = F_m$.

634 190

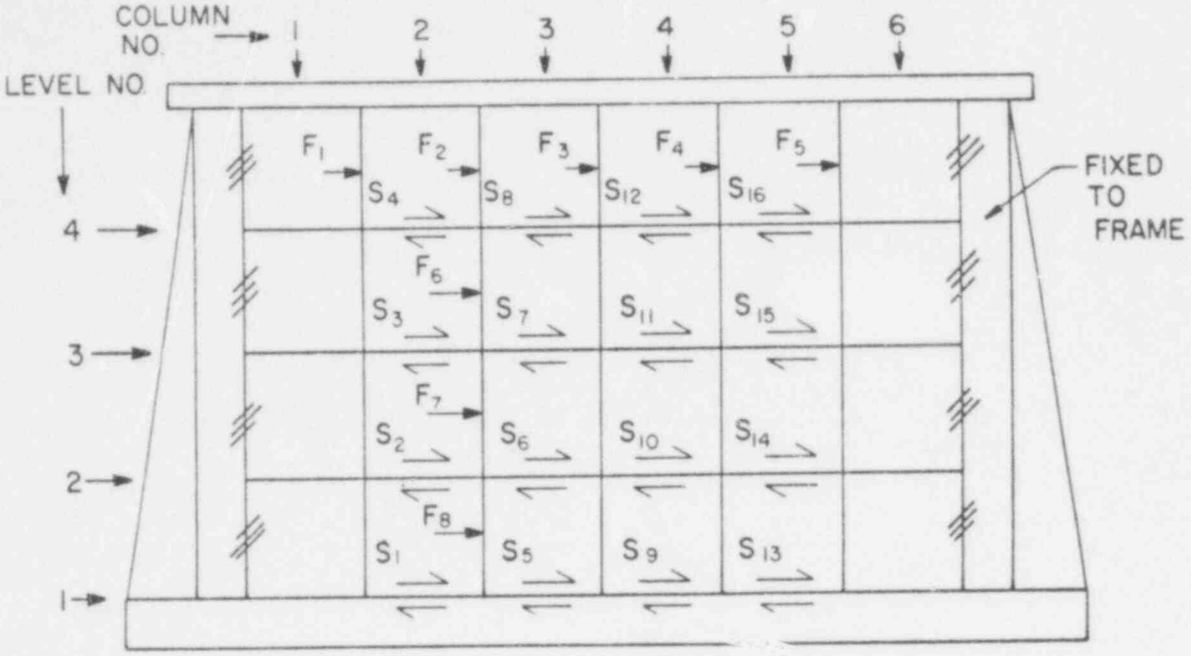

Fig. 84. Two-dimensional model -- force identification.

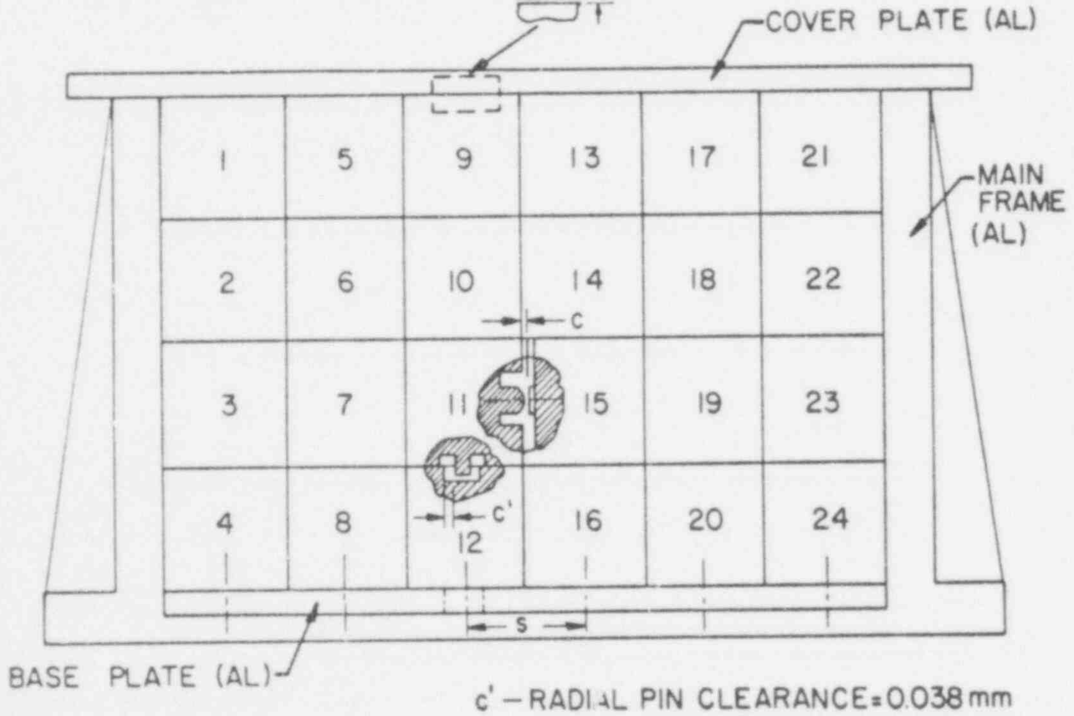

c' – RADIAL PIN CLEARANCE = 0.038 mm
c – SIDE WALL CLEARENCE = 0.254 mm
s – CENTER LINE SPACING OF HOLE IN BASE PLATE = 53.721 mm
d – TOP OF COLUMN CLEARANCE =

Fig. 85. Two-dimensional model -- clearance identification.

below. The side-wall gap clearance (C) is fixed by the centerline spacing (S) in the base plate. The bottom block in each column is pin connected to the base plate in the same way in which blocks in a column are pin connected to each other. However, there is no pin connection between the top block in each column and the cover plate.

For these particular values of radial pin clearance (C') and side-wall gap clearance (C) only the top row (above level 4 in Fig. 84) of blocks should experience side-wall collisions. However, buildup of tolerances may allow side-wall collisions between levels 3 and 4 (i.e., $F_6 \neq 0$). Side-wall contact was not expected to occur below level 3 (i.e., $F_7 = F_8 = 0$), however.

This system was subjected to three sinusoidal motion tests (10 hz, 1 g; 5 hz, 1 g; and 3 hz, 1 g) and to a 1 g simulated earthquake pulse (see Fig. 86a and 86b). The data obtained from these tests are shown in Figs. 87 and 88 and can be summarized as follows:

1. As expected (because of the relative side wall and pin clearances), intense side-wall impacts occurred only above level 4. F_6 was less than one half of F_2 and F_7 and F_8 were zero in all tests.
2. Side-wall contact forces are affected by both frequency and position of the block within the array as shown in Fig. 87. All of the contact forces (F_1, F_2, F_3, F_4, and F_5) show the same general relationship between force magnitude and excitation frequency.
3. How shear forces vary with block position within a column and with frequency is shown in Fig. 88. The data shown are for column 3, but data from all columns show the same relationship between magnitude of shear force and frequency. However, consideration of the data from all columns shows that the shear force at level 3 may be as large as level 4. The increase in magnitude of shear force from level 2 to level 1 is obvious and we speculate that it is due to the fact that the stiffness of a Lexan pin in an aluminum hole at level 1 is greater than the stiffness of a Lexan pin in a Lexan hole at level 2. This may be investigated further by retesting with a Lexan base plate.

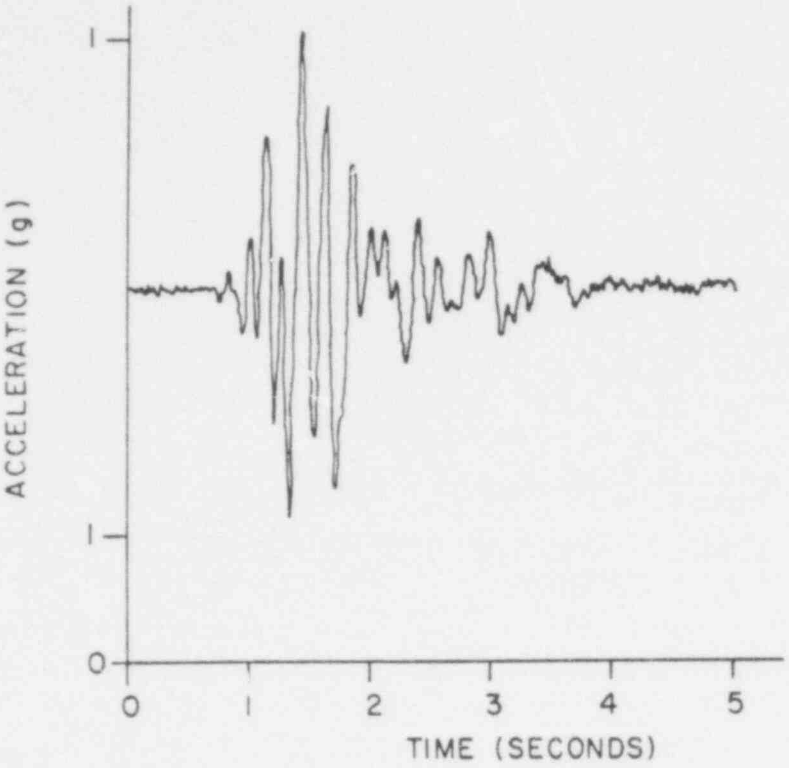

(a) Earthquake excitation acceleration vs time.

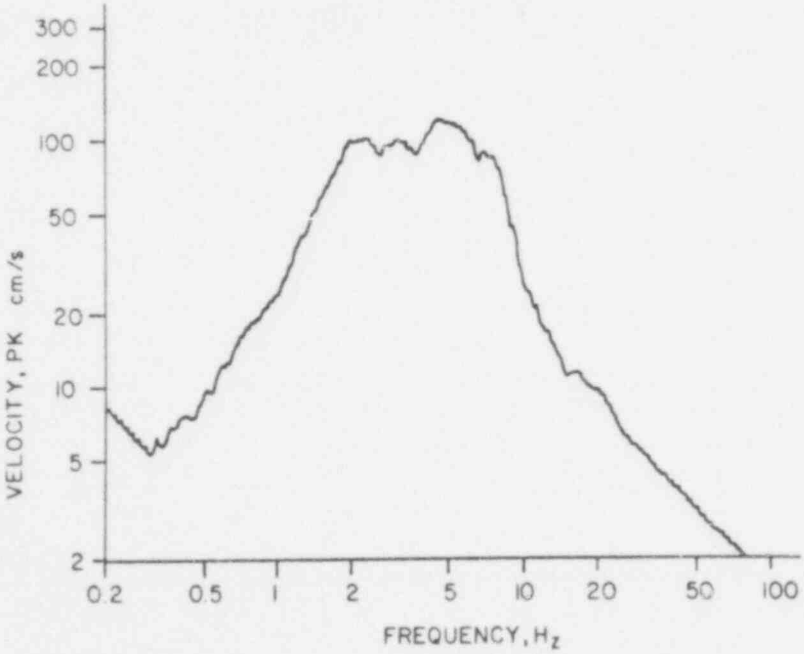

(b) Shock response spectra.

Fig. 86. Excitation and shock response spectra from simulated earthquake.

634 193

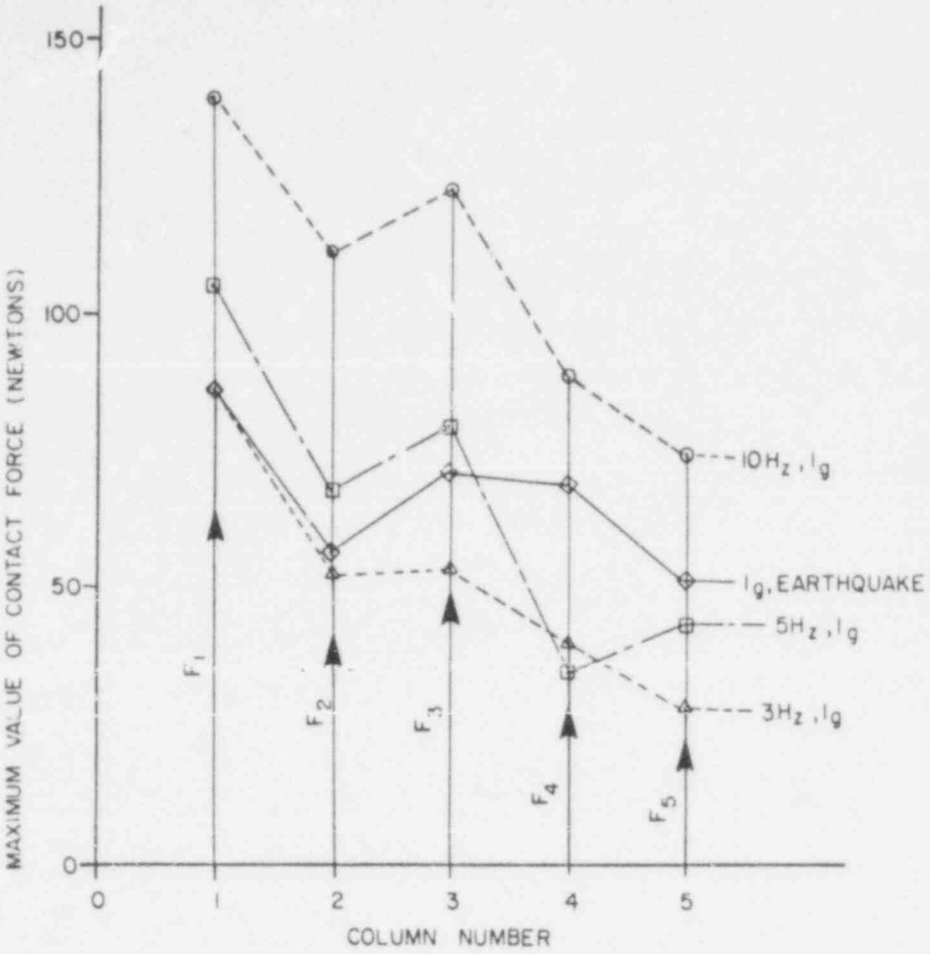

Fig. 87. Contact forces.

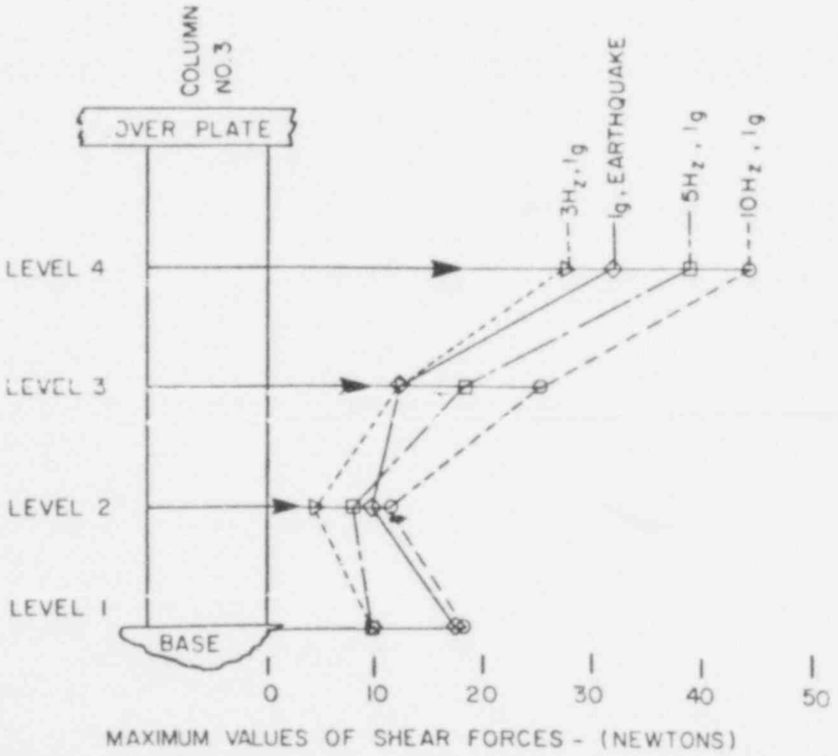

Fig. 88. Shear forces.

634 194

Following the completion of the tests discussed above, the two-dimensional Lexan model was remachined to increase the radial pin clearance (C'). The pin socket in each block was rebored to a nominal diameter of 13.106 mm; hence, since the nominal pin diameter of 12.700 mm was retained, the new radial pin clearance (C) is 0.203 mm. Four new aluminum base plates have also been constructed. All contain 13.106-mm-diam holes to provide the new radial pin clearance at level 1. These four base plates have been made with four different centerline spacings of the holes (S, see Fig. 85) as shown below:

Base #2, S = 53.721 mm
Base #3, S = 53.975 mm
Base #4, S = 54.483 mm
Base #5, S = 54.991 mm

With these four base plates, it will be possible to retest the model with radial pin to side-wall clearance ratios (i.e., C'/C) which will produce side-wall contact in the

1. top row only,
2. the top two rows,
3. the top three rows, and
4. in all rows.

These additional tests, which are expected to give valuable insight into how contact and shear forces vary with clearance gaps, will be conducted just as soon as the testing facility at the WSMR is available.

2. Fort St. Vrain Technical Assistance*

(J. G. Bennett, R. C. Dove, and C. A. Anderson, Q-13)

Presented below is an analysis of the effects of the Public Service Company of Colorado's (PSC) proposal to install core region constraint devices (RCDs) onto the top plane of the Fort St. Vrain (FSV) core with regard to the seismic safety of the core. The devices are being considered for installation in an effort to solve a temperature fluctuation problem currently experienced at FSV under certain operating conditions. The questions that we have addressed are how the addition of the RCDs will affect the dowel shear forces and fuel element impact forces during a seismic event.

a. FSAR Review

Since it was assumed in the Final Safety Analysis Report (FSAR) for the FSV reactor that the core was restrained during seismic events and the analysis used involved the application of an equivalent static load to this "restrained" core, it is not possible to extend this original analysis to determine how the addition of the RCDs will change the seismic loading on the individual core blocks.

A review of the FSAR reveals that for the FSV Nuclear Generating Station the Operating Basis Earthquake (OBE) is taken as 0.5 g horizontal and the Safe Shutdown Earthquake (SSE) is taken as 0.10 g horizontal. Further, dynamic analysis of the core support structure indicated that these ground accelerations result in accelerations at the core level of 0.19 g (OBE) and 0.26 g (SSE). At these relatively low acceleration levels the individual core blocks would not be expected to slip horizontally relative to each other until after an impact event. The reason for this is the fact that without some other driving force slippage does not occur until the base acceleration in "g's" is equal to or greater than the static coefficient of friction between blocks (graphite on graphite), and previous research indicates that this coefficient

---

*This work was partially supported by a contract from the Office of Nuclear Reactor Regulation, Division of Project Management.

is greater than 0.2 and probably greater than 0.3.* From this observation it follows that during seismic excitation the stacked core blocks will respond first as a column rather than as individual blocks moving (slipping) relative to each other.

b. Simplified Bounding Analysis

Three cases will be considered to investigate the effect of adding the RCDs on the seismic response. Since we wish to examine the effect in terms of dowel shear forces, we need a method to estimate the ratio of the column shear forces in the new configuration as compared with the original configuration. Let the original configuration be represented by a cantilever beam with a unit lateral load applied at the end for which the statical deflections give a good approximation to the first mode shape of the beam. Using simple beam theory, we can show that the relationship between the maximum shear force S_I and maximum deflection Z_I of the tip is

$$S_I = \frac{3EI}{L^3} Z_I , \tag{37}$$

where EI is the bending stiffness of the beam. (The term $3EI/L^3$ is the commonly known spring stiffness for the cantilever.) We define this approximation for the original configuration as case I.

With the addition of the RCDs, the fuel column will behave differently. Under the proper conditions, it can behave as a beam fixed at both ends and loaded in the center which we will define as case II. For case II, the relationship between the maximum shear forces and the maximum deflection can be shown to be

$$S_{II} = \frac{192EI}{2L^3} Z_{II} . \tag{38}$$

---

*Ref. 41 shows that the coefficient of kinetic friction of graphite is in excess of 0.3 in a dry, high temperature, helium environment. The static coefficient is known to be higher than the kinetic value.

The boundary condition at the RCD end of the column can also be approximated as a pinned condition which we define as case III. In case III,

$$S_{III} = 33\sqrt{5}\ \frac{EI}{L^3}\ Z_{III}\ . \tag{39}$$

We can conclude that the relationship between maximum shear forces S developed in these cases are as follows.

$$\frac{S_{II}}{S_I} = 32\ \frac{Z_{II}}{Z_I} \text{ and } \frac{S_{III}}{S_I} = 24\ \frac{Z_{III}}{Z_I}\ , \tag{40}$$

where Z_I are the maximum relative displacements. Furthermore, the ratios of the first mode natural frequencies for these cases are such that*

$$\frac{\omega_{II}}{\omega_I} = 6.4 \text{ and } \frac{\omega_{III}}{\omega_I} = 4.4\ . \tag{41}$$

The question to be answered is, "How will the stiffening (an increase in the natural frequency) affect the shear force(s) developed during a seismic event?"

The approach that we will use in answering this question can best be illustrated by assuming that the exciting function (x) is harmonic. Figure 89 taken from Ref. 43 shows the response curves for a horizontally base excited single degree of freedom system. Referring to Fig. 89 we can see that if the original system (case I) is relatively flexible (i.e., $\omega/\omega_n >> 1$, where ω is the forcing frequency), then increasing the stiffness as in case (I), will decrease the ratio of ω/ω_n. Such a decrease will result in an increase in the shear forces developed. As an example, assume $\omega/\omega_{n_I} = 10$ and h (the damping ratio) = 0.3. Then,

---

*For example, see Ref. 42.

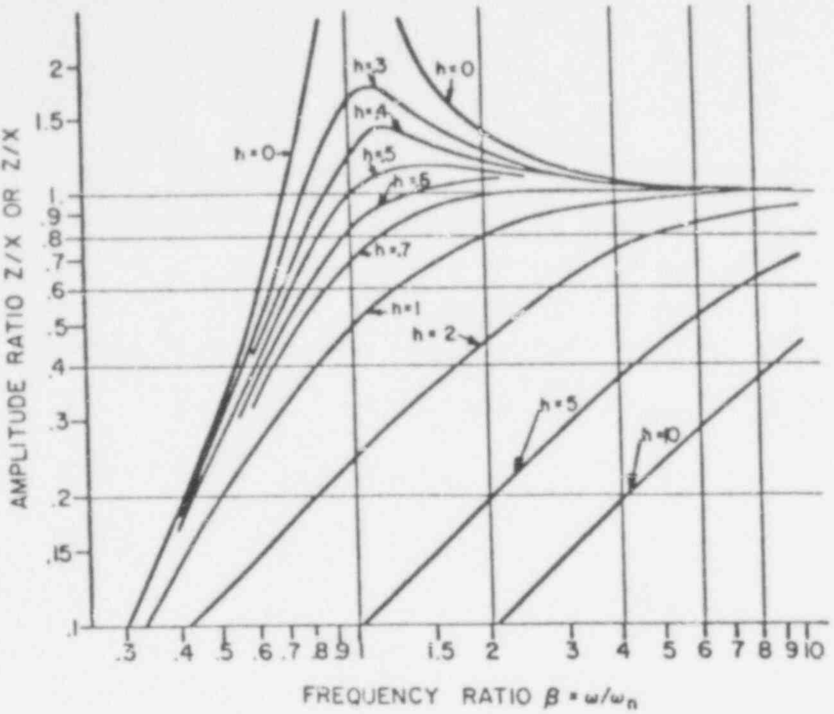

Fig. 89. Steady-state response of a seismic system to harmonic base displacement (from Ref. 43).

$$\frac{\omega}{\omega_{n_{II}}} = 1.56 .$$

From Fig. 89,

$$Z_I = X$$

where X is the input displacement and

$$Z_{II} = 1.48 X.$$

Then,

$$\frac{S_{II}}{S_I} = 32 \times \frac{1.48}{1}$$

whereupon

$$S_{II} = 47 S_I .$$

This example illustrates that the increase in shearing force can be quite severe under the proper conditions.

On the other hand, if the original system (case I) is near resonance or already a "stiff" system ($\omega/\omega_{n_I} \leqq 1$) then increasing the stiffness will decrease the shear force developed. For example, using case III data for which

$$\frac{\omega_{n_{III}}}{\omega_{n_I}} = 4.4 \ ,$$

assume we have

$$\frac{\omega}{\omega_{n_I}} = 1 \text{ and } h = 0.3 \ ,$$

then

$$\frac{\omega}{\omega_{n_{III}}} = 0.23 \ .$$

From Fig. 89 (extended) $Z_I = 1.6$ x and $Z_{III} = 0.03$ X. Then,

$$\frac{S_{III}}{S_I} = 24 \times \frac{0.03}{1.6}$$

whereupon

$$S_{III} = 0.45 \ S_I \ .$$

Clearly, the same analysis can be carried out if we work with an earthquake shaking function instead of harmonic excitation, provided we have the response curves similar to Fig. 89 in the form of a core support response spectra. In summary, if we approach the problem by assuming that the effect of the RCDs is to stiffen the fuel region, then whether pin shear forces will be reduced depends upon the natural frequency of the original system and the frequency spectra of the driving function.

c. Estimate of Fuel Column Frequencies

To apply this method to the FSV reactor core, we will describe the response of a core column in terms of a single degree of freedom or a single coordinate so that we can estimate the fuel column natural frequencies. Because of the relatively high friction between blocks and the relatively low known and predicted earthquake acceleration values, a fuel region can be expected to respond as seven base excited columns restrained to move together at their top (Fig. 90).

We can describe the lowest mode response for this system in terms of the tip response Z(t) relative to the base excitation $v_g(t)$. Let the absolute displacement of a fuel column be $v^a(x,t)$. Let the displacement of a point on the column relative to the base

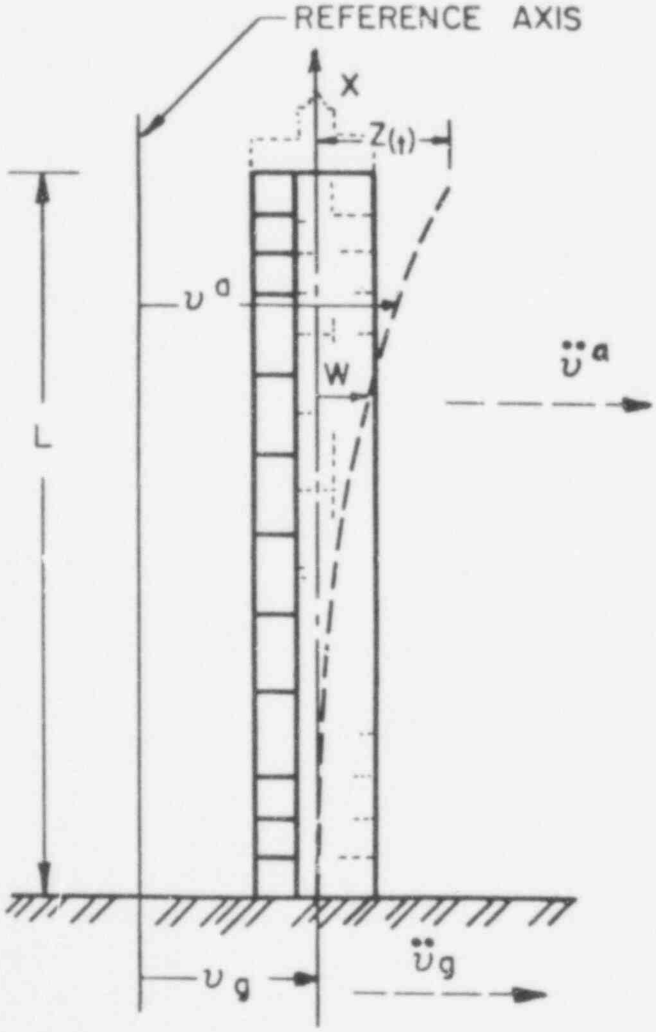

Fig. 90. Motion of a fuel region.

be w(x,t) (see Fig. 90). We will assume the predominate response to be in the first mode, and write

$$v^a(x,t) = v_g + w(x,t) \tag{42}$$

and that w(x,t) = ψ(x) Z(t) where ψ(x) is an admissible shape function. By writing the kinetic and potential energy expressions for all effects that we may wish to include, and applying Hamilton's principle to the result, we can develop an equation of motion of the form

$$m_{eff}\, Z(t) + k_{eff}\, Z(t) = - m_g\, v_g(t) - p_{eff}(t) \ , \tag{43}$$

where

m_{eff} = the effective mass,

k_{eff} = the effective stiffness, and

p_{eff} = the effective loading.

In this analysis, we will include a number of different terms in the effective stiffness so that we can assess their relative effects on the response. Thus, in the above equation,

$$k_{eff} = k_b = k_g - k_a - k_p + k_{sc} \ , \tag{44}$$

where

$$k_b = EI \int_0^L [\Psi''(x)]^2\, dx \tag{45}$$

is the bending stiffness of the column and

$$k_g = \int_0^L W(x)\,[\Psi'(x)]^2\, dx \tag{46}$$

is the geometric stiffness [W(x) is the axial load as a function of the length because of the weight of the column]. The term

$$k_a = N \int_0^L [\Psi'(x)]^2 \, dx \tag{47}$$

is an added geometric stiffness term accounting for the constant axial load (N) that occurs because of the keyed plenum blocks, RCDs, etc. The term

$$k_p = \int_o^L q(x) [\Psi(x)]^2 \, dx \tag{48}$$

is a stiffness effect because of the lateral pressure q(x) across a fuel column. The term

$$k_{sc} = \frac{\alpha^2 E^2 I^2}{A \; G} \int_o^L [\Psi'''(x)]^2 \, dx \tag{49}$$

is a term that represents the shear stiffness of the column. The two terms m_{eff} and m_g given by

$$m_{eff} = \int_o^L m(x) [\Psi(x)]^2 \, dx \tag{50}$$

and

$$m_g = \int_o^L m(x) \; [\Psi(x)] \, dx \; , \tag{51}$$

represent an effective mass for the fuel column and a mass-like term to convert the base motion to an effective force, respectively. In the above,

E = Young's modulus for graphite,
I = the cross-sectional moment of inertia,
$q(x)$ = the lateral pressure loading on the column,
α = the geometric shear correction factor,
A = the cross-sectional area of a fuel column,
G = the shear modulus of elasticity, and
$m(x)$ = the mass per unit column length.

By including all these terms separately, we can assess their relative effects on the undamped natural frequency and bound the possible frequencies such that the method that has been described can be applied.

Table XIX gives the result of carrying out the details of the analysis and using FSV column parameters with $\Psi(x) = 1\text{-}\cos(\pi X/2L)$, where

$$\omega = \sqrt{\frac{k_{eff}}{m_{eff}}} .$$

We have also included the irradiation effect on Young's modulus by taking the extreme values for H-327 graphite as given in Ref. 44.

d. Application to the FSV Core

Using the bounding values of natural frequency as 16 rad/s and 29 rad/s, and looking at the effects of the boundary conditions

TABLE XIX

FUEL COLUMN NATURAL FREQUENCIES (1/s)

Graphite Material Modulus H-327	ω_1	ω_2	ω_3	ω_4	ω_5
1.3×10^6 psi (unirradiated)	16.27	16.21	16.19	17.10	17.15
3.9×10^6 psi (irradiated)	28.19	28.15	28.14	28.68	28.93

ω_1 = bending only,

ω_2 = bending plus geometric stiffness due to weight,

ω_3 = bending plus geometric stiffness due to weight and end loads,

ω_4 = bending plus geometric stiffness and lateral pressure effects, and

ω_5 = bending plus geometric stiffness plus lateral pressure effects plus shear correction.

of cases II and III, we can compare the idealized ratios of maximum shearing stress in the new configuration (with RCDs) to the original configuration (without RCDs) during an earthquake just as in the harmonic excitation examples provided that we use the response curves for an earthquake exciting function.

The response spectra for the FSV core support floor is not available. However, two spectra are available that should allow a satisfactory estimate of the relative effects of the installation of the RCDs.

The first response spectra that we have used is shown in Fig. 91 by the dashed lines. This response spectra was obtained in the following manner. The original (solid line) is for the bottom head of the PCRV of a larger plant as given in GASSAR-6.[45] This response spectra was shifted to the right (dotted line) so that the peak response occurs at a period of 0.5 s to correspond to the measured natural period of the FSV PCRV as reported in Ref. 46. Note that because we are only interested in the relative effect of the RCDs, we are not concerned about the magnitudes in Fig. 91, and unless some very unusual "filtering" occurs leading to an extremely broad band peak response, the dotted spectra should be

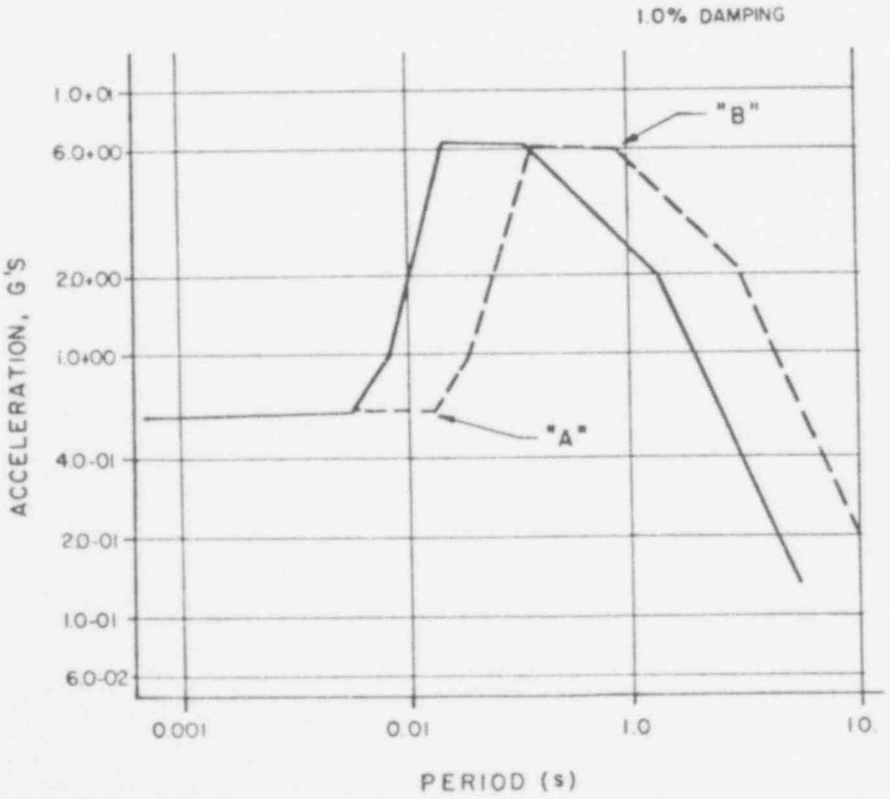

Fig. 91. Horizontal floor response spectra, safe shutdown earthquake.

representative of the PCRV for the FSV plant. Table XX, column 3, shows the results of the calculations using the dashed spectra of Fig. 91.

TABLE XX

EXPECTED CHANGE IN COLUMN MAXIMUM SHEAR FORCES

Case	Bounding natural frequency (rad/s)	Column maximum shear force
Case I	$\omega_I = 16$	S_I
(Cantilever column - i.e., no RCDs)	($T_I = 0.39$ s)	
	$\omega_I = 29$	S_I
	($T_I = 0.22$ s)	
Case II	$\omega_{II} = 6.4 \times 16$	Using Fig. 91
(RCDs produce	$= 102$	$S_{II} = 0.08\ S_I$
fixed condition	($T_{II} = 0.06$ s)	Using Fig. 92
at top of column)		$S_{II} = 0.47\ S_I$
	$\omega_{II} = 6.4 \times 29$	Using Fig. 91
	$= 185$	$S_{II} = 0.28\ S_I$
	($T_{II} = 0.03$ s)	Using Fig. 92
		$S_{II} = 0.19\ S_I$
Case III	$\omega_{III} = 4.4 \times 16$	Using Fig. 91
(RCDs produce	$= 70$	$S_{III} = 0.13\ S_I$
pinned condition)	($T_{III} = 0.09$ s)	Using Fig. 92
		$S_{III} = 0.58\ S_I$
	$\omega_{III} = 4.4 \times 29$	Using Fig. 91
	$= 127$	$S_{III} = 0.45\ S_I$
	($T_{III} = 0.05$ s)	Using Fig. 92
		$S_{III} = 0.99\ S_I$

If the actual FSV core plane response spectra is shifted even further to the right on Fig. 91, the fuel column shear stress will continue to be reduced by the installation of the RCDs with one exception. If the spectra is shifted so far to the right that point "A" (Fig. 91) is at a period of 0.22 s (ω = 29 rad/s) or greater, then the maximum shear forces could increase by 28% provided that the original natural frequency of the fuel column (ω_I) is as high as 29 rad/s and also that the RCDs result in a pinned end condition. Such conditions are not deemed likely for this structure.

We also note that if the true response spectra is shifted to the left (Fig. 91) so that point "B" is at a period of 0.09 s or less, then the shear forces may also be increased by the installation of the RCDs.

Figure 92 shows the floor response spectra for the FSV reactor and turbine building floor slabs. The dotted line shows the previously discussed response spectra of Fig. 91 scaled down to 1.5 g. It is likely that much of the high frequency (low period) would be

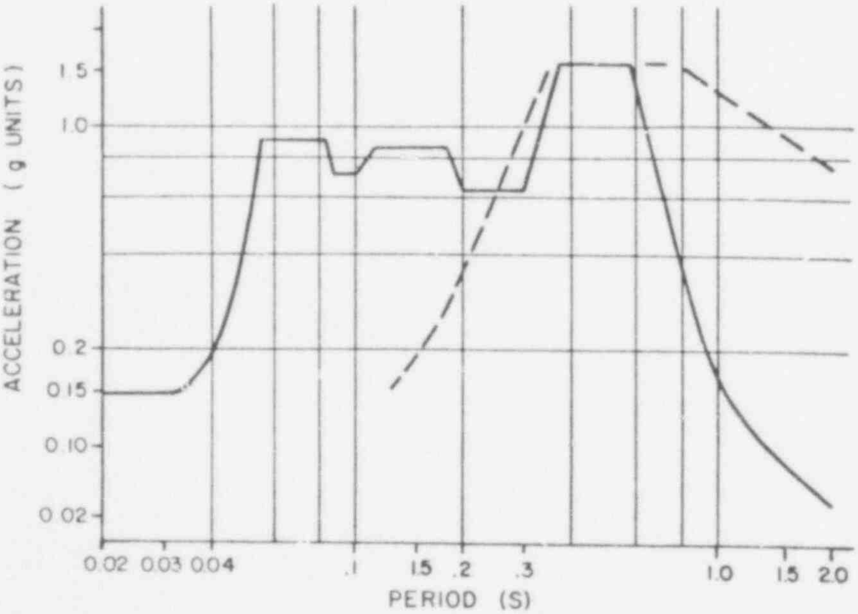

Fig. 92. Reactor bottom head horizontal response spectra for operating basis earthquake.

filtered out of a response spectra that applied only to the core support structure, and would appear much as the dashed line. However, we can use Fig. 92 as it is to estimate the effect of the RCDs on the maximum shear stresses. These results are also shown in Table XX, column 3.

e. Fuel Element Impact Velocities and Forces

Vibration studies[47,48,11] on core-like structures (stacked blocks) suggest that by far the largest forces produced during a seismic event are the forces produced by impact of block against block. In the FSV reactor even though the initial response of the core may be column bending, impact between a core block column and the side wall may be expected to occur (assuming the relative displacement response is greater than the gap between a boundary column and the side wall) and once the first impact occurs it will be followed by numerous block-to-block impacts. The vibration studies referred to above indicate that the larger the clearance between elements, the larger the impact forces.

The proposed RCDs will limit the accumulation of gaps between the fuel regions and therefore may limit the intensity of impact forces. Figure 93 is a model of the FSV core without RCDs (case I). If we assume an impulsive ground motion to the right, the fuel region on the left (#1) will impact the permanent reflector block after undergoing a relative displacement of approximately 0.12 in. The impact sequence will then propagate from left to right. Figure 94 is a model of the FSV core with RCDs in place (case II). If we again assume an impulsive ground motion to the right, the fuel region on the right (#7) will impact on the RCD after undergoing a relative motion of approximately 0.030 in. (0.150-0.120). The impact sequence will then propagate from right to left.

The analysis which follows illustrates the difference in the magnitude of the impact forces involved in the two cases.

Assume that the relative displacement (Z) and the relative velocity ($\dot{Z}$) of the core regions are as shown in Fig. 95. These curves represent the relative response motion that would be produced by the seismic motion x(t) at the core base for the case where no contact between core regions is allowed. Now, assume that

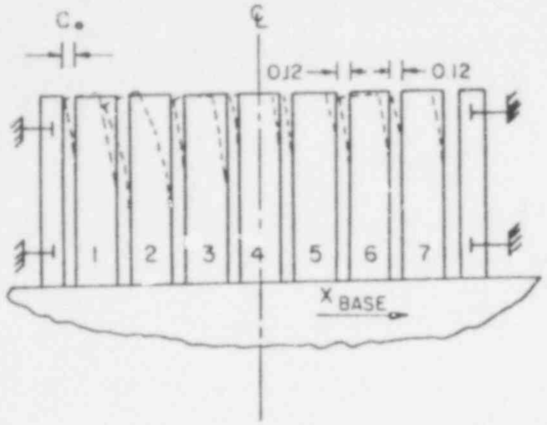

Fig. 93. Model illustrating initial impact sequence without RCDs.

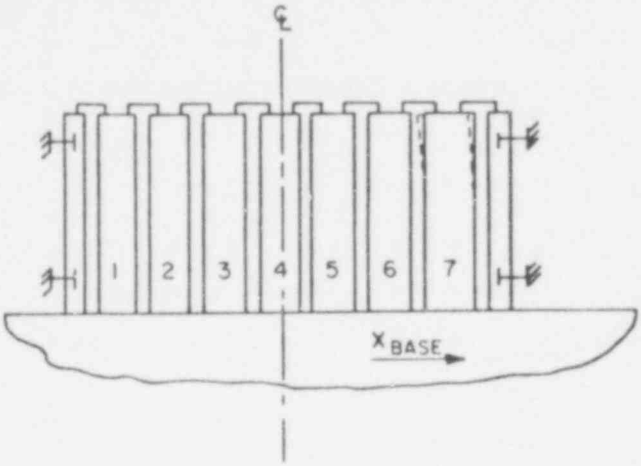

Fig. 94. Model illustrating initial impact sequence with RCDs.

in case I (Fig. 93, no RCDs) this initial (before contact) relative motion is such that contact occurs at some point to the left of line a-a in Fig. 95, say at pt. #1; then, the initial impact velocity is $\dot{Z}_1$. With RCDs present (case II) the initial contact will occur at pt. #2 with an impact velocity of $\dot{Z}_2$. Since forces are proportional to impact velocities, forces will be reduced.

If in case I (no RCDs) the first impact is to the right of line a-a, then the effect of adding RCDs (case II) could be to either increase or decrease the impact force. However, in general, for a system capable of large relative motion excursions without stops (a "soft" system), constraint involving the smallest clearance gaps will result in the lowest impact forces. The computations previously referred to in this report for the natural frequency of the FSV fuel columns show that the FSV is a "soft system" relative to the appropriate response spectra. Consequently, the addition of the RCDs can be expected to decrease the impact velocities and thus the impact forces.

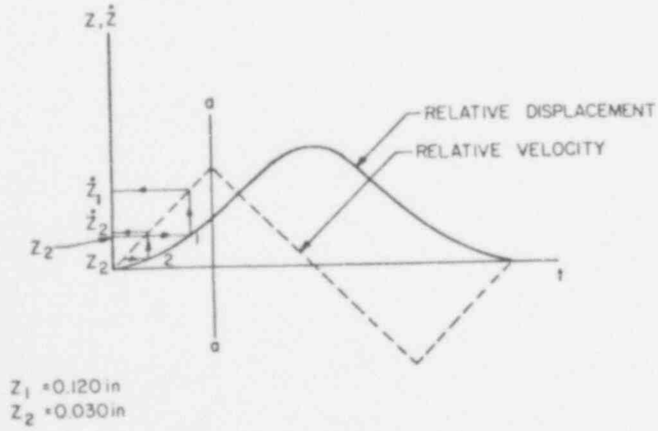

Fig. 95. Illustration for effects of increased displacement constraint on impact velocities.

f. Summary

With regard to the seismic response of the FSV core, the addition of the RCDs can be expected to decrease the maximum dowel shear forces as shown in column 3 of Table XX. One exception is noted. This exception involves FSV being a very "soft" (low natural frequency) or a very "hard" (high natural frequency) system. In these cases, maximum shear forces could increase. Based on general knowledge of large massive structures of the FSV type, these exceptions are not deemed credible. For motions produced when fuel block slippage occurs, the fuel element impact velocities and impact forces will also be decreased.

In summary, the addition of the RCDs should serve to make the FSV core a more seismically safe structure.

B. Phenomena Modeling, Systems Analysis and Accident Delineation

(P. A. Secker, Q-6)

Fission Product Release and Transport

(L. M. Carruthers, Q-13)

The DASH code is a multicomponent radioactive decay computer program that incorporates diffusion in the analysis. A preliminary version of DASH was completed in September 1978, and a first draft of a report was issued.[49] Since then, in checking out the code on "real" test problems, several errors and shortcomings in the code have been brought to light and major modifications to the code have been made. These include a rederivation of the equations used in DASH, a modification of the code to allow for source terms, inclusion of all system-dependent routines with the code, and modification of the graphics to use the DISSPLA system[50] so that the program is more exportable. Finally, a specific problem that studies the decay and diffusion of ^{90}Sr in graphite was modeled with DASH.[51] This problem is described below. The DASH report is now complete and in the final stages of publication.

a. Analysis of Relative Errors

The equations for DASH have undergone a number of revisions since they were originally specified. The basic equation for diffusion with decay and source terms is

$$V_k \frac{d\vec{C}_k}{dt} = \bar{A}_k \vec{C}_{k+1} - \bar{A}_k \vec{C}_k + \bar{B}_k \vec{C}_{k-1} - \bar{B}_k \vec{C}_k + V_k \vec{S}_k - V_k \lambda_k \vec{C}_k , \tag{52}$$

where $\vec{C}_k$ is the concentration of species (as a vector) in cell k, $\vec{S}_k$ is the source term, λ_k is the decay parameter, and V_k is the volume of the k^th cell.

The initial specification for the $\bar{A}_k$, $\bar{B}_k$ coefficient matrices was given[24] as

$$\bar{A}_k = \frac{2A_{k+1}^{\ 2}}{D_k^{-1} V_k + D_{k+1}^{-1} V_{k+1}} \tag{53}$$

and

$$\bar{B}_k = \frac{2\ A_k^{\ 2}}{D_{k-1}^{-1} V_{k-1} + D_k^{-1} V_k} , \tag{54}$$

where A_k is the area of the k^th cell and D_k the diffusion coefficient in the k^th cell.

Subsequently, these equations were rederived[52] with a different form:

$$\bar{A}_k = \frac{2A_{k+1/2}\ D_k (D_k + D_{k+1})^{-1}\ D_{k+1}}{\Delta r_k} \tag{55}$$

and

$$\bar{B}_k = \frac{2\ A_{k-1/2}\ D_{k-1}\ (D_{k-1} + D_k)^{-1}\ D_k}{\Delta r_{k-1}} . \tag{56}$$

Looking at the diagram for the mesh representation, Fig. 96, we see that Eqs. (55) and (56) suffer from an intuitive error in that the treatment of the cells on either side of a given cell is asymmetric. One can avoid this difficulty by writing

$$\bar{A}_k = \frac{2\ A_{k+1/2}\ D_k (D_k + D_{k+1})^{-1}\ D_{k+1}}{\Delta r_k} \tag{57}$$

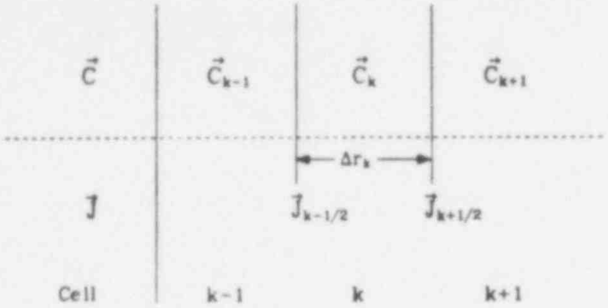

Fig. 96. Discrete mesh function representation.

and

$$\bar{B}_k = \frac{2\ A_{k-1/2}\ D_{k-1}\ (D_{k-1} - D_k)^{-1}\ D_k}{\Delta r_k}\ , \tag{58}$$

or

$$\bar{A}_k = \frac{4\ A_{k+1/2}\ D_k (D_k + D_{k+1})^{-1}\ D_{k+1}}{\Delta r_k + \Delta r_{k+1}} \tag{59}$$

and

$$\bar{B}_k = \frac{4\ A_{k-1/2}\ D_{k-1} (D_{k-1} + D_k)^{-1}\ D_k}{\Delta r_{k-1} + \Delta r_{k+1}}\ . \tag{60}$$

A simple test problem was set up to check these alternatives. A decay chain A→B was calculated for a four-cell slab test problem with each cell of 1 cm^3 volume. The diffusion constant used was 10^{-4} cm^2/s for both isotopes and the decay constant was set to $10^{-4}/s$ for A and 0.0 for B. The boundary conditions were reflective and an initial concentration of 10^{10} was used for A. After a time of one day, the total number of atoms present was calculated using each of the four sets of equations (53-60). The relative error in each case was 4.3×10^{-14}.

The boundary between cells 2 and 3 was moved from 2.0-1.01 cm and the exercise repeated. The relative errors in the four cases were 1.022×10^{-11}, 3.37×10^{-10}, 0.327×10^{0}, and 1.016×10^{-11}. Since the set of Eqs. (55-56) is asymmetric, we are left with a choice between Eqs. (53) and (54) and (59) and (60). To further test Eqs. (53) and (54) and (59) and (60), we set the boundary still closer to 1.0 and varied D in cells 1 and 2 vs 3 and 4. Results of the calculations are given in Table XXI. We thus selected Eqs. (59) and (60) for further use.

For a uniform mesh, $D = 10^{-4}$ cm^2/s, the relative error varies smoothly with λ as shown in Table XXII. Similar results for constant λ, varying D, are shown in Table XXIII.

b. Holdup of ^{90}Sr by Graphite

A parameter study of the release and diffusion decay of isotopes of strontium in a simplified one-dimensional slab model of an HTGR core block was carried out. A typical element of the core block and the coolant hole was modeled as shown in Fig. 97; the dimensions of each region were taken from Ref. 53.

The decay chain used for the test problem was

$$^{90}Sr \longrightarrow {}^{90}Y \longrightarrow {}^{90}Zr$$

with yields and decay constants shown in Table XXIV. The boundary conditions used reflection at x = 0 and zero concentration at x = 1.05.

TABLE XXI

TEST PROBLEM RESULTS

D of cell 1, 2	1.0×10^{-4} cm^2/s	1.0×10^{-4} cm^2/s	1.0×10^{-4} cm^2/s
D of cell 3, 4	1.0×10^{-4} cm^2/s	1.0×10^{-2} cm^2/s	1.0 cm^2/s
Boundary	1.000 001 cm	1.000 001 cm	1.000 001 cm
Relative Error Eqs. (53) and (54)	8.84×10^{-8}	5.06×10^{-6}	2.20×10^{-4}
Relative Error Eqs. (59) and (60)	8.84×10^{-8}	1.17×10^{-7}	2.23×10^{-7}

TABLE XXII

RESULTS FOR UNIFORM MESH, $D = 10^{-4}\ cm^2/s$

λ	Relative Error
0.0	7.9×10^{-14}
10^{-4}/s	4.9×10^{-14}
10^{-2}/s	1.32×10^{-11}
1.0/s	5.98×10^{-10}
10^{2}/s	2.30×10^{-8}
10^{4}/s	8.22×10^{-6}

TABLE XXIII

RESULTS FOR UNIFORM MESH, $\lambda = 10^{-4}/s$

$\frac{D}{cm^2/s}$	Relative Error
10^{-10}	0.6×10^{-14}
10^{-4}	4.9×10^{-14}
10^{-2}	2.10×10^{-11}
1.0	2.30×10^{-9}
10^{2}	6.91×10^{-8}
10^{4}	8.52×10^{-6}

The approach was to use data from the work of Appel and Roos[53] and calculate the distribution of the isotopes of this decay chain in the fuel matrix and structural graphite. The source term for ^{90}Sr was taken to be 7.3×10^{9} atoms/(cm^3s) as given in Ref. 53. The source terms for the other isotopes in the chain were taken in proportion to the yields of Table XXIV.

The temperatures change from the beginning to the end of

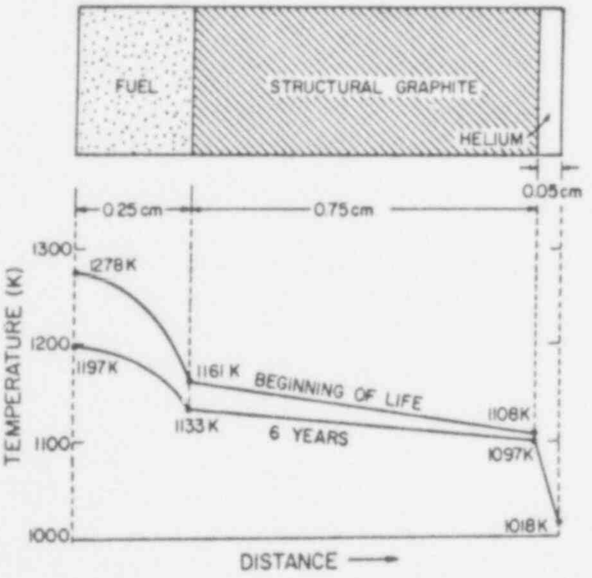

Fig. 97. Fuel-graphite-helium calculational model and beginning-of-life and six-year temperature profile.

TABLE XXIV

YIELDS AND DECAY CONSTANTS FOR ^{90}Sr CHAIN

Isotope	Yield	Decay Constants/s
^{90}Sr	5.77	7.844×10^{-10}
^{90}Y	5.77	2.994×10^{-6}
^{90}Zr	0.0	1.0×10^{-20}

the calculation (six years duration) is shown in Fig. 97. Temperatures at intermediate times are calculated by linear interpolation.

Data are given in Ref. 54 for the diagonal terms of the 3 x 3 diffusion matrix for the three species making up this problem. For the Arrhenius representation,

$$-\log_{10} D = A + 1000\ B/T; \tag{61}$$

the coefficients A and B are given in Table XXV.

Appel and Roos[53] assumed that the concentration of ^{90}Sr drops by a factor of 300 at the fuel-graphite interface corresponding to the distribution coefficient between the two substances. This was handled in DASH by putting a small region (10^{-5} cm thick) at the boundary and adjusting the diffusion coefficient of the region introduced until the ratio of ^{90}Sr concentrations was 300. Except for this boundary region, the mesh spacing was taken as 0.05 cm throughout.

To compare with the work of Appel and Roos, the concentrations of ^{90}Sr were calculated at the end of one year using the two sets of diffusion coefficient data given in Table XXV. It should be noted that the strontium diffusion coefficients for the two sets of data differ by a factor of 240 at 1 000°C.

It is apparent in looking at Table XXVI that the ^{90}Sr concentration in the fuel matrix, as given by Appel and Roos, is larger than that which a source of 7.3×10^9 atoms/(cm^3) would produce in one year with no diffusion. Further investigation leads us to believe that Appel and Roos used a source of 7.3×10^{11} atoms/(cm^{3}s)

TABLE XXV

DIFFUSION COEFFICIENT PARAMETERS

Specie	A	B
^{90}Sr (Ref. 53)	- 2.477	13.1
^{90}Sr (Ref. 54)	0.34	6.5

634 215

TABLE XXVI

COMPARISON OF ^{90}Sr CONCENTRATIONS AT 1 YEAR

Position (cm)	Material	Results from Ref. 53 (atoms/cm^3)	DASH Results: Ref. 53 Coefficients	DASH Results: Ref. 54 Coefficients
0.125	Fuel	1.7×10^{18}	2.27×10^{17}	1.80×10^{17}
0.30	Graphite	3.0×10^{15}	5.43×10^{14}	5.69×10^{14}
0.50	Graphite	6.0×10^{14}	1.06×10^{14}	4.31×10^{14}
0.75	Graphite	1.0×10^{13}	4.63×10^{12}	2.23×10^{14}

which probably explains the difference between DASH and the Appel and Roos results.

A more realistic treatment of the source[55] allows for an increased source strength in later years caused by an increase in fuel particle failure rates. We assumed that the initial source [$S_o = 7.3 \times 10^9$ atoms/(cm^{3}s)] increases with time such that S_o is used for the first year, $2S_o$ for the second year, $3S_o$ for the third year, etc. Numerical results for ^{90}Sr concentration are shown in Fig. 98 and listed in Table XXVII. The diffusion coefficient data of Ref. 54 was employed in this calculation. Comparison of the amount of ^{90}Sr produced with amount retained in the fuel and structural graphite indicates that even at six years almost half of this species is held up by the presence of the graphite.

634 216

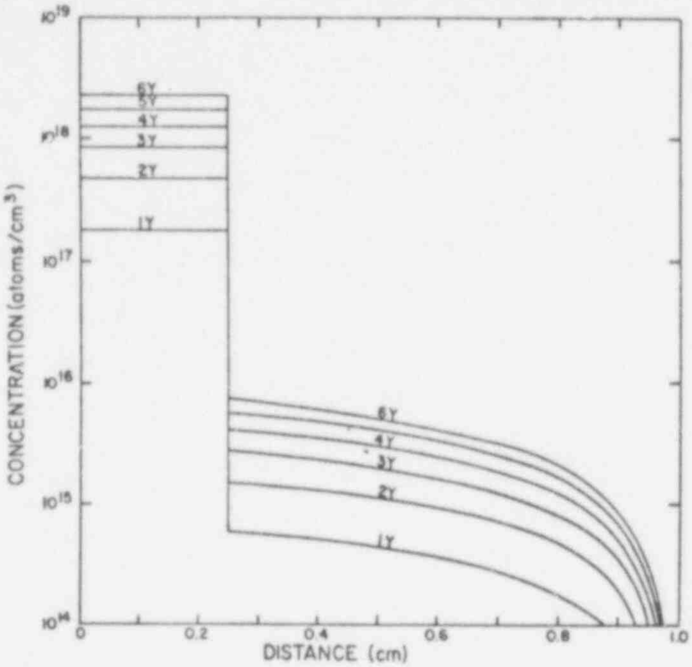

Fig. 98. ^{90}Sr concentration profiles.

TABLE XXVII

^{90}Sr CONCENTRATION IN FUEL MATRIX WITH INCREASING SOURCE

Time (y)	Total Source Units	Fuel Concentration (atom/cm^3)	Fuel Concentration If No Diffusion (atom/cm^3)	Fraction Retained
1	1	1.80×10^{17}	2.30×10^{17}	0.78
2	1 + 2 = 3	4.74×10^{17}	6.91×10^{17}	0.69
3	3 + 3 = 6	8.45×10^{17}	1.38×10^{18}	0.61
4	4 + 6 = 10	1.27×10^{16}	2.30×10^{18}	0.55
5	5 + 10 = 15	1.75×10^{18}	3.46×10^{18}	0.51
6	6 + 15 = 21	2.27×10^{18}	4.84×10^{18}	0.47

V. GCFR CORE DISRUPTIVE TEST PROGRAM

(D. L. Hanson, Q-13)

The basic assembly module of the GCFR core is a subassembly comprising 264 fuel rods, 6 corner support rods, 1 central rod (instrumented), and their surrounding duct. The duct is a right hexagonal cylinder. The purposes of this out-of-pile experimental program are to demonstrate the behavior of one of these GCFR core modules in the event of a loss-of-core coolant flow or pressure and subsequent shutdown of reactor power to the level resulting from decay heat alone. The loss-of-flow accident (LOFA) will be simulated in the Duct Melting and Fall-away Test (DMFT) and the loss-of-pressure accident will be simulated in the Depressurized Accident Condition (DAC) test. These experiments require the development of an electrically heated fuel rod simulator capable of delivering 2 kW of power while operating at surface temperatures exceeding 1 650 K, and the development of a fixture that will permit operation of an ensemble of 450 such rods (1 core module thermally guarded by segments of the 6 surrounding modules) at helium pressures up to 9.1 MPa. This Guarded Core Module (GCM) fixture will be the largest in a sequence of four test fixtures developed in the course of this program. The others are:

- Ten-inch, single-rod fixture,
- One-meter, seven-rod fixture, and
- Full-length Subgroup (37-rod) fixture.

The GCM fixture will be used first for the DMFT and subsequently for the DAC test.

A. Program Planning

(D. L. Hanson, Q-13)

Having already decided on a course of action regarding the development of spacer grids for FLS 2 in the last quarter, and

634 218

while awaiting a GAC decision regarding core upflow or downflow to be announced early in the next quarter, no further program planning was undertaken during this quarter.

B. Analysis

(D. Bennett and D. L. Hanson, Q-13)

1. Instrumentation

Further improvement of the HP 3052A data acquisition system with the HP 9825 controller consisted of developing techniques in both software and hardware that could significantly increase the acquisition rates observed during FLS-1 tests and benchmarking tests. Those techniques applicable to a scanning test situation are summarized by the peripheral equipment involved as follows:

HP 3455 digital voltmeter:

- external triggering from scanner,
- 5 digit resolution specified rather than 6 digit,
- auto calibration mode off, and
- auto range capabilities can be effectively utilized if care is used to group data signals by voltage range.

HP 3437 systems voltmeter:

- external triggering from scanner.

HP 3495 scanner:

- deletion of clear ("C") and execute ("E") commands from format statement.

Available memory can be increased by using array rather than string variable storage.

Original FLS-1 tests required a complex and time costly interleaving of data acquisition and power control. Planned expansion of the present system with the addition of a new HP 9825 controller and HP 3052A system (DVM, real-time clock, flexible disk drive, scanner with high speed, 20-channel relay cards) allows:

1. separation of data acquisition and power control functions,
2. a total capacity of over 200 data channels,
3. the DVM to operate at 19-20 channels/s with external triggering and 5 digit resolution, and
4. the SVM to operate in a scanning mode at upwards of 60 channels/s with 3 digit resolution.

The increased data acquisition rates and expanded instrumentation will provide greater flexibility and documentation of future GCFR tests.

2. FLS-2 Spacer Grids

The required geometrical characteristics were quantified for the wave-spring spacer grid concept that will be utilized in FLS-2. A number of calculations were also made to define the geometry of the special tooling required to produce these spacers.

C. Design

(D. Bennett, D. L. Hanson, and A. J. Giger, Q-13; and J. Churchman, SD-2)

1. Test Cell No. 1 Modifications

At this time, all pressure vessel ports are oriented on a 0-180° axis. Because of work pit and gas port priorities, the x-ray port may necessitate a slight modification to the high bay east wall for viewing access. However, interior layouts for equipment and test assemblies continue to address this and other location problems.

2. FLS-2 Spacer Grids

The spacer-grid design concept chosen for use in the FLS-2 test assembly consists of three identical sets of parallel-axes wave springs stacked so that the spring axes in each set are rotated 120° from those of the other two sets. Each set of wave springs provides metastable constraint at two diametrically opposed points on each rod. Three of these sets of springs, stacked together as described, provide stable constraint by six contact points distributed uniformly around the circumference of each rod and over three axial stations. Ten of these three-set stacks are required in the FLS-2 test assembly. A nominal diametral clearance of 0.1 mm between the springs and the rods was chosen for the FLS-2 spacers. We believe that this amount of clearance, although only half of that used in FLS-1, will result in minimal rod/spacer-grid interaction because of the large rotational compliance provided by the wave-spring spacer.

3. 271-Rod GCM Experiment

Detailing was completed on the support frame; but drawings have not yet been released. A possible restriction of the 10.67 m hook height of the crane in the assembly and test building caused some concern about protrusion height above the pressure vessel top cover. This now appears to be resolved with a full 10.67 m being available. In addition, a 1.2 m pit has been added. Enough lift height is now available to make it feasible to consider an externally manifolded support frame. This would require redesign.

For the sake of simplified assembly, it was decided to weld the support frame to the top cover. All the instrumentation pass-throughs and the top main electrical connection will be completed before the experiment is lowered into the pressure vessel. Some uncertainties occur in aligning the test package in the pressure vessel using this method but it is felt they can be resolved.

Because of the unknown thermal environment of the experiment support plate, a cooled version has been designed. It is probable that this will also be inexpensive since the exotic materials required for an uncooled plate would be eliminated. Nitronic 33, a nitrogen strengthened, low-nickel, austenitic stainless, has been tentatively selected for the plate. This material has a high weld efficiency, an advantage for this design, and a yield strength of 379 MPa.

D. Procurement and Fabrication

(R. Ortega, P. Renfro, D. Bennett, D. L. Hanson, A. J. Giger, and W. E. Dunwoody, Q-13)

1. Test Cell No. 1 Modifications

Construction on the 4 x 4.9 x 12.2 m high bay modification to test cell no. 1 (WA-16-TA-46) was slightly delayed because of an unexpected requirement to provide additional workspace beneath the 15-ton pressure vessel. A 1.4 x 2.4 m x 1.2 m deep pit was subsequently decided upon and has been constructed as requested.

The order for the 10-ton crane required for DMFT and DAC assembly has been placed. Delivery is expected in mid-July 1979.

2. Instrumentation

Orders have been placed for an additional Hewlett-Packard 3052A data acquisition system to be used in conjunction with our existing system. This will provide increased speed and capacity sufficient to satisfy the requirements for DMFT and DAC testing.

3. FLS-2 Spacer Grids

Fabrication of a full complement of wave-spring spacer grids for FLS-2 is now complete. The special tooling developed for this process consists of:

1. Wave-spring stretch-forming dies (Fig. 99),
2. Wave-spring shear (Fig. 100),
3. Wave-spring end-tab blanking die (Fig. 101),
4. Frame-segment brake (Fig. 102),
5. Frame welding fixture (Fig. 103),
6. Frame drilling jig (Fig. 104), and
7. Wave-spring welding fixture.

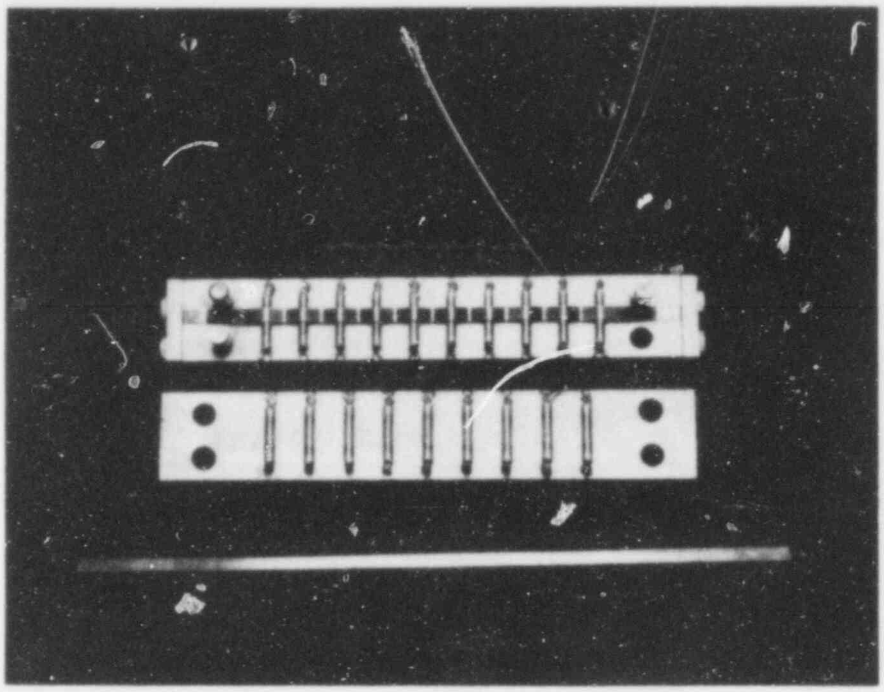

Fig. 99. Wave-spring stretch-forming dies.

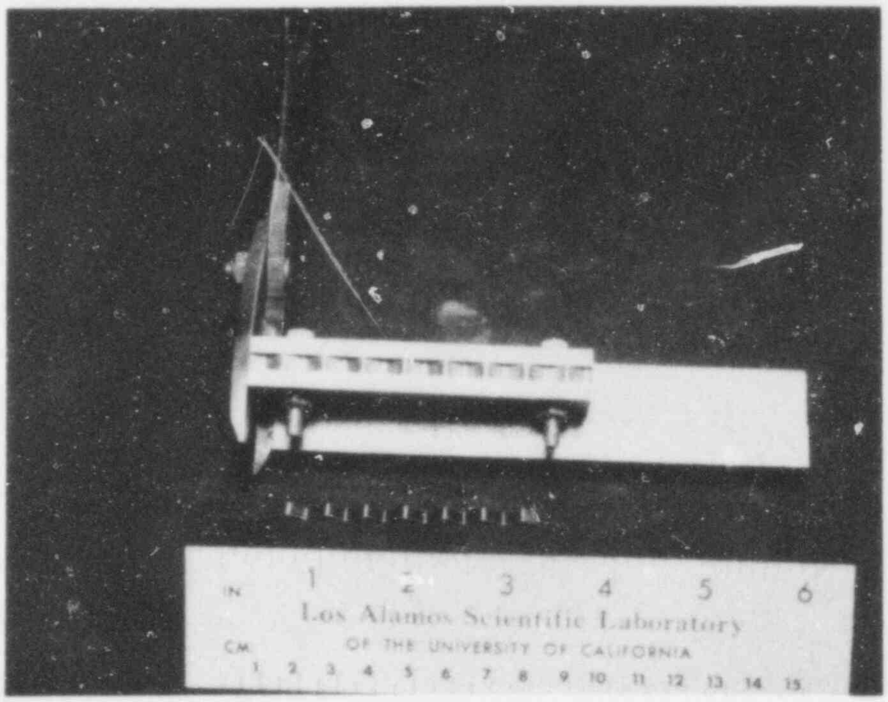

Fig. 100. Wave-spring shear.

634 223

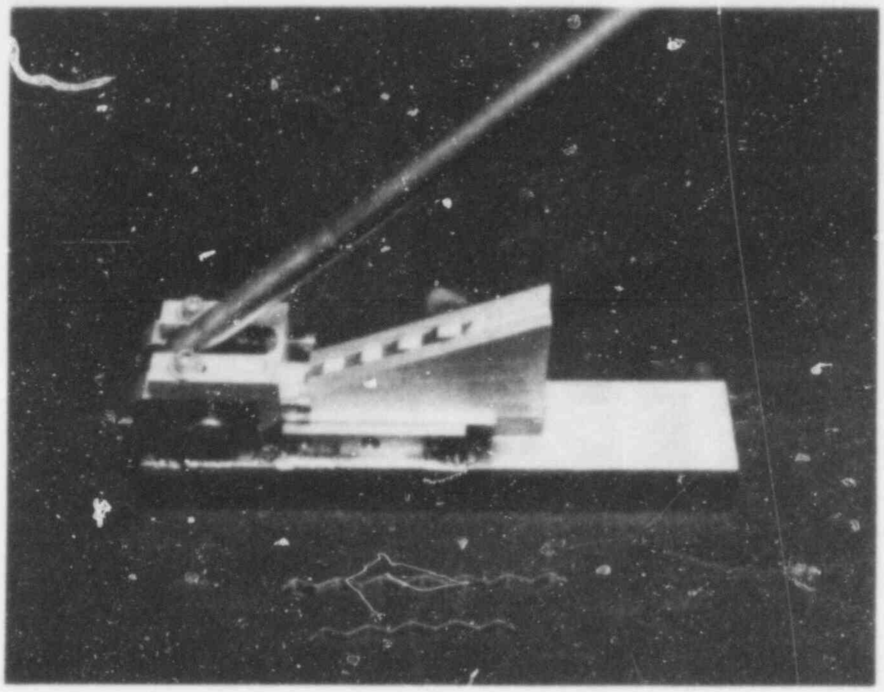

Fig. 101. Wave-spring end-tab blanking die.

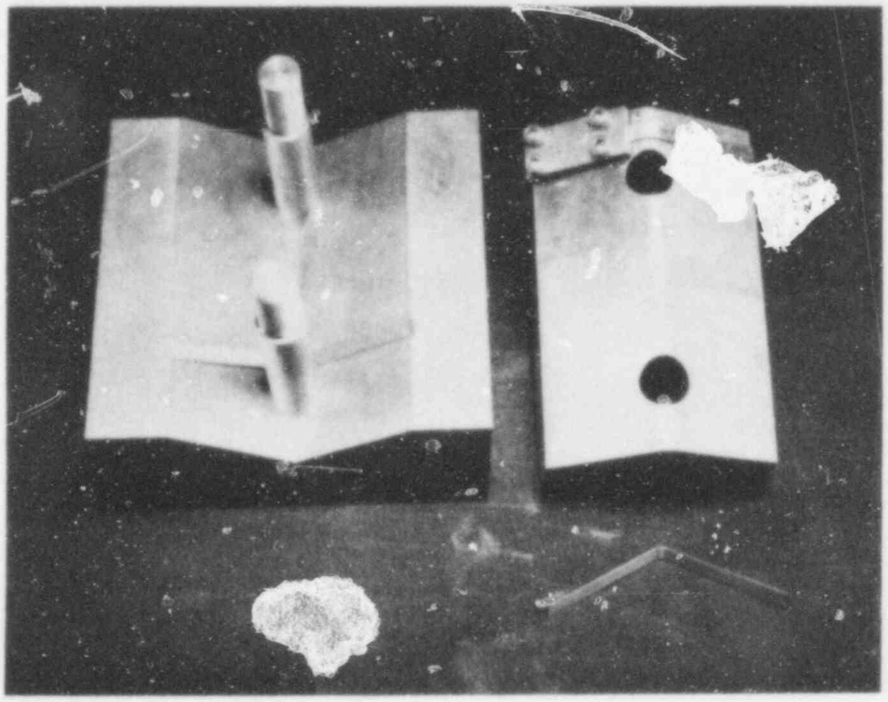

Fig. 102. Frame segment brake.

634 224

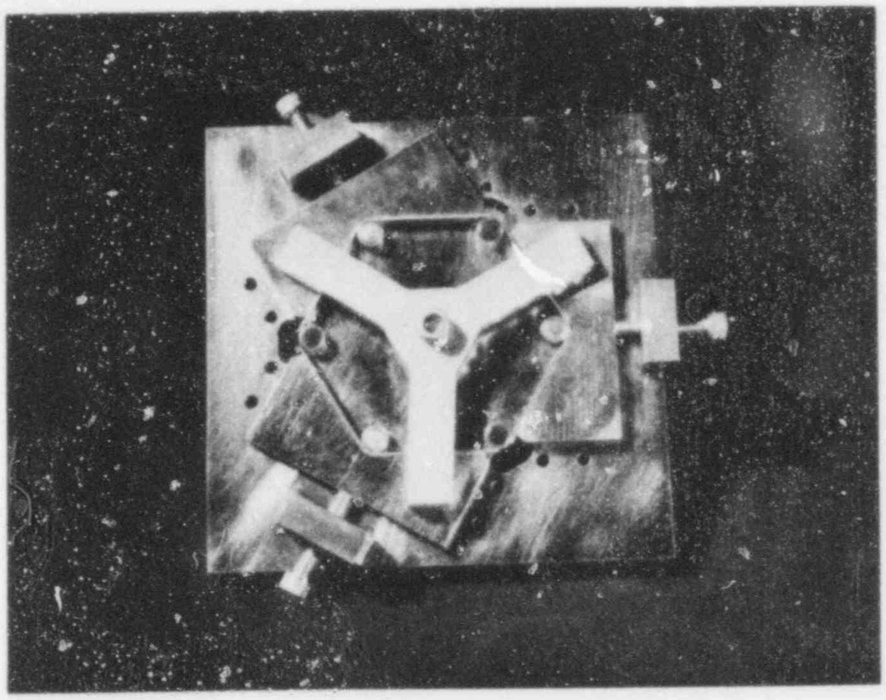

Fig. 103. Frame welding fixture.

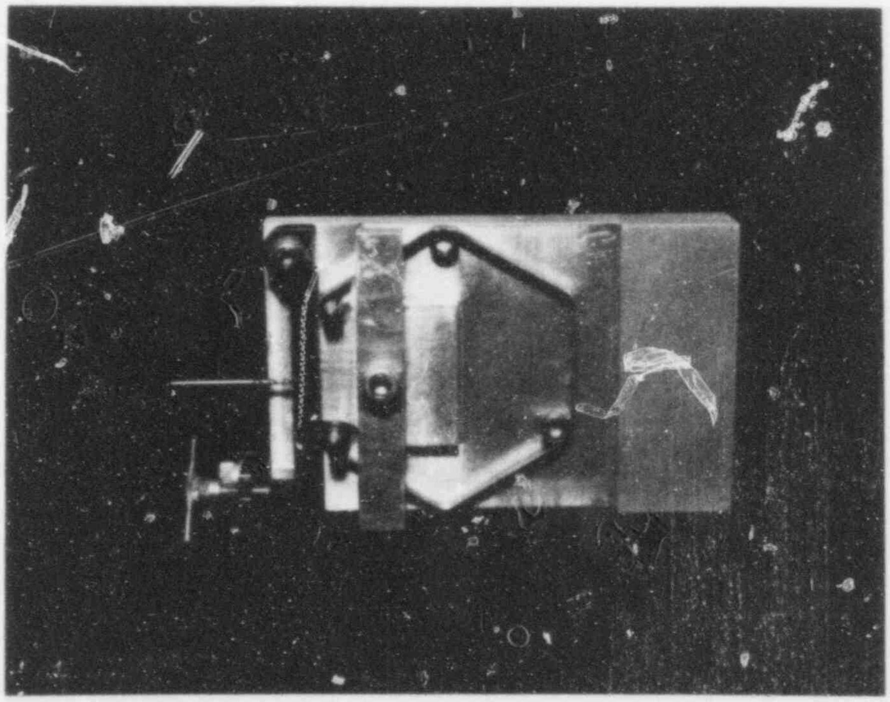

Fig. 104. Frame drilling jig.

Three sets of parallel wave-spring assemblies, stacked to form a complete spacer-grid, are shown in Fig. 105 together with their component elements. The spacer-grid is shown filled with rod cladding tubes in Fig. 106.

4. 37-Rod FLS-2, -3

A pilot lot of clad end fittings was completed and brazed to cladding. Furnace brazing caused clad warpage from stress relieving which necessitated straightening. Also, problems of uncontrolled braze flow occurred. It is probable that induction brazing will be used in future assemblies.

The test package hardware was strengthened at the attachment to the clad support plate and new clad support plates, spares, and miscellaneous hardware were procured. Molybdenum electrical passthroughs for the pressure vessel were made up to replace the water-cooled copper ones.

5. 271-Rod GCM Experiment

An order for clad end fittings was placed. The first module of the support frame insulation was sent out for bid and tentative cost information was received.

6. GCM Pressure Vessel

The pressure vessel for the DMFT is now in the process of fabrication at March Metalfab in Hayward, California. The main cylinder is currently being welded and radiographed in-house and is scheduled to go to a local shop for machining in April. The nozzle forgings are being fabricated in-house and scheduled for machining beginning in April. The cover plate materials are in-house except for one large end cover and machining on this is scheduled to start in April.

The last revised support system is being designed by March Metalfab for compliance with the ASME pressure vessel code so that the vessel can be installed partially into the pit of the modified test cell. This modification will add additional cost to the pressure vessel.

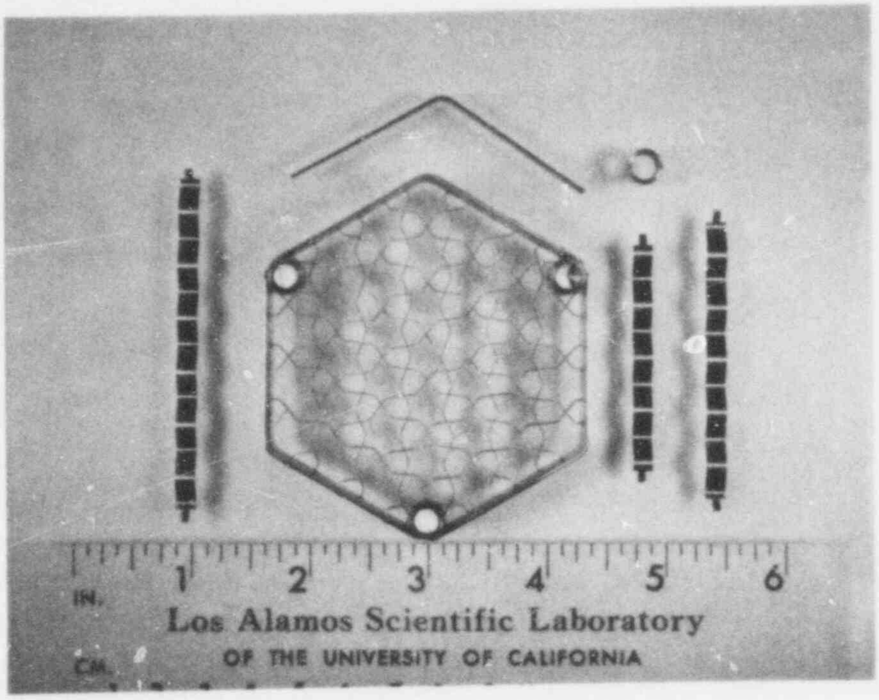

Fig. 105. Completed spacer-grid assembly and components.

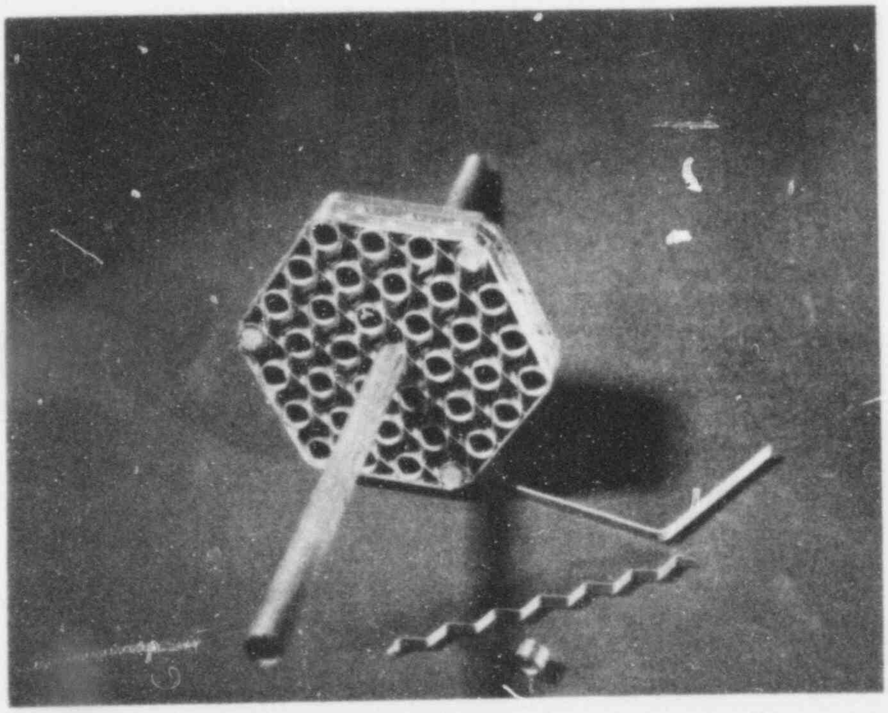

Fig. 106. Wave-spring spacer-grid assembly containing cladding segments.

E. Assembly, Installation, and Checkout

(R. Ortega and R. Renfro, Q-13)

Assembly of FLS-2 began on March 29, 1979.

F. Testing

(R. Ortega and D. L. Hanson, Q-13)

FLS-2 Spacer Grids

Preliminary examination of the interaction between the new wave-spring spacer-grids and the rod cladding indicated that the wave-spring concept does indeed improve the rotational compliance significantly in comparison with those of the ferrule-type spacer-grids used in FLS-1 and the prototype spacer-grid sample provided by General Atomic Co. Hopefully, the use of these new spacer-grids in FLS-2 will lead to longer simulated fuel rod life.

634 228

VI. CONTAINMENT SYSTEMS AND REACTOR SAFETY ANALYSES

(R. G. Gido, Q-6)

The following sections summarize the progress from two projects in the areas of containment systems and reactor safety funded by the NRC, Division of Systems Safety (DSS).

A. Containment Subcompartment Analysis

(R. G. Gido and J. S. Gilbert, Q-6)

A draft report on standard procedures for nuclear power plant subcompartment analysis has been prepared. This report is based on extensive sensitivity studies we have performed to determine the effects of various modeling assumptions on calculated component loads. The procedures developed were necessarily constrained by the currently applicable computer codes[56] and restrictions.[57]

B. Containment Code Verification

(G. J. E. Willcutt, Jr. and R. G. Gido, Q-6; and W. S. Gregory, WX-8)

The Battelle-Frankfurt Comparative Analysis Standard Problem (CASP) measurements have been compared with COMPARE code calculated values. Table XXVIII presents the calculated-to-measured pressure differences for the rooms involved in the experiment (see Fig. 107). Considerably greater calculated-to-measured differences are clearly indicated for rooms upstream of R5. This can be attributed to the current inability of the code to model the jet resulting from the flow from R7 through R4 and directly into R5. The code currently assumes the flow from R7 into R4 is brought to rest (i.e., stagnated) with the resulting pressure used to determine subsequent flow distribution. The error thereby introduced is approximately the difference between the calculated and measured R4 pressures. Application of this correction to all rooms upstream of R5 results in the favorable comparison between calculation and measurements shown in Table XXIX.

634 229

TABLE XXVIII

DIFFERENCE BETWEEN CALCULATED AND MEASURED ROOM PRESSURES FOR THE BATTELLE-FRANKFURT CASP

	Difference at 0.5 s		Difference at 1.0 s	
Room	Ba.	%	Bar	%
R6	0.14	9	0.20	13
R8	0.10	7	0.22	15
R7	0.08	6	0.18	13
R4	0.10	9	0.18	15
R5	- 0.02	-2	0.02	2
R9	0.01	1	0.01	1

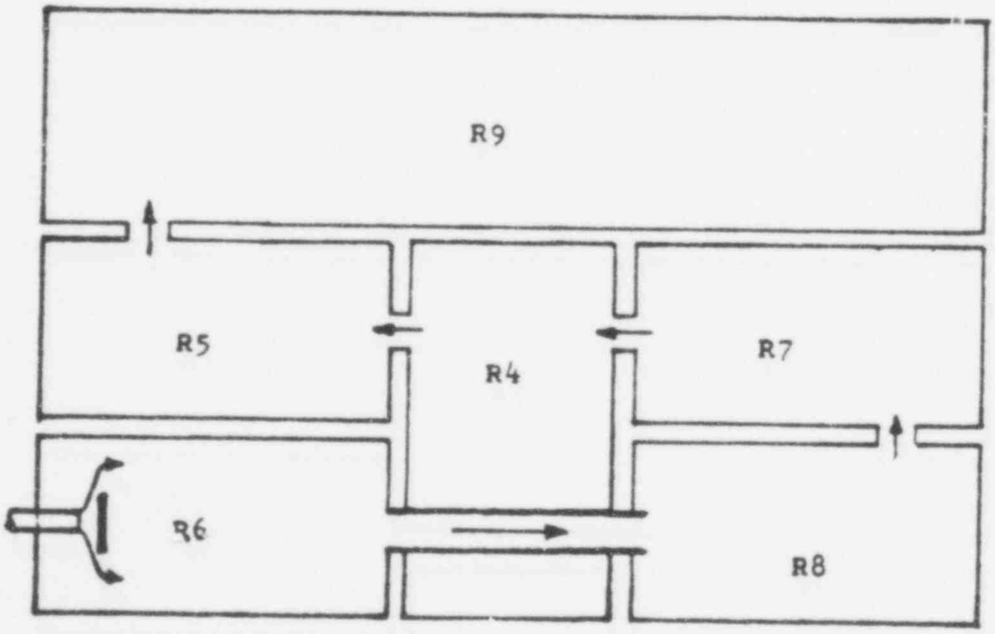

Fig. 107. Geometric arrangement: Battelle-Frankfurt Comparative Analysis Standard Problem (CASP).

634 230

TABLE XXIX

PER CENT DIFFERENCE BETWEEN CALCULATED AND MEASURED PRESSURES WITH R4 ERROR ACCOUNTING

Room	0.5 s	1.0 s
R6	3	4
R8	0	6
R7	-2	3
R4	0	3
R5	-2	2
R9	1	1

REFERENCES

1. D. Liles and W. Reed, "An Implicit Method for Two-Phase Fluid Dynamics," J. Comp. Phys. *26*, 390 (March 1978).
2. J. Mahaffy, "A Stability Enhancing Two-Step Method for One-Dimensional, Two-Phase Flow," Los Alamos Scientific Laboratory report (to be published).
3. C. William Gear, *Numerical Initial Value Problems in Ordinary Differential Equations* (Prentice Hall, New York, 1971).
4. "TRAC-P1: An Advanced Best Estimate Computer Code for PWR LOCA Analysis, Vol. 1. Methods, Models, User Information, and Programming Details,' Los Alamos Scientific Laboratory report LA-7279-MS (June 1978).
5. O. C. Iloeje, D. N. Plummer, P. Griffith, and W. M. Rohsenow, "An Investigation of the Collapse and Surface Rewet in Film Boiling in Forced Vertical Flow," ASME paper 73-WA/HT-29 (1973).
6. R. E. Henry, "A Correlation for the Minimum Film Boiling Temperature," AICHE Symposium Series *138*, 81-90 (1974).
7. James F. Jackson and Michael G. Stevenson, "Nuclear Reactor Safety Quarterly Progress Report for the Period October 1-December 31, 1978," Los Alamos Scientific Laboratory report LA-7769 (May 1979).
8. A. Premoli and W. T. Hancox, "An Experimental Investigation of Subcooled Blowdown with Heat Addition," Submission to Committee on the Safety of Nuclear Installation Specialists Meeting on Transient Two-Phase Flow (Toronto, Ontario, August 1976).
9. W. T. Hancox and A. Premoli, "Standard Problem 3: Subcooled Blowdown with Heat Addition," Submission to CSNI Ad Hoc Group on Emergency Core Cooling (Bethesda, Maryland, Revised March 1976).
10. W. T. Hancox to L. M. Shotkin, personal communication (August 31, 1976).
11. James F. Jackson and Michael G. Stevenson, "Nuclear Reactor Safety Quarterly Progress Report for the Period January 1-March 31, 1978," Los Alamos Scientific Laboratory report LA-7278-PR (June 1978).
12. B. Holzer, T. Kanzleiter, and F. Steinhoff, "Specification of OECD Standard Problem No. 6: Determination of Water Level and Phase Separation Effects During the Initial Blowdown Phase," Battelle-Institute, Frankfurt (February 1977).

13. "Flow of Fluids through Valves, Fittings, and Pipe," Crane Technical Paper No. 410 (1969).

14. E. Kerrings, GRS, Cologne, personal communication (1978).

15. V. Esparza, K. Sackett, and K. Stanger, "Experimental Data Report for Semiscale Mod-3 Integral Blowdown and Reflood Heat Transfer Test S-07-6 (Baseline Series)," Idaho National Engineering Laboratory report NUREG/CR-0467 (TREE-1226 (January 1979).

16. James F. Jackson and Michael G. Stevenson, "Nuclear Reactor Safety Progress Report for the Period April 1-June 30, 1978," Los Alamos Scientific Laboratory report LA-7481-PR (NUREG/CR-0385)(October 1978).

17. L. Rayleigh, "Pressure Due to Collapse of Bubbles," Phil. Mag. 34, 94 (1917).

18. M. S. Plesset and S. A. Zwick, "The Growth of Vapor Bubbles in Superheated Liquids," J. of Appl. Phys. 25, 493 (1954).

19. G. Birkhoff, R. S. Margulies, and W. A. Horning, "Spherical Bubble Growth," Phys. Fluids 1, 201 (1958).

20. V. Esparza and K. E. Sackett, "Experimental Data Report for Semiscale MOD-1 Test S-06-5 (LOFT Counterpart Test)," EG&G Idaho, Inc. report TREE-NUREG-1125 (1977).

21. D. G. Hall, "A Study of Critical Flow Prediction for Semiscale MOD-1 Loss-of-Coolant Accident Experiments," EG&G Idaho, Inc. report TREE-NUREG-1006 (1976).

22. K. A. Nilsson, "Large-Scale Critical Flow Testing," Electric Power Research Institute Journal 3 (May 1978).

23. W. C. Rivard and M. D. Torrey, "K-FIX: A Computer Program for Transient, Two-Dimensional, Two-Fluid Flow," Los Alamos Scientific Laboratory report LA-NUREG-6623 (1977).

24. K. D. Lathrop, "Reactor Safety and Technology Quarterly Progress Report for the Period October 1-December 31, 1976," Los Alamos Scientific Laboratory report LA-NUREG-6698-PR (February 1977).

25. J. G. Collier, Convective Boiling and Condensation (McGraw-Hill, New York, 1972) pp. 116-118.

26. V. G. Levich, Physicochemical Hydrodynamics (Prentice-Hall, Inc., Englewood Cliffs, New Jersey, 1962) p. 454.

27. D. Malnes, "Critical Two-Phase Flow Based on Non-Equilibrium Effects," Proc. of the ASME Heat Transfer Division Meeting, November 30-December 5, 1975 (Houston, Texas, 1975).

28. G. Friz, W. Riebold, and W. Schulze, "Studies on Thermodynamic Non-Equilibrium in Flashing Water," Proc. of the CSNI Specialists Meeting (Toronto, Canada, 1976).

29. J. R. Travis, C. W. Hirt, and W. C. Rivard, "Multidimensional Effects in Critical Two-Phase Flow," Nucl. Sci. Eng. 68, 338 (1978).

30. James F. Jackson and Michael G. Stevenson, "Nuclear Reactor Safety Quarterly Progress Report for the Period July 1-September 30, 1978," Los Alamos Scientific Laboratory report NUREG/CR-0522, LA-7567-PR.

31. C. W. Hirt, A. A. Amsden, and J. L. Cook, "An Arbitrary Lagrangian-Eulerian Computer Method for All Flow Speeds," J. Comp. Phys. 14, 227 (1974).

32. L. L. Smith, "SIMMER-II: A Computer Program for LMFBR Disrupted Core Analysis," Los Alamos Scientific Laboratory report LA-7515-M, NUREG/CR-0453 (October 1978).

33. P. E. Rexroth and A. J. Suo-Anttila, "SIMMER Analysis of SRI High Pressure Bubble Expansion Experiments," Los Alamos Scientific Laboratory report (to be published).

34. James F. Jackson and Michael G. Stevenson, "Nuclear Reactor Safety Progress Report for the Period April 1-June 30, 1977," Los Alamos Scientific Laboratory report LA-NUREG-6934-PR (1977).

35. W. J. Conover, Practical Nonparametric Statistics (Wiley, New York, 1971) p. 391.

36. C. Lipson and N. J. Sheth, Statistical Design and Analysis of Engineering Experiments (McGraw-Hill, New York, 1973) p. 496.

37. C. L. Fink, A. DeVolpi, and G. Stanford, "Advances in Clad Blockage Detection," Trans. of the Second Technical Exchange Meeting on Fuel- and Clad-Motion Diagnostics for LMFBR Safety Test Facilities, Argonne National Laboratory report ANL/RAS 76-34 (December 1976).

38. James F. Jackson and Michael G. Stevenson, "Nuclear Reactor Safety Progress Report for the Period October 1-December 21, 1977," Los Alamos Scientific Laboratory report LA-7195-PR (April 1978).

39. O. H. Nestor and C. Y. Huang, "Bismuth Germanate: A High-Z Gamma-Ray and Charged Particle Detector," IEEE Transact. Nucl. Sci. NS-22, 68-71 (February 1975).

634 234

40. A. E. Evans, B. Brown, and J. B. Marion, "Study of the $^{14}N(p,\gamma)^{15}O$ Reaction," Phys. Rev. 149, 863-879 (1966).

41. M. Stansfield, "Friction and Wear of Graphite in Dry Helium at 25, 400, and 800°C," Nuclear Applications 6, 313-320 (April 1969).

42. W. F. Thomson, Vibration Theory and Applications (Prentice Hall, Englewood Cliffs, New Jersey, 1965).

43. R. C. Dove and P. H. Adams, Experimental Stress Analysis and Motion Measurement (Charles E. Merrill Books, Inc., Columbus, Ohio, 1964).

44. R. J. Price, "Mechanical Properties of Graphite for High-Temperature Gas-Cooled Reactors: A Review," General Atomic report GA A13524 - UC77 (September 1975).

45. GASSAR-6, General Atomic Standard Safety Analysis Report.

46. Fort St. Vrain Generating Station - PSCo Document, "Core Fluctuation Investigation Status and Safety Evaluation Report," (August 1978).

47. K. D. Lathrop, "Reactor Safety and Technology Quarterly Progress Report for the Period July 1-September 30, 1976," Los Alamos Scientific Laboratory report LA-NUREG-6579-PR (December 1976).

48. J. G. Bennett, "A Physically Based Analytical Model for Predicting HTGR Core Seismic Response," Proceedings of the Japan-US Seminar on HTGR Safety Technology, Brookhaven National Laboratory report BNL-NUREG-50689, Vol. I. (September 1977).

49. C. E. Apperson and C. E. Lee, "DASH: A Multicomponent Time-Dependent Concentration Diffusion with Radioactive Decay Program," Los Alamos Scientific Laboratory preliminary version report (September 1979).

50. DISSPLA, a library of FORTRAN subroutines for data plotting, Integrated Software Systems Corporation, San Diego, California.

51. C. E. Apperson, L. M. Carruthers, and C. A. Anderson, "Fission Product Holdup in Graphite," Proceedings of the U.S.-Japan Seminar on HTGR Safety Technology, Vol. I (Fuji, Japan, November 1978).

52. C. E. Lee, unpublished notes (October 1977).

53. J. Appel and B. Roos, "A Study of the Release of Radioactive Metallic Isotopes from High-Temperature, Gas-Cooled Reactors," Nuclear Science and Engineering 34, 201-213 (1968).

54. M. Schwartz, D. Seagley, and M. Mendonca, "SORS: Computer Programs for Analyzing Fission Product Release from HTGR Cores During Transient Temperature Excursions," General Atomic Co. report GA A12462 (April 1974).

55. L. M. Carruthers and C. E. Lee, "LARC-1: A Los Alamos Release Calculation Program for Fission Product Transport in HTGRs During the LOFC Accident," Los Alamos Scientific Laboratory report LA-NUREG-6563-MS (1976).

56. R. G. Gido, J. S. Gilbert, R. G. Lawton, and W. L. Jensen, "COMPARE-MOD 1: A Code for the Transient Analysis of Volumes with Heat Sinks, Flowing Vents, and Doors," Los Alamos Scientific Laboratory report LA-7199-MS (March 1978).

57. "Standard Review Plan for the Review of Safety Analysis Reports for Nuclear Power Plants," Sec. 6.2.1.2, Office of Nuclear Reactor Regulation, U.S. Nuclear Regulatory Commission report NUREG-75-087, LWR edition (September 1975).

DISTRIBUTION

	Copies
Nuclear Regulatory Commission, Categories R-4, R-7, and R-8	763
Technical Information Center, Oak Ridge, Tennessee	2
Los Alamos Scientific Laboratory	200
	965

☆U.S. Government Printing Office: 1979 – 677-013/116

634 237

Available from
US Nuclear Regulatory Commission
Washington, DC 20555

Available from
National Technical Information Service
Springfield, VA 22161

Microfiche $3.00

001-025	4.00	126-156	7.25	251-275	10.75	376-400	13.00	501-525	15.25
026-050	4.50	151-175	8.00	276-300	11.00	401-425	13.25	526-550	15.50
051-075	5.25	176-200	9.00	301-325	11.75	426-450	14.00	551-575	16.25
076-100	6.00	201-225	9.25	326-350	12.00	451-475	14.50	576-600	16.50
101-125	6.50	226-250	9.50	351-375	12.50	476-500	15.00	601-up	

Note: Add $2.50 for each additional 100-page increment from 601 pages up.

634 238